Phase-Space Localization of Chaotic Resonance States due to Partial Transport Barriers

Dissertation
zur Erlangung des akademischen Grades
Doctor rerum naturalium

vorgelegt von

Martin Julius Körber
geboren am 05.04.1988 in Erfurt

Institut für Theoretische Physik
Fachrichtung Physik
Fakultät für Mathematik und Naturwissenschaften
Technische Universität Dresden
2016

Eingereicht am 21. September 2016

Begutachtung:

Prof. Dr. Roland Ketzmerick
Technische Universität Dresden

Prof. Dr. Henning Schomerus
Lancaster University

Abstract

Classical partial transport barriers govern both classical and quantum dynamics of generic Hamiltonian systems. Chaotic eigenstates of quantum systems are known to localize on either side of a partial barrier if the flux connecting the two sides is not resolved by means of Heisenberg's uncertainty. Surprisingly, in open systems, in which orbits can escape, chaotic resonance states exhibit such a localization even if the flux across the partial barrier is quantum mechanically resolved. We explain this using the concept of conditionally invariant measures by introducing a new quantum mechanically relevant class of such fractal measures. We numerically find quantum-to-classical correspondence for localization transitions depending on the openness of the system and on the decay rate of resonance states. Moreover, we show that the number of long-lived chaotic resonance states that localize on one particular side of the partial barrier is described by an individual fractal Weyl law. For a generic phase space, this implies a hierarchy of fractal Weyl laws, one for each region of the hierarchical decomposition of phase space.

Zusammenfassung

Klassische partielle Transportbarrieren bestimmen sowohl die klassische als auch die quantenmechanische Dynamik generischer hamiltonscher Systeme. Es ist bekannt, dass chaotische Eigenzustände von Quantensystemen jeweils nur auf einer Seite einer partiellen Barriere lokalisieren, solange der Fluss, der beide Seiten verbindet, im Sinne der heisenbergschen Unschärferelation quantenmechanisch nicht augelöst wird. Überraschenderweise zeigen chaotische Resonanzzustände in offenen Systemen, in denen Trajektorien das System verlassen können, eine ebensolche Lokalisierung, selbst wenn der Fluss durch die partielle Barriere quantenmechanisch aufgelöst ist. Wir erklären dies mithilfe von bedingt invariaten klassischen Maßen, indem wir eine neue, quantenmechanisch relevante Klasse solcher fraktalen Maße einführen. Am Beispiel zweier Lokalisierungsübergänge in Abhängigkeit der Stärke der Öffnung des Systems und der Zerfallsrate der Resonanzzustände können wir die Korrespondenz von Klassik und Quantenmechanik numerisch bestätigen. Überdies stellt sich heraus, dass die Anzahl langlebiger chaotischer Resonanzzustände, die auf einer bestimmten Seite der partiellen Barriere lokalisieren, durch ein individuelles fraktales Weylgesetz beschrieben wird. In einem generischen gemischten Phasenraum ergibt dies eine Hierarchie fraktaler Weylgesetze, jeweils eines für jede Region der hierarchischen Zerlegung des Phasenraumes.

Contents

Chapter 1

Introduction

The understanding of transport in its various manifestations lies at the heart of physics. One may think of the historically important examples of Ohm's law on the electric current through a conductor [1], of the flow of fluids as described by the Navier–Stokes equation [2], or of the diffusive transfer of heat [2]. Also in modern physics transport phenomena are constantly subject to research, such as the quantum Hall effect giving rise to quantized values of the Hall conductivity [3], superconductivity that implies vanishing electrical resistance [4], or quantum teleportation by entanglement [5]. Quite often in quantum mechanics, the transport behavior is deeply related to the localization of eigenstates or wave packets, e.g., strong Anderson localization due to disorder suppresses diffusion and implies a metal–insulator transition [6, 7], weak localization due to time-reversal invariance yields corrections to the classical Drude conductivity of a metal [8], localization of edge states due to topological protection is related to the quantized Hall conductivity [9], and many-body localization in Fock space implies a metal–insulator transition at finite temperatures for systems of interacting particles [10].

Quantum eigenstates can also exhibit localization due to classically restrictive phase-space structures [11–34]: A classical Hamiltonian system generically exhibits a mixed phase space of regular and chaotic motion [35]. The simplest systems to observe this coexistence are two-dimensional time-discrete symplectic maps, which originate for instance from autonomous Hamiltonian systems with two degrees of freedom or from time-dependent Hamiltonian systems with one degree of freedom. In such systems an invariant torus of regular motion is impenetrable under the time evolution, that is, classical transport from one side of the torus to the other is completely suppressed [23]. However, quantum mechanics allows for a small transmission of wave packets across the torus under time evolution by dynamical tunneling [36]. Still, the probability for this process is small and quantum eigenstates are essentially confined to one side of the torus. In this way, a regular torus is a total barrier for transport in phase space. On the other hand, there also exist partial transport barriers which are omnipresent in the chaotic component of a generic mixed phase space and typically occur in an infinite hierar-

chical pattern [16,17,23]. A partial barrier admits a small classical flux ϕ from one side to the other. Interestingly, a quantum wave packet can pass the partial barrier if its flux is quantum mechanically resolved by means of Heisenberg's uncertainty ($\phi \gg h$) but the wave packet remains on one side if the classical flux is not resolved ($\phi \ll h$) [17, 19, 20, 24, 31, 32, 37–39]. Here h refers to an effective size of Planck's cell. We emphasize that quantum mechanics can therefore suppress transport that is classically allowed, in contrast to the tunneling process [6, 32, 40, 41]. In the same spirit, chaotic eigenstates are equipartitioned with respect to the partial barrier if $\phi \gg h$, as if there were no partial barrier and they turn out to localize on either side of the partial transport barrier for $\phi \ll h$. In fact, there is a universal localization transition from one regime to the other, depending only on the scaling parameter ϕ/h [32].

So far, we considered systems isolated from their environment. This is a theoretical idealization that might be experimentally reasonable on problem specific time or energy scales. The description of a variety of phenomena, however, explicitly requires to incorporate the openness of the system such as depolarization, dephasing, or spontaneous emission [42]. In this thesis we consider a specific kind of open systems, namely systems that allow for escape [33, 34, 43–61]. Classically, one might think of a two-dimensional billiard with hole in the boundary or of more general types of scattering systems in which orbits can escape [55, 56, 62]. Quantum mechanically, this corresponds to a subunitary time-evolution operator where the subunitarity refers to the fact that its spectrum lies inside the unit circle accounting for the decay [48, 63–66]. Eigenstates of such open quantum systems are called resonance states. This theoretical framework is well suited to describe optical microcavities for instance [67]. Their emission pattern is determined by the phase-space localization of their resonance states [67–75]. As partial barriers can have a huge influence on the localization of eigenstates in closed systems it is reasonable to expect that they are also relevant for open systems like optical microcavities, cf. [75]. However, is the above theory on the localization of eigenstates for closed systems still relevant in presence of an opening?

In this thesis we demonstrate that chaotic resonance states can localize on either side of a partial barrier even in the regime of $\phi \gg h$, where in the closed system typical chaotic eigenstates are equipartitioned. In particular, we find a smooth transition from equipartition to localization of long-lived resonance states on one side of the partial barrier if the system is opened. In addition, we find a transition from localization on one side of the partial barrier to localization on the other side depending on the decay rate of the resonance states. This phenomenology shows that partial barriers are even more important in open systems than in closed systems. We explain both localization transitions using classical concepts. Based on the important work by Keating et al. [49] and Nonnenmacher et al. [51] the classical counterpart of a quantum resonance state is found to be given by a conditionally invariant measure (CIM). These measures are invariant under the classical dynamics up to a global

factor compensating the decay [43, 50, 56, 76]. However, for each decay rate γ there exist infinitely many different CIMs and it is not clear which of them is quantum mechanically relevant. We propose the class of γ-natural CIMs. By analytical and numerical analysis of the partial-barrier map, which is a model system with a single partial barrier, and of the generic standard map with a mixed phase space, we demonstrate quantum-to-classical correspondence between the localization of chaotic resonance states and of γ-natural CIMs. This explains both observed localization transitions of chaotic resonance states and gives a fundamental insight into quantum-to-classical correspondence for open systems. Moreover, using the localization of chaotic resonance states due to partial barriers we generalize the fractal Weyl law [47, 48, 51–53, 61, 71, 77–97] on the number of long-lived chaotic resonance states from chaotic open systems to generic open systems with a mixed phase space. To this end, we use the fact that the classical fractal repeller, that is, the set of points in phase space which do not escape under classical time evolution, effectively exhibits individual fractal dimensions associated with the hierarchical decomposition of phase space by partial barriers [98]. This gives rise to a hierarchy of fractal Weyl laws. We give a heuristic argument for their presence and support it numerically for the partial-barrier map and the generic standard map. The main results of this thesis have already been published in Refs. [33, 34].

The manuscript is organized as follows: In Chap. 2 we introduce resonance states and open quantum maps from a general perspective. The fundamentals on Hamiltonian chaos relevant for this thesis are discussed in Chap. 3, putting focus on the chaotic transport in presence of partial barriers and the escape from chaotic systems. Chapter 4 is dedicated to the detailed introduction of model systems with a single partial barrier that allow for an analytical and a numerical investigation over a broad range of parameters without the complexity of an infinite hierarchy of partial barriers. Following a review on the localization transition of chaotic eigenstates due to a partial barrier in closed systems in Chap. 5, we numerically observe the two new localization transitions for open systems in Chap. 6. A theoretical discussion on the semiclassical structure of chaotic resonance states, reviewing known results and introducing the new class of γ-natural CIMs, is presented in Chap. 7. In Chaps. 8 and 9 we investigate quantum-to-classical correspondence between chaotic resonance states and γ-natural CIMs for the partial-barrier map and the standard map. Based on these results, we generalize the fractal Weyl law to generic systems with a mixed phase space in Chap. 10. We give an extensive outlook in Chap. 11 where we discuss the next steps towards an application of our results for optical microcavities. Note that in order to appreciate the importance of some results we explicitly show their proofs or derivations in the main text even if they are rather technical and not essential for the further understanding. In such cases, the beginning and end of the proofs is clearly visible in the text and they may therefore be skipped if necessary.

Chapter 2

Open Quantum Systems

In this chapter we introduce resonance states of open quantum systems from a general perspective and discuss the relation to eigenvectors of subunitary quantum maps which are studied throughout this thesis. To this end, we briefly review a common modeling approach for open quantum systems in Sec. 2.1, which leads to the Lindblad master equation. In Sec. 2.2 we restrict our considerations to a special kind of open quantum systems, namely scattering systems, and discuss the phenomenon of resonance scattering. The widely used method to study resonances in terms of analytic properties of the scattering matrix is described in Sec. 2.3. In Sec. 2.4 it is outlined how to effectively model a scattering system by a nonhermitian Hamiltonian. Note that in Secs. 2.1–2.4 the derivation of some relations is presented only very short or not at all as these sections are mainly intended to embed our later results in a broader context. We conclude this chapter by introducing open quantum maps in Sec. 2.5, where we also discuss the eigenvalue problem for subunitary matrices.

2.1 General Theory

Every physically relevant system interacts with its environment. This interaction can be realized in terms of particle exchange or heat transfer for instance. Note that such an interaction can be desired or not. Think of a measurement device like a scanning electron microscope where information about the target object can be extracted from the scattered electrons [99], or of an optical cavity where losses should be reduced in order to improve the spectral coherence properties of a laser [67]. Full isolation of a physical system is a theoretical idealization which may be reasonable on certain problem specific time or energy scales.

Let us briefly review the typical theoretical modeling of open quantum systems. An ensemble of quantum states is described by a density operator ϱ, that is a hermitian, positive semidefinite operator of unit trace acting on the system's Hilbert space [100,101]. A reasonable model for the time evolution, regardless of the specific properties of the system, has to map

density operators to density operators. For a closed system described by the Hamiltonian H, this is ensured by von Neumann's equation,

$$\dot{\varrho}(t) = -\frac{i}{\hbar}[H, \varrho(t)], \quad \varrho(0) = \varrho_0, \tag{2.1}$$

which is solved by the unitary evolution

$$\varrho(t) = U(t)\varrho_0 U(t)^*, \quad U(t) = \exp\left[-\frac{i}{\hbar}Ht\right] \tag{2.2}$$

in the autonomous case [102, Sec. 20.2]. Here $U(t)^*$ denotes the adjoint of $U(t)$. Unitary time evolution, however, is too restrictive to describe typical phenomena in open systems such as depolarization, dephasing, or spontaneous emission [42, Sec. 6.1.6]. In order to describe such phenomena, it proves useful to consider the more general class of completely positive, trace preserving maps. Such maps also ensure that density operators are mapped to density operators. According to Stinespring's dilation theorem [103] any completely positive, trace preserving map $\mathcal{E}_t$ can be represented by

$$\varrho(t) = \mathcal{E}_t(\varrho_0) = \mathrm{tr}_{\,\mathrm{env}}\left[U(t)(\varrho_0 \otimes \varrho_{\mathrm{env}})U(t)^*\right], \tag{2.3}$$

with an appropriate density operator ϱ_{env} and a unitary operator $U(t)$ [104, Sec. 3.15]. Intuitively speaking, the initial state ϱ_0 of the open system is embedded in its closed environment by $\varrho_0 \otimes \varrho_{\mathrm{env}}$, the time evolution of which is unitary. Finally, the environmental degrees of freedom are traced out, giving the evolved density matrix $\varrho(t)$ in the open subsystem. Interestingly, the explicit time evolution in Eq. (2.3) allows a formulation in terms of a differential equation, so to say the open system's equivalent of the von Neumann equation, Eq. (2.1). Assuming the Markov property, $\mathcal{E}_{s+t} = \mathcal{E}_s\mathcal{E}_t$, one finds a hermitian operator H, an orthonormal operator basis $\{F_k\}_k$, and nonnegative coefficients $\{c_k\}_k$ such that

$$\dot{\varrho}(t) = \underbrace{-\frac{i}{\hbar}[H, \varrho(t)]}_{\text{conservative}} + \underbrace{\frac{1}{2}\sum_k c_k\big([F_k\varrho(t), {F_k}^*] + [F_k, \varrho(t){F_k}^*]\big)}_{\text{dissipative}}, \tag{2.4}$$

which contains a dissipative contribution in addition to the conservative von Neumann term as indicated [105, 106]. Equation (2.4) is known as the Lindblad master equation in diagonal form.

2.2 Resonance Scattering

Let us focus on a special category of open systems, namely scattering systems. The main idea of the scattering process is as follows [107–110]: One or more free particles approach a bounded region where they interact with an external potential, by collisions, or chemical reactions for example. The products then escape from the interaction region again as free particles. Although the general framework outlined above in Sec. 2.1 is in principle able to describe scattering processes, cf. Refs. [111,112], there are more adapted methods.

Consider the stationary Schrödinger equation,

$$\left[-\frac{\hbar^2}{2m}\triangle + V(r)\right]\psi(k,\mathbf{r}) = \frac{\hbar^2 k^2}{2m}\psi(k,\mathbf{r}), \tag{2.5}$$

for a nonrelativistic particle of mass m and energy $E = \hbar^2 k^2/(2m)$ subject to a central potential V with $\lim_{r\to\infty} rV(r) = 0$. It has solutions of the form $\psi_{\ell m}(k,\mathbf{r}) = r^{-1}u_\ell(k,r)Y_{\ell m}(\vartheta,\varphi)$ where $Y_{\ell m}$ denotes the spherical harmonics and u_ℓ solves the radial Schrödinger equation,

$$u_\ell''(k,r) - \left(\frac{\ell(\ell+1)}{r^2} + \frac{2m}{\hbar^2}V(r)\right)u_\ell(k,r) + k^2 u_\ell(k,r) = 0, \tag{2.6}$$

where the derivative is taken with respect to the variable r [100, §32]. Depending on the specific shape of V, the solutions of Eq. (2.5) correspond to bound states for discrete energy eigenvalues of $E < 0$, or to unbound scattering states for the continuous spectrum with $E > 0$ [100, §10]. However, there can exist scattering states which are particularly important. Scattering states tunneling through a potential barrier for instance are associated with an enhanced life time compared to scattering states with energy above the barrier threshold [100, §134], see illustration in Fig. 2.1. Such states are usually called resonance states, quasibound states, quasistationary states, or metastable states. They admit quasidiscrete energies within the continuous spectrum [100, §134]. Remarkably, resonance states give rise to characteristic peaks in the experimentally observable scattering cross section [100, §145].

In order to understand the appearance of these characteristic peaks, let us consider the historically important example of scattering of slow neutrons at a nucleus [113], where we closely follow the discussion in Sections T.3 and T.4 from Ref. [107]. In this case, it is useful to assume that the neutron does not interact with the nucleus for $r > R$, with the radius R of the nuclear sphere. Dealing with slow neutrons, the scattering process is dominated by the s-wave contribution, $\ell = 0$. Equation (2.6) thus reads

$$u''(k,r) + k^2 u(k,r) = 0 \tag{2.7}$$

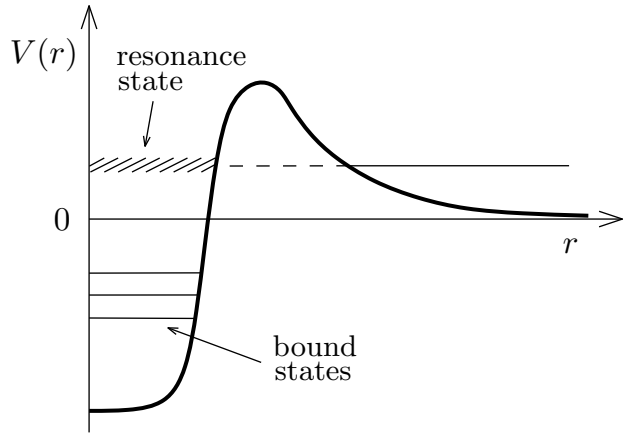

Figure 2.1. Sketch of central potential V with tunneling barrier (thick solid line). Discrete levels with energy below zero correspond to bound states while quasidiscrete levels with energy above zero but below the tunneling threshold correspond to long-lived resonance states.

for $r > R$, dropping the fixed index ℓ. This is solved by

$$u(k,r) = A\left(e^{-ikr} - S(k)e^{ikr}\right) \tag{2.8}$$

with an appropriate factor A and the scattering matrix element $S(k)$. The scattering matrix therefore describes how the incident wave is affected by the target depending on the wave number k. Defining $f(k) := R\,u'(k,R)/u(k,R)$ and inserting the solution u from Eq. (2.8), the scattering matrix element is given by

$$S(k) = \frac{f(k) + ikR}{f(k) - ikR}\, e^{-2ikR}. \tag{2.9}$$

With this, the experimentally relevant cross section[1] $\sigma = (\pi/k^2)\,|1 - S(k)|^2$ for elastic scattering reads

$$\sigma = \frac{\pi}{k^2}\left|\underbrace{\frac{-2ikR}{f(k) - ikR}}_{A_{\mathrm{res}}} + \underbrace{\left(e^{2ikR} - 1\right)}_{A_{\mathrm{pot}}}\right|^2, \tag{2.10}$$

where A_{pot} is referred to as potential scattering term and A_{res} implies a resonance phenomenon. To demonstrate this, a zero E_{res} of f is considered, where f is now understood as a function

[1] Note that there is a factor of π missing in Eq. (A37) in Ref. [107]. The correct expression may be found in Ref. [108, Sec. 2.6] or in Ref. [100, §142].

of energy, $E = \hbar^2 k^2/(2m)$. A first order Taylor expansion of f in the vicinity of E_{res} yields

$$A_{\text{res}} = \frac{i\Gamma}{(E - E_{\text{res}}) + i\frac{\Gamma}{2}} \tag{2.11}$$

with $\Gamma := -2kR/f'(E_{\text{res}})$. Close to E_{res}, A_{pot} is small compared to A_{res} such that

$$\sigma \approx \frac{\pi}{k^2} \frac{\Gamma^2}{(E - E_{\text{res}})^2 + \frac{\Gamma^2}{4}}. \tag{2.12}$$

This is the characteristic Breit–Wigner profile of isolated peaks in the scattering cross section. [107]

The intuitive interpretation of this resonance peak is based on Bohr's compound nucleus model [114], see also Refs. [107, Sec. T.2] or [100, §145]. At the resonance energy E_{res} the incoming neutron together with the target nucleus forms a compound nucleus in an excited state [107]. The energy of the incoming neutron is then distributed over all constituents such that a single particle does not have the energy necessary to escape from the compound [100]. Statistically, it takes a relatively long time until the event that sufficient energy is stored in a single particle of the compound which is then able to escape [100]. The compound nucleus, thus, represents a long-lived quasibound state, also called resonance state. The corresponding resonance peaks in the scattering cross section are indeed observed in experiment, see Fig. 2.2 [115, Fig. 6].

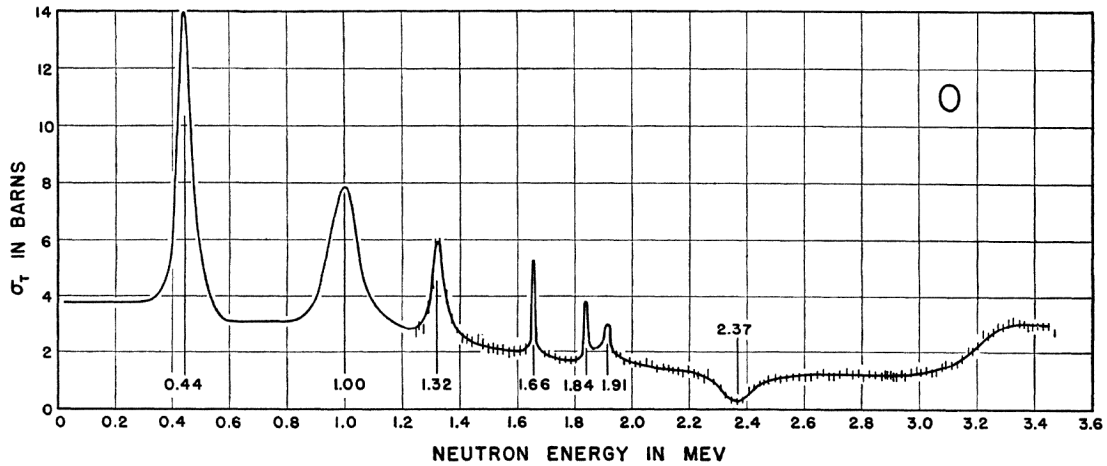

Figure 2.2. The experimentally measured total cross section of oxygen depending on the energy of the incoming neutrons exhibits clear resonance peaks. Reprinted figure with permission from [C. K. Bockelman, D. W. Miller, R. K. Adair, and H. H. Barschall, Phys. Rev. **84**, 69 (1951)] Copyright (2016) by the American Physical Society.

2.3 Analytic Properties of the Scattering Matrix

A common approach to investigate both resonance states as well as bound states on the same footing is the study of the analytic properties of the scattering matrix. To this end, the scattering matrix S is considered as a function of complex wave number k or of complex energy E, and one seeks for its poles within the complex plane. For the present case of s-wave scattering, it is useful to introduce Jost functions, see Refs. [110, Sec. 12.1] or [109, Secs. 11.1, 11.2]. It can be shown that physical s-wave scattering solutions of Eq. (2.6) obey the boundary conditions [100, §33]

$$u(k,0) = 0, \tag{2.13a}$$

$$u(k,r) \sim \sin(kr+\delta), \qquad (r\to\infty) \tag{2.13b}$$

with the scattering phase shift δ. There are also other solutions which obey the less restrictive regularity condition [109, 110]

$$u(k,0) = 0, \tag{2.14a}$$

$$u'(k,0) = 1. \tag{2.14b}$$

These regular solutions turn out to be useful as they allow for a specific representation of the scattering matrix. A regular solution can asymptotically be expressed as

$$u(k,r) \sim \frac{1}{2ik}\left[\mathscr{F}(-k)e^{ikr} - \mathscr{F}(k)e^{-ikr}\right], \qquad (r\to\infty) \tag{2.15}$$

with the analytic Jost function $\mathscr{F}$ [110][2]. Hence, comparing Eqs. (2.8) and (2.15), the scattering matrix element reads

$$S(k) = \frac{\mathscr{F}(-k)}{\mathscr{F}(k)}, \tag{2.16}$$

such that the poles of S are determined by the zeros of the analytic function $\mathscr{F}$. Given k_0 such that $\mathscr{F}(k_0)=0$, the regular solution u from Eq. (2.15) scales as $e^{ik_0 r}$ which is a square-integrable bound solution for $\operatorname{Im} k_0 > 0$ and unbound for $\operatorname{Im} k_0 < 0$. For bound solutions which have real negative energy $E = \hbar^2 k^2/(2m)$, it is necessarily $\operatorname{Re} k_0 = 0$. For unbound solutions, however, the real part of k_0 does not have to vanish. Due to a symmetry of $\mathscr{F}$, the poles for $\operatorname{Im} k_0 < 0$ appear in pairs on both sides of the imaginary axis [109]. Note that there are also poles with $\operatorname{Re} k_0 = 0$ and $\operatorname{Im} k_0 < 0$, which correspond to so-called virtual or

[2]Note that there are different versions of the Jost function $\mathscr{F}$ used in the literature varying in the sign of their argument k, cf. Refs. [109, 110]. Depending on this sign, its zeros associated with bound states are also related to $\operatorname{Im} k_0 < 0$ and, vice versa, for the unbound states to $\operatorname{Im} k_0 > 0$ [109]. We follow the notation in Ref. [110], such that the zeros of $\mathscr{F}$ coincide with the position of the poles of S.

antibound states, but they are of no relevance here, cf. [110, Sec. 12.1.4] or [116, Sec. 3.6.7]. The described typical structure of poles of $S(k)$ is sketched in Fig. 2.3(a). In order to see the relation of poles in $S(k)$ for $\operatorname{Im} k_0 < 0$ to resonance peaks in the scattering cross section, Eq. (2.12), it is useful to represent the scattering matrix in terms of the energy E. To this end, it is necessary to distinguish between the two different Riemann sheets

$$k = \sqrt{\frac{2m}{\hbar^2}|E|}\exp\left[i\frac{\arg(E)}{2}\right], \tag{2.17a}$$

$$k = \sqrt{\frac{2m}{\hbar^2}|E|}\exp\left[i\left(\frac{\arg(E)}{2}+\pi\right)\right], \tag{2.17b}$$

the first of which is related to the bound solutions (also called physical sheet), $\operatorname{Im} k > 0$, while the second describes unbound solutions (also called unphysical sheet), $\operatorname{Im} k < 0$. Note that by convention, the argument $\arg(E)$ of the complex number E is in $[0, 2\pi)$. The position of poles of the scattering matrix element as a function of E, distinguishing between both Riemann sheets, is sketched in Fig. 2.3(b).

Let us focus again on the relation of poles in the first sheet to bound states. It is useful to note, that the scattering matrix is more generally defined by $S = \Omega_-^*\Omega_+$ with the Møller operators $\Omega_\pm = \mathbb{1}+(E\pm i\varepsilon-H)^{-1}V$, $(\varepsilon \searrow 0)$, in terms of the Hamiltonian $H = -\hbar^2/(2m)\triangle+V$

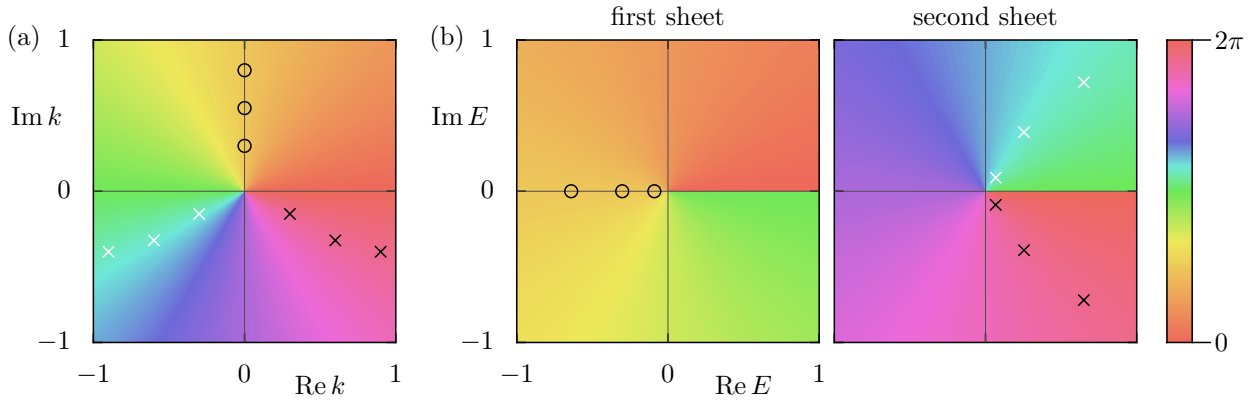

Figure 2.3. (a) Sketch of the position of poles in the scattering matrix element $S(k)$ as a function of complex wave number k. The color in the background represents the argument of the complex number k, see color code on the right. Poles on the imaginary axis in the physical sheet, $\operatorname{Im} k > 0$, visualized by circles, correspond to bound states. Poles off the imaginary axis in the unphysical sheet, $\operatorname{Im} k < 0$, visualized by crosses, correspond to resonance states. Note that the resonance poles come in pairs of a decaying resonance state (black) and an increasing resonance state (white). (b) Position of poles in the scattering matrix element as a function of complex energy, $E \sim k^2$, distinguishing between the first sheet (left), Eq. (2.17a), and the second sheet (right; same axes as first sheet), Eq. (2.17b). The color in the background represents the argument of k to demonstrate the relation to (a).

in the Lippmann–Schwinger representation [110]. Hence, poles of the scattering matrix are directly related to poles of the resolvent $(E - H)^{-1}$ [117, Sec. XI.6], which is an analytic operator-valued function of the energy E on the complement $\mathbb{C}\backslash\sigma(H)$ of the spectrum $\sigma(H)$ of H [118, Thm. VIII.2]. The discrete spectrum for $E < 0$ on the real axis, associated with bound states, therefore admits isolated singularities to the resolvent and, thus, also to the scattering matrix. Likewise, the continuous spectrum for real values $E > 0$ admits a branch cut as can be seen in Fig. 2.3(b). It is still possible to find an analytical (or meromorphic) continuation from the upper half plane to the lower half plane across the branch cut by switching to the second sheet [119, Sec. XII.6], see the color plot in the background of Fig. 2.3(b, c). Consider a well isolated simple pole at $E = E_{\mathrm{res}} - i\Gamma/2$ on the second sheet. The representation $\sigma = 4\pi|\mathcal{A}|^2$ of the elastic scattering cross section σ in terms of the partial s-wave scattering amplitude $\mathcal{A} = (S-1)/(2ik)$ [100, §123], suggests to investigate the influence of the second sheet pole on $\mathcal{A}$. A Laurent expansion of $\mathcal{A}$ around $E = E_{\mathrm{res}} - i\Gamma/2$ gives

$$\mathcal{A}(E) = \frac{\varrho}{E - (E_{\mathrm{res}} - i\frac{\Gamma}{2})} + \mathcal{A}_{\mathrm{b}}(E), \tag{2.18}$$

where ϱ denotes the residue of $\mathcal{A}$ at the pole and $\mathcal{A}_{\mathrm{b}}$ is the analytic background in an appropriate neighborhood of the pole [119, Sec. XII.6]. If the background is negligible, this imposes the Breit–Wigner resonance peak of width Γ in the scattering cross section, cf. Eq. (2.12). Hence, simple poles in the second sheet of the scattering matrix are interpreted as resonances. It can be seen by time evolution that the norm of a resonance state ψ at energy $E = E_{\mathrm{res}} - i\Gamma/2$ can describe decay or capture depending on the sign of Γ,

$$\|e^{-\frac{i}{\hbar}Et}\psi\|^2 = e^{-\frac{\Gamma}{\hbar}t}. \tag{2.19}$$

Such decay behavior is typically also characterized by the decay rate $\gamma = \Gamma/\hbar$ or the life time $\tau = 1/\gamma$. As a consequence of Heisenberg's energy–time uncertainty, $\Delta E\,\Delta t \sim \hbar$, the finite life time τ of a resonance state comes along with the finite width Γ of the quasidiscrete energy level [100, §44]. In this work, we only study decaying resonance states with $\Gamma > 0$ in the lower half plane of the second sheet, cf. Fig. 2.3(b).

2.4 Effective Nonhermitian Hamiltonian

Of particular importance for the interpretation of this thesis is the fact that the scattering problem can be described in terms of an effective nonhermitian Hamiltonian, or equivalently in terms of an effective subunitary time-evolution operator. There are different ways to obtain this effective Hamiltonian, a prominent one of which is known as complex scaling [119, Sec. XII.6]. Here, we review a formally more direct way. One starts with a Caley transform of the

scattering matrix,

$$S = (\mathbb{1} - iK)(\mathbb{1} + iK)^{-1}, \tag{2.20}$$

giving the reactance matrix $K = -i(\mathbb{1} - S)(\mathbb{1} + S)^{-1}$ [110]. The crucial idea is then to decompose the full scattering system into the bounded interaction region, described by an internal closed-system Hamiltonian H_{int}, and its coupling to open decay channels, mediated by the matrix W, which depends on energy in general [63–65]. This allows to express the reactance matrix in form of

$$K(E) = \pi W^*(E)(E - H_{\text{int}})^{-1}W(E). \tag{2.21}$$

It is typically assumed that W only depends weakly on energy, which eventually leads to the Mahaux–Weidenmüller formula [64, 65, 120],

$$S(E) = \mathbb{1} - 2\pi i\, W^*(E - H_{\text{eff}})^{-1}W, \tag{2.22}$$

with the nonhermitian effective Hamiltonian

$$H_{\text{eff}} = H_{\text{int}} - i\pi WW^*. \tag{2.23}$$

The derivation of Eq. (2.22) from Eqs. (2.20) and (2.21) can be found for instance in Ref. [121, Sec. II.B] or in [64]. Regarding Eq. (2.22), it is evident that the eigenvalues of H_{eff} correspond to the poles of S. Since the operator WW^* is positive, the spectrum of H_{eff} lies in the lower half of the complex plane including the real axis and, thus, describes decaying resonance states and also bound states. Note that this nonhermitian effective Hamiltonian is not to be interpreted as an observable but rather as an auxiliary quantity to describe the scattering process. We point out that there is a very similar expression for the scattering matrix in terms of an effective subunitary time-evolution operator [66].

2.5 Open Quantum Maps

In this thesis we study time discrete open quantum systems. They may be interpreted as scattering processes for which the interaction between the scattering region and the environment only acts at discrete equidistant times [66, Sec. 3.4.1]. Then the stroboscopic time evolution is characterized by the iteration of the subunitary operator $U_{\text{op}} = UP$, where the unitary operator U describes the closed system's time evolution between the opening events that are mediated by the orthogonal projection operator P which projects onto the subspace that remains within the scattering region. Since U_{op} is a partial isometry, its spectrum lies inside the

unit circle in the complex plane [122], which motivates the notion of subunitarity. Let $\lambda \in \mathbb{C}$ be such an eigenvalue of U_{op} with modulus $|\lambda| \leq 1$, together with a corresponding normalized eigenvector ψ. Then the time evolution of ψ,

$$\|U_{\text{op}}^n \psi\|^2 = |\lambda|^{2n} \|\psi\|^2 = e^{-\gamma n}, \tag{2.24}$$

gives an exponential decay of the norm with decay rate $\gamma = -2 \log |\lambda|$ in agreement with Eq. (2.19).

The definition of the subunitary time-evolution operator $U_{\text{op}} = UP$ is a convention as we could have equally well chosen $U_{\text{op}} = PU$ or $U_{\text{op}} = PUP$. In fact, all three projection types are used in the literature [48, 49, 94]. However, we can show that the set of eigenvalues for UP, PU, and PUP are equal. Hence, regarding decay in open systems the choice of the type of projection is not relevant. This result is not even restricted to unitary operators U but holds for any bijective, bounded linear operator on some separable Hilbert space.

Proposition. Let U be a bijective, bounded linear operator on the Hilbert space $\mathcal{H}$ and let P be a projection, i.e., $P^2 = P$. Then the point spectra $\sigma(UP)$, $\sigma(PU)$, and $\sigma(PUP)$ coincide.

Proof. The following proof is worked out in collaboration with Sascha Trostorff. At first, we separately answer the question whether zero is an eigenvalue. Recall that for any bounded linear operator A on $\mathcal{H}$, it is

$$\lambda \in \sigma(A) \quad :\Leftrightarrow \quad \exists\, \psi \in \mathcal{H},\ \psi \neq 0 :\ A\psi = \lambda\psi \tag{2.25}$$

$$\Leftrightarrow \quad \dim \ker(A - \lambda \mathbb{1}) > 0, \tag{2.26}$$

with

$$\ker A := \{\psi \in \mathcal{H} \ :\ A\psi = 0\}. \tag{2.27}$$

To decide whether zero is an eigenvalue of UP, PU, and PUP, we consider

$$\ker UP = \ker P, \qquad \ker PU = U^{-1} \ker P, \tag{2.28}$$

and

$$\ker PUP = \ker P + \operatorname{im} P \cap U^{-1} \ker P, \tag{2.29}$$

using that U is bijective, see Appendix B.1. If zero is an element of one of the three

considered point spectra, it is necessarily $\dim\ker P > 0$. Then, however, we find

$$\dim\ker UP > 0, \qquad \dim\ker PU > 0, \qquad \dim\ker PUP > 0, \tag{2.30}$$

which implies that $0 \in \sigma(UP) \cap \sigma(PU) \cap \sigma(PUP)$.
Now, let $\lambda \in \sigma(UP)$ with $\lambda \neq 0$. Then there exists $\psi \in \mathcal{H}$, $\psi \neq 0$ such that $UP\psi = \lambda\psi$. Multiplication from the left by P gives $PU(P\psi) = \lambda P\psi$. Since $\lambda\psi \neq 0$, it is $\psi \notin \ker UP = \ker P$ such that $P\psi \neq 0$ and $\lambda \in \sigma(PU)$. Furthermore, using $P^2 = P$ we find $PUP(P\psi) = \lambda P\psi$ with $P\psi \neq 0$ and, thus, $\lambda \in \sigma(PUP)$.
On the other hand, let $\lambda \in \sigma(PU)$ with $\lambda \neq 0$. Then there exists $\psi \in \mathcal{H}$, $\psi \neq 0$ such that $PU\psi = \lambda\psi$. Multiplication from the left by U gives $UP(U\psi) = \lambda U\psi$, where $U\psi \neq 0$ since U is bijective. Thus, $\lambda \in \sigma(UP)$ which is $\sigma(UP) = \sigma(PU)$.
Finally, let $\lambda \in \sigma(PUP)$ with $\lambda \neq 0$. Then there exists $\psi \in \mathcal{H}$, $\psi \neq 0$ such that $PUP\psi = \lambda\psi$. Multiplication from the left by P and using $P^2 = P$ gives $PU(P\psi) = \lambda P\psi$. Since $\lambda\psi \neq 0$, it is $\psi \notin \ker PUP \supseteq \ker P$ such that $P\psi \neq 0$ and $\lambda \in \sigma(PU) = \sigma(UP)$. To conclude, this gives $\sigma(UP) = \sigma(PU) = \sigma(PUP)$. □

Throughout this thesis we use the projection type UP. However, for numerical purposes it is more convenient to diagonalize PUP, which allows for truncation, and thus, for a reduction of the matrix dimension. Any eigenvalue λ and associated eigenvector ψ of PUP then provides the eigenvalue λ of UP associated with the eigenvector $U\psi$. To see this, it is important to note that $P\psi = \psi$ because

$$\psi = \frac{1}{\lambda}PUP\psi = \frac{1}{\lambda}P^2UP\psi = P\left(\frac{1}{\lambda}PUP\psi\right) = P\psi, \tag{2.31}$$

such that

$$UP(U\psi) = UP(UP\psi) = U(PUP\psi) = \lambda U\psi. \tag{2.32}$$

As the eigenvalue problem of nonhermitian Hamiltonians or subunitary time-evolution operators is more involved than for hermitian or unitary operators, we will revisit the general eigenvalue problem for finite-dimensional matrices in the following. In this overview we follow the discussion in Ref. [123, Sec. 2.2.2].

To this end, let us consider the linear map $K : \mathbb{C}^N \to \mathbb{C}^N$. A solution of

$$K\psi = \lambda\psi \tag{2.33}$$

is given by a pair of an eigenvalue $\lambda \in \mathbb{C}$ and a corresponding eigenvector $\psi \in \mathbb{C}^N$. Alternatively, one may consider the eigenvalue problem on the dual space $(\mathbb{C}^N)^*$ of $\mathbb{C}^N$, that is the

space of linear functionals on $\mathbb{C}^N$. Using the adjoint map $K^* : (\mathbb{C}^N)^* \to (\mathbb{C}^N)^*$, $f \mapsto f \circ K$, of K, the dual eigenvalue problem reads

$$K^*(f) = \mu f, \tag{2.34}$$

where $\mu \in \mathbb{C}$ and $f \in (\mathbb{C}^N)^*$. Typically, the dual eigenvalue problem is also formulated in $\mathbb{C}^N$ by virtue of the canonical isomorphism between $\mathbb{C}^N$ and its dual that is provided by the standard scalar product in $\mathbb{C}^N$: For any $f \in (\mathbb{C}^N)^*$ there exists a unique vector $\psi' \in \mathbb{C}^N$ with $f_{\psi'}(\cdot) := f(\cdot) = \langle \psi' | \cdot \rangle$ according to the Riesz representation theorem [118, Sec. II.2]. Hence, Eq. (2.34) gives

$$\begin{aligned} (K^* f_{\psi'})(\varphi) &\overset{\text{def}}{=} f_{\psi'}(K\varphi) = \langle \psi' | K\varphi \rangle \\ &\overset{(2.34)}{=} \mu f_{\psi'}(\varphi) = \mu \langle \psi' | \varphi \rangle = \langle \overline{\mu}\psi' | \varphi \rangle \end{aligned} \tag{2.35}$$

for all $\varphi \in \mathbb{C}^N$, where $\overline{\mu}$ denotes the complex conjugate of μ. Identifying the adjoint map K^* with its matrix representation $K^* = \overline{K}^{\mathrm{T}}$, the dual eigenvalue problem formulated in $\mathbb{C}^N$ reads

$$K^*\psi' = \overline{\mu}\psi'. \tag{2.36}$$

Due to the representation $\langle \psi' | K(\cdot) \rangle = \mu \langle \psi' | \cdot \rangle$ one distinguishes between the so-called left eigenvector $\psi^{\mathrm{L}} := \psi'$ of K associated with the eigenvalue μ and the right eigenvector $\psi^{\mathrm{R}} := \psi$ from Eq. (2.33) of K associated with the eigenvalue λ [124, Chap. 6]. As can be seen by

$$0 = \det(K - \lambda \mathbb{1}) = \det \overline{(K - \lambda \mathbb{1})} = \det(K^* - \overline{\lambda}\mathbb{1}) \tag{2.37}$$

the spectra of K and K^* are complex conjugate to each other. Following Ref. [125], we define the matrices R and L the columns of which contain the right or left eigenvectors of K, and the diagonal matrix Λ containing the corresponding eigenvalues. Then Eqs. (2.33) and (2.36) are in matrix notation given by

$$KR = R\Lambda, \tag{2.38a}$$

$$K^*L = L\overline{\Lambda}. \tag{2.38b}$$

Thus, for hermitian matrices, $K^* = K$, with real spectrum, right and left eigenspaces coincide. The same holds true for unitary matrices, $K^* = K^{-1}$, with $\overline{\Lambda} = \Lambda^{-1}$, for that

$$KL = KL\overline{\Lambda}\Lambda = KK^*L\Lambda = L\Lambda. \tag{2.39}$$

In general, however, there is no simple relation between right and left eigenvectors. We emphasize that the eigenvectors of K do not have to form an orthogonal basis unless K is

hermitian or unitary. For a basis expansion in terms of eigenvectors it is therefore useful to recognize that right and left eigenvectors form a pair of dual bases as follows [126]. Consider the adjoint of Eq. (2.38b), i.e., $L^*K = \Lambda L^*$. Multiplying both sides with R from the right hand side, and multiplying both sides of Eq. (2.38a) by L^* from the left hand side yields

$$L^*KR = \Lambda L^*R = L^*R\Lambda, \tag{2.40}$$

that is

$$[L^*R, \Lambda] = 0. \tag{2.41}$$

Since Λ is a diagonal matrix, L^*R must therefore be a diagonal matrix as well. Thus, from the off-diagonal elements of L^*R one finds

$$(L^*R)_{ik} = \sum_{j=1}^{N} L^*_{ij} R_{jk} = \sum_{j=1}^{N} \overline{L}_{ji} R_{jk} = \langle\, \psi_i^{\mathrm{L}} \,|\, \psi_k^{\mathrm{R}} \,\rangle = 0 \qquad (i \neq k) \tag{2.42}$$

This is the essential property of dual bases. By appropriate normalization, it is possible to choose

$$\|\psi_k^{\mathrm{L}}\| = \|\psi_k^{\mathrm{R}}\|, \quad \langle\, \psi_k^{\mathrm{L}} \,|\, \psi_k^{\mathrm{R}} \,\rangle = 1 \qquad (1 \leq k \leq N), \tag{2.43}$$

as commonly used more in the mathematical literature. From the physics point of view, it is more convenient to normalize the eigenvectors by

$$\|\psi_k^{\mathrm{L}}\| = 1, \quad \|\psi_k^{\mathrm{R}}\| = 1 \qquad (1 \leq k \leq N), \tag{2.44}$$

such that $\langle\, \psi_k^{\mathrm{L}} \,|\, \psi_k^{\mathrm{R}} \,\rangle$ is not a fixed value independent of k. This choice allows for the probabilistic quantum-mechanical interpretation of right and left eigenvectors. Assuming that K is diagonalizable, the expansion of a vector $\varphi \in \mathbb{C}^N$ in terms of right or left eigenvectors thus reads

$$\varphi = \sum_{k=1}^{N} \frac{\langle\, \psi_k^{\mathrm{L}} \,|\, \varphi \,\rangle}{\langle\, \psi_k^{\mathrm{L}} \,|\, \psi_k^{\mathrm{R}} \,\rangle}\, \psi_k^{\mathrm{R}} = \sum_{k=1}^{N} \frac{\langle\, \psi_k^{\mathrm{R}} \,|\, \varphi \,\rangle}{\langle\, \psi_k^{\mathrm{R}} \,|\, \psi_k^{\mathrm{L}} \,\rangle}\, \psi_k^{\mathrm{L}}. \tag{2.45}$$

Chapter 3

Chaotic Dynamics

In the previous chapter on open quantum system, we mainly focused on how to describe the interaction of a confined scattering region with its environment. In this chapter we specify the kind of dynamics that we assume within the scattering region in terms of classical mechanics. To this end we provide an overview on the classical theory of Hamiltonian dynamical systems in Sec. 3.1. In particular, we discuss the generic structure of a mixed phase space with regions of regular and chaotic motion. The difference between chaotic dynamics in globally chaotic systems and the chaotic dynamics within the chaotic part of a generic mixed phase space is presented in Sec. 3.2. We particularly consider the influence of the generic hierarchy of partial transport barriers. The bridge to open systems is built in Sec. 3.3. There we introduce classical open maps and discuss the structure of sets that are trapped although the system is open. It turns out that the trapped sets of chaotic systems have fractal properties.

3.1 Generic Hamiltonian Dynamics

A common formulation of the theory of classical mechanics is the Hamiltonian approach as it nicely paves the way towards the theory of quantum mechanics. The Hamiltonian equations of motion,

$$\dot{q}_k(t) = \frac{\partial H}{\partial p_k}\big(q(t), p(t), t\big), \qquad \dot{p}_k(t) = -\frac{\partial H}{\partial q_k}\big(q(t), p(t), t\big), \tag{3.1}$$

determine the evolution of generalized position and momentum coordinates, $q = (q_1, \ldots, q_f)$ and $p = (p_1, \ldots, p_f)$, by the Hamilton function $H : \Gamma \times \mathscr{T} \to \mathbb{R}$. This defines a dynamical system with f degrees of freedom on the extended phase space $\Gamma \times \mathscr{T} \subseteq \mathbb{R}^{2f} \times \mathbb{R}$, cf. Refs. [127,128]. In general the phase space Γ is considered to be a symplectic manifold [129–132]. Darboux's theorem, however, allows us to treat Γ locally as a flat Euclidean vector space [129,130]. In this thesis we study two-dimensional, time-discrete, symplectic maps. They originate for instance

from restricting the time-continuous dynamics of a time-independent Hamilton function with $f = 2$ from the energy shell to a Poincaré section, or from stroboscopic solutions of a (periodically) time-dependent Hamilton function with $f = 1$ [133]. A diffeomorphism $T : \Gamma \to \Gamma$ on a two-dimensional symplectic manifold Γ with the canonical differential form $\omega = dq \wedge dp$ is called symplectic if ω remains invariant under the pullback by virtue of T [129, 130]. In charts of the $\mathbb{R}^2$, where ω is represented by the skew-symmetric matrix

$$\Omega = \begin{pmatrix} 0 & 1 \\ -1 & 0 \end{pmatrix}, \tag{3.2}$$

symplecticity of T means that

$$DT|_x^{\mathrm{T}}\, \Omega\, DT|_x = \Omega \tag{3.3}$$

for all $x \in \Gamma$. Here $DT|_x$ denotes the Jacobian of T at the point x. Especially for the considered two-dimensional case, Eq. (3.3) reduces to [23]

$$\det DT|_x = +1 \qquad (x \in \Gamma). \tag{3.4}$$

This admits the intuitive interpretation that a symplectic map is characterized by preserving the phase-space volume and the orientation. Note that this simple interpretation holds true only for the two-dimensional case. Remarkably, an equivalent formulation of Eq. (3.4) is that the two eigenvalues of $DT|_x$ multiply to unity. Hence, if λ is an eigenvalue of $DT|_x$ so is λ^{-1}. Moreover, since $DT|_x$ is real, if λ is an eigenvalue then $\overline{\lambda}$ lies in the spectrum as well. As the two eigenvalues of $DT|_x$ characterize the linearized dynamics around any fixed point $x \in \Gamma$, $T(x) = x$, the spectral restrictions due to symplecticity imply restrictions on the possible types of fixed points. It turns out that symplectic two-dimensional maps only allow for elliptic (λ imaginary), hyperbolic (λ real), or parabolic (λ equals $+1$ or -1) fixed points [23].

If there exists a constant of motion, that is an observable $G : \Gamma \to \mathbb{R}$ for which globally $G \circ T = G$, then the dynamical system is called integrable or regular [132]. In this case, the Arnold–Liouville theorem says that the motion takes place on one-dimensional tori when looked at in action–angle variables [130, 132]. On the other hand, if there is no such constant of motion, orbits are not confined to one-dimensional submanifolds of Γ. The dynamics is then referred to as chaotic or irregular. Note that, typically, the absence of regular motion comes along with a sensitive dependence on initial conditions which motivates the notion of deterministic chaos. This is usually formulated in terms of the Lyapunov exponent: In general, the dynamical behavior of points started in a neighborhood of $x \in \Gamma$ is not isotropic but depends on the direction. Characteristic directions are given by the eigenvectors of the

Jacobian of T at x. Let $\lambda_1(x,n)$ and $\lambda_2(x,n)$ be the two eigenvalues of

$$\left[DT|_{T^{n-1}(x)} \cdot \ldots \cdot DT|_{T(x)} \cdot DT|_x\right]^{\frac{1}{n}}. \tag{3.5}$$

The characteristic Lyapunov exponents in x are defined by [133]

$$\Lambda^{(i)}(x) := \lim_{n\to\infty} \log|\lambda_i(x,n)|, \qquad (i \in \{1,2\}). \tag{3.6}$$

Note that for symplectic maps the sum of both Lyapunov exponents is zero. The greater of the two exponents is denoted by $\Lambda(x)$, and if it is essentially independent of x the functional dependence is also dropped in the notation. The notion of chaotic dynamics is usually reserved for motion with a nonzero Lyapunov exponent. In general symplectic maps or Hamiltonian dynamical systems are not globally regular or chaotic. A generic phase space rather exhibits both regions of regular motion and regions of chaotic motion [35]. The involved structure of such a mixed phase space is governed by the Kolgomorov–Arnold–Moser theorem and the Poincaré–Birkhoff theorem [132, 133].

In order to illustrate the generic mixed phase space, let us consider the Chirikov standard map as a popular example for generic two-dimensional symplectic maps [134]. It is defined by the time-periodically kicked Hamilton function

$$H(q,p,t) = \mathcal{T}(p) + \mathcal{V}(q)\sum_{n\in\mathbb{Z}}\delta(t-n), \tag{3.7}$$

where $\mathcal{T}(p) = p^2/2$ denotes the kinetic term and $\mathcal{V}(q) = [\kappa/(4\pi^2)]\cos(2\pi q)$ denotes the potential term with the kicking strength parameter κ. By solving Hamilton's equations of motion stroboscopically at times $n \in \mathbb{Z}$, one obtains the standard map

$$T(q,p) = \begin{pmatrix} q + p + \frac{\kappa}{4\pi}\sin(2\pi q) \mod 1 \\ \left\{p + \frac{\kappa}{4\pi}\left[\sin(2\pi q) + \sin\left(2\pi(q+p+\frac{\kappa}{2}\sin(2\pi q))\right)\right] + \frac{1}{2} \mod 1\right\} - \frac{1}{2} \end{pmatrix}. \tag{3.8}$$

Intuitively, the chosen stroboscopic times correspond to looking at the dynamics always after half a kick, which nicely symmetrizes the phase-space portraits. Since the map intrinsically exhibits periodicity in phase space, it is convenient to restrict the standard map, Eq. (3.8), to the torus with unit cell $[0,1)\times\left[-\frac{1}{2},\frac{1}{2}\right)$. Depending on the kicking strength κ, the standard map exhibits the typical patterns of regular, mixed, and chaotic dynamics, see Fig. 3.1. We emphasize that the case of mixed dynamics provides a selfsimilar island-around-island structure according to the Poincaré–Birkhoff theorem [133].

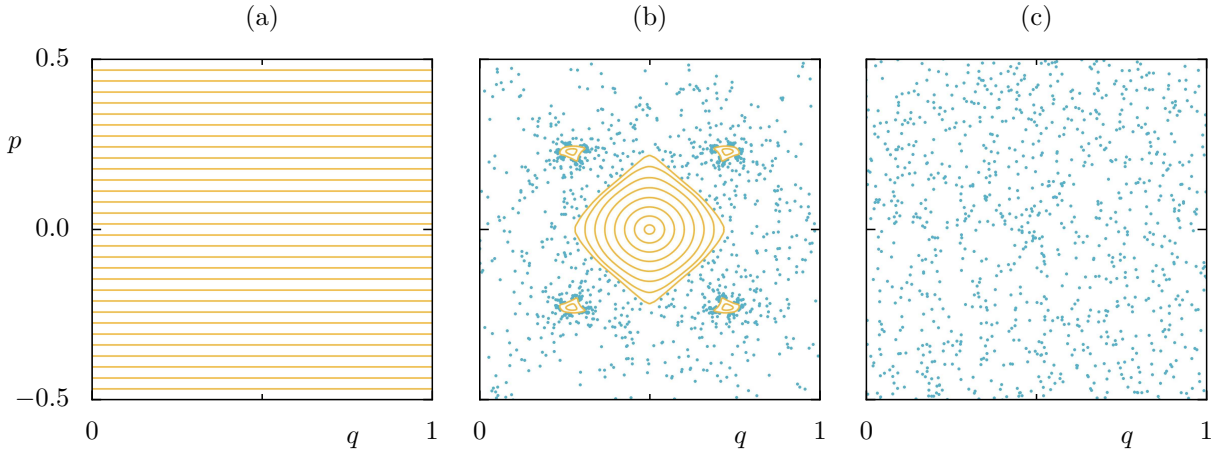

Figure 3.1. Phase-space portraits of the standard map, Eq. (3.8), with (a) regular dynamics at $\kappa = 0$, (b) mixed dynamics at $\kappa = 2.9$, and (c) chaotic dynamics at $\kappa = 10$. Regular orbits are colored in orange and chaotic orbits are colored in blue. All panels share the same vertical axis.

3.2 Chaotic Phase-Space Transport

The transport properties of chaotic motion in a generic system with mixed phase space are very different from the transport properties in a globally chaotic system. This is already indicated by the shown chaotic orbits in Fig. 3.1(b, c): While chaotic orbits in the globally chaotic system (c) explore the phase space rather uniformly, the chaotic orbits in the mixed system (b) remain longer in the vicinity of the regular regions which leads to an enhanced density of blue points there. This visual impression can be formulated more rigorously by considering Poincaré recurrence times: According to the Poincaré recurrence theorem almost all orbits initialized in a subset $M \subset \Gamma$ of the bounded phase space Γ with positive Lebesgue measure, $|M| > 0$, will return to M [132]. The statistical distribution of the corresponding recurrence times contains information about the transport properties of the system. For globally chaotic systems, the probability $R(t)$ for an orbit to return to M after t iterations decays exponentially. The chaotic motion in generic systems, however, gives rise to an algebraic decay, i.e., R scales as a power law [16, 17, 23, 135]. This is a signature of the fact that phase-space transport is systematically suppressed in the vicinity of regular regions. This is explained by the concept of partial transport barriers [23]: Let $\mathcal{C}$ be a curve that decomposes the phase space into two regions A_1 and A_2. Then the transport between both regions is governed by the flux

$$\phi_{\mathcal{C}} := |T(A_1) \cap A_2| \tag{3.9}$$

that is transmitted between A_1 and A_2 in one iteration. Due to the symplecticity of the map T, A_1 and A_2 may be exchanged in the above definition, and T may be replaced by T^{-1}. If $\mathcal{C}$ is an invariant curve, $T(\mathcal{C}) = \mathcal{C}$, like for a regular torus, the corresponding flux $\phi_{\mathcal{C}}$

vanishes such that there is no transport between A_1 and A_2, and $\mathcal{C}$ may be interpreted as a transport barrier. In the same spirit, a curve $\mathcal{C}$ for which $\phi_\mathcal{C}$ does not vanish is called a partial transport barrier. The most interesting partial barriers are the ones which suppress transport, corresponding to a relatively small flux $\phi_\mathcal{C}$ compared to the phase-space volumes $|A_1|$ and $|A_2|$. There are two common types of partial barriers [23]: A so-called Cantorus barrier originates from the remnants of a regular torus of irrational winding number that is broken by a small perturbation as in the Kolmogorov–Arnold–Moser scenario. Restrictive partial barriers can also originate from a combination of the stable manifold

$$W_\mathrm{s}(x) := \{\xi \in \Gamma \,:\, \lim_{k\to\infty} \|T^{nk}(\xi) - x\| = 0\} \tag{3.10}$$

and the unstable manifold

$$W_\mathrm{u}(x) := \{\xi \in \Gamma \,:\, \lim_{k\to\infty} \|T^{-nk}(\xi) - x\| = 0\} \tag{3.11}$$

of a hyperbolic n-periodic point x, that is a hyperbolic fixed point of the n-fold iterate map T^n. Let us point out though that the specific origin of a partial barrier is of minor relevance in this thesis. We are rather interested in the signatures of a given partial barrier in terms of classical and quantum mechanical localization and transport. Therefore, instead of going into the details of the construction of partial barriers we focus on discussing their transport mechanism. To this end, it is useful to introduce the so-called turnstile of the partial barrier, sometimes also referred to as revolving door. The turnstile of the partial barrier $\mathcal{C}$ is the set

$$\big\{A_1 \cap T^{-1}(A_2)\big\} \cup \big\{T^{-1}(A_1) \cap A_2\big\}, \tag{3.12}$$

where $A_1 \cap T^{-1}(A_2)$ is the subset of A_1 mapped to A_2 under one iteration of the map T, and vice versa, $T^{-1}(A_1) \cap A_2$ is the subset of A_2 that is mapped to A_1. The turnstile is also characterized by being the set enclosed by the preimage $T^{-1}(\mathcal{C})$ of the partial barrier $\mathcal{C}$ and $\mathcal{C}$ itself. An orbit initialized in A_1 will remain in A_1 unless it enters the turnstile region $A_1 \cap T^{-1}(A_2)$ and is then mapped to A_2 in the next step. This so-called turnstile mechanism is visualized in Fig. 3.2 for a kicked model system with an isolated partial barrier as introduced in Refs. [32, 136]. Its phase space, shown in Fig. 3.2(c), exhibits regular regions at the top and the bottom and a large chaotic sea in between. Although chaotic orbits explore the entire chaotic component uniformly in the long run, the orbit started at the red point in Fig. 3.2(a) remains in the upper half for surprisingly many iterations, Fig. 3.2(a–c). In fact, it turns out that the stable and unstable manifold of a hyperbolic fixed point in the center of the phase space form a partial barrier such that the upper (green) and lower region (orange) become almost invariant, see Fig. 3.2(d, e). In a single iteration of the map, only a small part of the

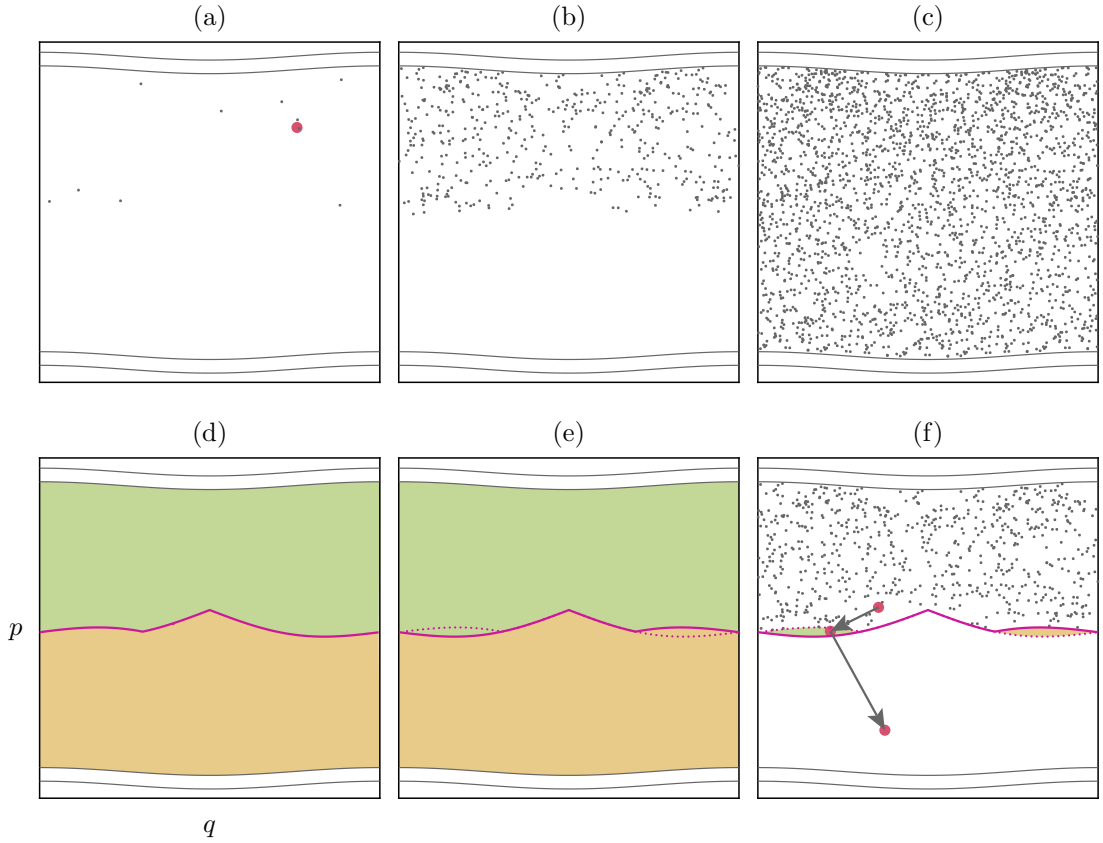

Figure 3.2. Time evolution of a chaotic orbit (gray points) in the kicked model system, Sec. (4.3), initialized at the red point in (a), for (a) 10 iterations, (b) 500 iterations, and (c) 2500 iterations. One iteration of the green and orange almost invariant sets in (d) gives the green and orange sets in (e), respectively. They are separated by a partial transport barrier (solid magenta line in (e)) the preimage of which is shown as a dotted line in (e) and as a solid line in (d). (f) The chaotic orbit (a–c) crosses the partial barrier through turnstile during the iterations 672 to 674 (red points). Regular tori are shown as solid gray lines in all panels.

green region is mapped inside the orange one, just as the other way around. This small region of exchange is formed by the turnstile of the partial barrier, cf. Fig. 3.2(f). The chaotic orbit crosses the partial barrier only by entering the corresponding loop of the turnstile. For the details of the used map, which are not relevant at the moment, we refer to Sec. 4.3.

Let us briefly mention that the notion and usage of partial barriers is ambiguous to some extent: Due to the symplecticity of the dynamics any iterate or preimage of a partial barrier is again a partial barrier of the same flux. For instance, it is not mandatory that we refer to the solid magenta line in Fig. 3.2(e) as partial barrier and not to its preimage in (d). Both are equally relevant. The question of relevance of a partial barrier depends on the considered problem: If one wants to investigate the transport from a specific phase-space region A_1 with clear inside and outside to its complement $A_2 = \Gamma \setminus A_1$, then the unique boundary between them is the relevant partial barrier. One the other hand, if one observes that orbits remain

in an almost invariant region, the boundary of which is usually not precisely known, it is tempting to uncover the reason for the low exchange. Then, however, it is sufficient to identify the Cantorus or the hyperbolic periodic point which in principle generates partial barriers that enclose the almost invariant region. In this case, it is usually not important to specify the particular combination of stable and unstable manifolds, the exact preimage or iterate, since the physical origin of the trapping is found. Note that particularly in the latter case, where we started with the observation of an almost invariant region, it is typically relevant that the partial barrier decomposes phase space into regions of simple shape and not into regions that are wildly spread over phase space. This also reduces the number of interesting partial barriers.

Restrictive partial transport barriers occur on all scales of a generic mixed phase space. This is a consequence of the selfsimilar island-around-island pattern [23]. In the vicinity of regular islands, there are infinitely many partial barriers that are hierarchically organized with decreasing fluxes towards the regular regions. The first levels of such a hierarchical structure of partial barriers are shown in Fig. 3.3 for the generic standard map, Eq. (3.8), at $\kappa = 2.9$. The outer partial barrier (purple) is generated by the stable and unstable manifolds of a hyperbolic orbit of period four. One loop of its turnstile is magnified in the second panel. Around the chain of regular islands of period four, one can already see another partial barrier (red) generated by the stable and unstable manifolds of a hyperbolic orbit of period 28. The turnstile of this partial barrier is much smaller than that of the outer partial barrier. Even in the second magnification, the loop which consists of a small inside-to-outside part on the right and a small outside-to-inside part on the lower left corner, can easily be overlooked. Note that a third partial barrier (pink) separates the large central island. Its flux is even smaller and not visible on the shown scale. By zooming deeper into phase space, further islands and restrictive partial barriers appear. The transport within such a hierarchical structure can be

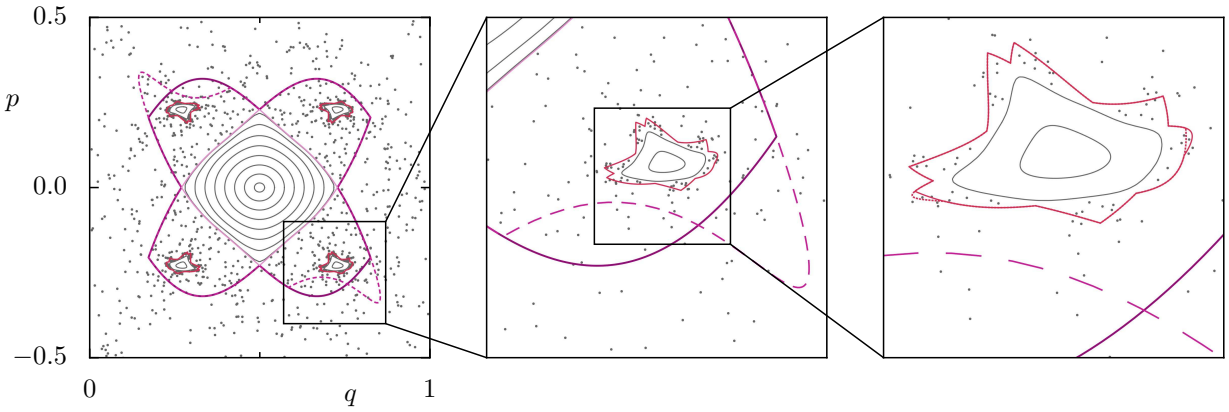

Figure 3.3. Phase-space portrait of the standard map, Eq. (3.8), at $\kappa = 2.9$ with regular orbits (solid gray lines) and chaotic orbits (gray points). Three partial barriers (solid colored lines) are shown together with their preimage (dashed colored lines).

modeled by a Markov tree [135, 137]: The partial barriers provide a partition of the chaotic phase-space component. As long as the dwell times within each element of this partition are much larger than the transition times between them, i.e., for sufficiently small transition probabilities, the dynamics in each element may be regarded as instantaneously mixing and can therefore be neglected. Then the transition probabilities become time independent which implies Markovianity. The notion of tree refers to the topology of the island-around-island structure of a generic mixed phase space. That is, an orbit can go deeper into the hierarchy on different paths but can escape from it only on a single path. By assuming a certain scaling of the areas of the elements of the partition and of the fluxes between them, one can indeed show the algebraic decay of Poincaré recurrence time statistics mentioned before. It turns out that also the Markov chain model with a simpler linear topology is capable of producing this algebraic decay [138]. This model will be used later in Sec. 10.3.3 and will therefore be introduced in a little more detail now.

For the Markov chain model [138], one assumes that the phase space Γ is decomposed by partial barriers into a sequence $(A_k)_{k\in\mathbb{N}}$ of subsets $A_k \subset \Gamma$, where only transitions between adjacent sets are allowed. In the simplest model, one expects a scaling of areas as $|A_{k+1}|/|A_k| = \alpha$ and for the flux ϕ_k connecting A_k and A_{k+1} one uses $\phi_{k+1}/\phi_k = \varphi$ [30, 138]. To ensure that the size of the flux never exceeds the area of the corresponding level of the hierarchy, it is necessarily $\varphi \leq \alpha \leq 1$. The transition probability $p_{k\to k+1}$ between A_k and A_{k+1} is then given by $p_{k\to k+1} = \phi_k/|A_k|$ and obeys the scaling $p_{k-1\to k}/p_{k\to k+1} = \alpha/\varphi$. Note that the transition probability from A_k to A_{k+1} is different from that for going from A_{k+1} to A_k which follows $p_{k\to k+1}/p_{k+1\to k} = \alpha$. With this the time evolution of a given probability distribution $(P_k)_{k\in\mathbb{N}}$ associated with $(A_k)_{k\in\mathbb{N}}$ reads

$$P_k \mapsto P_k - (p_{k\to k-1} + p_{k\to k+1}) \cdot P_k + p_{k-1\to k} \cdot P_{k-1} + p_{k+1\to k} \cdot P_{k+1}. \tag{3.13}$$

The different terms allow for a very intuitive interpretation: The probability P_k is reduced by the part $(p_{k\to k-1} + p_{k\to k+1}) \cdot P_k$ that leaves A_k to A_{k-1} or A_{k+1}, and it gains from the adjacent regions A_{k-1} the contribution $p_{k-1\to k} \cdot P_{k-1}$ and from A_{k+1} the contribution $p_{k+1\to k} \cdot P_{k+1}$. Note that for A_1 there is only one direction of transport and Eq. (3.13) needs to be adapted straightforwardly.

Think of an orbit started in A_1 which at some point enters A_2. Now, one may ask about the probability $R(t)$ to return to A_1 after exactly t further iterations, the so-called recurrence probability. In a globally chaotic system, R would decay exponentially with rate

$$\gamma = -\log(1 - |A_1|). \tag{3.14}$$

To see this, think of the iteration in the globally chaotic system as a random process where

the orbit ends up in A_1 with probability $|A_1|$ and in $\Gamma \setminus A_1$, $|\Gamma| = 1$, with probability $1 - |A_1|$. The probability for the orbit to return to A_1 after exactly t iterations is then given by

$$R(t) = |A_1|\,(1 - |A_1|)^{t-1} = |A_1|\,e^{-\gamma(t-1)}, \tag{3.15}$$

that is the probability to remain in $\Gamma \setminus A_1$ for $t - 1$ iterations and to be mapped into A_1 once. In contrast, for the Markov chain introduced above the same experiment yields a power-law decay, see Fig. 3.4. More precisely, the recurrence probability in this case is computed as follows: We apply an auxiliary absorption to A_1, i.e., we set P_1 to zero in each iteration according to Eq. (3.13). Then the sum $S(t) := \sum_{k\in\mathbb{N}} P_k(t)$ as a function of the iteration step t describes the probability to remain in $\Gamma \setminus A_1$ for t iterations. The quantity S is also referred to as survival probability. In Ref. [138] it is shown that $S(t) \sim t^{-\gamma}$ with

$$\gamma = \frac{1}{1 - \frac{\log(\alpha)}{\log(\varphi)}}, \tag{3.16}$$

see also Fig. 3.4. Note that if the initial probability is chosen deep within the hierarchy, e.g., a uniform distribution on the entire phase space, S scales as $S(t) \sim t^{-(\gamma-1)}$ [139]. Using the survival probability S, the probability to return to A_1 after t iterations reads $R(t) = S(t-1) - S(t)$. In the continuum limit, this is the negative derivative of S with respect to t,

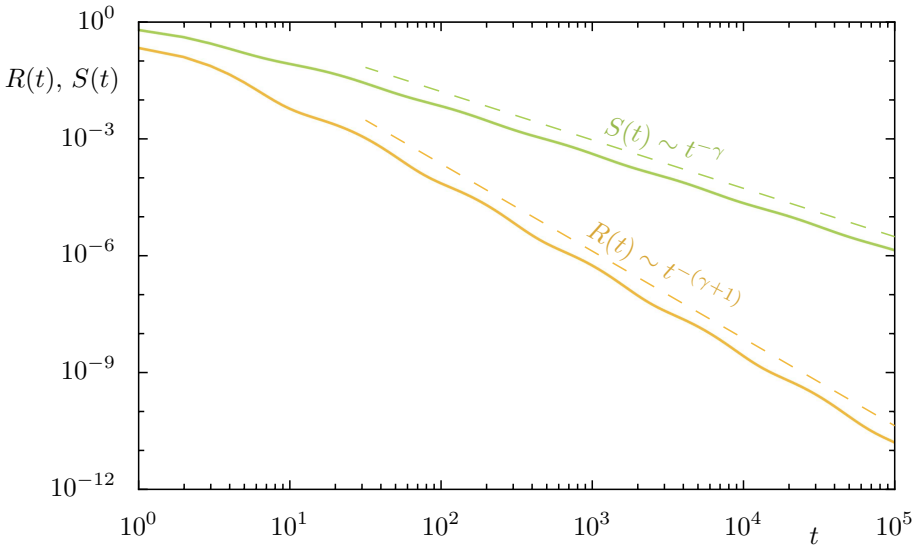

Figure 3.4. Recurrence probability R (orange) and survival probability S (green) for the time evolution in a Markov chain according to Eq. (3.13) ($\alpha = 2/3$, $\varphi = 1/8$, $\phi_1/A_1 = 1/4$). The chain is truncated to 100 hierarchical levels. The region of return or escape, respectively, is A_1, and the initial distribution is taken as $P_2 = 1$. The expected power law (dashed lines) is defined by γ from Eq. (3.16).

such that

$$R(t) \sim t^{-(\gamma+1)}. \tag{3.17}$$

Basically, the power-law decay results from a superposition of exponential decays associated with the different levels of the hierarchy as can also be seen in the figure by the oscillatory behavior. Due to the specific hierarchical scaling of the transition probabilities the different exponential decays add up to an overall power-law scaling.

3.3 Chaotic Systems with Escape

So far, we discussed phase-space transport for closed Hamiltonian systems. Even the recurrence and survival probability are meant to describe properties of the closed system despite the fact that an auxiliary absorption was implemented for their numerical computation. In this thesis, however, the focus is put on open systems as introduced in Chap. 2 in the context of quantum dynamics. Coming back to the example of the recurrence probability one observes that for specific questions closed and open systems are closely related: The recurrence probability to return to region A_1 is identical to the probability to escape from the same system if opened by absorption in A_1. This is due to the fact the orbits which once returned to A_1 are neglected afterwards just like orbits which left the system through A_1. From the above considerations on the decay of the survival probability $S(t)$ for closed systems, we can thus immediately conclude that open systems exhibit the analogous phenomenology: It is $S(t) \sim e^{-\gamma t}$ for globally chaotic systems and $S(t) \sim t^{-\gamma}$ for generic systems with an infinite hierarchical structure of partial transport barriers. The corresponding decay coefficients γ are again given by Eq. (3.14) and by Eq. (3.16), respectively.

In order to discuss the properties of systems with escape more rigorously, let us introduce the notion of an open map [56]. To this end, we start with a symplectic map $T_{\mathrm{cl}} : \Gamma \to \Gamma$ describing closed system dynamics and define the opening by the absorbing phase-space region $\Omega \subset \Gamma$. We extend the phase space Γ by the auxiliary point ∞, $\Gamma_\infty := \Gamma \cup \{\infty\}$, to which the opening Ω will be mapped, i.e., ∞ models the environment from where nothing returns to the bounded part Γ. With this the open map $T : \Gamma_\infty \to \Gamma_\infty$ is defined by

$$T(x) := \begin{cases} T_{\mathrm{cl}}(x) & : x \in \Gamma \setminus \Omega, \\ \infty & : x \notin \Gamma \setminus \Omega. \end{cases} \tag{3.18}$$

Hence, T acts just like T_{cl} all over phase space except for the opening Ω, from which points are mapped to ∞. By extending also T_{cl} to a map on Γ_∞ by setting $T_{\mathrm{cl}}(\infty) := \infty$, the map T

may be written as $T = T_{\mathrm{cl}} \circ O$, with

$$O(x) = \begin{cases} x & : x \in \Gamma \setminus \Omega, \\ \infty & : x \notin \Gamma \setminus \Omega. \end{cases} \tag{3.19}$$

Note that again the order of $T_{\mathrm{cl}} \circ O$ describes open dynamics equally well as $O \circ T_{\mathrm{cl}}$ or $O \circ T_{\mathrm{cl}} \circ O$. We choose this order in agreement with our definition of open quantum maps, Sec. 2.5. In contrast to closed systems, which are invertible due to symplecticity, for open systems a symbol like T^{-1} needs some explanation. When applied to a set $X \in \Gamma$ then the so-called preimage

$$T^{-1}(X) := \{x \in \Gamma \, : \, T(x) \in X\} \tag{3.20}$$

is the set of all points that are mapped to X under one iteration by T. We stress that this is well defined regardless of whether T is invertible or not. Using that $T^{-1}(X) = O^{-1}\big(T_{\mathrm{cl}}^{-1}(X)\big)$ and that $O^{-1}(X) = O(X)$ when restricted to Γ, it is $T^{-1}(X) = O \circ T_{\mathrm{cl}}^{-1}(X)$ within Γ. As O and T_{cl}^{-1} are well defined maps we may define the map $T^{-1} := O \circ T_{\mathrm{cl}}^{-1}$ with $T^{-1}\big(T(x)\big) = x$ for $x \in \Gamma \setminus \Omega$ and $T\big(T^{-1}(x)\big) = x$ for $x \in \Gamma \setminus T_{\mathrm{cl}}(\Omega)$.

A specific example of such a map that will be useful for the purpose of illustration throughout this thesis is the open Baker map. It is based on the ternary Baker map $T_{\mathrm{cl}} : [0,1)^2 \to [0,1)^2$, cf. Ref. [140, p. 42],

$$T_{\mathrm{cl}}(q,p) = \begin{pmatrix} 3q - \lfloor 3q \rfloor \\ (p + \lfloor 3q \rfloor)/3 \end{pmatrix}, \tag{3.21}$$

the action of which is illustrated in Fig. 3.5. The ternary Baker map is a uniformly hyperbolic map with Lyapunov exponent $\Lambda = \log 3$. For the open map, one typically uses the central third $\Omega = [1/3, 2/3) \times [0,1)$ as opening, see Fig. 3.5.

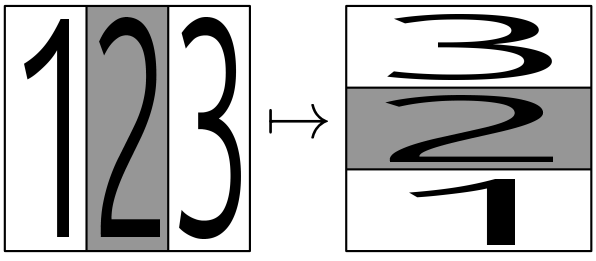

Figure 3.5. Illustration of the ternary Baker map, Eq. (3.21), which stretches by a factor 3 in the unstable (horizontal) direction and contracts by a factor 1/3 in the stable (vertical) direction. The initial three stripes (left) are rescaled and discontinuously stacked on top of each other (right). If used in the open version, $T = T_{\mathrm{cl}} \circ O$, the central gray stripe in the left panel escapes and nothing is mapped to the middle gray stripe of the right panel.

Complementary to the question of escape, one is typically also interested in properties of the surviving orbits. Particularly relevant are the forward trapped set

$$\Gamma_{\text{fwd}} := \{x \in \Gamma \,:\, T^n(x) \in \Gamma \quad (n \in \mathbb{N}_0)\} \tag{3.22}$$

and the backward trapped set

$$\Gamma_{\text{bwd}} := \{x \in \Gamma \,:\, T^{-n}(x) \in \Gamma \quad (n \in \mathbb{N}_0)\} \tag{3.23}$$

of all points that remain in the system for an arbitrary number of forward or backward iterations, respectively, cf. [49]. The trapped sets of the open Baker map are shown in Fig. 3.6(a, b) by a finite-time approximation, i.e., Γ_{fwd} and Γ_{bwd} are approximated by the set of points that survive three (a) forward or (b) backward iterations. Due to the simple structure of the Baker map, one can intuitively understand the structure of the trapped sets, where we focus on the example of the forward trapped set Γ_{fwd}, Fig. 3.6(a): First of all, the opening Ω escapes

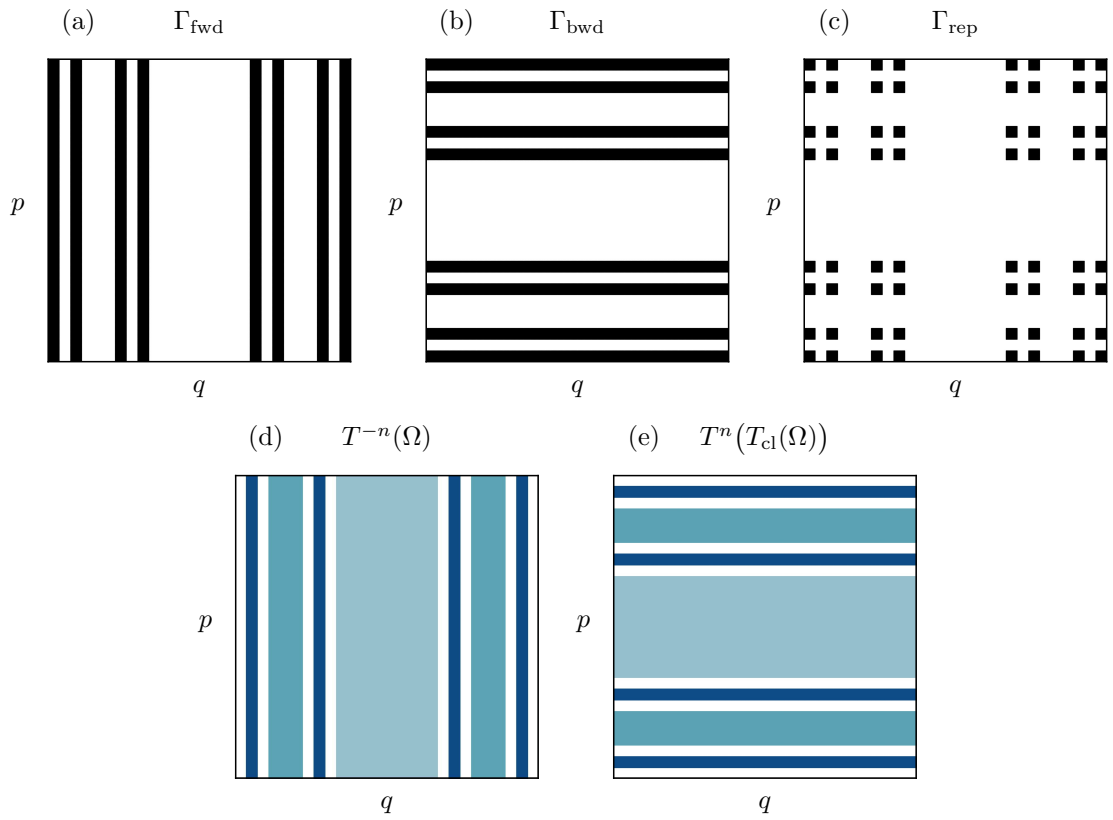

Figure 3.6. (a) Forward trapped set Γ_{fwd}, (b) backward trapped set Γ_{bwd}, and (c) repeller $\Gamma_{\text{rep}} = \Gamma_{\text{fwd}} \cap \Gamma_{\text{bwd}}$ of the open Baker map. The sets in (a–c) are approximated by being trapped for at least three iterations in the corresponding time direction. (e, f) Set of points which escape under $n+1$ (d) forward and (e) backward iterations ($n = 0$: light blue, $n = 1$: medium blue, $n = 2$: dark blue).

from Γ already in the first iteration and is therefore excluded from Γ_{fwd}. This is the central light blue stripe in Fig. 3.6(d) which gives rise to the large central gap in Γ_{fwd} in (a). The set that will escape in the second iteration must be contained in the opening Ω after the first iteration, that is $T^{-1}(\Omega)$ (two medium blue stripes in Fig. 3.6(d)). The set $T^{-1}(\Omega)$ is therefore excluded from Γ_{fwd} just like $T^{-2}(\Omega)$ (four dark blue stripes in Fig. 3.6(d)) which escapes in the third iteration by the open Baker map T. Since the finite-time approximation of Γ_{fwd} shown in Fig. 3.6(a) has exactly the first three forward escaping sets $T^{-n}(\Omega)$, $0 \leq n \leq 2$, as gaps, it describes the points which remain in Γ for at least three iterations. This construction illustrates that the forward trapped set can also be represented by [49]

$$\Gamma_{\text{fwd}} = \Gamma \setminus \bigcup_{n\in\mathbb{N}_0} T^{-n}(\Omega). \tag{3.24}$$

An analogous construction applies to the backward trapped set Γ_{bwd}, Fig. 3.6(b), by excluding the backward escaping sets shown in Fig. 3.6(e). The first phase-space region that escapes under the backward iteration $T^{-1} = O \circ T_{\text{cl}}^{-1}$ is $T_{\text{cl}}(\Omega)$ (middle light blue stripe in Fig. 3.6(e)). The region that escapes in the second backward iteration is the one that is mapped into $T_{\text{cl}}(\Omega)$ in the first backward iteration, $T(T_{\text{cl}}(\Omega))$ (two medium blue stripes in Fig. 3.6(e)). Analogously, $T^2(T_{\text{cl}}(\Omega))$ (four dark blue stripes in Fig. 3.6(e)) escapes in the third backward iteration such that $T^n(T_{\text{cl}}(\Omega))$, $n \in \mathbb{N}_0$, are the backward escaping sets. This gives another representation of the backward trapped set [49],

$$\Gamma_{\text{bwd}} = \Gamma \setminus \bigcup_{n\in\mathbb{N}_0} T^n\big(T_{\text{cl}}(\Omega)\big). \tag{3.25}$$

While Γ_{fwd} and Γ_{bwd} are trapped either under forward or backward iteration, respectively, their intersection $\Gamma_{\text{rep}} := \Gamma_{\text{fwd}} \cap \Gamma_{\text{bwd}}$ is trapped both under forward and backward iteration. This trapped set Γ_{rep} is called (hyperbolic) repeller or chaotic saddle [49, 56, 62, 76]. The repeller of the open Baker map is shown in Fig. 3.6(c) and is clearly the intersection of the trapped sets shown in panels (a) and (b). Remarkably, the forward trapped set Γ_{fwd} is invariant under backward iteration, $T^{-1}(\Gamma_{\text{fwd}}) = \Gamma_{\text{fwd}}$, the backward trapped set Γ_{bwd} is invariant under forward iteration, $T(\Gamma_{\text{bwd}}) = \Gamma_{\text{bwd}}$, and the repeller is Γ_{rep} invariant both under forward and backward iteration [56, 76].

As can be seen in Fig. 3.6(a), the forward trapped set Γ_{fwd} is continuous along the vertical direction and strongly gapped along the horizontal direction. This intuitively originates from the fact that a set of points in phase space is exponentially stretched along the unstable (horizontal) direction and exponentially contracted along the stable (vertical) direction. Due to the bounded phase space, the iterates of this set wind along the unstable manifold and overlap with the opening infinitely many times. In contrast, the stable direction leads to

a contraction of the set and not to a systematic overlap with the opening. Likewise, the backward trapped set is gapped along the vertical direction which is the unstable direction for the backward iteration. The filamentary pattern along the gapped direction has fractal properties.

Fractal sets are characterized by having a noninteger dimension [141]. Certainly, a noninteger dimension can only be the result of a generalized notion of dimension, called fractal dimension. A common example is the box-counting dimension, which defines the dimension of a bounded set M through its scaling behavior. Let $N_{\mathrm{bc}}(M,\varepsilon)$ be the smallest number of boxes of edge length ε that are necessary to cover M, then the box-counting dimension $D(M)$ is given by [141]

$$D(M) := -\lim_{\varepsilon \searrow 0} \frac{\log N_{\mathrm{bc}}(M,\varepsilon)}{\log \varepsilon}. \tag{3.26}$$

That means that $N_{\mathrm{bc}}(M,\varepsilon)$ scales as a power law,

$$N_{\mathrm{bc}}(M,\varepsilon) \sim \varepsilon^{-D(M)}, \qquad (\varepsilon \searrow 0), \tag{3.27}$$

the exponent of which is governed by the fractal dimension $D(M)$. Equivalently, $N_{\mathrm{bc}}(M,\varepsilon)$ can be defined by the number of boxes of a grid with lattice constant ε that have a nonempty intersection with M [142, p. 43]. This characterization is particularly useful for the numerical implementation and will be used in this thesis. The box-counting dimension of a set can be different from an integer number due to a selfsimilar structure. In view of the trapped sets of the open Baker map, Fig. 3.6(a–c), that means that the gaps appear in a selfsimilar pattern and obey a certain scaling.

Before coming to the explicit computation of the box-counting dimensions of Γ_{fwd}, Γ_{bwd}, and Γ_{rep}, let us point out that their fractal dimension can be decomposed into the partial fractal dimensions δ^{s} and δ^{u} along the stable and unstable manifolds [76, Chap. 6.3.2],

$$D(\Gamma_{\mathrm{fwd}}) = \delta^{\mathrm{s}}(\Gamma_{\mathrm{fwd}}) + \delta^{\mathrm{u}}(\Gamma_{\mathrm{fwd}}), \tag{3.28}$$

and analogously for Γ_{bwd} and Γ_{rep}. This is a consequence of their product structure. We already argued that $\delta^{\mathrm{s}}(\Gamma_{\mathrm{fwd}}) = 1$ and that $\delta^{\mathrm{u}}(\Gamma_{\mathrm{bwd}}) = 1$. Moreover, due to time-reversal symmetry, it is

$$\delta^{\mathrm{u}}(\Gamma_{\mathrm{fwd}}) = \delta^{\mathrm{s}}(\Gamma_{\mathrm{bwd}}) =: \delta, \tag{3.29}$$

see Ref. [56], and as the repeller is defined by the intersection of Γ_{fwd} and Γ_{bwd}, it is $D(\Gamma_{\mathrm{rep}}) = 2\delta$. Hence, by computing the partial fractal dimension δ, one obtains the fractal dimension

of Γ_{fwd}, Γ_{bwd}, and Γ_{rep} at once. A particularly elegant approach is given by the Kantz–Grassberger relation [44, 76],

$$\delta = 1 - \frac{\gamma}{\Lambda}, \tag{3.30}$$

relating the fractality of the trapped sets with the decay rate γ and the Lyapunov exponent Λ. Let us motivate this relation for the open Baker map with $\Lambda = \log(3)$ and $\gamma = -\log(2/3)$ in terms of the box-counting algorithm. Consider the one-dimensional grid of boxes of edge length

$$\varepsilon_n = e^{-\Lambda n} = \left(\frac{1}{3}\right)^n, \tag{3.31}$$

which defines a testing sequence $(\varepsilon_n)_{n\in\mathbb{N}}$ for the convergence of Eq. (3.26). We stress that this sequence $(\varepsilon_n)_{n\in\mathbb{N}}$ is particularly well adapted to the fractal structure of the open Baker map as ε_n exactly agrees with the width of stripes of the fine-time approximations of the trapped sets. Recall that the Lyapunov exponent Λ describes the stretching and contraction of sets in phase space under time evolution. The number $N_{\mathrm{bc}}(\varepsilon_n)$ of boxes of this one-dimensional grid that are occupied by the trapped set along its fractal direction follows from

$$N_{\mathrm{bc}}(\varepsilon_n)\,\varepsilon_n = e^{-\gamma n} = \left(\frac{2}{3}\right)^n, \tag{3.32}$$

which describes the decay of the occupied phase-space fraction between consecutive levels of approximation. In combination, this gives

$$N_{\mathrm{bc}}(\varepsilon_n) = e^{(\Lambda-\gamma)n} = e^{\Lambda n(1-\gamma/\Lambda)} = \varepsilon_n^{-(1-\gamma/\Lambda)}, \tag{3.33}$$

in agreement with Eq. (3.30). Accordingly, the partial fractal dimension of the open Baker map reads $\delta = \log(2)/\log(3)$.

The box-counting dimension is a special choice ($q = 0$) from the class of Rényi dimensions [143],

$$D_q(M) := \frac{1}{q-1} \lim_{\varepsilon\searrow 0} \frac{\log \sum_{i=1}^{N_{\mathrm{bc}}(M,\varepsilon)} p_i(\varepsilon)^q}{\log \varepsilon} \qquad (q \in \mathbb{R}_{\geq 0},\ q \neq 1), \tag{3.34}$$

where the sum is taken over all $N_{\mathrm{bc}}(M,\varepsilon)$ boxes that are occupied by M and with $p_i(\varepsilon)$ being the measure of M within the i-th box. Strictly speaking, the Kantz–Grassberger relation, Eq. (3.30), is formulated in terms of the information dimension

$$D_1(M) := \lim_{q\to 1} D_q(M) = -\lim_{\varepsilon\searrow 0} \frac{\sum_{i=1}^{N_{\mathrm{bc}}(M,\varepsilon)} p_i(\varepsilon)\,\log\big(p_i(\varepsilon)\big)}{\log \varepsilon^{-1}}, \tag{3.35}$$

using l'Hôpital's rule, and not in terms of the box-counting dimension D_0 as suggested above. However, for uniform fractals all Rényi dimensions coincide [143]. This is usually the case for globally chaotic open maps. For other systems with nonuniformly fractal trapped sets, which are also studied in this thesis, we will specifically explain how to apply the above concepts.

To conclude this short introduction on fractal dimensions, let us point out that the fractal dimension coincides with the common notion of dimension for sets which reasonably allow the association with an integer dimension. Moreover, the trapped sets of the open Baker map are based on the so-called middle third Cantor set. Being Cantor sets, the trapped sets have the following properties which are usually expected also for other fractal sets, cf. Refs. [144, Sec. 7.1d] and [145, p. 66]: A Cantor set is uncountable but of Lebesgue measure zero; it consists only of cluster points and contains all its cluster points (perfect set); it has no interior points (nowhere dense); it contains no connected subsets (totally disconnected).

Chapter 4

Model Systems with a Single Partial Transport Barrier

The chaotic phase-space transport in generic Hamiltonian systems is governed by the intricate hierarchical structure of partial transport barriers, as was discussed in the previous chapter. In fact, partial barriers also have a strong influence on quantum-mechanical properties as will become clear later. As a first crucial step towards a thorough understanding of the aggregate behavior of the hierarchical structure of partial barriers, both classically and quantum mechanically, we begin with studying systems with a single partial barrier. To this end we design a simple model system, the partial-barrier map, in Sec. 4.1. The partial-barrier map is the main dynamical system studied in this thesis. Its quantization is explained in detail in Sec. 4.2. The partial-barrier map was initially developed in collaboration with Matthias Michler [123]. A random matrix model derived from this map was already presented in Refs. [136, Sec. 4.4] and [32]. Moreover, in Sec. 4.3 we briefly present a kicked model system with a generic mixed phase space and an isolated partial barrier as introduced in Refs. [32, 136]. This model will be used in Chap. 5.

4.1 Partial-Barrier Map

Recall that a partial barrier is characterized by decomposing phase space into two regions A_1 and A_2 that are almost invariant under the map T. The degree to which A_1 and A_2 are invariant is reflected in the magnitude of the flux $\phi = |T(A_1) \cap A_2|$ between them. The larger ϕ the less invariant are A_1 and A_2, respectively, cf. Sec. 3.2. We mimic this behavior of a partial barrier in a system with an opening by the partial-barrier map,

$$T := M \circ E \circ O, \tag{4.1}$$

which is the composition of three maps, see Fig. 4.1 for illustration: The map M describes the unconnected chaotic dynamics within the two regions $A_1 := [0, |A_1|) \times [-\frac{1}{2}, \frac{1}{2})$ and $A_2 := \Gamma \setminus A_1$ for $\Gamma := [0, 1) \times [-\frac{1}{2}, \frac{1}{2})$. The map E induces a flux ϕ between A_1 and A_2 by exchanging the regions $\Phi_1 := [|A_1| - \phi, |A_1|) \times [-\frac{1}{2}, \frac{1}{2}) \subseteq A_1$ and $\Phi_2 := [|A_1|, |A_1| + \phi) \times [-\frac{1}{2}, \frac{1}{2}) \subseteq A_2$ with $|\Phi_1| = |\Phi_2| = \phi$. The map O opens the system by the absorbing region Ω, which is contained in region A_1. Note that the order of the maps M, E, and O is mere convention.

Throughout this thesis, we use two different dynamics for M. First, for the numerical analysis, we use the standard map, Eq. (3.8), acting individually on each of the regions A_k, $k \in \{1, 2\}$, after appropriate rescaling: The rescaled standard map $\mathcal{S}_A$ acting on the torus $A := [a, a + |A|) \times [-\frac{1}{2}, \frac{1}{2})$ is deduced from the kicked Hamiltonian from Eq. (3.7) by using

$$\mathcal{T}(p) = \frac{|A|}{2} p^2, \qquad \mathcal{V}(q) = \kappa \frac{|A|}{4\pi^2} \cos\left(\frac{2\pi(q-a)}{|A|}\right), \tag{4.2}$$

which gives

$$\mathcal{S}_A(q,p) = \begin{pmatrix} \left\{q + \mathcal{T}'(p - \frac{1}{2}\mathcal{V}'(q)) - a \mod |A|\right\} + a \\ \left\{p - \frac{1}{2}\left[\mathcal{V}'(q) + \mathcal{V}'\left(q + \mathcal{T}'(p - \frac{1}{2}\mathcal{V}'(q))\right)\right] + \frac{1}{2} \mod 1\right\} - \frac{1}{2} \end{pmatrix} \tag{4.3}$$

instead of Eq. (3.8). In application to the mixing step M of the partial-barrier map T, we use

$$M : \Gamma \to \Gamma, \quad x \mapsto \begin{cases} \mathcal{S}_{A_1}(x) & : x \in A_1, \\ \mathcal{S}_{A_2}(x) & : x \in A_2, \end{cases} \tag{4.4}$$

for fixed $\kappa = 10$, where the standard map displays a fully chaotic phase space. When using the

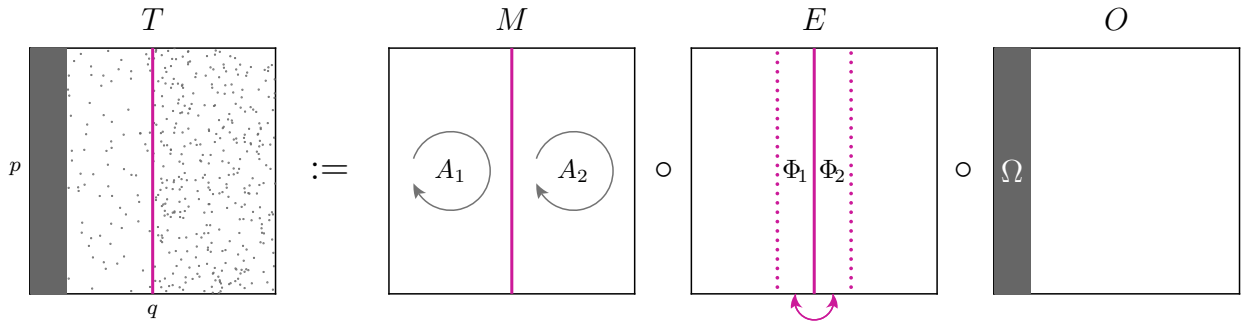

Figure 4.1. Illustration of the partial-barrier map $T := M \circ E \circ O$ as a composition of the unconnected mixing dynamics M within the two regions A_1 and A_2 on each side of the partial barrier (solid magenta line) as depicted symbolically by gray circular arrows, the map E that exchanges regions Φ_1 and Φ_2 (bounded by dotted magenta lines), and the map O that opens the system by the absorbing region Ω (gray shaded stripe). The gray orbit (random numbers) in the left panel visualizes the restrictive effect on transport across the partial barrier.

standard map for M, we choose $\Omega = [0, |\Omega|) \times [-\frac{1}{2}, \frac{1}{2})$ and refer to the corresponding map T as partial-barrier standard map.

Second, for analytical considerations below in Chap. 8, we use the uniformly hyperbolic ternary Baker map, Eq. (3.21), acting individually on each of the regions A_k, $k \in \{1, 2\}$, after appropriate rescaling: The Baker map $\mathcal{B}_A$ acting on the region $A := [a, a + |A|) \times [-\frac{1}{2}, \frac{1}{2})$ is defined by

$$\mathcal{B}_A(q,p) = \begin{pmatrix} \{3(q-a) \mod |A|\} + a \\ \frac{1}{3}\left(p + \frac{1}{2} + \lfloor 3(q-a)/|A| \rfloor\right) - \frac{1}{2} \end{pmatrix}. \tag{4.5}$$

The application to the mixing step M of the partial-barrier map T reads

$$M : \Gamma \to \Gamma, \quad x \mapsto \begin{cases} \mathcal{B}_{A_1}(x) & : x \in A_1, \\ \mathcal{B}_{A_2}(x) & : x \in A_2, \end{cases} \tag{4.6}$$

where we choose $|A_1| = 1/2$, $\phi = 1/6$, and $\Omega = [\frac{1}{6}, \frac{2}{6}) \times [-\frac{1}{2}, \frac{1}{2})$, as illustrated in Fig. 4.2. We refer to the corresponding map T as partial-barrier Baker map.

The explicit form of the exchange map E is given by

$$E(q,p) = \begin{pmatrix} \{(q - |A_1| + 2\phi) \mod 2\phi\} + |A_1| - \phi \\ p \end{pmatrix} \tag{4.7}$$

for $q \in [|A_1| - \phi, |A_1| + \phi)$, and otherwise by the identical transformation. The opening O acts as defined in Eq. (3.19). It can be shown that both, the partial-barrier standard map as well as the partial-barrier Baker map are symplectic, and thus, describe Hamiltonian dynamics up to escape through the absorbing region, and both maps are equipped with an anticanonical symmetry, comparable to the time-reversal invariance [123].

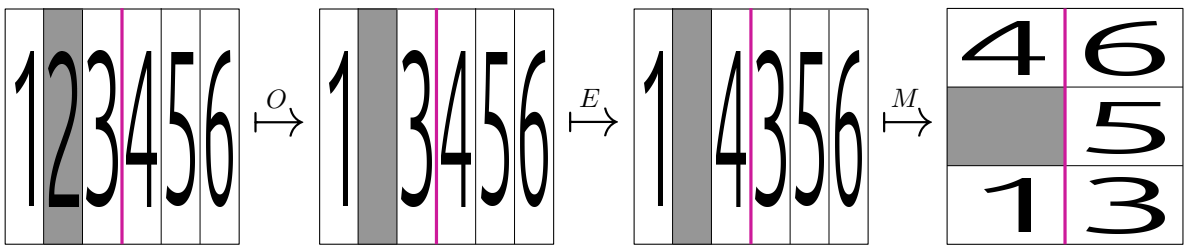

Figure 4.2. Illustration of the partial-barrier Baker map $T = M \circ E \circ O$. Magenta line indicates partial barrier and gray shaded region marks opening Ω (first three panels from left) and image $M(E(\Omega))$ of opening (right panel).

4.2 Quantized Partial-Barrier Map

In contrast to Hamiltonian flows there exists no canonical quantization procedure for time-discrete maps. There are rather system specific methods which are restricted by just a few constraints as reviewed in Ref. [146, Sec. 2.5.1]: A quantization of a symplectic map T has to establish a sequence of unitary operators $(U_N)_{N\in\mathbb{N}}$, such that U_N is acting on an N-dimensional Hilbert space $\mathbb{C}^N$. The dimension of the Hilbert space is associated with the size of Planck's cell by $h = 1/N$ for a phase space of unit area. Most importantly, in order to ensure correspondence between classical and quantum dynamics it is required that

$$U_N^{-n}\mathrm{op}(f)_N U_N^n = \mathrm{op}(f\circ T^n)_N + \mathcal{O}(N^{-1}) \qquad (n\in\mathbb{Z}). \tag{4.8}$$

This means that time evolution and quantization commute for all observables in the semiclassical limit, $h \searrow 0$. The quantization $\mathrm{op}(f)$ of a classical observable $f : \Gamma \to \mathbb{R}$ is explained by the Weyl quantization. Note that for the common canonical quantization procedures for Hamiltonian flows like the Weyl or the anti-Wick quantization [27], this property, Eq. (4.8), is guaranteed by Egorov's theorem. The quantization scheme for symplectic maps as outlined above can be formulated rigorously in terms of the pseudodifferential operator formalism, cf. [147, Chap. 2.2.5]. In some paradigmatic cases there are more direct ways to quantization. The generic standard map allows for a Floquet approach [148] due to the periodic kicking potential. Another approach based on generating functions, cf. [149], will be useful to quantize the Baker map. For the quantization of the partial-barrier map we take advantage from the decomposition $T = M \circ E \circ O$ which translates into an ordinary matrix product of the individually quantized maps. The N dependence of U_N will be suppressed in the notation in the following.

4.2.1 Quantized Standard Map

Recall that the standard map, Eq. (3.8), originates from a periodically kicked Hamilton function, Eq. (3.7), by a stroboscopic solution scheme. The same holds true for the rescaled version in Eq. (4.3). These singular kicks give rise to the factorization of the quantum time-evolution operator,

$$U = e^{-\frac{i}{2\hbar}\mathcal{V}} e^{-\frac{i}{\hbar}\mathcal{T}} e^{-\frac{i}{2\hbar}\mathcal{V}}. \tag{4.9}$$

We emphasize that this factorization is not an approximation by means of the split operator method [150, Sec. 2.3.2]. The specific factors correspond to the chosen observation times for the stroboscopic solution, that is, the potential kick is split into halves and free motion takes place in between as in the classical case. When applied in position representation, the term

$e^{-\frac{i}{2\hbar}\mathcal{V}}$ is an operator-valued function of the multiplication operator q (position), $[q\psi](x) = x\,\psi(x)$, and $e^{-\frac{i}{\hbar}\mathcal{T}}$ is an operator-valued function of the differential operator p (momentum), $[p\psi](x) = -i\hbar\,\psi'(x)$, by means of functional calculus [118]. It is useful to transform the kinetic term $e^{-\frac{i}{\hbar}\mathcal{T}}$ into a function of the multiplication operator by Fourier transform $\mathscr{F}$, using that

$$\begin{aligned}
[\mathscr{F}p\psi](x) &= -i\hbar[\mathscr{F}\psi'](x) && (4.10)\\
&= \frac{-i\hbar}{\sqrt{2\pi\hbar}}\int_{\mathbb{R}} e^{-\frac{i}{\hbar}xy}\psi'(y)\,dy && (4.11)\\
&= \frac{i\hbar}{\sqrt{2\pi\hbar}}\int_{\mathbb{R}} \left(-\frac{i}{\hbar}x\right) e^{-\frac{i}{\hbar}xy}\psi(y)\,dy && (4.12)\\
&= x[\mathscr{F}\psi](x) = [q\mathscr{F}\psi](x), && (4.13)
\end{aligned}$$

with integration by parts and vanishing boundary contribution [151, §12.2.2]. Then the time evolution of a state ψ formally reads

$$U\psi = e^{-\frac{i}{2\hbar}\mathcal{V}}\mathscr{F}^{-1}\mathscr{F}e^{-\frac{i}{\hbar}\mathcal{T}}e^{-\frac{i}{2\hbar}\mathcal{V}}\psi = e^{-\frac{i}{2\hbar}\mathcal{V}}\mathscr{F}^{-1}e^{-\frac{i}{\hbar}\mathcal{T}}\mathscr{F}e^{-\frac{i}{2\hbar}\mathcal{V}}\psi, \tag{4.14}$$

where in the last expression, $e^{-\frac{i}{\hbar}\mathcal{T}}$ now acts as a function of the multiplication operator. With the explicit form of $\mathscr{F}$, it is

$$U\psi(q) = \frac{1}{2\pi\hbar}e^{-\frac{i}{2\hbar}\mathcal{V}(q)}\int_{\mathbb{R}}\int_{\mathbb{R}} \underbrace{e^{\frac{i}{\hbar}p(q-q')}e^{-\frac{i}{\hbar}\mathcal{T}(p)}e^{-\frac{i}{2\hbar}\mathcal{V}(q')}}_{=:u(q,q',p)}\psi(q')\,dq'\,dp, \tag{4.15}$$

where neither $\mathcal{T}$ nor $\mathcal{V}$ are operator-valued functions anymore and q, q', and p represent usual coordinates. Assuming periodicity of $e^{-\frac{i}{\hbar}\mathcal{T}}$ as a function of p with period M_{mom}, the integral over p may be decomposed into an integral over a single period $[p_{\min}, p_{\min}+M_{\mathrm{mom}})$ and a sum over the other intervals,

$$U\psi(q) = \frac{1}{2\pi\hbar}e^{-\frac{i}{2\hbar}\mathcal{V}(q)}\int_{\mathbb{R}}\left[\sum_{k\in\mathbb{Z}}\int_{p_{\min}}^{p_{\min}+M_{\mathrm{mom}}} e^{\frac{i}{\hbar}kM_{\mathrm{mom}}(q-q')}u(q,q',p)\,dp\right]\psi(q')\,dq'. \tag{4.16}$$

Poisson's summation formula [152, p. 153] yields

$$\sum_{k\in\mathbb{Z}} e^{\frac{i}{\hbar}kM_{\mathrm{mom}}(q-q')} = \sum_{k\in\mathbb{Z}}\delta\left(\tfrac{M_{\mathrm{mom}}(q-q')}{2\pi\hbar} - k\right) = \sum_{k\in\mathbb{Z}}\tfrac{2\pi\hbar}{M_{\mathrm{mom}}}\,\delta\left(q-q'-k\tfrac{2\pi\hbar}{M_{\mathrm{mom}}}\right), \tag{4.17}$$

and thus restricts the q values to the lattice

$$q_k = \frac{2\pi\hbar}{M_{\mathrm{mom}}}(k+\vartheta_{\mathrm{mom}}), \qquad (k\in\mathbb{Z}), \tag{4.18}$$

with fixed Bloch phase $\vartheta_{\mathrm{mom}} \in [0,1)$. This gives

$$U\psi(q_n) = \frac{1}{M_{\mathrm{mom}}} e^{-\frac{i}{2\hbar}\mathcal{V}(q_n)} \sum_{k\in\mathbb{Z}} \int_{p_{\min}}^{p_{\min}+M_{\mathrm{mom}}} u(q_n, q_k, p)\psi(q_k)\, dp. \tag{4.19}$$

Additionally, we assume periodicity of $e^{-\frac{i}{2\hbar}\mathcal{V}}$ as a function of q with period M_{pos} and $q_{k+N} = q_k + M_{\mathrm{pos}}$. Then one obtains

$$\sum_{k\in\mathbb{Z}} u(q_n, q_k, p)\psi(q_k) = \sum_{k=0}^{N-1} u(q_n, q_k, p)\psi(q_k) \cdot \frac{M_{\mathrm{mom}}}{N} \sum_{m\in\mathbb{Z}} \delta\left(p - \frac{M_{\mathrm{mom}}(\vartheta_{\mathrm{pos}} - m)}{N}\right), \tag{4.20}$$

analogously to the above discussion by applying Poisson's summation formula and using the quasiperiodicity of ψ. This restricts also the p values to a lattice defined through

$$p_k = \frac{2\pi\hbar}{M_{\mathrm{pos}}}(k + \vartheta_{\mathrm{pos}}), \qquad (k \in \mathbb{Z}) \tag{4.21}$$

with the Bloch phase $\vartheta_{\mathrm{pos}} \in [0,1)$. To ensure compatibility of the position and momentum lattice, it needs to be required that

$$N = \frac{M_{\mathrm{pos}} M_{\mathrm{mom}}}{2\pi\hbar} \in \mathbb{N}. \tag{4.22}$$

Hence, the quantization of the standard map (3.8) on the torus reads

$$U\psi(q_n) = \sum_{k=0}^{N-1} U_{nk}\psi(q_k), \tag{4.23}$$

with

$$U_{nk} = \frac{1}{N} e^{-\frac{i}{2\hbar}\mathcal{V}(q_n)} \sum_{m=0}^{N-1} e^{\frac{i}{\hbar}p_m(q_n - q_k)} e^{-\frac{i}{\hbar}\mathcal{T}(p_m)} e^{-\frac{i}{2\hbar}\mathcal{V}(q_k)}, \tag{4.24}$$

and we set $M_{\mathrm{pos}} = M_{\mathrm{mom}} = 1$. Note that the discretization of position and momentum space is not an approximation in this context. It rather follows quite naturally from the toroidal phase-space structure and leads to the finite dimensional Hilbert space $\mathbb{C}^N$ with Euclidean scalar product, see also [153].

4.2.2 Quantized Baker Map

Another common approach for the quantization of symplectic maps is based on the semiclassical Gutzwiller–van Vleck propagator [152, Sec. 10.2],

$$\langle\, Q \,|\, Uq \,\rangle = \sqrt{\frac{|\det S''(Q,q)|}{2\pi i\,\hbar}}\, \exp\left\{\frac{i}{\hbar}S(Q,q) - i\frac{\pi}{2}\nu_S(Q,q)\right\}, \tag{4.25}$$

with $\sqrt{i} = e^{i\pi/4}$, which was first formulated for quantum maps in Ref. [154]. It describes the transition amplitude for the unitary time evolution from the initial position q to the final position Q within one iteration of the quantum map U. The essential ingredient is the discrete classical action S as explained shortly below. The Morse index $\nu_S(Q,q)$ is the number of negative eigenvalues of the Hessian $S''(Q,q)$, see [155, Sec. 5.8].

Consider a sufficiently smooth function $S : \mathbb{R}^2 \to \mathbb{R}^2$, restricted to some appropriate domain. Then the map $T : \Gamma \to \Gamma$, $\Gamma \subseteq \mathbb{R}^2$, defined by

$$(Q,P) = T(q,p) \quad \Leftrightarrow \quad p = -\partial_2 S(Q,q),\ P = \partial_1 S(Q,q), \tag{4.26}$$

is symplectic provided that such a T exists, see Sec. B.2. The function S is called generating function (of first type) for T. Moreover, $S(Q,q)$ assumes the role of a discrete action for a path leading from (q,p) to (Q,P) within one iteration of the map T, as discussed in [23, Sec. V.D.]. Using this generating function S, Eq. (4.25) provides a scheme to obtain a quantization U for the symplectic map T. Note that if there exists no unique solution T by means of Eq. (4.26) it is necessary to sum over the different solutions in Eq. (4.25), cf. [156, Sec. 5.]. If no such solution exists, it is useful to make use of a different type of generating function that may be obtained from S by Legendre transformation. In the following, we only need the particular type

$$G(P,q) := S(\tilde{Q}(P,q),q) - P\,\tilde{Q}(P,q), \tag{4.27}$$

where the function $\tilde{Q}$ is defined by

$$Q = \tilde{Q}(P,q) \quad \Leftrightarrow \quad P = \partial_1 S(Q,q). \tag{4.28}$$

The function G generates a symplectic map T by

$$(Q,P) = T(q,p) \quad \Leftrightarrow \quad Q = -\partial_1 G(P,q),\ p = -\partial_2 G(P,q), \tag{4.29}$$

which can be shown analogous to the derivation in Sec. B.2. The quantization U of T in terms

of G then reads [157, Sec. 2.4.7][1]

$$\langle\, p_m \,|\, U q_n \,\rangle \sim \exp\left\{2\pi i N\, G(p_m, q_n)\right\}, \tag{4.30}$$

evaluated on a grid with positions $q_0, \ldots, q_{N-1}$ and $p_0, \ldots, p_{N-1}$. Note that the Hessian G'' is constant for all examples used in this thesis, such that we may neglect global factors associated with $|\det G''(p_m, q_n)|$ or with the Morse index. In general, it is necessary to verify the unitarity of U anyway, which fixes the prefactor up to a phase, and global phase factors are irrelevant for quantum-to-classical correspondence by means of the Egorov property, Eq. (4.8). Moreover, the $\hbar$ dependence is replaced by the dependence on the Hilbert space dimension $N = 1/(2\pi\hbar) \in \mathbb{N}$.

It is straightforward to show that

$$G_j(P, q) := -3Pq + j(P + q) \tag{4.31}$$

is a generating function for the Baker map, Eq. (3.21), for $q \in [j/3, (j+1)/3)$ and $P \in [j/3, (j+1)/3)$ with $j \in \{0, 1, 2\}$. For the purpose of simplicity in the notation, we restrict ourselves to the discussion of the usual ternary Baker map. The stretched version, Eq. (4.5), may be treated analogously. Inserting the above generating function into Eq. (4.30), shows that the quantized Baker map U obeys

$$\langle\, p_m \,|\, U q_n \,\rangle \sim \exp\left\{2\pi i N\, \left[-3p_m q_n + j(p_m + q_n)\right]\right\}. \tag{4.32}$$

For the lattice of positions and momenta we use

$$q_n = \frac{n + \vartheta_{\mathrm{mom}}}{N}, \qquad p_m = \frac{m + \vartheta_{\mathrm{pos}}}{N}, \tag{4.33}$$

with $j\,N/3 \leq m, n < (j+1)\,N/3$, $N \in 3\mathbb{N}$, and arbitrary phases ϑ_{pos}, $\vartheta_{\mathrm{mom}} \in [0, 1)$. We identify the element q_n of the position lattice in position representation with the standard basis vector $(0, \ldots, 0, 1, 0, \ldots, 0) \in \mathbb{C}^N$, where unity occupies the n-th entry. Owing to Heisenberg's uncertainty, or the canonical commutation relation of position and momentum operators, respectively, an element p_m of the momentum lattice is associated with a vector in Hilbert space by discrete inverse Fourier transformation of the position vectors, that is,

$$\langle\, q_n \,|\, p_m \,\rangle = \frac{1}{\sqrt{N}}\, e^{2\pi i N\, q_n p_m} \tag{4.34}$$

is the n-th component of the m-th momentum vector in position representation. Note that we allow for an ambiguity in the notation by using the same symbol for the element $q_n \in [0, 1)$ in

[1] Note that, given the notation used in [157], there is a minus sign missing in the exponential in Eq. (2.4.101).

the position lattice and the corresponding position vector $q_n \in \mathbb{C}^N$ in Hilbert space, and vice versa, for the momenta. It is convenient to rearrange Eq. (4.32) to

$$\langle\, p_m \,|\, U q_n \,\rangle \sim \exp\left\{-2\pi i\, 3N\,(p_m - j/3)(q_n - j/3)\right\}, \tag{4.35}$$

again neglecting a global phase factor. Subtracting $j/3$ from p_m and q_n corresponds to an index shift in m and n by $j\,N/3$, such that $\langle\, p_m \,|\, U q_n \,\rangle$ gives the same value for each j. In other words, for $0 \le m, n < N/3$ it is

$$\langle\, p_m \,|\, U q_n \,\rangle = \langle\, p_{m+N/3} \,|\, U q_{n+N/3} \,\rangle = \langle\, p_{m+2N/3} \,|\, U q_{n+2N/3} \,\rangle \tag{4.36}$$

with

$$\langle\, p_m \,|\, U q_n \,\rangle \sim \exp\left\{-2\pi i\, \frac{(n+\vartheta_{\mathrm{mom}})(m+\vartheta_{\mathrm{pos}})}{N/3}\right\}, \tag{4.37}$$

and all other components are zero. This corresponds to the more intuitive block-matrix notation

$$(\langle\, p_m \,|\, U q_n \,\rangle)_{0\le m,n\le N-1} = \begin{pmatrix} \mathscr{F}_{N/3} & 0 & 0 \\ 0 & \mathscr{F}_{N/3} & 0 \\ 0 & 0 & \mathscr{F}_{N/3} \end{pmatrix} \tag{4.38}$$

with the matrix $\mathscr{F}_N$ of the discrete Fourier transformation,

$$[\mathscr{F}_N]_{mn} := \frac{1}{\sqrt{N}} e^{-2\pi i (n+\vartheta_{\mathrm{mom}})(m+\vartheta_{\mathrm{pos}})/N}. \tag{4.39}$$

Using

$$\langle\, q_m \,|\, U q_n \,\rangle = \sum_{k=0}^{N-1} \langle\, q_m \,|\, p_k \,\rangle \langle\, p_k \,|\, U q_n \,\rangle \tag{4.40}$$

to get from the mixed representation $\langle\, p_k \,|\, U q_n \,\rangle$ to the position representation $\langle\, q_m \,|\, U q_n \,\rangle$, one obtains the quantized Baker map [158–160],

$$U = \mathscr{F}_N^{-1} \begin{pmatrix} \mathscr{F}_{N/3} & 0 & 0 \\ 0 & \mathscr{F}_{N/3} & 0 \\ 0 & 0 & \mathscr{F}_{N/3} \end{pmatrix}. \tag{4.41}$$

It is recommended to choose $\vartheta_{\mathrm{mom}} = \vartheta_{\mathrm{pos}} = 0.5$ to ensure expected symmetries [160].

4.2.3 Decomposition of Quantum Dynamics

Already in the classical context, the simplicity of the partial-barrier map $T = M \circ E \circ O$, being a composition of three elementary maps and having only rectangular subdomains of type $I \times [-\frac{1}{2}, \frac{1}{2})$ with some $I \subseteq [0,1)$, is rather convenient. For the quantization of T, however, this structure turns out to be a real advantage. The composition of classical maps translates to an ordinary matrix product of the individually quantized maps, and due to the Cartesian product structure of the subdomains, their quantization in position representation is feasible on an intuitive level.

We construct the quantum dynamics on the N dimensional Hilbert space $\mathscr{H} := \mathbb{C}^N$, equipped with the Euclidean standard scalar product, that is associated with the phase-space grid $\mathcal{Q} \times \mathcal{P}$ with

$$\mathcal{Q} := \{(k + \vartheta_{\mathrm{mom}})/N \,:\, k \in \{0, \ldots, N-1\}\} \subset [0,1), \tag{4.42a}$$

$$\mathcal{P} := \{(k + \vartheta_{\mathrm{pos}})/N - \tfrac{1}{2} \,:\, k \in \{0, \ldots, N-1\}\} \subset [-\tfrac{1}{2}, \tfrac{1}{2}), \tag{4.42b}$$

for $\vartheta_{\mathrm{pos}}, \vartheta_{\mathrm{mom}} \in [0,1)$. Starting with the quantization M of the unconnected mixing dynamics M, we decompose $\mathscr{H}$ into the subspaces

$$\mathscr{H}_1 := \mathrm{span}\left\{q_k \in \mathscr{H} \,:\, q_k \in \mathcal{Q} \cap [0, |A_1|)\right\}, \tag{4.43a}$$

$$\mathscr{H}_2 := \mathrm{span}\left\{q_k \in \mathscr{H} \,:\, q_k \in \mathcal{Q} \cap [|A_1|, 1)\right\}, \tag{4.43b}$$

such that $\mathscr{H} \simeq \mathscr{H}_1 \oplus \mathscr{H}_2$ with the direct orthogonal sum $\oplus$, cf. Ref. [118, Sec II.1]. This decomposition corresponds to the partition $\Gamma = A_1 \cup A_2$, $A_1 \cap A_2 = \emptyset$, of phase space. Recall that M is acting individually in each of the regions A_1 and A_2, where the individual maps are given by the chaotic standard map, Eq. (4.3), or the ternary Baker map, Eq. (4.5). The quantization for both of these maps is presented in Secs. 4.2.1 and 4.2.2. For the general construction of M, however, we do not have to distinguish between the standard and the Baker map: Let M_1 denote the quantum map acting on $\mathscr{H}_1$ and M_2 be the quantum map acting on $\mathscr{H}_2$, respectively. Then the quantization of the unconnected mixing dynamics M reads

$$\mathsf{M} = \begin{pmatrix} \mathsf{M}_1 & 0 \\ 0 & \mathsf{M}_2 \end{pmatrix}, \tag{4.44}$$

using the block-matrix notation as introduced in Ref. [161, §3] for instance. This is also illustrated in Fig. 4.3. We emphasize that the simple block structure of M in position representation, Eq. (4.44), is a direct consequence of the simple Cartesian phase-space structure of the designed partial-barrier map. In general, such a block structure in the quantization of a classical dynamical system that is composed of two invariant phase-space regions requires the

construction of an appropriate basis in Hilbert space, which is just the position basis in our case. Note that the Bloch phase ϑ_{mom} of the overall position lattice $\mathcal{Q}$ can result in different individual Bloch phases in terms of the quantum maps M_1 and M_2. Specifically, when using the Baker map with $|A_1| = 0.5$, $\vartheta_{\mathrm{mom}} = 0.5$ must be assured for both sides of the partial barrier [160]. Let us further mention that it is of course possible to use realizations of a random matrix ensemble for M_1 and M_2, which can be advantageous for specific questions. In this thesis, we are interested in systems equipped with a generalized time-reversal symmetry which corresponds to the circular orthogonal ensemble [152]. By using random matrices, system specific fractal properties may be switched off.

Although one can very well already guess a valid quantization E of exchange map E and then verify that it obeys quantum-to-classical correspondence, we attempt to make the quantization a little more comprehensible and derive it from a more general quantization scheme. We present the quantization following the generating function approach as is reviewed in Sec. 4.2.2. The exchange map E, Eq. (4.7), is determined by the generating function

$$G(P,q) := \begin{cases} -Pq & : \; q \in [0, |A_1| - \phi) \cup [|A_1| + \phi, 1), \\ -P(q+\phi) & : \; q \in [|A_1| - \phi, |A_1|), \\ -P(q-\phi) & : \; q \in [|A_1|, |A_1| + \phi), \end{cases} \tag{4.45}$$

as can easily be verified using Eq. (4.29). We apply Eq. (4.30) to each of the cases in Eq. (4.45) individually. First, the identity mapping for $q_n \in [0, |A_1| - \phi) \cup [|A_1| + \phi, 1)$ gives

$$\langle\, p_m \,|\, \mathsf{E} q_n \,\rangle = \frac{1}{\sqrt{N}}\, e^{-2\pi i\, N\, p_m q_n} = \langle\, p_m \,|\, q_n \,\rangle, \tag{4.46}$$

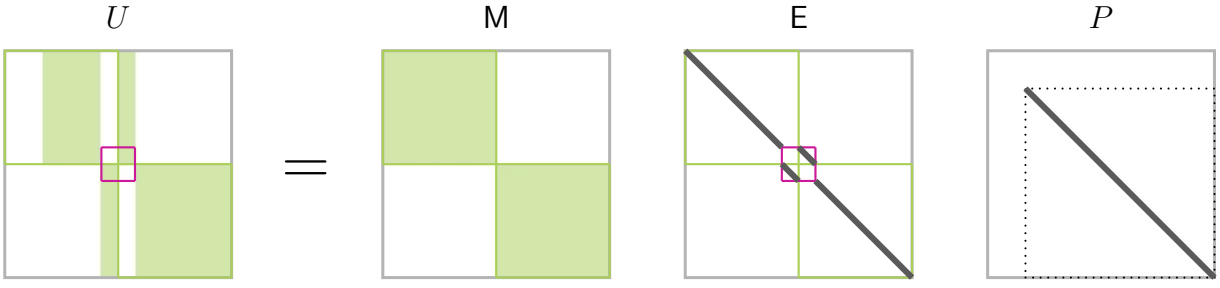

Figure 4.3. Illustration of the quantum time-evolution matrix of the partial-barrier map U in position representation. The full quantum map $U = U_{\mathrm{cl}} P$ with $U_{\mathrm{cl}} = \mathsf{ME}$ is a composition of three maps: The matrix M is block diagonal (zero on white squares) and, thus, provides the unconnected mixing dynamics within the two regions A_1 and A_2. The matrix E has unit entries on the dark diagonal lines and is zeros otherwise, and thus, exchanges the regions Φ_1 and Φ_2 by a shift within the exchange region (indicated by magenta frame). The projection P (unity on dark diagonal, zero else) opens the system by the absorbing region Ω.

which are just the components of the discrete Fourier transformation. Switching from the mixed position–momentum representation to a pure position representation by

$$\langle\, q_m \,|\, \mathsf{E} q_n \,\rangle = \sum_{k=0}^{N-1} \langle\, q_m \,|\, p_k \,\rangle \underbrace{\langle\, p_k \,|\, \mathsf{E} q_n \,\rangle}_{\langle\, p_k \,|\, q_n \,\rangle} = \langle\, q_m \,|\, q_n \,\rangle = \delta_{m,n}, \tag{4.47}$$

it turns out that, quite intuitively, the quantization of the identity map is the unit matrix. We proceed analogously with the shifting part of E for $q_n \in [|A_1| - \phi, |A_1|)$ and obtain

$$\langle\, p_m \,|\, \mathsf{E} q_n \,\rangle = \frac{1}{\sqrt{N}}\, e^{-2\pi i\, N\, p_m (q_n + \phi)} = \langle\, p_m \,|\, q_{n+C} \,\rangle, \tag{4.48}$$

where we restrict the shift ϕ to the position lattice, $C := N\phi \in \mathbb{N}_0$, i.e., $q_n + \phi = q_{n+C}$. In position representation this reads

$$\langle\, q_m \,|\, \mathsf{E} q_n \,\rangle = \sum_{k=0}^{N-1} \langle\, q_m \,|\, p_k \,\rangle \underbrace{\langle\, p_k \,|\, \mathsf{E} q_n \,\rangle}_{\langle\, p_m \,|\, q_{n+C} \,\rangle} = \langle\, q_m \,|\, q_{n+C} \,\rangle = \delta_{m,n+C}. \tag{4.49}$$

Thus, again very intuitively, by quantization the shift map translates into an index shift. Certainly, the same arguments apply for the shifting part of E in opposite direction for $q_n \in [|A_1|, |A_1| + \phi)$, giving

$$\langle\, q_m \,|\, \mathsf{E} q_n \,\rangle = \delta_{m,n-C}. \tag{4.50}$$

Altogether, the quantization E of the exchange map E exhibits the form as illustrated in Fig. 4.3. The quantized partial-barrier map without opening thus reads $U_{\mathrm{cl}} = \mathsf{ME}$.

In order to obtain the quantized partial-barrier map $U = U_{\mathrm{cl}} P$ with opening, we associate an orthogonal projection operator P with the map O. Quantum-to-classical correspondence is ensured by choosing

$$\ker P := \{\psi \in \mathscr{H} \;:\; P\psi = 0\} = \mathrm{span}\,\big\{q_k \in \mathscr{H} \;:\; q_k \in \mathcal{Q} \cap \Omega\big\}. \tag{4.51}$$

Again, owing to the simple Cartesian product structure, we explicitly obtain

$$P = \mathrm{diag}\,(\underbrace{0, \ldots, 0}_{L}, \underbrace{1, \ldots, 1}_{N-L}) \tag{4.52}$$

in position representation, for the example that $\Omega = [0, |\Omega|)$ with $L := \#(\mathcal{Q} \cap \Omega)$. This is illustrated in Fig. 4.3. To conclude, the subunitary time-evolution operator $U = U_{\mathrm{cl}} P$ with $U_{\mathrm{cl}} = \mathsf{ME}$ provides a quantization of the partial-barrier map $T = M \circ E \circ O$.

4.3 Kicked Model System

A different approach to model a dynamical system with a well isolated partial barrier is put forward in Refs. [32, 136] in terms of a kicked model system. We came across this system already in the discussion of Fig. 3.2. In this section we briefly review the definition of the map closely following the original references [32, 136]. Before coming to that, let us mention that in contrast to the partial-barrier map the kicked model system allows for studying values of $\phi/h \notin \mathbb{N}$ which is necessary for the considerations in Chap. 5. However, for the main part of this thesis, we focus on the partial-barrier map as it admits a clean phase-space structure and as it is easy to vary relevant parameters over a broad range.

The kicked model system $T = T_{\text{rot}} \circ T_{\text{kick}}$ is a composition of two maps. The map T_{kick} originates from a kicked Hamiltonian, Eq. (3.7), with

$$\mathcal{T}(p) = \begin{cases} \nu p + c_1 & : \; p < p_{\text{reg}}, \\ \nu p + b_{\text{left}} \, (p - p_{\text{reg}})^2/2 + c_2 & : \; p_{\text{reg}} \leq p < p_{\text{fix}} - p_{\text{low}}, \\ a p + b \, (p - p_{\text{fix}})^2/2 + c_3 & : \; p_{\text{fix}} - p_{\text{low}} \leq p < p_{\text{fix}} + p_{\text{up}}, \\ \nu p + b_{\text{right}} \, (p - p_{\text{fix}} - p_{\text{up}})^2/2 + c_4 & : \; p_{\text{fix}} + p_{\text{up}} \leq p < 1 - p_{\text{reg}}, \\ \nu p + c_5 & : \; 1 - p_{\text{reg}} \leq p, \end{cases} \tag{4.53}$$

and

$$\mathcal{V}(q) = -\frac{1}{8\pi^2} \cos(2\pi q), \tag{4.54}$$

with parameters $a = 20$, $\nu = 0.411$, $p_{\text{reg}} = 0.125$, $p_{\text{fix}} = 0.533$, $p_{\text{low}} = 0.15$, $p_{\text{up}} = 0.015$, and $b = 0.6$. The parameters b_{left} and b_{right} follow from

$$b_{\text{left}} = \frac{a + b p_{\text{low}} - \nu}{p_{\text{fix}} - p_{\text{low}} - p_{\text{reg}}}, \tag{4.55}$$

$$b_{\text{right}} = \frac{\nu - a - b p_{\text{up}}}{1 - p_{\text{fix}} - p_{\text{low}} - p_{\text{reg}}}. \tag{4.56}$$

The constants $c_1, \ldots, c_5 \in \mathbb{R}$ may be chosen such that $\mathcal{T}$ is continuous. A stroboscopic solution of the corresponding Hamiltonian yields the map

$$T_{\text{kick}}(q, p) = \begin{pmatrix} q + \mathcal{T}'(p - \frac{1}{2}\mathcal{V}'(q)) \\ p - \frac{1}{2}\mathcal{V}'(q) - \frac{1}{2}\mathcal{V}'(q + \mathcal{T}'(p - \frac{1}{2}\mathcal{V}'(q))) \end{pmatrix}. \tag{4.57}$$

The phase space of the map T_{kick} basically looks very similar to the one shown in Fig. 3.2. However, the map T_{kick} still has more than one dominating partial barrier. In order to destroy

additional partial barriers, T_{kick} is composed with the map

$$T_{\text{rot}}(q,p) = \begin{pmatrix} q_{\text{c}} \\ p_{\text{c}} \end{pmatrix} + \begin{pmatrix} \cos(\omega_{\text{c}}) & -\sin(\omega_{\text{c}}) \\ \sin(\omega_{\text{c}}) & \cos(\omega_{\text{c}}) \end{pmatrix} \begin{pmatrix} q - q_{\text{c}} \\ p - p_{\text{c}} \end{pmatrix}, \tag{4.58}$$

within a circle of radius r_{c} around $(q_{\text{c}}, p_{\text{c}})$. The map T_{rot} is applied at two positions with parameters $q_{\text{c}} = 0.5$, $p_{\text{c}} = 0.33$, $r_{\text{c}} = 0.2$, $\omega_{\text{c}} = 3.0$, and $q_{\text{c}} = 0.2$, $p_{\text{c}} = 0.66$, $r_{\text{c}} = 0.15$, $\omega_{\text{c}} = 3.0$. The phase space shown in Fig. 3.2 corresponds to the map $T = T_{\text{rot}} \circ T_{\text{kick}}$ with a single dominating partial transport barrier of flux $\phi \approx 0.00532 \approx 1/200$. The partial barrier decomposes phase space into two chaotic regions of area $|A_1| \approx 0.422$ and $|A_2| \approx 0.421$.

The quantization $U = U_{\text{rot}} U_{\text{kick}}$ of the kicked model map $T = T_{\text{rot}} \circ T_{\text{kick}}$ is obtained from the quantizations U_{rot} of T_{rot} and U_{kick} of T_{kick}. The quantization of U_{kick} is the same as the quantized standard map, Eq. (4.23), when using the definitions of $\mathcal{T}$ and $\mathcal{V}$ from Eq. (4.53) and Eq. (4.54), respectively. The quantum map U_{rot} is obtained as follows: It is convenient to use a basis of N_{ho} harmonic oscillator eigenstates $\eta_0, \ldots \eta_{N_{\text{ho}}-1}$ inside the circle of radius r_{c}, which provides the projector

$$P_{\text{ho}} = \sum_{k=0}^{N_{\text{ho}}-1} \langle\, \eta_k \,|\, \cdot \,\rangle \eta_k \tag{4.59}$$

that semiclassically corresponds to the region inside the circle. Then

$$U_{\text{rot}} = (\mathbb{1} - P_{\text{ho}}) + U_{\text{ho}} P_{\text{ho}} \tag{4.60}$$

with

$$U_{\text{ho}} = \sum_{k=0}^{N_{\text{ho}}-1} e^{i(k+1/2)\,\omega_{\text{c}}} \langle\, \eta_k \,|\, \cdot \,\rangle \eta_k \tag{4.61}$$

is used as quantization of T_{rot}.

Chapter 5

Quantum Localization Transition in Closed Systems

This thesis is concerned with the phase-space localization of chaotic resonance states due to partial transport barriers. Before coming to the investigation of this central problem, let us review two relevant results from Ref. [32] on the analogous question addressed for closed systems. First, in Sec. 5.1, we discuss that eigenstates of the unitary time-evolution operator can localize on either side of a partial transport barrier or they can be equipartitioned on both sides depending on a single universal scaling parameter. This gives a smooth transition between the two regimes of localization and equipartition. In Sec. 5.2 we examine the relation between the localization of eigenstates of the time-evolution operator and transport properties of the system.

5.1 Localization Transition

It is well known that partial transport barriers can have a huge impact on quantum mechanical properties of a dynamical system [19, 20, 24, 30–34, 75, 162–166], such as the localization of eigenstates [19, 20, 30, 32, 34, 75] or fractal conductance fluctuations [162, 163, 165]. Focusing on the localization of chaotic eigenstates of the time-evolution operator, the influence of a partial transport barrier is essentially governed by the following question: How strong does an eigenstate in its phase-space representation deviate from a uniform distribution within the chaotic sea? This is motivated by the fact that in a fully chaotic system without restrictive transport barriers, quantum ergodicity ensures that the majority of eigenstates approaches the uniform distribution in the semiclassical limit [27]. Hence, any characteristic deviation from a uniform distribution which is not covered by exceptions of the quantum ergodicity theorem, i.e., any deviation different from ordinary quantum fluctuations or scarring effects [29], may be attributed to the presence of a restrictive partial transport barrier. We will discuss quantum

ergodicity in more detail in Sec. 7.1.1.

We first need to clarify what is meant by phase-space representation of a quantum state. In order to investigate quantum-to-classical correspondence, it is often very useful to consider the localization of quantum eigenstates in phase space. However, typically quantum mechanics is formulated either in position or momentum representation. The full phase-space picture is achieved for instance by the so-called Husimi representation [167,168]. Note that there are also other prominent phase-space representations introduced by Wigner [169] or by Glauber and Sudarshan [170,171] with their own advantages and disadvantages. The Husimi representation H_ψ of a quantum state ψ is defined by

$$H_\psi(q,p) := \frac{1}{h} \left| \langle\, \alpha_{(q,p)} \,|\, \psi \,\rangle \right|^2 \tag{5.1}$$

for $(q,p) \in \Gamma$, and describes the overlap of the state ψ with a minimal uncertainty wave packet $\alpha_{(q,p)}$ centered around (q,p). In more detail, $\alpha_{(q,p)}$ is chosen to be a coherent state, i.e., an eigenstate of the annihilation operator

$$\sqrt{\frac{m\omega}{2\hbar}} \left(q + \frac{i}{m\omega} p \right) \tag{5.2}$$

of the harmonic oscillator

$$H = \frac{1}{2m} p^2 + \frac{m\omega^2}{2} q^2, \tag{5.3}$$

cf. [172, Chap. 12]. Its width is chosen symmetrically and ideally localized by means of Heisenberg's uncertainty principle, $\Delta q = \Delta p = \sqrt{\hbar/2}$. The center (q,p) of $\alpha_{(q,p)}$ is determined by the expectation values of the position and momentum operator in this state. In dimensionless formulation, it is

$$\alpha_{(q,p)}(x) \propto \exp\left\{ -\frac{1}{h} \left(\pi (x-q)^2 - 2\pi i\, px \right) \right\}, \tag{5.4}$$

up to normalization [168, Eq. (2.29)].

Let us now consider the kicked model system with a single partial barrier introduced in Sec. 4.3. Its classical phase-space portrait is shown again in Fig. 5.1 compared to the Husimi distribution of quantum eigenstates for two different values of the effective size h of Planck's cell. While for $h = 1/50$, Fig. 5.1(c, d), the shown eigenstates localize dominantly (c) in region A_2 below the partial barrier or (d) in region A_1 above the partial barrier, the eigenstate shown in Fig. 5.1(b) for $h = 1/1000$ does not exhibit striking signatures of the partial barrier. Hence, the eigenstates in Fig. 5.1(c, d) for a rather large value of h are clearly affected by the partial barrier whereas the eigenstate in Fig. 5.1(b) for a smaller value of h totally ignores the

presence of the partial barrier.

It seems intuitive to some extent that chaotic eigenstates resemble the semiclassical expectation of uniform distribution for small values of h. Note that the classical chaotic dynamics explores the chaotic component rather uniformly on sufficiently large time scales. However, which criterion determines whether h is sufficiently small? And when is the drastic confinement to either side of the partial barrier to be expected? Apart from the evident dependence on the effective size h of Planck's cell, one could easily think of a dependence on the flux ϕ across the partial barrier, the size of the regions A_1 and A_2 on both sides of the partial barrier, or the chaoticity in terms of the Lyapunov exponent for instance. Remarkably, as already conjectured in Ref. [17], the crucial parameter is the ratio of ϕ and h. Chaotic eigenstates tend to localization if the transmission region of the partial barrier is quantum mechanically not resolved, i.e., if the flux across the partial barrier is small compared to Planck's cell ($\phi \ll h$). On the other hand, if the transmission region is quantum mechanically resolved ($h \ll \phi$), chaotic eigenstates are equipartitioned in the chaotic component as if there were no partial barrier at all [19, 20, 24, 31, 32, 37].

The precise behavior of the transition between the two regimes of localization and equipar-

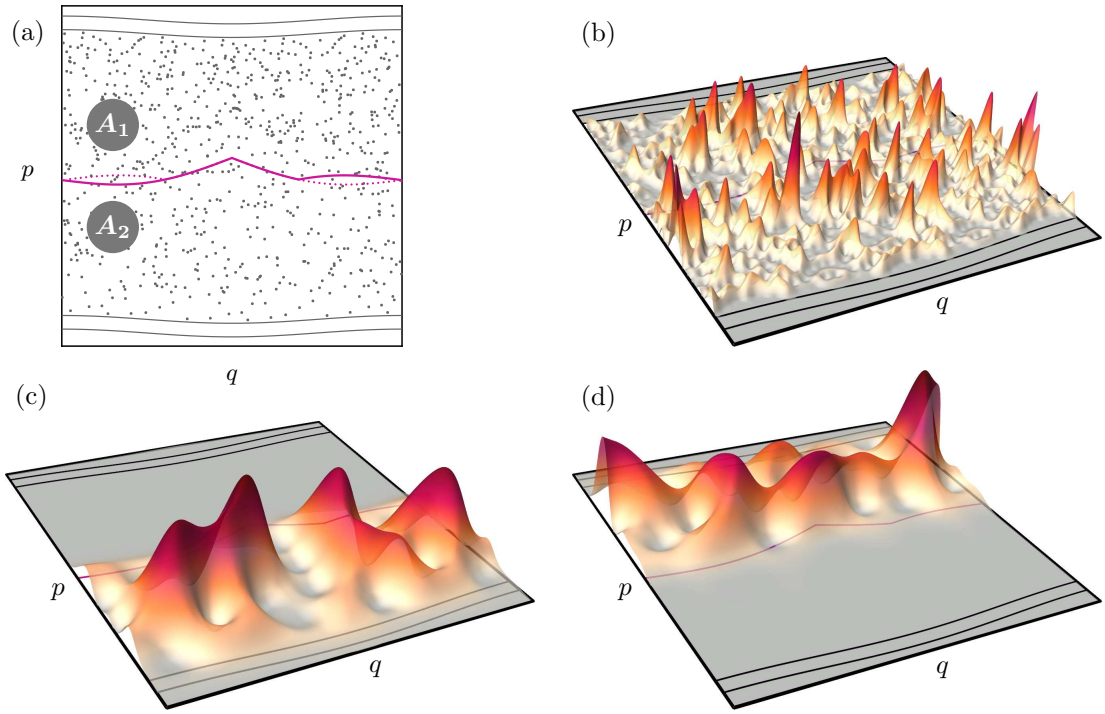

Figure 5.1. (a) Phase space of the kicked model system introduced in Sec. 4.3 with one dominant partial barrier (solid magenta line) of flux $\phi \approx 1/200$ in the chaotic sea. (b–d) Husimi representation of characteristic chaotic eigenstates for (b) $h = 1/1000$ and (c, d) $h = 1/50$.

titioned is investigated in Ref. [32]. The authors study the equipartition measure

$$w_{\mathrm{eq}}(\psi_k) := \frac{\|P_1\psi_k\|^2}{|A_1|}\frac{\|P_2\psi_k\|^2}{|A_2|}, \tag{5.5}$$

of the chaotic eigenstate ψ_k with respect to the two chaotic regions A_1 and A_2, which are separated by the partial barrier. Here, P_1 and P_2 denote orthogonal projections onto the Hilbert spaces associated with A_1 and A_2, and we assume without loss of generality that the chaotic region has unit phase-space volume. Note that numerically it may be useful to consider the Husimi weight of ψ_k in region A_n instead of $\|P_n\psi_k\|^2$. The equipartition measure of ψ_k is zero if the state is confined to one of the regions since the projection onto the other region then yields zero. The equipartition measure reaches unity if $\|P_n\psi_k\|^2 = |A_n|$ for both $n \in \{1,2\}$. This corresponds to the case that ψ_k is distributed like the classical Liouville measure. We point out that it is convenient to consider the relative weight $\|P_n\psi_k\|^2/|A_n|$ instead of the absolute weight $\|P_n\psi_k\|^2$ for that $\|P_n\psi_k\|^2$ approaches $|A_n|$ if there is no partial barrier. Moreover, the symmetry of A_1 and A_2 in the formulation of Eq. (5.5) accounts for the fact that it is not relevant in this setup to distinguish between the localization on A_1 and the localization on A_2. This comes at the cost of the ambiguity that a state ψ_k with $\|P_1\psi_k\|^2 = |A_2|$ and $\|P_2\psi_k\|^2 = |A_1|$ also yields $w_{\mathrm{eq}}(\psi_k) = 1$, a value which should be reserved for a truly equipartitioned state. We will comment on this issue again later. From numerical studies and supported by a heuristic 2×2 matrix model, the authors conclude that the average equipartition measure of chaotic eigenstates obeys

$$\langle w_{\mathrm{eq}}\rangle := \frac{1}{N_{\mathrm{ch}}}\sum_{k=1}^{N_{\mathrm{ch}}}\frac{\|P_1\psi_k\|^2}{|A_1|}\frac{\|P_2\psi_k\|^2}{|A_2|} \approx \frac{\phi/h}{1+\phi/h}, \tag{5.6}$$

where N_{ch} denotes the number of chaotic eigenstates [32]. Thus, the average equipartition measure of eigenstates follows a smooth transition from zero to unity, i.e., from localization on either side of the partial barrier to equipartition, see Fig. 5.2. It only depends on the single universal scaling parameter ϕ/h. Figure 5.2 shows that the transition curve is symmetric around the transition point $\phi/h = 1$, $\langle w_{\mathrm{eq}}\rangle = 0.5$ and has a width of two orders of magnitude in ϕ/h. Note that the algebraic structure of Eq. (5.6) can be derived by a Laurent expansion of the inverse of $\langle w_{\mathrm{eq}}\rangle$ in lowest order. It must be assumed that the equipartition measure is zero for $\phi/h = 0$, monotonically increases, and linearly approaches unity for $\phi/h \to \infty$.

Let us briefly argue that the mentioned ambiguity in the equipartition measure of a single chaotic eigenstate, Eq. (5.5), is not a serious problem for the averaged quantity in Eq. (5.6). The question at hand is whether it is possible that the average equipartition measure equals unity and the states localize as $\|P_1\psi_k\|^2 = |A_2|$ and $\|P_2\psi_k\|^2 = |A_1|$ on average. To this end,

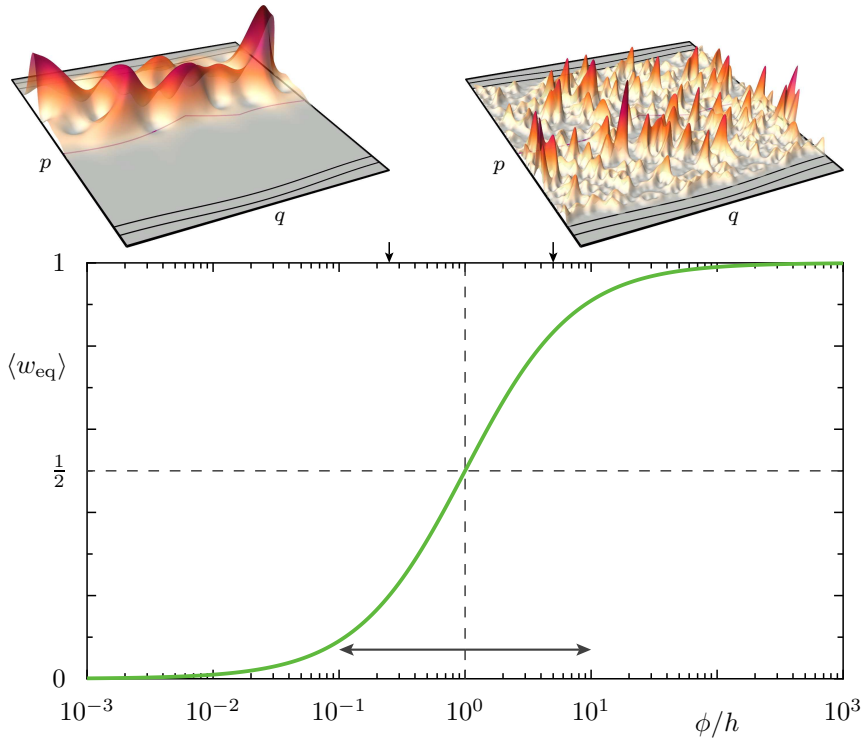

Figure 5.2. Theoretical expectation for the average equipartition measure $\langle w_{\mathrm{eq}} \rangle$ of chaotic eigenstates depending on the ratio of the flux ϕ across the partial barrier and the effective size h of Planck's cell, according to Eq. (5.6). Upper panels: Husimi representation of eigenstates as in Fig. 5.1, illustrating the different regimes of localization with ϕ/h indicated by arrows.

we compute the average weight of ψ_k in region A_n, giving

$$\frac{1}{N_{\mathrm{ch}}} \sum_{k=1}^{N_{\mathrm{ch}}} \|P_n \psi_k\|^2 = \frac{1}{N_{\mathrm{ch}}} \sum_{k=1}^{N_{\mathrm{ch}}} \langle\, \psi_k \,|\, P_n \psi_k \,\rangle, \tag{5.7}$$

since P_n is an orthogonal projection, $P_n^* = P_n$ and $P_n^2 = P_n$. We introduce the orthonormal basis $\{\eta_k\}_{k=1}^{N_n}$ in the subspace $\mathrm{im}\, P_n$ associated with A_n and find

$$\frac{1}{N_{\mathrm{ch}}} \sum_{k=1}^{N_{\mathrm{ch}}} \|P_n \psi_k\|^2 = \frac{1}{N_{\mathrm{ch}}} \sum_{k=1}^{N_{\mathrm{ch}}} \langle\, \psi_k \,|\, \sum_{j=1}^{N_n} \langle\, \eta_j \,|\, \psi_k \,\rangle \eta_j \,\rangle \tag{5.8}$$

$$= \frac{1}{N_{\mathrm{ch}}} \sum_{j=1}^{N_n} \langle \sum_{k=1}^{N_{\mathrm{ch}}} \langle\, \psi_k \,|\, \eta_j \,\rangle \psi_k \,|\, \eta_j \,\rangle. \tag{5.9}$$

Although $\{\psi_k\}_{k=1}^{N_{\mathrm{ch}}}$ is not a basis of the full Hilbert space, it is certainly possible to expand η_j

in terms of ψ_k as $\operatorname{im} P_n$ lies within the chaotic component. Thus, we obtain

$$\frac{1}{N_{\mathrm{ch}}} \sum_{k=1}^{N_{\mathrm{ch}}} \|P_n \psi_k\|^2 = \frac{1}{N_{\mathrm{ch}}} \sum_{j=1}^{N_n} \|\eta_j\|^2 = \frac{N_n}{N_{\mathrm{ch}}} \approx |A_n|. \tag{5.10}$$

The last relation holds true in the semiclassical limit, recalling that we assumed unit phase-space volume for the chaotic region as mentioned above. Hence, on average chaotic eigenstates will not localize as $\|P_1 \psi_k\|^2 = |A_2|$ and $\|P_2 \psi_k\|^2 = |A_1|$, and the ambiguity which is possible for individual states may be considered irrelevant for Eq. (5.6). The issue that single eigenstates can oddly localize unrecognized by the equipartition measure can for instance be overcome by studying the weight within only one of the two regions.

5.2 Localization and Transport

In Ref. [32] it is pointed out that there is a fundamental and very intuitive relation between the localization of eigenstates with respect to two phase-space regions A_1 and A_2, and the weight that is asymptotically transmitted between both regions when initializing a wave packet in one of them. The basic idea is as follows: Any wave packet may be expanded in the basis of eigenstates of the time-evolution operator. The more localized these eigenstates are the less are they coupled to each other. Thus, if the eigenstates predominantly localize in one of the regions, transport between both regions is suppressed. This is formulated more precisely in the following theorem.

Theorem. Let U be a unitary operator on the Hilbert space $\mathbb{C}^N$ with nondegenerate spectrum together with a basis of normalized eigenvectors $\{\psi_k\}_{k=1}^N$, and let $P_{\mathcal{A}}$ denote an orthogonal projection onto an arbitrary subspace $\mathcal{A} \subseteq \mathbb{C}^N$. Then it is

$$\frac{1}{N} \sum_{k=1}^{N} \lim_{t\to\infty} \frac{1}{t} \sum_{n=0}^{t-1} \|P_{\mathcal{A}_2} U^n P_{\mathcal{A}_1} \psi_k\|^2 = \frac{1}{N} \sum_{k=1}^{N} \|P_{\mathcal{A}_1} \psi_k\|^2 \|P_{\mathcal{A}_2} \psi_k\|^2, \tag{5.11}$$

for all subspaces $\mathcal{A}_1$ and $\mathcal{A}_2$ of $\mathbb{C}^N$.

Proof. It is convenient to define the shorthand notation

$$W_\infty(P_{\mathcal{A}_1} \psi_k) := \lim_{t\to\infty} \frac{1}{t} \sum_{n=0}^{t-1} \|P_{\mathcal{A}_2} U^n P_{\mathcal{A}_1} \psi_k\|^2 \tag{5.12}$$

for the absolute weight of $P_{\mathcal{A}_1}\psi_k$ that is asymptotically transmitted to the subspace $\mathcal{A}_2$. To begin with, we write

$$W_\infty(P_{\mathcal{A}_1}\psi_k) = \lim_{t\to\infty}\frac{1}{t}\sum_{n=0}^{t-1}\langle\, P_{\mathcal{A}_2}U^nP_{\mathcal{A}_1}\psi_k \,|\, P_{\mathcal{A}_2}U^nP_{\mathcal{A}_1}\psi_k\,\rangle, \tag{5.13}$$

and insert the expansion

$$P_{\mathcal{A}_1}\psi_k = \sum_{r=1}^{N}\langle\, \psi_r \,|\, P_{\mathcal{A}_1}\psi_k\,\rangle\psi_r. \tag{5.14}$$

Denoting the eigenvalue of U associated with ψ_k by $e^{i\varphi_k}$, this gives

$$\begin{aligned} W_\infty(P_{\mathcal{A}_1}\psi_k) &= \sum_{r=1}^{N}\sum_{s=1}^{N}\overline{\langle\, \psi_r \,|\, P_{\mathcal{A}_1}\psi_k\,\rangle}\langle\, \psi_s \,|\, P_{\mathcal{A}_1}\psi_k\,\rangle \times \\ &\quad \times \lim_{t\to\infty}\frac{1}{t}\sum_{n=0}^{t-1}\langle\, P_{\mathcal{A}_2}U^n\psi_r \,|\, P_{\mathcal{A}_2}U^n\psi_s\,\rangle \qquad (5.15) \\ &= \sum_{r=1}^{N}\sum_{s=1}^{N}\overline{\langle\, \psi_r \,|\, P_{\mathcal{A}_1}\psi_k\,\rangle}\langle\, \psi_s \,|\, P_{\mathcal{A}_1}\psi_k\,\rangle\langle\, P_{\mathcal{A}_2}\psi_r \,|\, P_{\mathcal{A}_2}\psi_s\,\rangle \times \\ &\quad \times \lim_{t\to\infty}\frac{1}{t}\sum_{n=0}^{t-1}e^{i(\varphi_s-\varphi_r)n}, \qquad (5.16) \end{aligned}$$

where $\lim_{t\to\infty}\frac{1}{t}\sum_{n=0}^{t-1}\exp[i(\varphi_s-\varphi_r)n] = \delta_{rs}$ as long as there are no degeneracies in the spectrum of U. We obtain

$$W_\infty(P_{\mathcal{A}_1}\psi_k) = \sum_{\ell=1}^{N}|\langle\, \psi_\ell \,|\, P_{\mathcal{A}_1}\psi_k\,\rangle|^2\,\|P_{\mathcal{A}_2}\psi_\ell\|^2 \tag{5.17}$$

and perform the average over the full basis of eigenstates,

$$\begin{aligned} \frac{1}{N}\sum_{k=1}^{N}W_\infty(P_{\mathcal{A}_1}\psi_k) &= \frac{1}{N}\sum_{k=1}^{N}\sum_{\ell=1}^{N}|\langle\, \psi_\ell \,|\, P_{\mathcal{A}_1}\psi_k\,\rangle|^2\,\|P_{\mathcal{A}_2}\psi_\ell\|^2 \qquad (5.18) \\ &= \frac{1}{N}\sum_{\ell=1}^{N}\|P_{\mathcal{A}_2}\psi_\ell\|^2\sum_{k=1}^{N}\langle\, P^*_{\mathcal{A}_1}\psi_\ell \,|\, \psi_k\,\rangle\langle\, \psi_k \,|\, P^*_{\mathcal{A}_1}\psi_\ell\,\rangle \qquad (5.19) \\ &= \frac{1}{N}\sum_{\ell=1}^{N}\|P^*_{\mathcal{A}_1}\psi_\ell\|^2\,\|P_{\mathcal{A}_2}\psi_\ell\|^2. \qquad (5.20) \end{aligned}$$

Using that $P^*_{\mathcal{A}_1} = P_{\mathcal{A}_1}$ for orthogonal projections, this gives Eq. (5.11) and concludes the

proof. Note that, in fact, we did not use the projection property of $P_{\mathcal{A}_1}$ or $P_{\mathcal{A}_2}$ but only their selfadjointness. □

Equation (5.11) relates the average equipartition measure of eigenstates (right hand side) to the asymptotic transmission of weight from one side of the partial barrier to the other (left hand side). In view of the ϕ/h dependence of the equipartition measure discussed in Sec. 5.1, this means that also the asymptotically transmitted weight obeys the same ϕ/h dependence [32]. Hence, for small values of ϕ/h, such that the transmission region of the partial barrier is quantum mechanically not resolved, a wave packet initialized in one of the regions will remain there for all times and will essentially not penetrate into the other phase-space region. We stress that a classical trajectory will explore the entire chaotic phase-space component in the long run. Hence, one might think of the localization due to a partial transport barrier as exhibiting the opposite phenomenology compared to the famous tunneling effect [32]: The tunneling process allows quantum transport in cases where there is no classical transport [100, §50]. Here, one observes suppression of quantum transport although classical transport is allowed. We emphasize that comparable relations between localization and transport have been studied in other situations before. To mention a few examples: strong Anderson localization due to disorder suppresses diffusion and implies a metal–insulator transition [6,7]; weak localization due to time-reversal invariance yields corrections to the classical Drude conductivity of a metal [8]; localization of edge states due to topological protection is related to the quantized Hall conductance [3,9]; and many-body localization in Fock space implies a metal–insulator transition at finite temperatures for systems of interacting particles [10].

The original formulation of Eq. (5.11) in Refs. [32] is slightly different. There, the left hand side of the equality, which is related to transport, contains a sum over an arbitrary basis of wave packets in region A_1. Instead we use the basis of eigenstates of U and project it onto A_1. The advantage of the latter is that it reveals a remarkable relation to ergodicity as we will now demonstrate. To this end, we first show that Eq. (5.11) semiclassically reads

$$\frac{1}{N}\sum_{k=1}^{N}\lim_{t\to\infty}\frac{1}{t}\sum_{n=0}^{t-1}\mu_{\psi_k}(\mathcal{A}_2\cap U^n\mathcal{A}_1)=\frac{1}{N}\sum_{k=1}^{N}\mu_{\psi_k}(\mathcal{A}_1)\mu_{\psi_k}(\mathcal{A}_2), \tag{5.21}$$

where $\mu_{\psi_k}(\mathcal{A}) := \|P_{\mathcal{A}}\psi_k\|^2$ defines a probability measure on subspaces of $\mathbb{C}^N$ which is invariant under U. Recall that an orthogonal projection $P_{\mathcal{A}}$ on a subspace $\mathcal{A}\subseteq\mathbb{C}^N$ can be represented by

$$P_{\mathcal{A}}=\sum_{k=1}^{M}\langle\,\eta_k\,|\,\cdot\,\rangle\eta_k \tag{5.22}$$

in terms of an orthonormal basis $\{\eta_k\}_{k=1}^M$ of $\mathcal{A}$. Since $\{U\eta_k\}_{k=1}^M$ denotes an orthonormal basis

of $U\mathcal{A}$, we obtain

$$P_{U\mathcal{A}} = \sum_{k=1}^{M} \langle\, U\eta_k \,|\, \cdot \,\rangle U\eta_k = U \sum_{k=1}^{M} \langle\, \eta_k \,|\, U^* \cdot \,\rangle \eta_k = U P_{\mathcal{A}} U^*. \tag{5.23}$$

Semiclassically, the concatenation of two projections $P_{\mathcal{A}}$, $P_{\mathcal{B}}$ associated with phase-space regions A and B projects onto $A \cap B$, that is $P_{\mathcal{A}} P_{\mathcal{B}} = P_{\mathcal{A}\cap\mathcal{B}}$. We stress that in general, i.e., away from the semiclassical regime, this relation is only valid if $P_{\mathcal{A}}$ and $P_{\mathcal{B}}$ commute. Having said this it is

$$\begin{aligned} \|P_{\mathcal{A}_2} U^n P_{\mathcal{A}_1} \psi_k\|^2 &= |e^{-i\varphi_k n}|^2 \, \|P_{\mathcal{A}_2} U^n P_{\mathcal{A}_1} U^{-n} \psi_k\|^2 && (5.24)\\ &= \|P_{\mathcal{A}_2} P_{U^n \mathcal{A}_1} \psi_k\|^2 && (5.25)\\ &= \|P_{\mathcal{A}_2 \cap U^n \mathcal{A}_1} \psi_k\|^2. && (5.26) \end{aligned}$$

Inserting this into Eq. (5.11) and using the notation $\mu_{\psi_k}(\mathcal{A}) = \|P_{\mathcal{A}} \psi_k\|^2$, we find Eq. (5.21). We still have to show that μ_{ψ_k} is a probability measure which is invariant under U. This follows from

$$\mu_{\psi_k}(U^{-1}\mathcal{A}) = \|P_{U^*\mathcal{A}} \psi_k\|^2 = \|U^* P_{\mathcal{A}} U \psi_k\|^2 = |e^{i\varphi_k}|^2 \, \|P_{\mathcal{A}} \psi_k\|^2 = \mu_{\psi_k}(\mathcal{A}), \tag{5.27}$$

and

$$\|\mu_{\psi_k}\| = \mu_{\psi_k}(\mathbb{C}^N) = \|P_{\mathbb{C}^N} \psi_k\|^2 = \|\psi_k\|^2 = 1. \tag{5.28}$$

As a rather technical remark, note that in order to define a proper measure on an appropriate σ-algebra, the union of sets needs to be replaced by the span of vector spaces.

As mentioned above, Eq. (5.21) is related to ergodicity in an interesting way. Recall that a probability measure μ that is invariant under the map T is ergodic if and only if

$$\lim_{t\to\infty} \frac{1}{t} \sum_{n=0}^{t-1} \mu(A_2 \cap T^{-n}(A_1)) = \mu(A_1)\mu(A_2) \tag{5.29}$$

for all measurable sets A_1 and A_2 [173, Prop. 9.1]. Ergodicity it often referred to as »spatial average equals temporal average« following Birkhoff's ergodic theorem [118, Thm. II.12], and thus relates localization properties and transport properties. Intuitively speaking, the left hand side of Eq. (5.29) describes how much the set A_1 penetrates into region A_2 under time evolution, weighted with μ (transport property), while the right hand side describes how equipartitioned the measure μ is with respect to A_1 and A_2 (localization property). Comparing Eqs. (5.29) and (5.21), the latter may thus be interpreted as describing an averaged ergodicity. Note, however, that this does not give any indication of chaotic dynamics or mixing behavior for U,

apart from the assumption of nondegeneracy of the spectrum which could be due to chaotic level repulsion for instance. Still, also the left hand side of Eq. (5.21) describes transport while the right hand side describes localization. Consider two subspaces $\mathcal{A}_1$ and $\mathcal{A}_2$ such that the eigenstates ψ_k of U are predominantly localized on one of the two subspaces, e.g., due to a restrictive partial transport barrier. This implies that for each ψ_k one of the values $\mu_{\psi_k}(\mathcal{A}_1)$ and $\mu_{\psi_k}(\mathcal{A}_2)$ is close to unity while the other one is close to zero. Thus, the right hand side of Eq. (5.21) is small. On the other hand, this implies that the overlap $\mathcal{A}_2 \cap U^n \mathcal{A}_1$ must also be small, which corresponds to weak coupling or suppressed transport. Vice versa, given that the eigenstates ψ_k are equipartitioned with respect to $\mathcal{A}_1$ and $\mathcal{A}_2$, the right hand side of Eq. (5.21) maximizes. Correspondingly, the overlap $\mathcal{A}_2 \cap U^n \mathcal{A}_1$ is large such that transport between both regions is enhanced.

Chapter 6

Observation of Localization Transitions in Open Quantum Systems

In this chapter we present two numerical observations on localization transitions of chaotic resonance states in open quantum systems. They have originally been reported in Ref. [34]. Their explanation will be the main subject of this thesis. We conclude this chapter by a discussion of the relation between localization of resonance states and transport for open systems. It turns out that their relation in open systems is quite different from their intimate relation in closed systems examined in Sec. 5.2.

6.1 Localization Transitions

To introduce the basic phenomenon, let us again consider the kicked model system with an isolated partial barrier studied in the previous chapter, see phase-space portrait in Fig. 6.1(a). Following Ref. [32], we have discussed that chaotic eigenstates of the time-evolution operator are equipartitioned with respect to the two sides of the partial barrier if the flux ϕ across the partial barrier is quantum mechanically well resolved, $\phi \gg h$, see Fig. 6.1(b). This is the case for closed systems. Once the system is opened by an absorbing region this changes drastically, see Fig. 6.1(c). Although the condition $\phi \gg h$ is satisfied for the open system just as for the closed system, the shown long-lived chaotic resonance state clearly localizes above the partial barrier. Note that the shown localized state is a typical example and not just an exception. Moreover, this localization is even present for a much smaller size of Planck's cell, see Fig. 6.1(d), where the quantum resolution of the flux across the partial barrier is even improved. This localization of chaotic resonance states with respect to the partial transport barrier, in cases where one observes equipartition of eigenstates in the corresponding closed system, demonstrates that the presence of partial transport barriers in open systems is even more influential than in closed systems. This phenomenon was first reported in Refs. [33, 123].

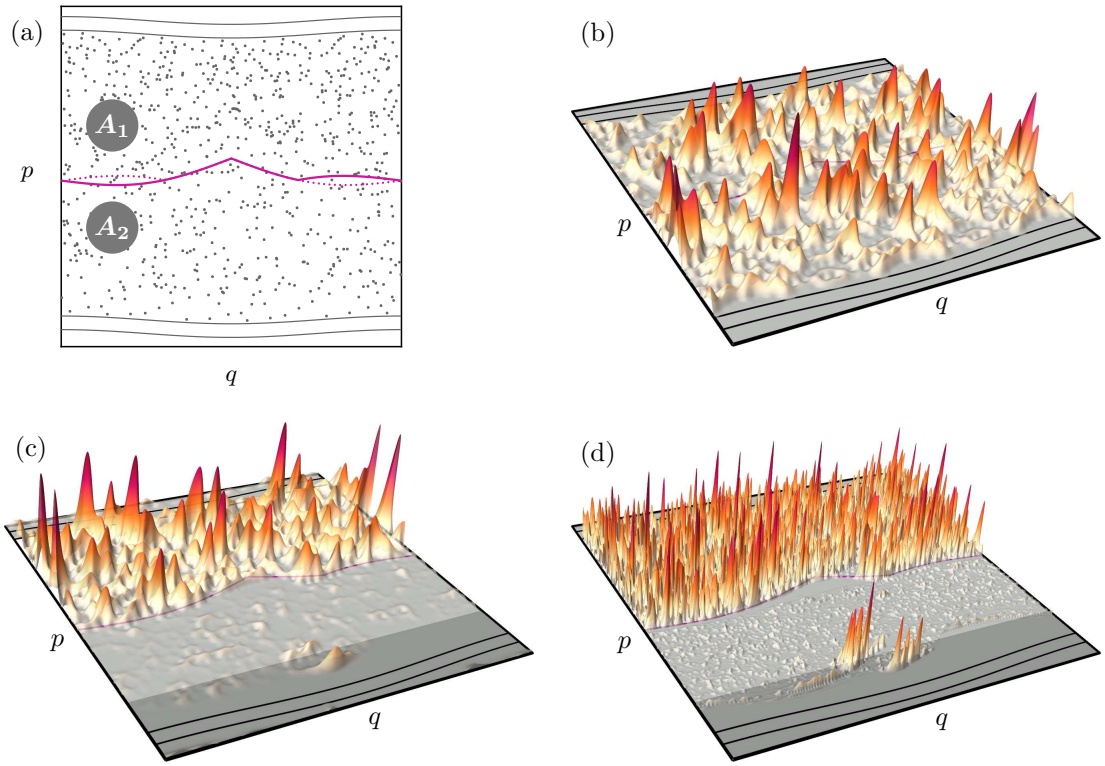

Figure 6.1. (a) Phase space of the kicked model system introduced in Sec. 4.3 with one dominant partial barrier (solid magenta line) of flux $\phi \approx 1/200$ in the chaotic sea. (b) Husimi representation of a characteristic chaotic eigenstate for $h = 1/1000$. (c, d) Husimi representation of a characteristic long-lived chaotic resonance state of the opened system with $|\Omega| = 0.25$ (gray region) for (c) $h = 1/1000$ and (d) $h = 1/10000$.

Let us at first numerically investigate the transition from equipartition to localization when increasing the size of the opening, shown in Fig. 6.2. In order to reveal the parameter dependence of such a transition, it is useful to have the opportunity to change the relevant system parameters arbitrarily. This is simple for parameters like the size h of Planck's cell or the opening Ω of the system. However, as we also want to change the flux ϕ across the partial barrier and later also the areas $|A_1|$ and $|A_2|$ of the chaotic regions on either side of the partial barrier, we consider a different model system, namely the partial-barrier standard map introduced in Chap. 4. Also for this map, we observe the phenomenon that a typical long-lived resonance state localizes on one side of the partial barrier while a typical eigenstate of the corresponding closed system is equipartitioned if $\phi \gg h$, see Fig. 6.2 (upper panels). The transition from equipartition to localization is investigated as follows: For a fixed set of system parameters ($h = 1/6000$, $|A_1| = |A_2| = 1/2$), particularly for a fixed pair of ϕ and Ω, the time-evolution is described by a single subunitary matrix U. This matrix has $N = 1/h$ different eigenstates with a broad range of decay rates. In the first place, we focus on long-lived states with a decay rate of $\gamma \approx \gamma_{\mathrm{nat}}$. The natural decay rate γ_{nat} describes the asymptotic

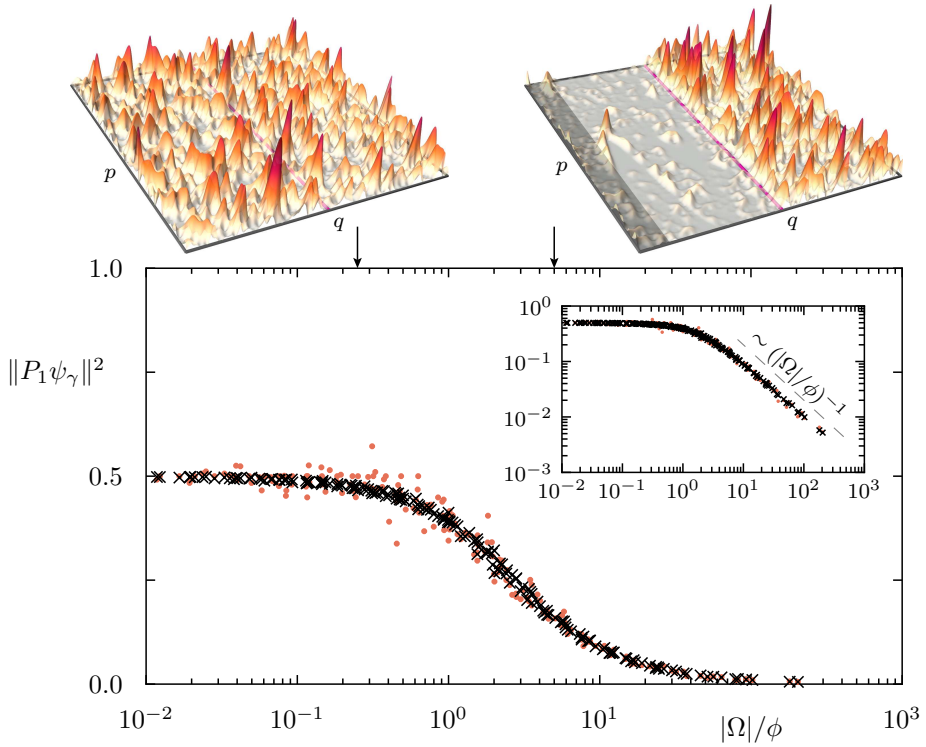

Figure 6.2. Weight $\|P_1\psi_\gamma\|^2$ of resonance states in region A_1 vs ratio of size $|\Omega|$ of opening and flux ϕ across partial barrier for different parameters of the partial-barrier standard map ($10 \leq \phi/h, |\Omega|/h \leq 2048$; $|A_1| = 1/2$; $h = 1/6000$). Weight of state with γ closest to γ_{nat} (red points) and averaged over states with decay rates $\gamma \in [\gamma_{\text{nat}}/1.1, \gamma_{\text{nat}} \cdot 1.1]$ (black crosses). Inset: Same data shown on double-logarithmic scale. Upper panels: Husimi representation of typical resonance states with $\gamma \approx \gamma_{\text{nat}}$ for $h = 1/1000$, $\phi/h = 20$, and two values $|\Omega|/\phi$ indicated by arrows.

decay of an initially uniform distribution under the classical open dynamics. We will discuss this natural decay in much more detail later. For the moment it is sufficient to think of it as a characteristic decay rate for long-lived resonance states. We compute the absolute weight $\|P_1\psi_\gamma\|^2$ of all chaotic resonance states ψ_γ having a decay rate $\gamma \in [\gamma_{\text{nat}}/1.1, \gamma_{\text{nat}} \cdot 1.1]$ within a small window around γ_{nat}. Here P_1 denotes the projection onto the subspace that is semiclassically associated with the phase-space region A_1 (containing the opening Ω), such that $\|P_1\psi_\gamma\|^2$ is the weight of the resonance state ψ_γ within A_1. By taking the arithmetic mean of the different weights $\|P_1\psi_\gamma\|^2$ quantum fluctuations are reduced. Note that the factor 1.1 defining the window of decay rates is balanced such that there are sufficiently many resonance states under consideration in order to reduce the fluctuations significantly and that all resonance states in the decay-rate window still exhibit approximately the same magnitude of localization. The weight $\|P_1\psi_\gamma\|^2$ averaged over resonance states with decay rate close to γ_{nat} provides a simple characteristic quantity to describe the localization of long-lived resonance states in a single open quantum system, shown in Fig. 6.2 as a black cross. It is

$\|P_1\psi_\gamma\|^2 = |A_1| = 1/2$ if the states are equipartitioned with respect to the partial barrier, it is $\|P_1\psi_\gamma\|^2 = 0$ if the states entirely localize in region A_2, and it is $\|P_1\psi_\gamma\|^2 = 1$ if the states entirely localize in region A_1. By variation of both ϕ and $|\Omega|$ we can monitor the whole transition from equipartition to localization. In Fig. 6.2, we use all combinations of

$$\phi/h \in \{10, 22, 32, 68, 84, 122, 172, 238, 402, 508, 848, 1032, 1622, 2048\}, \tag{6.1a}$$

$$|\Omega|/h \in \{10, 20, 34, 58, 78, 124, 190, 236, 376, 516, 788, 1022, 1804, 2044\}, \tag{6.1b}$$

where pairs of $|\Omega|/h$ and ϕ/h with $|\Omega| + \phi \geq |A_1|$ (or $\phi \geq |A_2|$) are omitted. Note that the values of ϕ/h and $|\Omega|/h$ are chosen such that we obtain many different values of $|\Omega|/\phi$, and that there is no deeper meaning in their exact values. With this, we find a smooth transition from equipartition, $\|P_1\psi_\gamma\|^2 = |A_1|$, for $|\Omega| \ll \phi$ to localization on A_2 for $|\Omega| \gg \phi$, see Fig. 6.2. The transition, in fact, universally depends only on the ratio of the openness $|\Omega|$ and the flux ϕ. The double-logarithmic visualization in the inset reveals that $\|P_1\psi_\gamma\|^2$ decreases as $(|\Omega|/\phi)^{-1}$ starting roughly at the order of $|\Omega|/\phi \approx 1$. We stress that this localization transition in the open system occurs even though $\phi/h \geq 10$, where in the closed system eigenstates are equipartitioned [32]. Moreover, we point out that already individual states nicely display this localization transition. To demonstrate this, we consider the single chaotic resonance state ψ_γ with decay rate closest to γ_{nat} on a logarithmic scale, i.e., the state for which $|\log(\gamma) - \log(\gamma_{\text{nat}})|$ is minimal. Its localization is shown in Fig. 6.2 by a red point for each fixed system setting. Up to fluctuations, which are rather confined in this setup, the individual state exhibits the transition from equipartition to localization on A_2 for increasing $|\Omega|/\phi$.

In the above numerical study, we simplified the problem of localization of resonance states due to a partial barrier by picking one typically relevant decay rate and associating a single localization value to an entire quantum system. Indeed, even for a single quantum system there is a broad range of decay rates, cf. [174] for instance. As shown in [49] in the context of fully chaotic systems, the distribution of weights of a resonance state in phase space depends on its decay rate. This indicates that also the localization with respect to a partial barrier in terms of the weight $\|P_1\psi_\gamma\|^2$ could change with the decay rate. In Fig. 6.3, we consider the single quantum system for fixed parameters $\phi/h = 100$ and $|\Omega|/h = 1000$ such that $|\Omega| \gg \phi$, for which the long-lived resonance states localize on A_2, cf. Fig. 6.2. We diagonalize the corresponding time-evolution matrix U and show the γ-dependence of the weights $\|P_1\psi_\gamma\|^2$ for all resonance states. We find a transition from resonance states which localize on A_2 for small γ to resonance states which localize on A_1 for large γ, including equipartitioned resonance states in between. Let us emphasize that this transition between the two extreme cases of localization on both sides of the partial barrier even for a single quantum system is important for the correct interpretation of Fig. 6.2 where we focused on γ_{nat}, only.

To conclude, we observe (i) a transition from equipartition to localization of long-lived

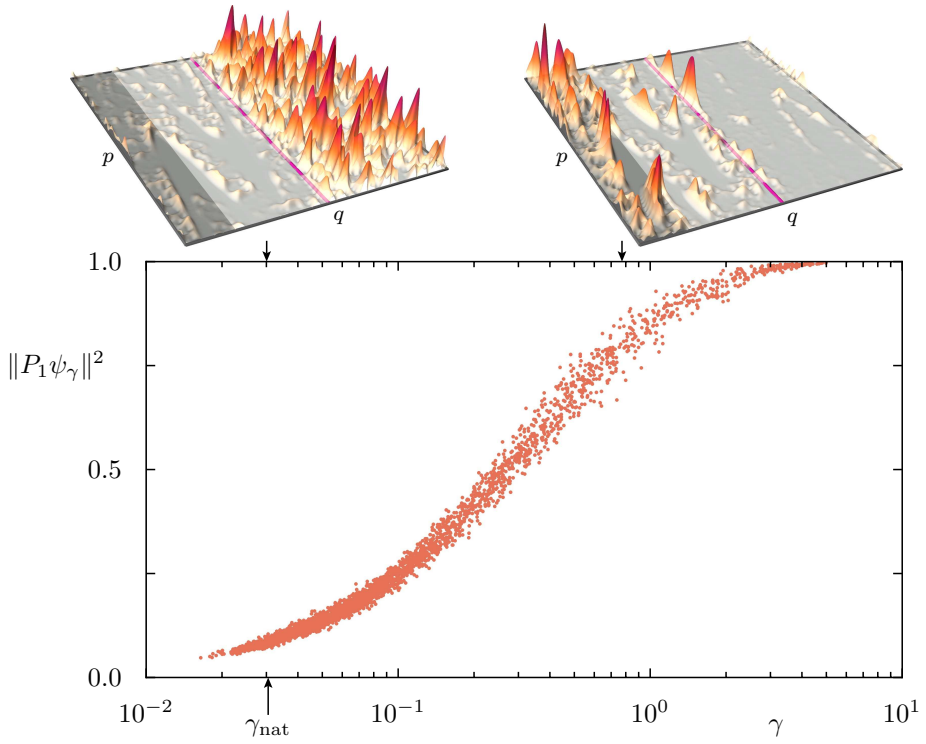

Figure 6.3. Weight $\|P_1\psi_\gamma\|^2$ (red points) of resonance states ψ_γ in region A_1 vs decay rate γ for the partial-barrier standard map ($\phi/h = 100$; $|\Omega|/h = 1000$; $|A_1| = 1/2$; $h = 1/6000$). Upper panels: Husimi representation of typical long-lived (left) and short-lived (right) resonance state for $h = 1/1000$ with γ values indicated by arrows.

chaotic resonance states on A_2 for increasing size $|\Omega|$ of the opening, see Fig. 6.2, and (ii) a transition from localization on A_2 to localization on A_1 for increasing γ, see Fig. 6.3. Transition (i) is surprising as localization occurs for $\phi \gg h$, where in the closed system the eigenstates are equipartitioned. Transition (ii) shows that in open systems the localization depends on the decay rate γ. The fact that both transitions (i) and (ii) occur for $\phi \gg h$ suggests that the localization transitions could be of classical origin. Furthermore, from the point of view of decaying classical phase-space distributions the observed transitions qualitatively seem to be rather intuitive: In Fig. 6.2, for a larger size of the opening one has less weight in region A_1 that contains the opening. In Fig. 6.3, a larger weight in A_1 corresponds to a larger decay rate. For a quantitative description, however, one needs suitable classical distributions, that is, one has to find the classical counterpart of a quantum resonance state. Chapter 7 is dedicated to this question. Before coming to that, let us discuss the relation between the localization of resonance states and phase-space transport for open systems.

6.2 Localization and Transport

For open systems, there is no straightforward generalization of the relation between localization and transport from closed systems discussed in Sec. 5.2. This basically relies on the fact that the structural result, Eq. (5.21), uses averaging arguments which hold true for asymptotically large times. In open systems, the resonance states are subject to decay with an individual decay rate. Thus, any initial wave packet φ will eventually die out under the proper subunitary time evolution by U. Still, one might wonder what the wave packet looks like under an artificial renormalized time evolution $\tilde{U}$ compensating the decay. To this end, we consider the nonlinear but norm-preserving operator

$$\tilde{U}\varphi := \frac{\|\varphi\|}{\|U\varphi\|} U\varphi. \tag{6.2}$$

The iteration of $\tilde{U}$ reads

$$\begin{aligned}
\tilde{U}^2\varphi &= \tilde{U}\left(\frac{\|\varphi\|}{\|U\varphi\|}U\varphi\right) && (6.3)\\
&= \frac{\left\|\frac{\|\varphi\|}{\|U\varphi\|}U\varphi\right\|}{\left\|U\left(\frac{\|\varphi\|}{\|U\varphi\|}U\varphi\right)\right\|} U\left(\frac{\|\varphi\|}{\|U\varphi\|}U\varphi\right) && (6.4)\\
&= \frac{\frac{\|\varphi\|}{\|U\varphi\|}\|U\varphi\|}{\frac{\|\varphi\|}{\|U\varphi\|}\|U^2\varphi\|}\frac{\|\varphi\|}{\|U\varphi\|}U^2\varphi && (6.5)\\
&= \frac{\|\varphi\|}{\|U^2\varphi\|}U^2\varphi, && (6.6)
\end{aligned}$$

giving

$$\tilde{U}^n\varphi = \frac{\|\varphi\|}{\|U^n\varphi\|}U^n\varphi \tag{6.7}$$

for the n-th iterate. In words, the n-th iterate of the renormalized time-evolution operator $\tilde{U}$ is simply given by the renormalization of the n-th iterate of the original time evolution U. We express φ in terms of eigenstates $\{\psi_k\}_{k=1}^N$ of U, $U\psi_k = \lambda_k\psi_k$, and obtain

$$U^n\varphi = \sum_{k=1}^{N} c_k\lambda_k^n\psi_k \tag{6.8}$$

with coefficients c_k as in Eq. (2.45). Since U is subunitary, the modulus of λ_k is below unity such that asymptotically, i.e., for sufficiently large n, the time evolution of φ is governed by the ψ_k with largest value $|\lambda_k|$ and $c_k \neq 0$. All other eigenstates with larger decay rate are exponentially suppressed.

Hence, in order to understand the asymptotic evolution of wave packets in open systems, one only has to understand the localization of the longest-lived resonance states. Resonance states of larger decay rate are relevant only for the initial temporal regime. To demonstrate this dominance of long-lived resonance states, we consider the example of the standard map at $\kappa = 2.9$ with a mixed phase space opened in the chaotic sea by two stripes of width 0.05, cf. Sec. 3.1. The longest-lived state is the regular ground state located at the central elliptic fixed point. It is coupled to the opening only by the rather slow process of dynamical tunneling [36]. Still, a wave packet initialized in the chaotic sea resembles the ground state for sufficiently large times as can be seen in Fig. 6.4. As a technical remark, we mention that numerically these large iteration times, $t = 2^n$, are achieved by an n-fold loop multiplying U with itself in each loop cycle.

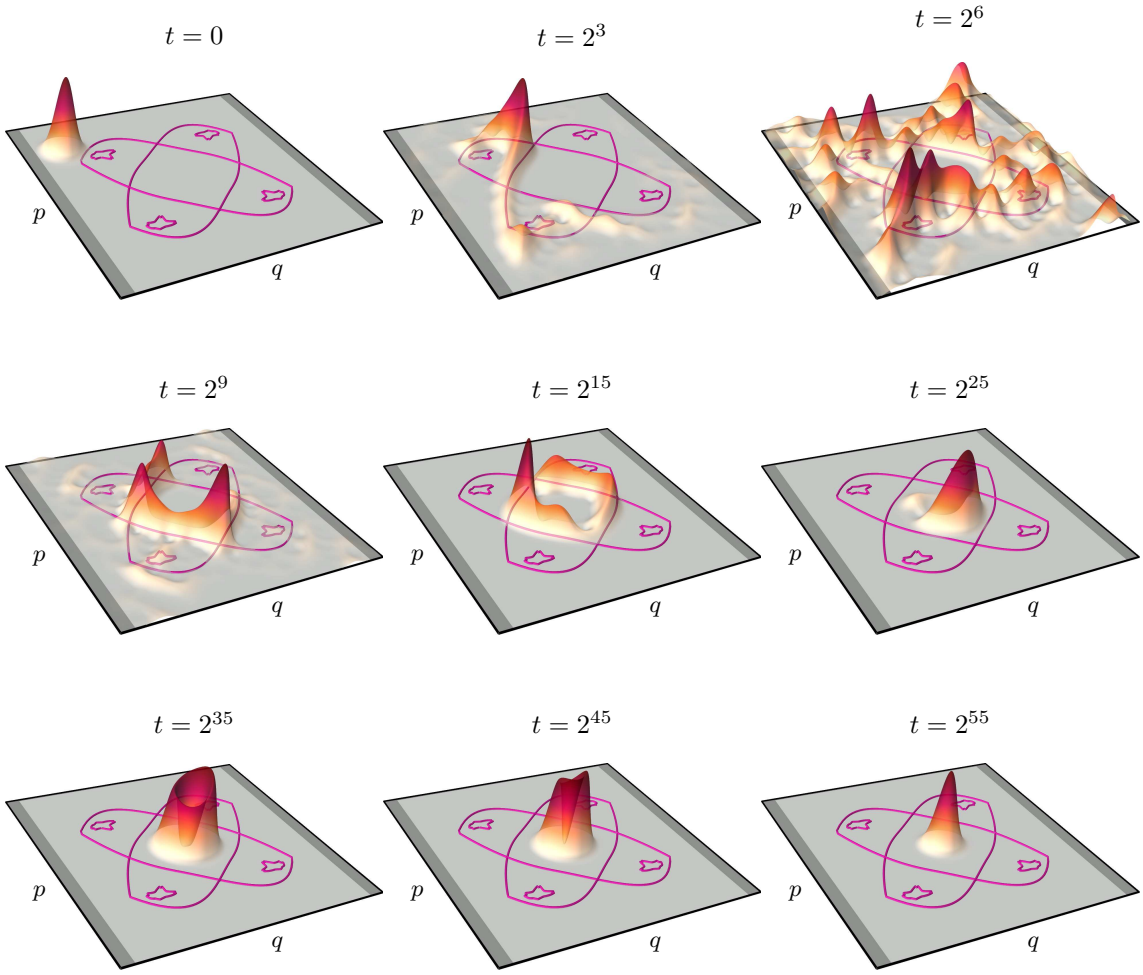

Figure 6.4. Husimi representation of the renormalized time evolution of a wave packet for the standard map, $\kappa = 2.9$, $h = 1/150$, for different number t of iterations as indicated above each panel. The system is opened by absorbing stripes (gray shaded) of total area $|\Omega| = 0.1$. The magenta lines show the dominant partial barriers of the system.

Chapter 7

Semiclassical Structure of Chaotic Resonance States

The observations on the semiclassical localization of chaotic resonance states due to a partial transport barrier in Sec. 6.1 led us to the question: What is the classical counterpart of a quantum resonance state? This is the central topic of this chapter. First, we review basic results on the semiclassical structure of quantum eigenstates for closed systems in Sec. 7.1. We particularly discuss the relevance of invariant measures in this context. In Sec. 7.2 we fathom the structure of chaotic resonance states for open systems based on the work by Keating et al. [49]. Semiclassically, this leads to the study of conditionally invariant measures. We introduce the class of γ-natural conditionally invariant measures, originally published in [34], for which quantum-to-classical correspondence with chaotic resonance states will be demonstrated in Chaps. 8 and 9.

7.1 Quantum–Classical Correspondence in Closed Systems

For closed systems the semiclassical phase-space localization of quantum eigenstates is well understood. Following the line of arguments as presented in Ref. [146, Sec. 3] we review fundamental results on the semiclassical localization of regular and chaotic eigenstates in the following. It turns out that the relevant classical objects are invariant measures which correspond to uniform phase-space distributions for Hamiltonian systems.

7.1.1 Semiclassical Structure of Quantum Eigenstates

Let us begin with the case of integrable dynamics. Here, the classical dynamics takes place as periodic or quasi-periodic (ergodic) motion on invariant tori. From the semiclassical eigenfunction hypothesis [11, 14, 15], one knows that quantum eigenstates are concentrated in their

Husimi representation on such invariant tori with minimal uncertainty as defined by the size h of Planck's cell. For an example of such a regular eigenstate for the standard map, see Fig. 7.1(a). The quantizing tori $\mathcal{C}_n$ obey the Bohr–Sommerfeld quantization condition [102, Sec. 11.3],

$$\oint_{\mathcal{C}_n} p(q)\,dq = \left(n + \frac{1}{2}\right) h, \qquad (n \in \mathbb{N}_0) \tag{7.1}$$

where p denotes the (multivalued) momentum along the irreducible circuit of the torus $\mathcal{C}_n$ as a function of the position q, such that $\oint_{\mathcal{C}_n} p(q)\,dq$ is the phase-space area enclosed by $\mathcal{C}_n$. From the approximation scheme by Wentzel, Kramers, and Brillouin, one even has an explicit representation for a regular eigenstate ψ that is semiclassically correct, namely

$$\psi(q) = \sum_{\pm} \frac{c_\pm}{\sqrt{|p(q)|}} \exp\left\{\pm \frac{i}{\hbar} \int^q p(x)\,dx\right\}, \tag{7.2}$$

with appropriate expansion coefficients $c_\pm$ [175, Sec. VII]. It has been shown in [13, Sec. 3] that this approaches a uniform distribution along the regular torus for $h \searrow 0$, using the Wigner–Weyl formalism. We emphasize that, quite intuitively, this uniform distribution on the torus is *invariant* under the classical time evolution.

For chaotic systems there is in general no explicit semiclassical expression like Eq. (7.2) for eigenstates [146, Sec. 3.2]. The generic behavior, however, is captured by the quantum ergodicity theorem [27]: Consider a unitary quantum map $U_N : \mathbb{C}^N \to \mathbb{C}^N$ corresponding to an ergodic symplectic map on a toric phase space with a basis of normalized eigenstates, $\psi_n^N \in \mathbb{C}^N$, $n \in \{1, \ldots, N\}$. Then there exists a sequence $(E_N)_{N\in\mathbb{N}}$ of sets $E_N \subseteq \{1, \ldots, N\}$ satisfying $\lim_{N\to\infty} \#E_N/N = 1$, such that for every sequence $(n_N)_{N\in\mathbb{N}}$ with $n_N \in E_N$, the sequence $(H_{\psi^N_{n_N}})_{N\in\mathbb{N}}$ of Husimi distributions converges towards the uniform distribution (in

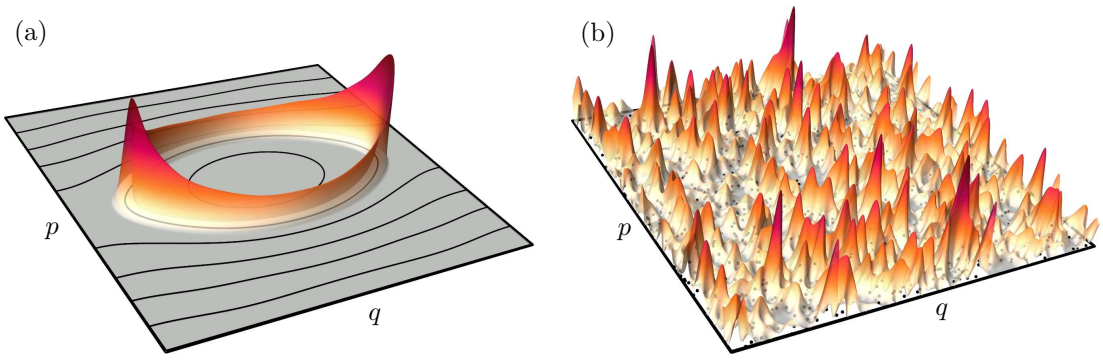

Figure 7.1. Husimi representation of a typical eigenstate of the standard map, $h = 1/1000$, for (a) $\kappa = 0.5$ and (b) $\kappa = 10.0$, that is (a) concentrated on a regular torus and (b) distributed over the chaotic sea, cf. underlying phase-space portrait (black lines and dots).

the w*-topology). The restriction to sequences $(n_N)_{N\in\mathbb{N}}$ is necessary as there exist exceptional eigenstates that are scarred with enhanced localization in the vicinity of unstable periodic orbits [29]. Obviously, such states do not correspond to the uniform distribution. An example of a typical uniformly distributed chaotic eigenstate of the standard map is shown in Fig. 7.1(b). There are other and more general formulations of the quantum ergodicity theorem available, see e.g., the fundamental results in [12, 18, 21], results on quantum ergodic billiards in [25, 26, 29], on ergodic Hamiltonian flows on energy surfaces [22], on ergodic quantum maps in general [27,28], and on the quantum Baker map with its discontinuities [176]. Thus, similar to the integrable case, up to dimensionality, typical chaotic eigenstates approach the classically *invariant* uniform phase-space distribution in the semiclassical limit.

Let us discuss such classically invariant distributions in a little more detail. We choose a rather abstract approach in terms of measures here, which is suitable as it allows to rigorously include fractal properties for open systems below. For a short overview on measure theory we refer to Sec. A in the appendix.

7.1.2 Invariant Measures

The forward time evolution of a probability measure μ under the map $T:\ \Gamma\to\Gamma$ is given by the pushforward measure $T_*\mu$, which is defined by

$$T_*\mu(X) := \mu\big(T^{-1}(X)\big) \tag{7.3}$$

for all measurable sets $X\subseteq\Gamma$. Note that the preimage $T^{-1}(X)$ of X under T is well-defined even in the case that T is not invertible, which is relevant for open systems below. Let us give an intuitive argument, why $T_*\mu$ may be interpreted as the iterate of μ: Suppose that μ has a density $\varrho:\ \Gamma\to[0,1]$ with respect to the Lebesgue measure Λ, that is,

$$\mu(X) = \int_X \varrho\, d\Lambda \tag{7.4}$$

for all measurable $X\subseteq\Gamma$. In Fig. 7.2 this is illustrated by a two-dimensional Gaussian distribution for ϱ in the left panel. Let $\tilde{\varrho}$ denote the probability distribution after one iteration by the map T. In Fig. 7.2 this corresponds to the density distribution in the right panel after iteration by the Baker map. Numerically, this may be realized by generating a sample of random points in phase space which are distributed according to the probability distribution ϱ by an acceptance–rejection algorithm for instance [177,178], and by iterating these points once by virtue of T. The distribution of the iterates obeys a new density function $\tilde{\varrho}$. This function $\tilde{\varrho}$ is the density of the measure $T_*\mu$ as defined by Eq. (7.3). With this it becomes clear that the weight of $T_*\mu$ on the set X is, in fact, the weight of μ on the set $T^{-1}(X)$ since the

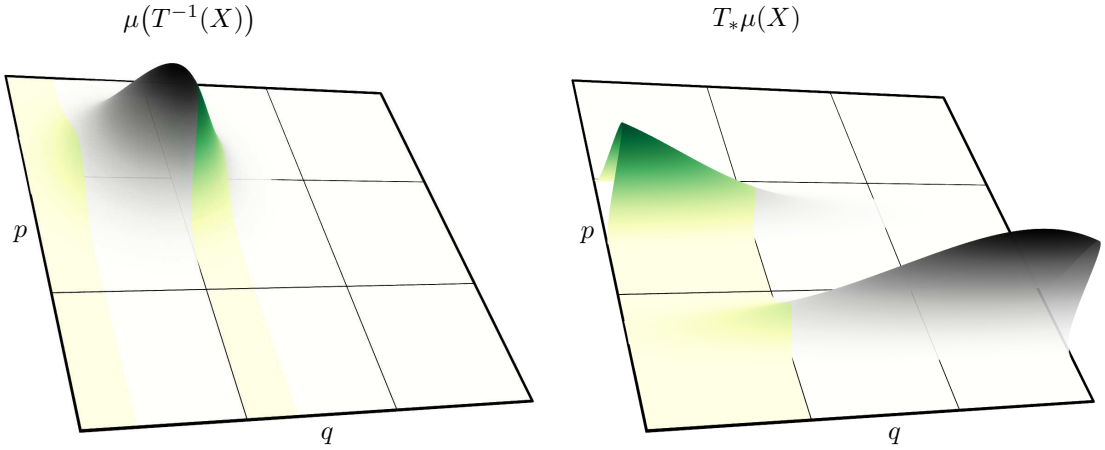

Figure 7.2. Sketch motivating the definition of the pushforward measure $T_*\mu$ in terms of densities: The weight of the Gaussian density defining μ within the set $T^{-1}(X)$ (colored region; left panel) is the same as the weight of the iterated density corresponding to $T_*\mu$ within the iterated set X (colored region; right panel). The map T is chosen to be the Baker map; the black lines in the background decomposing the phase space vertically and horizontally into thirds are a guide to the eye.

overlap of a density with a given set does not change if both the density and the set are iterated. This is visualized in Fig. 7.2 for $X = [0, 1/3) \times [0, 2/3)$, the preimage of which is $T^{-1}(X) = \{[0, 1/9) \times [0, 1)\} \cup \{[1/3, 4/9) \times [0, 1)\}$. In the general situation that μ does not provide a proper density ϱ, Eq. (7.3) must be taken as a definition. We stress that $T_*\mu$ corresponds to the forward iteration of μ even though the inverse iteration T^{-1} enters in Eq. (7.3).

We are now able to define invariance for a measure as motivated by the above discussion on the classical counterpart of quantum states in closed systems. A measure μ is called invariant under the map T if $T_*\mu = \mu$. Liouville's theorem states that for Hamiltonian systems, or symplectic maps respectively, the uniform Lebesgue measure is invariant [129, Prop. 3.3.4]. In chaotic systems the invariant measure is particularly important for the asymptotic time evolution as any generic initial measure converges towards it: Since a typical orbit explores the entire phase space uniformly in the long run, it seems reasonable to expect some kind of convergence of $(T_*^n\nu)_{n\in\mathbb{N}}$ for suitable initial measures ν towards the invariant Lebesgue measure μ. First of all, we focus on measures ν that are absolutely continuous with respect to μ, i.e., $\mu(X) = 0$ implies $\nu(X) = 0$ for all measurable sets $X \subseteq \Gamma$. This particularly excludes exceptional Dirac measures localized on periodic orbits for instance. Moreover, let us consider the special case that the considered chaotic system is ergodic. The symplectic map T together with its invariant measure μ is called ergodic if for any invariant measurable set X, $T(X) = X$, it is $\mu(X) = 0$ or $\mu(X) = 1$ [173, Sec. 6.3]. As a consequence of the mean ergodic theorem by

von Neumann [118, Thm. II.11], ergodicity implies

$$\lim_{N\to\infty} \frac{1}{N} \sum_{n=0}^{N-1} T_*^n \nu(X) = \mu(X) \tag{7.5}$$

for all measurable X. In other words, for ergodic Hamiltonian systems the so-called Cesàro average of any absolutely continuous measure indeed converges towards the invariant Lebesgue measure as expected. In order to obtain convergence of the sequence $(T_*^n \nu)_{n\in\mathbb{N}}$ itself, and not only convergence on average, ergodicity is not sufficient. However, if the map T is (strongly) mixing, i.e., if for all measurable X, Y it holds that [173, Sec. 9.1]

$$\lim_{n\to\infty} \mu(T^{-n}(X) \cap Y) = \mu(X)\mu(Y), \tag{7.6}$$

it can be shown that

$$\lim_{n\to\infty} T_*^n \nu(X) = \mu(X) \tag{7.7}$$

for all measurable X. Hence, in mixing Hamiltonian systems any absolutely continuous measure converges towards the invariant Lebesgue measure under time evolution. An idea of the proofs for Eqs. (7.5) and (7.7) is given in Sec. B.3 in the appendix.

7.2 Quantum–Classical Correspondence in Open Systems

Invariant measures also exist for symplectic maps that are opened by an absorbing region. First, if the dynamical system displays regular motion away from the opening, this phase-space region supports invariant measures as in closed systems. But invariant measures exist even in the chaotic component of phase space that contains an opening [58]. They are supported by the maximal invariant set in the chaotic part of phase space, the fractal repeller, cf. Sec. 3.3. However, by definition, such invariant measures do not display decay and therefore cannot be the classical counterpart of quantum resonance states.

In this section we first discuss the structure of chaotic resonance states based on the work by Keating et al. [49]. It turns out that classical conditionally invariant measures, which in contrast to invariant measures exhibit decay, obey localization conditions analogous to quantum resonance states. Thus, they are ideal candidates for quantum-to-classical correspondence. Still, it is necessary to identify the conditionally invariant measures that are quantum mechanically relevant. To this end, we propose the class of γ-natural conditionally invariant measures [34].

7.2.1 Semiclassical Structure of Chaotic Resonance States

For open systems, quantum-to-classical correspondence between the structure of quantum chaotic eigenstates and classical properties is by far not as well explored as for closed systems. Still, a few fundamental results are presented in Refs. [46, 48, 49, 51] or reviewed in a broader context in Refs. [56, 58]. We will briefly discuss them here. Note that there are other related works on a short periodic orbit approach to resonances [92, 179, 180], discussing scarring effects [54, 181], and investigations on localization on manifolds [182] for open systems. As we focus on the generic behavior of quantum resonance states in the spirit of quantum ergodicity, these issues are not taken into account.

Following the seminal paper by Keating et al. [49] we discuss two fundamental semiclassical properties of the localization of quantum resonance states in their Husimi representation: (i) Chaotic resonance states are semiclassically supported by the backward trapped set. (ii) Their weight on semiclassically resolved forward escaping sets decays by $e^{-\gamma}$ between consecutive levels, determined by the decay rate γ of the resonance state. In the following, it is instructive to illustrate the explanation of both statements using the example of the open Baker map. Its resonance states exhibit the characteristic features of (i) being supported on backward trapped set (horizontal stripes), and of (ii) having an additional γ-depending profile governed by the forward escaping sets (vertical stripes), as shown in Fig. 7.3.

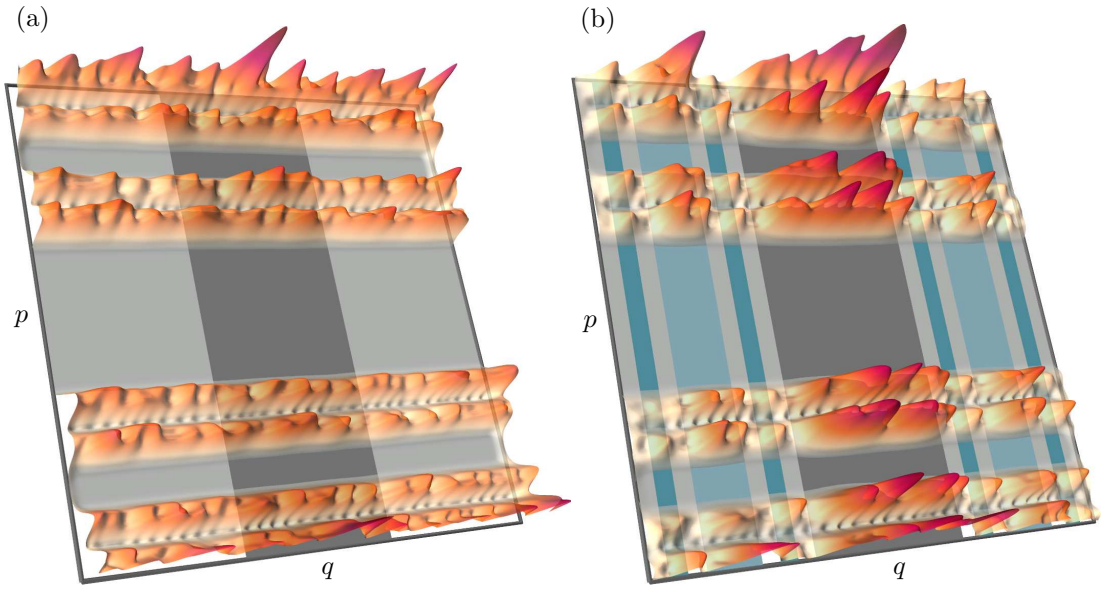

Figure 7.3. Average Husimi distribution of chaotic resonance states of the Baker map ($1/h = 729$; $\Omega = [1/3, 2/3) \times [0, 1)$; $\gamma_{\text{nat}} = -\log(2/3) \approx 0.405$) with (a) $\gamma \in [\gamma_{\text{nat}}/1.1, \gamma_{\text{nat}} \cdot 1.1]$ (20 states) and (b) short $\gamma \in [0.8/1.1, 0.8 \cdot 1.1]$ (17 states). Colored regions in the background show the opening (Ω, dark gray), the first forward escaping set ($T^{-1}(\Omega)$, light blue), and the second forward escaping set ($T^{-2}(\Omega)$, medium blue)

(i) The Husimi distribution H_ψ of a resonance state ψ is invariant under the quantum time evolution UP up to normalization, where U denotes the unitary part of the quantum map and P is the projection onto the complement of the opening Ω. More precisely, the time evolution $\psi \mapsto UP\psi$ reads $H_\psi \mapsto H_{UP\psi}$ in terms of the Husimi representation. The invariance of H_ψ under time evolution up to normalization particularly means that even though a substantial part of the distribution H_ψ leaves the system through the opening Ω, the entire phase-space distribution H_ψ has to reconstruct itself after one iteration by UP up to decay. This invariance property of ψ implies that H_ψ must not have any weight on the iterate $T_{\mathrm{cl}}(\Omega)$ of the opening Ω under the classical closed system dynamics T_{cl}: Semiclassically speaking, under the open dynamics $T = T_{\mathrm{cl}} \circ O$ nothing is mapped to $T_{\mathrm{cl}}(\Omega)$ since

$$T(\Gamma) = T_{\mathrm{cl}}(O(\Gamma)) = T_{\mathrm{cl}}(\Gamma \setminus \Omega) \cup \{\infty\} = (\Gamma \setminus T_{\mathrm{cl}}(\Omega)) \cup \{\infty\} \tag{7.8}$$

as T_{cl} is bijective. For illustration, see Fig. 7.4 for the Baker map. Here, by iterating the entire

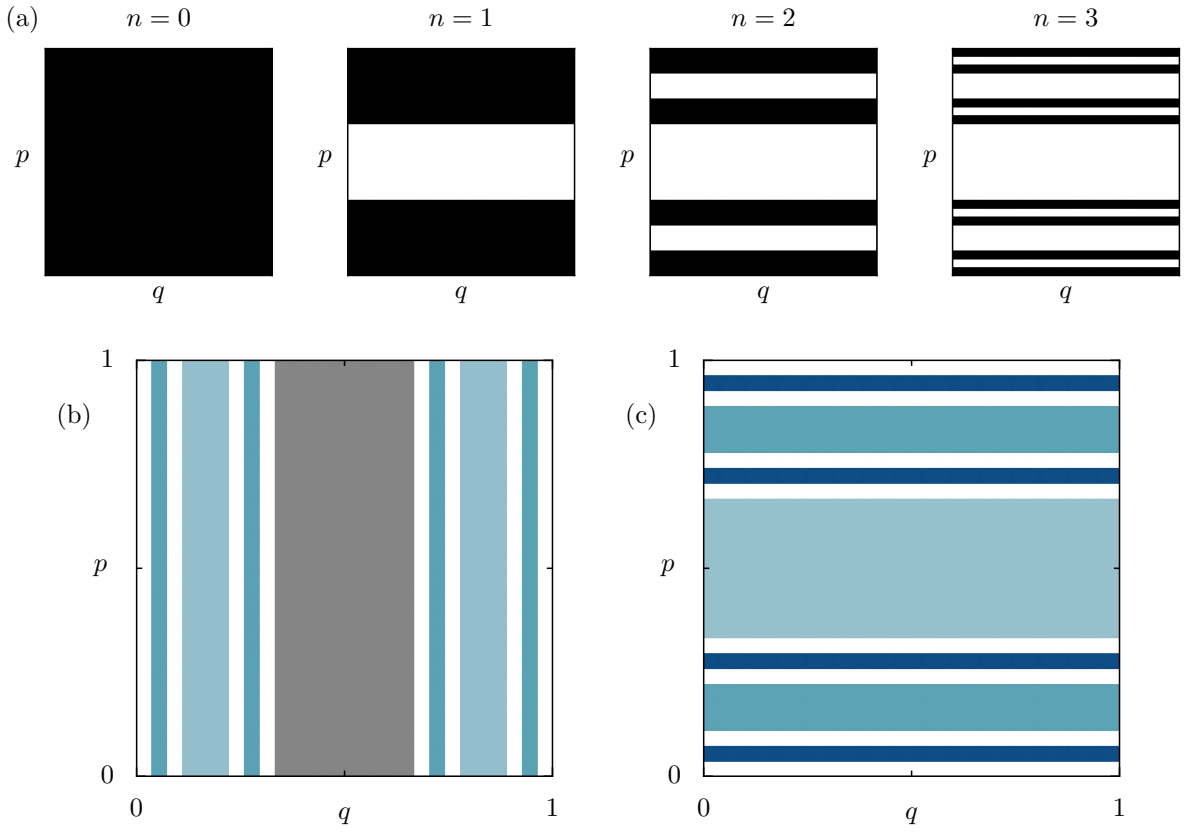

Figure 7.4. (a) Forward iteration of the uniform phase-space distribution under the open Baker map (iteration number n as indicated above each panel). (b) Forward escaping sets $T^{-n}(\Omega)$ for $n = 0$ (gray), $n = 1$ (light blue), $n = 2$ (medium blue). (c) Disjoint representation of the iterates $T_{\mathrm{cl}}^n(\Omega)$ of the opening under the closed Baker map T_{cl} for $n = 1$ (light blue), $n = 2$ (medium blue), and $n = 3$ (dark blue).

phase space once under the open map, Fig. 7.4(a), nothing is mapped to the middle horizontal third which is $T_{\rm cl}(\Omega)$, Fig. 7.4(c). Suppose H_ψ does not vanish on $T_{\rm cl}(\Omega)$. While the weight of H_ψ in $T_{\rm cl}(\Omega)$ will redistribute over phase space within one iteration, nothing enters $T_{\rm cl}(\Omega)$ such that H_ψ cannot reconstruct. Hence, any invariant Husimi distribution H_ψ must not have any weight in $T_{\rm cl}(\Omega)$. The same line of semiclassical argument applies to all images $T_{\rm cl}^n(\Omega)$ of the opening up to the Ehrenfest time, $n \leq \tau_{\rm Ehr}$, which is the time scale of quantum-to-classical correspondence [48]. Therefore, H_ψ is semiclassically supported by the set of points in phase space that are trapped in the system at least $\tau_{\rm Ehr}$ backward iterations. This is confirmed by the averaged Husimi distributions of chaotic resonance states in Fig. 7.3 which are zero on the sets $T_{\rm cl}^n(\Omega)$ for $n \lesssim 3$ (horizontal gaps), cf. Fig. 7.4(c). The remaining weight is supported by the threefold backward trapped set. Note that the finite-time approximation of the backward trapped set corresponds to its spatially finite approximation on the Planck scale h.

We can also show this localization on the backward trapped set from a more general perspective: Let ψ be a resonance state of the quantum map UP, i.e., $UP\psi = \lambda\psi$, $\lambda \neq 0$. This implies

$$(UP)^n \frac{\psi}{\lambda^n} = \psi \tag{7.9}$$

for $n \in \mathbb{N}_0$, such that $\psi \in \operatorname{im}(UP)^n$ for each n. Here,

$$\operatorname{im} S := \{S\psi \,:\, \psi \in \mathcal{D}(S)\} \tag{7.10}$$

denotes the image or range of an operator S with domain $\mathcal{D}(S)$. Using the general relation $\operatorname{im} S \subseteq (\ker S^*)^\perp$ between the image of S and the orthogonal complement of the kernel of S^*, cf. Eq. (2.27), for a bounded linear operator S on some Hilbert space [151, §21.3.5], we conclude

$$\psi \in \left(\ker(PU^{-1})^n\right)^\perp, \qquad (n \in \mathbb{N}_0). \tag{7.11}$$

In words, a resonance state ψ is orthogonal to all subspaces that are mapped to zero under the backward open quantum time evolution PU^{-1}. Semiclassically, that describes precisely the localization on the classical backward trapped set. As the semiclassical argument is only valid for $n \leq \tau_{\rm Ehr}$, we recover the above result (i). We emphasize that Eq. (7.11) is the quantum-mechanical generalization of the semiclassical localization on the backward trapped set. In the original work [49], the argument for the semiclassical localization on the $\tau_{\rm Ehr}$-fold backward trapped set is slightly more technical, analyzing the backward time evolution of the coherent state which enters the definition of the Husimi representation of the resonance state. Note that fractal properties in the localization of quantum resonance states have first

been observed and attributed to the classical backward trapped set in the pioneering work by Casati et al. [46].

(ii) We now focus on the weight of resonance states on forward escaping sets $T^{-n}(\Omega)$. For the Baker map the forward escaping sets are vertical stripes in phase space, see Fig. 7.4(b). Let us start from the eigenvalue equation $UP\psi = \lambda\psi$ with $|\lambda| = e^{-\gamma/2}$ which implies the norm decay of the resonance state,

$$\|UP\psi\|^2 = e^{-\gamma}. \tag{7.12}$$

Denoting the orthogonal projection onto the opening by $P_0 := \mathbb{1} - P$, this gives

$$\begin{aligned} \|UP\psi\|^2 &= \|(\mathbb{1} - P_0)\psi\|^2 && (7.13)\\ &= \|\psi\|^2 - \langle\, \psi \,|\, P_0\psi \,\rangle - \langle\, P_0\psi \,|\, \psi \,\rangle + \|P_0\psi\|^2 && (7.14)\\ &= 1 - \|P_0\psi\|^2, && (7.15) \end{aligned}$$

using that

$$\langle\, \psi \,|\, P_0\psi \,\rangle = \langle\, \psi \,|\, P_0^2\psi \,\rangle = \langle\, P_0\psi \,|\, P_0\psi \,\rangle = \|P_0\psi\|^2. \tag{7.16}$$

Equations (7.12) and (7.15) establish the simple but important relation

$$\|P_0\psi\|^2 = 1 - e^{-\gamma}. \tag{7.17}$$

We stress that this result is remarkable as it relates the localization of the resonance state ψ with its decay rate γ. Qualitatively, this is very intuitive: The more weight of ψ lies in the opening the faster its decay. This is also confirmed by the averaged chaotic resonance states in Fig. 7.3. The resonance state with larger decay rate (b) has more weight on the opening (gray region) than the resonance state shown in (a) with smaller decay rate. Note that Eq. (7.17) is important beyond the study of chaotic resonance states, e.g., it can also be used for the computation of dynamical-tunneling rates from the regular to the chaotic phase-space region of mixed systems as initially worked out in collaboration with Normann Mertig [183, 184].

Proceeding with the iterated operators $P_n := (UP)^{*n} P_0 (UP)^n$, $n \in \mathbb{N}_0$, one finds

$$\begin{aligned} \langle\, \psi \,|\, P_n\psi \,\rangle &= \langle\, (UP)^n\psi \,|\, P_0(UP)^n\psi \,\rangle && (7.18)\\ &= e^{-\gamma n}\, \|P_0\psi\|^2 && (7.19)\\ &= e^{-\gamma n}(1 - e^{-\gamma}), && (7.20) \end{aligned}$$

which generalizes Eq. (7.17). Semiclassically, for $n \leq \tau_{\mathrm{Ehr}}$, P_n corresponds to the projection onto the forward escaping set $T^{-n}(\Omega)$ such that $\langle\, \psi \,|\, P_n\psi \,\rangle$ describes the weight on that set.

We point out though that the operators P_n, $n \neq 0$, are strictly speaking not projections if not considered semiclassically. This is essentially due to the fact that in general $U^{-1}P_0UP \neq PU^{-1}P_0UP$, although they are equal semiclassically. To conclude, Eq. (7.20) explicitly relates the weight of a resonance state in each of the forward escaping sets $T^{-n}(\Omega)$ up to τ_{Ehr} with its decay rate γ. The ratio of weights $\langle\,\psi\,|\,P_{n+1}\psi\,\rangle/\langle\,\psi\,|\,P_n\psi\,\rangle$ between consecutive levels equals $e^{-\gamma}$ for all $n \in \mathbb{N}_0$, cf. Eq. (7.20). Qualitatively, this agrees with the localization of chaotic resonance states shown in Fig. 7.3. A precursor on this kind of semiclassical decomposition of resonance states can be found already in the work by Schomerus and Tworzydło [48], where the authors identify regions of ballistic escape in order to study the number of instantaneous decay modes.

Let us point out that the Ehrenfest time τ_{Ehr} being the temporal threshold between classical and quantum-mechanical behavior is not sharp but rather defines a scale, meaning there is a smooth transition from one regime to the other. In the same spirit, it is not essential in the following whether there is quantum-to-classical correspondence both in forward and backward time direction up to τ_{Ehr} or in each direction only up to $\tau_{\mathrm{Ehr}}/2$, which seems more appropriate. In this regard, the above discussion should be rather seen as a proof of concept.

Given the discussed results from [49], we have now seen some fundamental semiclassical properties of quantum resonance states. Still, this leaves the question about the correct classical framework to capture these properties. The work by Nonnenmacher and Rubin [51] suggests the concept of conditionally invariant measures. Before we discuss a few important results from [51], let us introduce conditionally invariant measures as developed in Refs. [43,50].

7.2.2 Conditionally Invariant Measures

A probability measure μ is called conditionally invariant measure (CIM) with respect to the classical map $T:\ \Gamma \to \Gamma$, if it obeys the condition

$$T_*\mu = \|T_*\mu\|\,\mu, \tag{7.21}$$

with $\|T_*\mu\| = T_*\mu(\Gamma)$ and the pushforward measure $T_*\mu$ as defined in Eq. (7.3). In contrast to an invariant measure, $T_*\mu = \mu$, a CIM is invariant under T only up to a global factor $\|T_*\mu\|$. In fact, the n-fold iteration

$$T_*^n\mu = \|T_*\mu\|^n\mu = e^{-\gamma n}\mu, \tag{7.22}$$

using $T_*(\|T_*\mu\|\,\mu) = \|T_*\mu\|\,T_*\mu$, yields an exponential decay with rate

$$\gamma = -\log(\|T_*\mu\|). \tag{7.23}$$

For the special case that the opening O is performed before the closed map iteration T_{cl}, $T = T_{\mathrm{cl}} \circ O$, it is

$$\|T_*\mu\| \overset{\text{def}}{=} \mu\left(T^{-1}(\Gamma)\right) = \mu\big(O\big(\underbrace{T_{\mathrm{cl}}^{-1}(\Gamma)}_{=\Gamma}\big)\big) = \mu\left(\Gamma \setminus \Omega\right) \overset{(\Omega\subseteq\Gamma)}{=} \underbrace{\mu(\Gamma)}_{=1} - \mu(\Omega), \tag{7.24}$$

such that the decay rate γ may be written as

$$\gamma = -\log\left(1 - \mu(\Omega)\right). \tag{7.25}$$

With this, Eq. (7.21) states that the measure $\mu\big(T^{-1}(X)\big)$ of the set $T^{-1}(X)$ that will be mapped to X is smaller than $\mu(X)$ by the factor $e^{-\gamma}$.

By definition, CIMs obey the same localization conditions as quantum resonance states do semiclassically in terms of (i) being supported by the backward trapped set, Eq. (7.11), and (ii) having decay-rate depending weights in the forward escaping sets according to Eq. (7.20):

(i) By mathematical induction we show $\mu\left(T_{\mathrm{cl}}^n(\Omega)\right) = 0$ for $n \in \mathbb{N}$, that is, a CIM μ is supported by the backward trapped set, cf. Eq. (3.25),

$$\Gamma_{\mathrm{bwd}} = \Gamma \setminus \bigcup_{n=1}^{\infty} T_{\mathrm{cl}}^n(\Omega). \tag{7.26}$$

First, for the base case $n = 1$, it is

$$\begin{aligned}
\mu\big(T_{\mathrm{cl}}(\Omega)\big) &\overset{\text{Eq. (7.21)}}{=} e^{\gamma}\, T_*\mu\big(T_{\mathrm{cl}}(\Omega)\big) && (7.27)\\
&= e^{\gamma}\, \mu\big(O \circ T_{\mathrm{cl}}^{-1} \circ T_{\mathrm{cl}}(\Omega)\big) && (7.28)\\
&= e^{\gamma}\, \mu\big(O(\Omega)\big) && (7.29)\\
&= e^{\gamma}\, \mu(\emptyset) && (7.30)\\
&= 0. && (7.31)
\end{aligned}$$

For the inductive step, we show that $\mu\big(T_{\mathrm{cl}}^n(\Omega)\big) = 0$ impies $\mu\big(T_{\mathrm{cl}}^{n+1}(\Omega)\big) = 0$,

$$\begin{aligned}
\mu\big(T_{\mathrm{cl}}^{n+1}(\Omega)\big) &= e^{\gamma}\, T_*\mu\big(T_{\mathrm{cl}}^{n+1}(\Omega)\big) && (7.32)\\
&= e^{\gamma}\, \mu\big(O \circ T_{\mathrm{cl}}^{-1} \circ T_{\mathrm{cl}}^{n+1}(\Omega)\big) && (7.33)\\
&= e^{\gamma}\, \mu\big(T_{\mathrm{cl}}^{n}(\Omega) \setminus \Omega\big) && (7.34)\\
&\leq e^{\gamma}\, \mu\big(T_{\mathrm{cl}}^{n}(\Omega)\big) && (7.35)\\
&= 0. && (7.36)
\end{aligned}$$

A more intuitive argument analogous to the discussion for quantum resonance states applies for CIMs as well, i.e., a CIM must not have any weight in any iterate $T_{\mathrm{cl}}^n(\Omega)$ of the opening as

any contribution on $T_{\mathrm{cl}}^n(\Omega)$ leaves the region under iteration by T but no weight enters again. Figure 7.5 shows the localization of CIMs on the backward trapped set (horizontal stripes) for the Baker map.

(ii) In addition to the localization on the backward trapped set, the weights of CIMs in the forward escaping sets obey a decay-rate depending relation just like Eq. (7.20) for chaotic resonance states. Directly from the definition of CIMs, Eq. (7.21), one finds

$$\mu\big(T^{-n}(\Omega)\big) = T_*^n\mu(\Omega) = e^{-\gamma n}\mu(\Omega) \overset{(7.25)}{=} e^{-\gamma n}(1-e^{-\gamma}), \tag{7.37}$$

the classical equivalent of Eq. (7.20). Examples for CIMs with decay-rate depending weights in the forward escaping sets are shown in Fig. 7.5 for the open Baker map.

We have seen that CIMs are invariant up to decay and obey the same two fundamental localization properties as quantum chaotic resonance states. Hence, they are the ideal candidates for quantum-to-classical correspondence. So far, however, we have not addressed the question how many different CIMs actually exist, i.e., whether there are too few CIMs to find a counterpart for each quantum resonance state or, vice versa, whether there are too many CIMs such that one needs to investigate which of them are quantum mechanically relevant. In Ref. [51, Thm. 1], it is proved that quantum resonance states necessarily converge towards CIMs in the semiclassical limit, provided that they converge at all. The authors also develop a method, originally presented in [50, Thm. 3.1], to construct uncountably many CIMs for each decay rate γ [51, Prop. 2]. They emphasize that it is not clear which of these infinitely many CIMs are quantum mechanically relevant. In other words, if one expects that for each γ there exists a single CIM that captures the semiclassical behavior of generic chaotic resonance states with the same decay rate γ then one needs to be able to select this CIM out of the huge variety of infinitely many different CIMs that exist for this γ.

Let us begin with the following simpler problem: Which of these infinitely many CIMs are classically relevant? An appealing attempt to answer this question is put forward in [50, Sec. 5.1]. Recall that for closed systems, ergodicity and mixing imply a convergence of almost arbitrary initial measures towards the invariant uniform Lebesgue measure, cf. Eqs. (7.5) or (7.7). For open systems, an analogue consideration is based on the nonlinear iteration by

$$\nu \mapsto \frac{T_*\nu}{\|T_*\nu\|}, \tag{7.38}$$

where the nonlinearity compensates the decay. Any CIM is a fixed point of this iteration as follows immediately from the definition, Eq. (7.21). Likewise, if the iteration converges, the limit measure is conditionally invariant. Note that this relation between CIMs and Eq. (7.38) actually motivates the notion of conditional invariance as the n-th iterate applied to $X \subseteq \Gamma$ is the conditional probability for being in X after n iterations under the condition of being in Γ

after n iterations [43]. Moreover, note that in order to achieve convergence, it might also be useful to consider convergence on average in the Cesàro sense as performed in Eq. (7.5). The relevance of CIMs may now be classified by the stability of the corresponding fixed point of Eq. (7.38). This means, the more different initial measures ν converge towards a CIM μ, the more important μ becomes. A first reasonable candidate for which one could expect classical relevance [55, 56] is the so-called natural CIM μ_{nat}, defined by the limit measure according to Eq. (7.38) when using the Lebesgue measure for ν [50]. This yields the uniform distribution on its support, i.e., the backward trapped set, as visualized in Fig. 7.5(b) for the Baker map, see also Fig. 7.4(a). Numerically, one observes that not only the Lebesgue measure but rather any generic initial measure converges towards μ_{nat} (not shown). This seems reasonable in view of Eqs. (7.5) and (7.7) for closed chaotic systems. Notice, however, that even the mere existence of μ_{nat}, i.e., the convergence of Eq. (7.38) for the Lebesgue measure ν, is in general not guaranteed [50, Sec. 5.1].

Quantum mechanically, the natural CIM describes typical long-lived resonance states in the semiclassical limit up to system specific scarring effects, as is already pointed out in [46] without using the notion of a natural CIM though. For instance, compare the natural CIM μ_{nat} of the Baker map, Fig. 7.5(b), with the average chaotic resonance state with $\gamma \approx \gamma_{\text{nat}}$, Fig. 7.3(a). In the context of optical microcavities the natural CIM coincides with the steady probability distribution, for which quantum-to-classical correspondence is observed [70]. Note that optical microcavities are modeled with partial absorption, i.e., by quantum maps UP with a unitary part U and a subunitary part $P = \mathbb{1} - \alpha P_0$, with the absorption coefficient $\alpha \in [0, 1]$ and the projection P_0 onto the opening, cf. [56]. Throughout this thesis we use $\alpha = 1$, which simplifies some arguments. For a generalization of our results to systems with partial absorption, we refer to a short discussion in the outlook in Chap. 11.

As the natural CIM has a single decay rate only, it cannot be the classical counterpart for all quantum resonance states with a wide range of decay rates. CIMs with other decay rates may be constructed as follows [50, 51]: Let ν be an arbitrary probability measure on $\Omega \cap \Gamma_{\text{bwd}}$, that is $\nu(\Gamma) = \nu(\Omega \cap \Gamma_{\text{bwd}}) = 1$. Then for each $\gamma > 0$, the measure defined by[1]

$$\mu := (1 - e^{-\gamma}) \sum_{n \in \mathbb{N}_0} e^{-\gamma n} \, T^{*n} \nu \tag{7.39}$$

is conditionally invariant with decay rate γ. Here, $T^*\nu$ denotes the pullback measure of ν, obeying

$$T^*\nu(X) := \nu\big(T(X)\big) \tag{7.40}$$

[1] Note that, given the different notation used in [51], there is a typo in Eq. (2.14): The authors accidentally use the pushforward measure instead of the pullback measure.

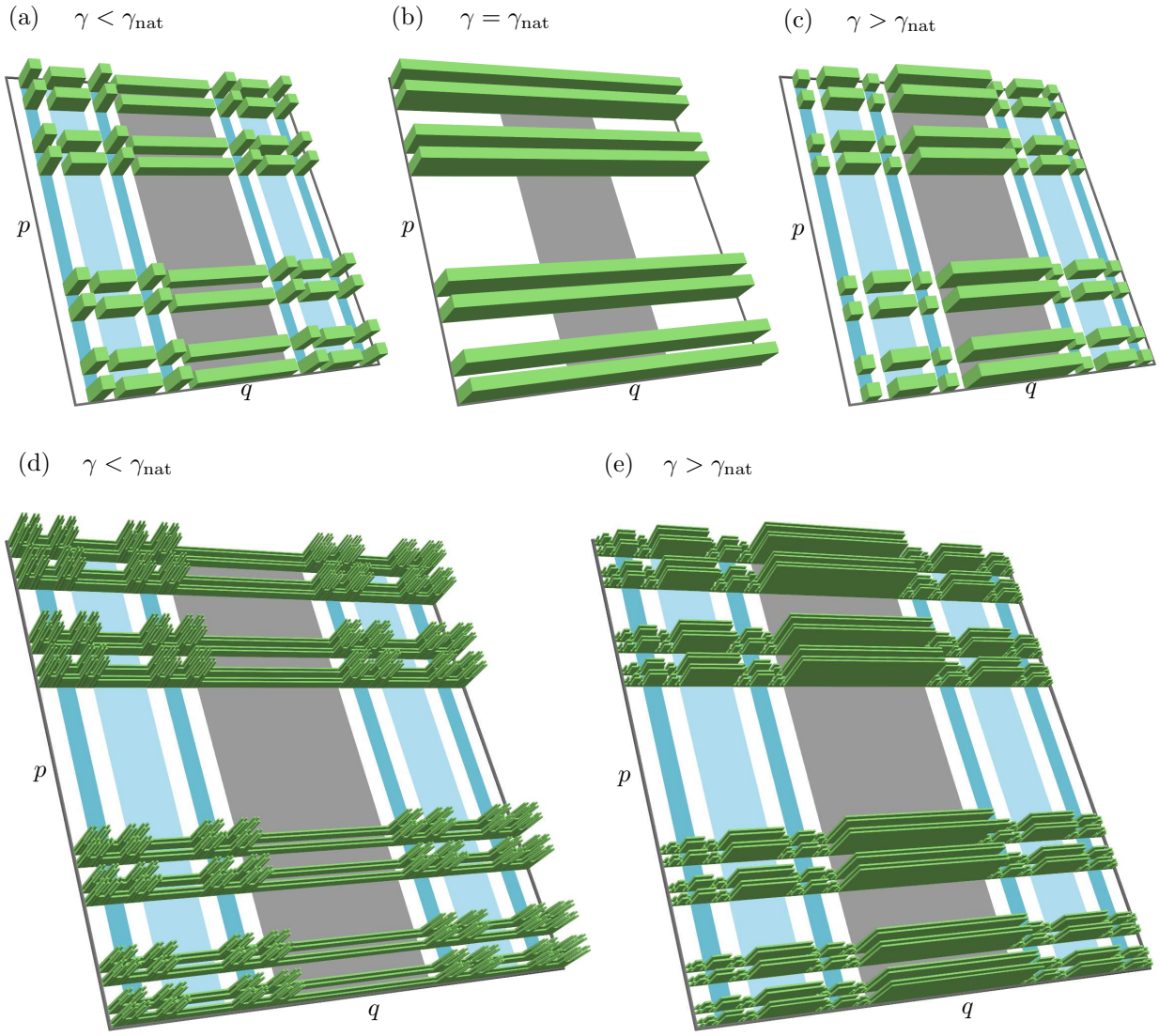

Figure 7.5. (a, c) Construction of γ-natural CIMs for the Baker map by truncation of the series in Eq. (7.49) to $n \leq 2$ for (a) $\gamma < \gamma_{\text{nat}}$ and (c) $\gamma > \gamma_{\text{nat}}$. This is based on the natural CIM shown in (b) for which the weight in Ω (gray stripe), $T^{-1}(\Omega)$ (light blue stripes), and $T^{-2}(\Omega)$ (medium blue stripes) is adapted. (d, e) Finer resolution of γ-natural CIMs for (d) $\gamma < \gamma_{\text{nat}}$ and (e) $\gamma > \gamma_{\text{nat}}$ computed by the integration method discussed on page 82.

for measurable $X \subseteq \Gamma$ for maps T such that $T(X)$ is measurable as well. The conditional invariance of μ as defined by Eq. (7.39) can be seen by

$$T_*\mu = (1-e^{-\gamma})\left\{\underbrace{T_*\nu}_{=0} + \sum_{n=1}^{\infty} e^{-\gamma n}\,\underbrace{T_*T^{*n}\nu}_{=T^{*(n-1)}\nu}\right\} \tag{7.41}$$

$$= (1-e^{-\gamma})\,e^{-\gamma}\sum_{n=0}^{\infty} e^{-\gamma n}\,T^{*n}\nu \tag{7.42}$$

$$= e^{-\gamma}\mu. \tag{7.43}$$

The pushforward measure $T_*\nu$ equals zero because for each $X \subseteq \Gamma$ the preimage $T^{-1}(X)$ is in $\Gamma \setminus \Omega$ and thus has no overlap with the support $\Omega \cap \Gamma_{\mathrm{bwd}}$ of ν. The relation $T_* T^{*n}\nu = T^{*(n-1)}\nu$ also follows from the restriction of ν to $\Omega \cap \Gamma_{\mathrm{bwd}}$. Due to the arbitrariness of ν, this construction demonstrates that there exist uncountably many CIMs for each γ. Interestingly, a construction of chaotic resonance states analogous to Eq. (7.39) can be proved, see Sec. B.4, which further indicates quantum-to-classical correspondence.

So again, the question arises, which of these infinitely many CIMs is relevant for classical or quantum mechanical considerations. Classically, CIMs other than μ_{nat} tend to be irrelevant in terms of the stability for the iteration by Eq. (7.38) as introduced above. An initial measure ν in the notation of Eq. (7.38) must fulfill exceptional selfsimilarity properties in order to converge towards a specific CIM μ as represented by Eq. (7.39). That is, the initial measure ν of sets that will escape through the opening under forward iteration must be chosen according to the decay rate γ such that μ is essentially already contained in the fine structure of ν up to localization on the backward trapped set and therefore exceptional. For a detailed study of appropriate initial measures as worked out in collaboration with Tobias Becker and Konstantin Clauß we refer to Ref. [185]. Still, the results presented in Refs. [49,51] suggest that CIMs with $\gamma \neq \gamma_{\mathrm{nat}}$ are quantum mechanically relevant even though they may be exceptions classically. Which CIM out of the huge variety of CIMs for a single decay rate γ is quantum mechanically important? We here propose the class of γ-natural CIMs and show in Chaps. 8 and 9 that they are, in fact, quantum mechanically relevant, as they describe the localization of quantum resonance states on both sides of a partial barrier. We use the construction described by Eq. (7.39) for the particularly simple case that

$$\nu(X) := \frac{\mu_{\mathrm{nat}}(X \cap \Omega)}{\mu_{\mathrm{nat}}(\Omega)}, \tag{7.44}$$

which is the normalized restriction of the natural CIM μ_{nat} to Ω. This choice of a measure, which is constant on its support, is motivated in analogy to quantum ergodicity for closed fully chaotic systems, where eigenstates in the semiclassical limit approach the constant invariant measure [29, 186]. Then we may write

$$\begin{aligned}
T^{*n}\nu(X) &= \nu\big(T^n(X)\big) && (7.45)\\
&= \frac{\mu_{\mathrm{nat}}(T^n(X) \cap \Omega)}{\mu_{\mathrm{nat}}(\Omega)} && (7.46)\\
&= \frac{e^{\gamma_{\mathrm{nat}} n}}{1 - e^{-\gamma_{\mathrm{nat}}}}\, T_*^n \mu_{\mathrm{nat}}\big(T^n(X) \cap \Omega\big) && (7.47)\\
&= \frac{e^{\gamma_{\mathrm{nat}} n}}{1 - e^{-\gamma_{\mathrm{nat}}}}\, \mu_{\mathrm{nat}}\big[\underbrace{T^{-n}\big(T^n(X) \cap \Omega\big)}_{X \cap T^{-n}(\Omega)}\big]. && (7.48)
\end{aligned}$$

Note that in general, $T^{-n}\big(T^n(X)\cap\Omega\big)\supseteq X\cap T^{-n}(\Omega)$ as T is not bijective (open system). However, here it is sufficient for equality to hold that T is invertible within all forward escaping sets $T^{-n}(\Omega)$. Inserting Eq. (7.48) in Eq. (7.39), we obtain the CIM

$$\mu_\gamma(X):=\frac{1-e^{-\gamma}}{1-e^{-\gamma_{\mathrm{nat}}}}\sum_{n\in\mathbb{N}_0}e^{(\gamma_{\mathrm{nat}}-\gamma)n}\mu_{\mathrm{nat}}\big(X\cap T^{-n}(\Omega)\big) \tag{7.49}$$

of arbitrary decay rate γ, which we refer to as γ-natural CIM. This series multiplies μ_{nat} in each forward escaping set $T^{-n}(\Omega)$ by an appropriate factor which imposes the overall decay rate γ according to Eq. (7.21). The γ-natural CIM μ_γ is constant on $T^{-n}(\Omega)\cap\Gamma_{\mathrm{bwd}}$ for each $n\in\mathbb{N}_0$. With increasing n, this constant is decreasing (increasing) for $\gamma>\gamma_{\mathrm{nat}}$ ($\gamma<\gamma_{\mathrm{nat}}$), in particular short-lived measures μ_γ have more weight in the opening. This is shown in Fig. 7.5 for the Baker map. Note that for $\gamma<\gamma_{\mathrm{nat}}$ the density within the intersection $T^{-n}(\Omega)\cap\Gamma_{\mathrm{bwd}}^{\mathrm{num}}$ of forward escaping sets with the coarse-grained backward trapped set $\Gamma_{\mathrm{bwd}}^{\mathrm{num}}$ increases with n,

$$\frac{\mu_\gamma\big(T^{-n}(\Omega)\big)}{|T^{-n}(\Omega)\cap\Gamma_{\mathrm{bwd}}^{\mathrm{num}}|}\sim\frac{\mu_\gamma\big(T^{-n}(\Omega)\big)}{\mu_{\mathrm{nat}}\big(T^{-n}(\Omega)\big)}=\frac{1-e^{-\gamma}}{1-e^{-\gamma_{\mathrm{nat}}}}\,e^{(\gamma_{\mathrm{nat}}-\gamma)n}, \tag{7.50}$$

although the weight $\mu_\gamma\big(T^{-n}(\Omega)\big)$ decreases according to Eq. (7.37). The class of γ-natural CIMs defined by Eq. (7.49) is the central object of our classical studies.

The conditional invariance of μ_γ is already shown above as it satisfies Eq. (7.39). Let us briefly demonstrate its normalization. By definition, it is

$$\|\mu_\gamma\|=\frac{1-e^{-\gamma}}{1-e^{-\gamma_{\mathrm{nat}}}}\sum_{n\in\mathbb{N}_0}e^{(\gamma_{\mathrm{nat}}-\gamma)n}\mu_{\mathrm{nat}}\big(\Gamma\cap T^{-n}(\Omega)\big). \tag{7.51}$$

Using

$$\mu_{\mathrm{nat}}\big(\Gamma\cap T^{-n}(\Omega)\big)=T_*^n\mu_{\mathrm{nat}}(\Omega)=e^{-\gamma_{\mathrm{nat}}n}(1-e^{-\gamma_{\mathrm{nat}}}), \tag{7.52}$$

one finds

$$\|\mu_\gamma\|=(1-e^{-\gamma})\sum_{n\in\mathbb{N}_0}e^{-\gamma n}=1, \tag{7.53}$$

such that μ_γ is indeed a conditionally invariant probability measure with decay rate γ.

Numerical Computation

Conceptually, the structure of γ-natural CIMs is thoroughly described above. A γ-natural CIM μ_γ of decay rate γ is constructed by the following steps: Compute the backward trapped set Γ_{bwd}, that is, remove all iterates $T_{\mathrm{cl}}(\Omega)$ of the opening Ω under the closed map T_{cl}. Uniformly

distribute the weight $\mu_\gamma(T^{-n}(\Omega)) = e^{-\gamma n}(1-e^{-\gamma})$ on the intersection $T^{-n}(\Omega)\cap\Gamma_{\text{bwd}}$ of the n-th forward escaping set $T^{-n}(\Omega)$ and the backward trapped set Γ_{bwd}. This gives the γ-natural CIM of decay rate γ, regardless of the considered map T. However, the numerical implementation of the above steps is not straightforward. Let us therefore explain an algorithm that is capable of providing γ-natural CIMs for generic maps as presented in [34].

First, one has to approximate (the chaotic part of) the backward trapped set Γ_{bwd}. To this end, one may define a uniform grid of N_{grid} points in phase space of which one has to discard points which leave the system within N_{iter} iterations of the map T in backward time direction. Points within a generically existing regular phase-space region should be omitted manually. The remaining points provide the finite-time approximation $\Gamma_{\text{bwd}}^{\text{num}}$ of Γ_{bwd} and need to be classified by their forward escaping times. Finally, assuming equidistribution for the points in $T^{-n}(\Omega) \cap \Gamma_{\text{bwd}}^{\text{num}}$, we find

$$\mu_\gamma(X \cap T^{-n}(\Omega)) \approx f_n(X)\, e^{-\gamma n}(1 - e^{-\gamma}), \tag{7.54}$$

with

$$f_n(X) := \frac{\#\left(X \cap T^{-n}(\Omega) \cap \Gamma_{\text{bwd}}^{\text{num}}\right)}{\#\left(T^{-n}(\Omega) \cap \Gamma_{\text{bwd}}^{\text{num}}\right)}, \tag{7.55}$$

for each measurable subset X of phase space. Using $\mu_\gamma(X) = \sum_{n=0}^{\infty} \mu_\gamma(X \cap T^{-n}(\Omega))$ we have a numerical estimate for the γ-natural CIM μ_γ. As the sample $\Gamma_{\text{bwd}}^{\text{num}}$ is only finite the series will terminate and the numerically approximated measure is not perfectly normalized. This method is not appropriate for exceedingly small γ since the weight on forward escaping sets $T^{-n}(\Omega) \cap \Gamma_{\text{bwd}}^{\text{num}}$ with large escape times n becomes increasingly important while they are approximated by a few points only.

7.2.3 Perron–Frobenius Theory

Another approach to compute CIMs is based on the Perron–Frobenius theory on the time evolution of phase-space densities briefly reviewed in this section. This approach will be used for the analytical study of CIMs of the partial-barrier Baker map in Chap. 8. To this end, we restrict ourselves to absolutely continuous measures with densities and focus on their time evolution. In order to illustrate the general idea, consider the simple case of a closed autonomous Hamiltonian system with Hamilton function H. In this case the continuous time evolution of a phase-space density $\varrho : \Gamma \times \mathbb{R} \to \mathbb{R}_{\geq 0}$ is given by the Liouville equation,

$$\partial_t \varrho(x,t) = \mathcal{L}_H \varrho(x,t), \tag{7.56}$$

with the Liouville operator $\mathcal{L}_H \varrho := \{H, \varrho\}$ in terms of the Poisson bracket, cf. Ref. [187, Sec. 2.3]. Then the explicit time evolution of ϱ reads

$$\varrho(x,t) = \mathcal{F}_H(t)\varrho(x,0), \tag{7.57}$$

with the so-called Perron–Frobenius operator

$$\mathcal{F}_H(t) := \exp\bigl(\mathcal{L}_H t\bigr). \tag{7.58}$$

Here, we are interested in maps rather than time-continuous dynamical systems, which are not necessarily described by a Hamilton function. For closed systems, the most general case of importance in this thesis is a symplectic map T in a two-dimensional phase space Γ, such that $\det DT = 1$. Note that this particularly implies the local invertibility of T. Given an absolutely continuous measure μ with respect to the Lebesgue measure Λ and the corresponding density $\varrho : \Gamma \to \mathbb{R}_{\geq 0}$, i.e.,

$$\mu(X) = \int_X \varrho \, d\Lambda, \tag{7.59}$$

the temporal iterate $\mathcal{F}_T\varrho$ of ϱ is given by the density of $T_*\mu$,

$$T_*\mu(X) = \int_X \mathcal{F}_T\varrho \, d\Lambda. \tag{7.60}$$

By the change of variables formula for pushforward measures, cf. Eq. (A.2), it is

$$T_*\mu(X) = \int_\Gamma \chi_X \, dT_*\mu = \int_\Gamma \chi_X \circ T \, d\mu = \int_\Gamma \chi_{T^{-1}(X)} \, d\mu, \tag{7.61}$$

with the indicator function χ. Using that μ has density ϱ, one obtains

$$T_*\mu(X) = \int_{T^{-1}(X)} \varrho \, d\Lambda \tag{7.62}$$

$$= \int_X \bigl(\varrho \circ T^{-1}\bigr) \cdot |\det DT^{-1}| \, d\Lambda. \tag{7.63}$$

Since T is symplectic the Jacobian determinant is identical to unity (Liouville theorem) and the Perron–Frobenius operator $\mathcal{F}_T$ simply reads

$$\mathcal{F}_T\varrho = \varrho \circ T^{-1}, \tag{7.64}$$

cf. Ref. [187, Sec. 2.2]. If T is not symplectic but the composition $T = T_{\mathrm{cl}} \circ O$ of a symplectic map T_{cl} and the opening map O on region Ω, the above derivation is valid up to Eq. (7.62),

where $T^{-1}(X)$, Eq. (3.20), is the preimage of X as the inverse map T^{-1} does not exist. In order to apply the transformation law leading to Eq. (7.63), the domain $T^{-1}(X)$ of integration needs to be decomposed. For $X \subseteq T_{\mathrm{cl}}(\Omega)$, it is $T^{-1}(X) \cap \Gamma = \emptyset$ such that $T_*\mu(X) = 0$ and $(\mathcal{F}_T\varrho)|_X = 0$. Otherwise, for $X \cap T_{\mathrm{cl}}(\Omega) = \emptyset$, the inverse T^{-1} exists and one obtains Eq. (7.64) again. In total, this gives

$$\mathcal{F}_T\varrho(x) = \begin{cases} \varrho \circ T_{\mathrm{cl}}^{-1}(x) & : \quad x \notin T_{\mathrm{cl}}(\Omega), \\ 0 & : \quad x \in T_{\mathrm{cl}}(\Omega). \end{cases} \tag{7.65}$$

The advantage of using densities instead of measures is that it immediately provides thoroughly developed Hilbert space methods for the time-evolution operator $\mathcal{F}_T$ like the spectral theorem [173]. To this end, one needs to restrict the set of allowed density functions on phase space Γ to the space $L^2(\Gamma)$ provided that such densities exist at all. We stress that solving the eigenvalue problem for $\mathcal{F}_T$, i.e., $\mathcal{F}_T\varrho = \lambda\varrho$, $\lambda \in \mathbb{C}$, in principle establishes all absolutely continuous CIMs. However, there is a crucial drawback: Numerically feasible finite-dimensional approximations of $\mathcal{F}_T$ provide the natural CIM only, as we will discuss now.

First, let us briefly explain what is meant by finite-dimensional approximations of $\mathcal{F}_T$. The Perron–Frobenius operator $\mathcal{F}_T$ acting on the Hilbert space $L^2(\Gamma)$ is of infinite dimensionality. In order to treat $\mathcal{F}_T$ numerically, an approximation scheme for $\mathcal{F}_T$ is desired, which approximates $\mathcal{F}_T$ by a sequence of finite-dimensional matrices and provides some kind of convergence of the finite-dimensional eigenvectors towards the infinite-dimensional eigenfunctions of $\mathcal{F}_T$. A common approach is the Ulam method [188, Chap. 4]: One defines a finite partition of phase space Γ into disjoint subsets S_k, $k \in \{1, \ldots, n\}$, $\bigcup_k S_k = \Gamma$, and associates a transition probability with each pair of phase-space regions S_i and S_k. Usually, this transition probability is defined by

$$F_{\mathrm{nat}}^{k \to i} := \frac{|S_k \cap T^{-1}(S_i)|}{|S_k|} \tag{7.66}$$

for the transition from S_k to S_i, that is the fraction of S_k which is mapped to S_i under T [188, Chap. 4]. Numerically, this corresponds to iterating a uniform sample of initial conditions in S_k and to counting how many of these points end up in S_i after one iteration. This gives an $n \times n$ matrix approximation $(F_{\mathrm{nat}}^{k \to i})_{ik}$ for $\mathcal{F}_T$.

In general, one may also use initial distributions other than the uniform distribution to compute the transition probability from S_i to S_k. We will comment on the dependence on initial distributions below. For systems with a two-dimensional mixed phase space it is useful to derive the transition probabilities from a single long orbit instead of many orbits that are iterated only once. This preserves the invariance of phase-space regions [189, 190]. Another important generalization is the Ulam–Galerkin method [188, Chap. 4], where one selects a

finite number of appropriate basis functions and projects $\mathcal{F}_T$ onto their span. The advantage of this method is that the basis functions may be chosen adapted to a specific system. In Ref. [191, 192] for instance, spherical harmonics are used for the kicked top on a spherical phase space. The common Ulam method may be interpreted as a special case of the Ulam–Galerkin method by choosing indicator functions that are supported by the elements of the used phase-space partitions.

The understanding of the asymptotic dynamics that one can obtain from finite-dimensional approximations of $\mathcal{F}_T$ is limited essentially due to the Perron–Frobenius theorem [193, Sec. 1.1]. For reference it is stated here in full detail followed by an interpretation.

Theorem. Let $F \in \mathbb{R}_{\geq 0}^{N\times N}$ be an irreducible matrix with nonnegative entries, spectrum $\sigma(F)$ and spectral radius $r := \max_{\lambda\in\sigma(F)} |\lambda|$. Then the following assertions hold:

(i) The spectral radius r is an algebraically simple eigenvalue of F, i.e., $\dim\ker(F - r\mathbb{1}) = 1$; moreover it is $r > 0$ if $F \neq 0$,

(ii) There exists a normalized eigenvector ϱ corresponding to the eigenvalue $r \in \sigma(F)$, that has only positive components,

(iii) Any eigenvector of F that has exclusively nonnegative components is a multiple of ϱ,

(iv) If F has exactly q eigenvalues λ with $|\lambda| = r$, then these eigenvalues are given by $r\, e^{2\pi i\, k/q}$ for $0 \leq k < q$,

(v) If the components of F are strictly positive, it is $|\lambda| < r$ for each $\lambda \in \sigma(F)$ with $\lambda \neq r$.

For the proof see Refs. [194, Secs. 15.3, 15.4] and [195, Secs. 8.2, 8.3]. The Perron–Frobenius theorem basically states that the eigenvalue $r \in \sigma(F)$ of maximal modulus lies on the positive real axis. It is called Perron–Frobenius eigenvalue. The corresponding eigenspace is one-dimensional and provides the only eigenvector ϱ that has purely nonnegative components, called Perron–Frobenius eigenvector. In contrast to all other eigenvectors it may therefore be interpreted as a classical probability density. Since r has maximal modulus, ϱ is the eigenvector of slowest decay interpreting the Perron–Frobenius theorem as though $r < 1$ like in our studies. Note that the irreducibility of F excludes that there are invariant subregions in phase space. If there are any, the theorem may be applied to each of them individually.

In application to the Perron–Frobenius operator $\mathcal{F}_T$ this theorem implies that any finite-

dimensional matrix approximation provides an approximation for a single CIM, only. It is not clear whether the other eigenstates, which have negative entries, carry encoded information about other CIMs. They are certainly important for the transient time evolution by means of spectral decomposition of initial distributions. In principle, for any CIM μ a Perron–Frobenius matrix $F_\mu = \big(F_\mu^{k\to i}\big)_{ik}$ which approximates μ by its Perron–Frobenius eigenstate $\varrho := \big(\mu(S_1),\ldots,\mu(S_n)\big)$ can be constructed by a generalized Ulam method, if the transition probabilities are not chosen according to Eq. (7.66) but with respect to μ itself as

$$F_\mu^{k\to i} := \frac{\mu\big(S_k \cap T^{-1}(S_i)\big)}{\mu(S_k)}. \tag{7.67}$$

This can be verified by explicitly calculating the i-th component of $F_\mu\varrho$,

$$\begin{aligned}
[F_\mu\varrho]_i &= \sum_{k=1}^{n} F_\mu^{k\to i}\mu(S_k) && (7.68)\\
&= \sum_{k=1}^{n} \mu\big(S_k \cap T^{-1}(S_i)\big) && (7.69)\\
&= \sum_{k=1}^{n} T_*\mu\big(T(S_k) \cap S_i\big) && (7.70)\\
&= T_*\mu(S_i) && (7.71)\\
&= \|T_*\mu\|\,\mu(S_i), && (7.72)
\end{aligned}$$

where we use that $T^{-1}\big(T(S_k)\cap S_i\big) = S_k \cap T^{-1}(S_i)$ because $T^{-1}(S_i)\cap\Omega = \emptyset$, and that the sets $T(S_k)$, $k\in\{1,\ldots,n\}$, provide a partition of the support of $T_*\mu$.

This construction, however, is based on the CIM μ one is eventually interested in. It is therefore not useful to obtain μ. For the natural CIM μ_{nat} this is not an issue since generic initial distributions converge towards μ_{nat} as discussed on page 79. Thus, the transition probabilities of the Perron–Frobenius matrix $F_{\mu_{\text{nat}}}$ do not need to be chosen carefully in order to obtain μ_{nat}. For instance, in view of the definition of μ_{nat} by the asymptotic behavior of an initial Lebesgue measure Λ, $F_{\text{nat}} = F_\Lambda$ is an ideal substitute for $F_{\mu_{\text{nat}}}$. For γ-natural CIMs μ_γ with $\gamma \neq \gamma_{\text{nat}}$, however, only exceptional initial distributions converge towards μ_γ as discussed on page 81. Hence, one has to find the correct Perron–Frobenius matrix F_{μ_γ} without knowing μ_γ. To the best of our knowledge it is not known how to solve this problem.

As a technical remark, we mention that fractal measures are nonzero even on sets of Lebesgue measure zero, and thus, cannot be absolutely continuous with respect to the Lebesgue measure. Hence, they do not have a proper density. Therefore, a naive approach using Perron–Frobenius operators for open systems, where fractal measures are omnipresent, is not fruitful. This issue can be overcome for CIMs that are absolutely continuous with respect to the Lebesgue measure on the backward trapped set [50]. In the physics literature, a rigorous

discussion of this issue is usually omitted as finite-resolution approximations of densities for fractal measures are often sufficient.

Chapter 8

Localization in the Partial-Barrier Baker Map

In order to eventually understand the localization phenomena of chaotic resonance states due to a partial transport barrier presented in Chap. 6, we have introduced the class of γ-natural CIMs in Sec. 7.2.2 for which we expect quantum-to-classical correspondence. In this chapter we investigate the localization of both classical γ-natural CIMs and quantum resonance states for the partial-barrier Baker map. We show that, indeed, the classical and quantum-mechanical localization due to a partial barrier semiclassically coincide. We start with an analytical construction of an Ulam approximation of the Perron–Frobenius operator on arbitrary fine scales in Sec. 8.1. In Sec. 8.2 we prove that the eigenvalue problem of the Perron–Frobenius operator of arbitrary resolution can be rigorously reduced to the solution of a 2×2 matrix. This allows us to calculate the Perron–Frobenius eigenvector and eigenvalue, which corresponds to the natural CIM in Sec. 8.3, where we also demonstrate quantum-to-classical correspondence with resonance states of natural decay rate. In Sec. 8.4 we generalize the natural CIM to the class of γ-natural CIMs and show quantum-to-classical correspondence with resonance states of arbitrary decay rate. We emphasize that the subsequent study of localization in generic systems strongly relies on our insights gained in this chapter. The idea to study the partial-barrier Baker map and a first solution for the localization of the natural CIM of a related one-dimensional problem goes back to Roland Ketzmerick. The tensor formulation established in Sec. 8.1, which is the key to rigorously prove the reduction in Sec. 8.2, is worked out in collaboration with Marcus Waurick.

8.1 Perron–Frobenius Operator: Ulam Approximations

Let us start with an introductory example. We consider a grid of three cells on each side of the partial barrier as illustrated in Fig. 8.1, and want to understand the Perron–Frobenius

operator as applied to this grid. As we neglect anything that happens on finer scales than this grid, this is a very coarse Ulam approximation of the true dynamics. We will generalize this approach to arbitrary fine approximations below.

Consider an initial density $v = (v_1, \ldots, v_6)^{\mathrm{T}}$ on this grid, where the enumeration follows Fig. 8.1. The first component (lower left cell) after one iteration of the map is given by

$$v_1' = \frac{1}{3}v_1 + \frac{1}{3}v_2 + \frac{1}{3}v_3 =: \langle v_1\, v_2\, v_3\rangle, \tag{8.1}$$

which is the average weight that has been on the left hand side of the partial barrier before the iteration. This step is visualized by the green shaded regions in Fig. 8.1. We stress that there is no information contained in the initial distribution v that corresponds to scales which are finer than the grid. Hence, each cell on the left contributes a third of its total weight to the lower left cell after one iteration. Proceeding analogously for the other cells of the grid, the full iteration is described by the map

$$v = (v_1, \ldots, v_6)^{\mathrm{T}} \mapsto T_1 v = (\langle v_1\, v_2\, v_3\rangle, 0, \langle v_4\, v_5\, v_6\rangle, \langle v_1\, v_2\, v_3\rangle, \langle v_4\, v_5\, v_6\rangle, \langle v_4\, v_5\, v_6\rangle)^{\mathrm{T}}, \tag{8.2}$$

with the Ulam approximation

$$T_1 = \frac{1}{3}\begin{pmatrix} 1 & 1 & 1 & 0 & 0 & 0 \\ 0 & 0 & 0 & 0 & 0 & 0 \\ 0 & 0 & 0 & 1 & 1 & 1 \\ 1 & 1 & 1 & 0 & 0 & 0 \\ 0 & 0 & 0 & 1 & 1 & 1 \\ 0 & 0 & 0 & 1 & 1 & 1 \end{pmatrix} \tag{8.3}$$

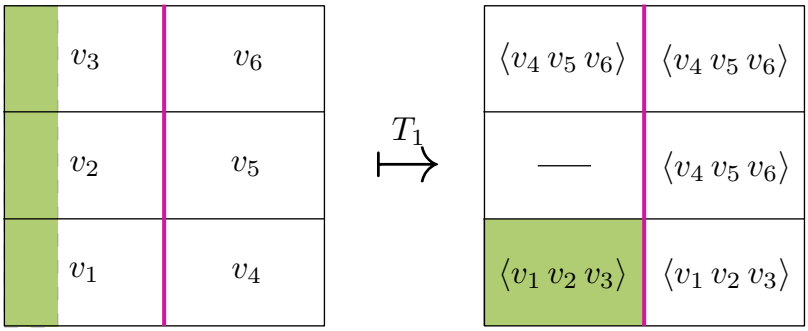

Figure 8.1. Illustration of Ulam approximation T_1 for the partial-barrier Baker map. After one iteration, the value in each cell is given by the average over the initial values either on the left hand side or on the right hand side of the partial barrier (magenta line). The weight in the middle left cell drops to zero due to the opening.

of the partial-barrier Baker map. For the following generalization it is useful to decompose T_1 into the averaging matrix $A_3 := (1,1,1)/3 \in \mathbb{R}^{1\times 3}$ and the sorting matrix

$$\sigma_3 := \begin{pmatrix} 1 & 0 & 0 & 1 & 0 & 0 \\ 0 & 0 & 1 & 0 & 1 & 1 \end{pmatrix}^{\mathrm{T}} \in \mathbb{R}^{6\times 2}, \tag{8.4}$$

which yields

$$T_1 = \sigma_3 \otimes A_3. \tag{8.5}$$

The Kronecker product $\otimes$ of the $m \times n$ matrix $A = (A_{ik})_{ik}$ and the $p \times q$ matrix B is given by the $mp \times nq$ matrix

$$A \otimes B := \begin{pmatrix} A_{11}B & A_{12}B & \dots & A_{1n}B \\ A_{21}B & A_{22}B & \dots & A_{2n}B \\ \vdots & & \ddots & \vdots \\ A_{m1}B & A_{m2}B & \dots & A_{mn}B \end{pmatrix}. \tag{8.6}$$

It represents the tensor product of the two linear maps A and B in a suitable basis.

In order to generalize this Ulam approximation scheme of the Perron–Frobenius operator to arbitrary fine grids, we define for any given $k \in \mathbb{N}$ the cells of the partition by

$$[0, \tfrac{1}{2}) \times [(n-1)/3^k, n/3^k), \quad (1 \le n \le 3^k) \tag{8.7a}$$

and

$$[\tfrac{1}{2}, 1) \times [(n-1)/3^k, n/3^k), \quad (1 \le n \le 3^k), \tag{8.7b}$$

having 3^k cells on each side of the partial barrier. Note that for the purpose of a convenient notation, we here consider the partial-barrier Baker map on $[0,1) \times [0,1)$ instead of $[0,1) \times [-\frac{1}{2}, \frac{1}{2})$ as was introduced for the general partial-barrier map in Chap. 4. This grid is exactly that of Fig. 8.1 for $k = 1$. In order to eventually define a vector $v \in \mathbb{R}^{2\cdot 3^k}$ which describes a density on this grid, we order the cells corresponding to the above index n on the left and $n + 3^k$ on the right.

The general iteration scheme for any k is depicted in Fig. 8.2, decomposing a single iteration into two parts: First, the phase-space regions on each side are shrunk by one third in their height. This is achieved by an average on the highest order of resolution, that is an average over consecutive triples for a given vector. In matrix notation, this reads

$$E_k = \mathbb{1}_{3^{k-1}} \otimes A_3 \in \mathbb{R}^{3^{k-1}\times 3^k}. \tag{8.8}$$

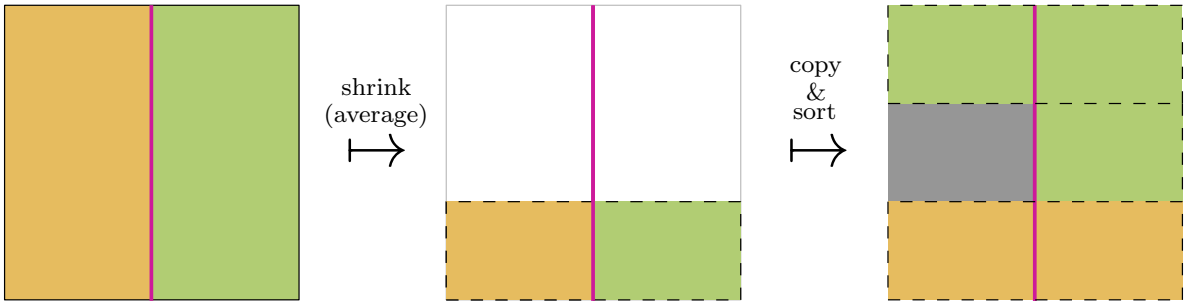

Figure 8.2. Sketch of the action of the Perron–Frobenius operator of the partial-barrier Baker map as applied to the grid in Eqs. (8.7a) and (8.7b). In a first step, the two regions on each side of the partial barrier are shrunk to a third of their initial height by averaging over the highest order of resolution defined by k. In a second step, these regions are copied and sorted into the corresponding phase-space parts.

For the example of $k = 2$, the matrix E_2 is

$$E_2 = \frac{1}{3}\begin{pmatrix} 1 & 1 & 1 & 0 & 0 & 0 & 0 & 0 & 0 \\ 0 & 0 & 0 & 1 & 1 & 1 & 0 & 0 & 0 \\ 0 & 0 & 0 & 0 & 0 & 0 & 1 & 1 & 1 \end{pmatrix}, \tag{8.9}$$

and clearly maps a vector of dimension nine to a vector of a third of this dimension by averaging over consecutive triples. In a second step, these averaged objects are sorted in just the same way as in the introductory example before, that is, by virtue of the sorting matrix σ_3. In total, the Ulam approximation of order k of the Perron–Frobenius operator for the partial-barrier Baker map is given by

$$T_k := \sigma_3 \otimes E_k. \tag{8.10}$$

Finally, we generalize this Ulam approximation scheme to a more general map: Instead of the partial-barrier Baker map based on the ternary Baker map, we consider the partial-barrier N_B-Baker map. The action of this map for the example of $N_\mathrm{B} = 5$ is illustrated in Fig. 8.3. This generalization is an important step in order to investigate different values for the opening $|\Omega|$ and the flux ϕ. For the partial-barrier Baker map based on the ternary Baker map the openness and the coupling is always given by $|\Omega| = \phi = 1/6$. In contrast, using an arbitrary integer N_B instead of the specific case $N_\mathrm{B} = 3$ allows us to adapt the coupling across the partial barrier and the size of the opening by choosing C coupling stripes and L opening stripes instead of a single one. To this end, we adapt the grid, Eqs. (8.7a) and (8.7b), to the new parameter N_B, and obtain the N_B^k cells

$$[0, \tfrac{1}{2}) \times [(n-1)/N_\mathrm{B}^k, n/N_\mathrm{B}^k), \quad (1 \le n \le N_\mathrm{B}^k) \tag{8.11a}$$

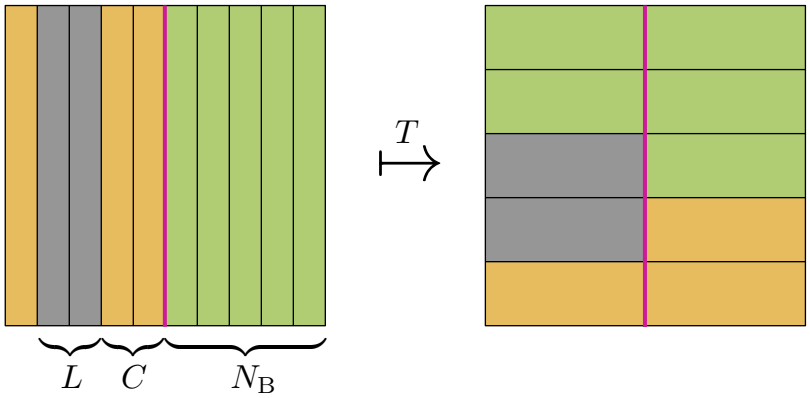

Figure 8.3. Illustration of the partial-barrier map T based on the 5-Baker map with $N_\mathrm{B} = 5$, $C = 2$, $L = 2$. The action of T within each stripe is given by horizontal stretching and vertical compression just as for the usual partial-barrier Baker map, cf. Fig. 4.2.

on the left hand side of the partial barrier, and vice versa the N_B^k cells

$$[\tfrac{1}{2}, 1) \times [(n-1)/N_\mathrm{B}^k, n/N_\mathrm{B}^k), \quad (1 \le n \le N_\mathrm{B}^k) \tag{8.11b}$$

on the right hand side. This grid is exactly that of Fig. 8.1 for $N_\mathrm{B} = 3$ and $k = 1$. Again, the cells are ordered corresponding to the above index n on the left and $n + N_\mathrm{B}^k$ on the right. Now, the averaging matrix is

$$A_{N_\mathrm{B}} := \frac{1}{N_\mathrm{B}} (\underbrace{1, \ldots, 1}_{N_\mathrm{B}}) \in \mathbb{R}^{1 \times N_\mathrm{B}}, \tag{8.12}$$

with the corresponding operator

$$E_k := \mathbb{1}_{N_\mathrm{B}^{k-1}} \otimes A_{N_\mathrm{B}} \in \mathbb{R}^{N_\mathrm{B}^{k-1} \times N_\mathrm{B}^k}, \tag{8.13}$$

and the sorting matrix reads

$$\sigma_{N_\mathrm{B}} := \begin{pmatrix} \underbrace{1 \ \ldots \ 1}_{N_\mathrm{B}-L-C} & \underbrace{0 \ \ldots \ 0}_{L} & \underbrace{0 \ \ldots \ 0}_{C} & \underbrace{1 \ \ldots \ 1}_{C} & \underbrace{0 \ \ldots \ 0}_{N_\mathrm{B}-C} \\ \underbrace{0 \ \ldots \ 0}_{N_\mathrm{B}-L-C} & \underbrace{0 \ \ldots \ 0}_{L} & \underbrace{1 \ \ldots \ 1}_{C} & \underbrace{0 \ \ldots \ 0}_{C} & \underbrace{1 \ \ldots \ 1}_{N_\mathrm{B}-C} \end{pmatrix}^\mathrm{T} \in \mathbb{R}^{2N_\mathrm{B} \times 2}. \tag{8.14}$$

The iteration in Ulam approximation of order k then obeys

$$T_k := \sigma_{N_\mathrm{B}} \otimes E_k. \tag{8.15}$$

8.2 Perron–Frobenius Operator: Selfsimilarity Reduction

Recall that we treat the Perron–Frobenius operator of the partial-barrier Baker map in order to compute its Perron–Frobenius vector φ and eigenvalue λ, i.e., the density distribution and decay rate corresponding to the natural CIM. In this section we will proof that the full information about the Perron–Frobenius pair (λ_k, φ_k) of T_k lies in the combination of a simple 2×2 matrix and the sorting operator σ_{N_B}. Actually, this reducibility is already suggested by the tensor structure of T_k as developed in the previous section.

Proposition. Let T_k for $k \in \mathbb{N}$ be defined as in Eq. (8.15). There exist at most two nontrivial solutions (λ_k, φ_k) of the eigenvalue problem $T_k\varphi_k = \lambda_k\varphi_k$. They are given by

$$\lambda_k = \lambda_0, \qquad \varphi_k = \hat{\sigma}_{N_\mathrm{B}}(k-1)\cdots\hat{\sigma}_{N_\mathrm{B}}(0)\varphi_0, \tag{8.16}$$

with $\hat{\sigma}_{N_\mathrm{B}}(n) := \sigma_{N_\mathrm{B}} \otimes \mathbb{1}_{N_\mathrm{B}^n}$, $n \in \mathbb{N}_0$, and where (λ_0, φ_0) solves the eigenvalue problem for

$$T_0 := \frac{1}{N_\mathrm{B}} \begin{pmatrix} N_\mathrm{B} - L - C & C \\ C & N_\mathrm{B} - C \end{pmatrix}. \tag{8.17}$$

Proof. First, we show that the eigenstates of T_0 give eigenstates of T_k as stated in the proposition. To this end, we prove that

$$T_{k+1}\hat{\sigma}_{N_\mathrm{B}}(k) = \hat{\sigma}_{N_\mathrm{B}}(k)T_k \tag{8.18}$$

for $k \in \mathbb{N}$. By definition, it is

$$T_{k+1}\hat{\sigma}_{N_\mathrm{B}}(k) = (\sigma_{N_\mathrm{B}} \otimes E_{k+1})(\sigma_{N_\mathrm{B}} \otimes \mathbb{1}_{N_\mathrm{B}^k}). \tag{8.19}$$

Furthermore, we find

$$E_{k+1} = \mathbb{1}_{N_\mathrm{B}^k} \otimes A_{N_\mathrm{B}} = \mathbb{1}_{N_\mathrm{B}} \otimes \mathbb{1}_{N_\mathrm{B}^{k-1}} \otimes A_{N_\mathrm{B}} = \mathbb{1}_{N_\mathrm{B}} \otimes E_k. \tag{8.20}$$

Using that the Kronecker product is associative, $A \otimes (B \otimes C) = (A \otimes B) \otimes C$, and that $(A \otimes B)(C \otimes D) = (AC) \otimes (BD)$ as long as the matrix products AC and BD are

well-defined, we obtain

$$\begin{aligned}
T_{k+1}\hat{\sigma}_{N_\mathrm{B}}(k) &= ((\sigma_{N_\mathrm{B}} \otimes \mathbb{1}_{N_\mathrm{B}}) \otimes E_k)(\sigma_{N_\mathrm{B}} \otimes \mathbb{1}_{N_\mathrm{B}^k}) && (8.21)\\
&= ((\sigma_{N_\mathrm{B}} \otimes \mathbb{1}_{N_\mathrm{B}})\sigma_{N_\mathrm{B}}) \otimes \left(E_k \mathbb{1}_{N_\mathrm{B}^k}\right) && (8.22)\\
&= ((\sigma_{N_\mathrm{B}} \otimes \mathbb{1}_{N_\mathrm{B}})\sigma_{N_\mathrm{B}}) \otimes \left(\mathbb{1}_{N_\mathrm{B}^{k-1}} E_k\right) && (8.23)\\
&= \left((\sigma_{N_\mathrm{B}} \otimes \mathbb{1}_{N_\mathrm{B}}) \otimes \mathbb{1}_{N_\mathrm{B}^{k-1}}\right)(\sigma_{N_\mathrm{B}} \otimes E_k) && (8.24)\\
&= \left(\sigma_{N_\mathrm{B}} \otimes \mathbb{1}_{N_\mathrm{B}^k}\right)(\sigma_{N_\mathrm{B}} \otimes E_k) && (8.25)\\
&= \hat{\sigma}_{N_\mathrm{B}}(k) T_k. && (8.26)
\end{aligned}$$

Thus, given $T_k\varphi_k = \lambda_k\varphi_k$, we define $\varphi_{k+1} := \hat{\sigma}_{N_\mathrm{B}}(k)\varphi_k$ which obeys

$$T_{k+1}\varphi_{k+1} = T_{k+1}\hat{\sigma}_{N_\mathrm{B}}(k)\varphi_k = \hat{\sigma}_{N_\mathrm{B}}(k)T_k\varphi_k = \lambda_k\hat{\sigma}_{N_\mathrm{B}}(k)\varphi_k = \lambda_k\varphi_{k+1}, \tag{8.27}$$

i.e., $\varphi_{k+1} = \hat{\sigma}_{N_\mathrm{B}}(k)\varphi_k$ is an eigenvector of T_{k+1} associated with the eigenvalue $\lambda_{k+1} := \lambda_k$ for $k \in \mathbb{N}$.

Moreover, let (λ_0, φ_0) be a solution of the eigenvalue problem for T_0. By ordinary matrix multiplication, it is straightforward to show that $T_1\sigma_{N_\mathrm{B}} = \sigma_{N_\mathrm{B}}T_0$, which just as before yields that $\hat{\sigma}_{N_\mathrm{B}}(0)\varphi_0 = \sigma_{N_\mathrm{B}}\varphi_0$ is an eigenvector of $T_1 = \sigma_{N_\mathrm{B}} \otimes E_1 = \sigma_{N_\mathrm{B}} \otimes A_{N_\mathrm{B}}$ corresponding to the eigenvalue λ_0, cf. Eq. (8.27).

Hence, from the at most two different solutions of the eigenvalue problem for T_0, we can deduce two solutions for T_k, $k \in \mathbb{N}$, as claimed in the proposition. We still have to show that these are the only nontrivial solutions. This will be accomplished by demonstrating that it is possible to reduce an eigenvector of T_{k+1} to an eigenvector of T_k and that this reduction is injective. To this end, we have to study the *left* inverse

$$\sigma_{N_\mathrm{B}}^{-1} = \begin{pmatrix}
\underbrace{\begin{matrix}\frac{1}{N_\mathrm{B}-L} & \cdots & \frac{1}{N_\mathrm{B}-L}\\ 0 & \cdots & 0\end{matrix}}_{N_\mathrm{B}-L-C} & \underbrace{\begin{matrix}0 & \cdots & 0\\ 0 & \cdots & 0\end{matrix}}_{L} & \underbrace{\begin{matrix}0 & \cdots & 0\\ \frac{1}{N_\mathrm{B}} & \cdots & \frac{1}{N_\mathrm{B}}\end{matrix}}_{C} & \underbrace{\begin{matrix}\frac{1}{N_\mathrm{B}-L} & \cdots & \frac{1}{N_\mathrm{B}-L}\\ 0 & \cdots & 0\end{matrix}}_{C} & \underbrace{\begin{matrix}0 & \cdots & 0\\ \frac{1}{N_\mathrm{B}} & \cdots & \frac{1}{N_\mathrm{B}}\end{matrix}}_{N_\mathrm{B}-C}
\end{pmatrix} \tag{8.28}$$

of σ_{N_B}, i.e., $\sigma_{N_\mathrm{B}}^{-1}\sigma_{N_\mathrm{B}} = \mathbb{1}_2$. This immediately provides the left inverse

$$\hat{\sigma}_{N_\mathrm{B}}(n)^{-1} = \sigma_{N_\mathrm{B}}^{-1} \otimes \mathbb{1}_{N_\mathrm{B}^n} \tag{8.29}$$

of $\hat{\sigma}_{N_\mathrm{B}}(n)$ because

$$\hat{\sigma}_{N_\mathrm{B}}(n)^{-1}\hat{\sigma}_{N_\mathrm{B}}(n) = \left(\sigma_{N_\mathrm{B}}^{-1}\sigma_{N_\mathrm{B}}\right) \otimes \left(\mathbb{1}_{N_\mathrm{B}^n}\mathbb{1}_{N_\mathrm{B}^n}\right) = \mathbb{1}_2 \otimes \mathbb{1}_{N_\mathrm{B}^n} = \mathbb{1}_{2N_\mathrm{B}^n} \tag{8.30}$$

for $n \in \mathbb{N}_0$.

We emphasize that $\sigma_{N_\mathrm{B}} \sigma_{N_\mathrm{B}}^{-1} \neq \mathbb{1}_{2N_\mathrm{B}}$, that is, the left inverse is not the right inverse. Nevertheless, for an arbitrary eigenvector φ_{k+1} of T_{k+1}, it is

$$\hat{\sigma}_{N_\mathrm{B}}(k) \hat{\sigma}_{N_\mathrm{B}}(k)^{-1} \varphi_{k+1} = \varphi_{k+1} \tag{8.31}$$

for $k \in \mathbb{N}_0$ as we now show. At first

$$\varphi_{k+1} \in \operatorname{im} T_{k+1} = \operatorname{im} (\sigma_{N_\mathrm{B}} \otimes \mathbb{1}_{N_\mathrm{B}^k} \otimes A_{N_\mathrm{B}}) = \operatorname{span}\{\operatorname{cols}(\sigma_{N_\mathrm{B}} \otimes \mathbb{1}_{N_\mathrm{B}^k})\}, \tag{8.32}$$

where $\operatorname{cols}(X)$ denotes the set of columns of the matrix X. Note that the Kronecker product with A_{N_B} does not generate additional linearly independent columns, such that the dimension of $\operatorname{im} T_{k+1}$ is $2N_\mathrm{B}^k$. The columns of $\sigma_{N_\mathrm{B}} \otimes \mathbb{1}_{N_\mathrm{B}^k}$ may be written as

$$\sigma_{N_\mathrm{B}}^{(1)} \otimes \mathbb{1}_{N_\mathrm{B}^k}^{(j)}, \quad \sigma_{N_\mathrm{B}}^{(2)} \otimes \mathbb{1}_{N_\mathrm{B}^k}^{(j)}, \qquad (1 \leq j \leq N_\mathrm{B}^k), \tag{8.33}$$

where the two columns of σ_{N_B} are denoted by $\sigma_{N_\mathrm{B}}^{(1)}$ and $\sigma_{N_\mathrm{B}}^{(2)}$, and the j-th column of $\mathbb{1}_{N_\mathrm{B}^k}$ is denoted by $\mathbb{1}_{N_\mathrm{B}^k}^{(j)}$, respectively. With this, the eigenvector φ_{k+1} can be represented as

$$\varphi_{k+1} = \sum_{j=1}^{N_\mathrm{B}^k} \left(s_1^{(j)} \sigma_{N_\mathrm{B}}^{(1)} \otimes \mathbb{1}_{N_\mathrm{B}^k}^{(j)} + s_2^{(j)} \sigma_{N_\mathrm{B}}^{(2)} \otimes \mathbb{1}_{N_\mathrm{B}^k}^{(j)} \right), \tag{8.34}$$

with appropriate coefficients $s_1^{(j)}$, $s_2^{(j)}$. Using

$$\begin{aligned}
\hat{\sigma}_{N_\mathrm{B}}(k)^{-1} \left(\sigma_{N_\mathrm{B}}^{(\ell)} \otimes \mathbb{1}_{N_\mathrm{B}^k}^{(j)} \right) &= (\sigma_{N_\mathrm{B}}^{-1} \otimes \mathbb{1}_{N_\mathrm{B}^k}) \left(\sigma_{N_\mathrm{B}}^{(\ell)} \otimes \mathbb{1}_{N_\mathrm{B}^k}^{(j)} \right) && (8.35) \\
&= \left(\sigma_{N_\mathrm{B}}^{-1} \sigma_{N_\mathrm{B}}^{(\ell)} \right) \otimes \left(\mathbb{1}_{N_\mathrm{B}^k} \mathbb{1}_{N_\mathrm{B}^k}^{(j)} \right) && (8.36) \\
&= \left(\mathbb{1}_2^{(\ell)} \otimes \mathbb{1}_{N_\mathrm{B}^k}^{(j)} \right) && (8.37)
\end{aligned}$$

for $\ell \in \{1, 2\}$, such that

$$\begin{aligned}
\hat{\sigma}_{N_\mathrm{B}}(k) \hat{\sigma}_{N_\mathrm{B}}(k)^{-1} \left(\sigma_{N_\mathrm{B}}^{(\ell)} \otimes \mathbb{1}_{N_\mathrm{B}^k}^{(j)} \right) &= (\sigma_{N_\mathrm{B}} \otimes \mathbb{1}_{N_\mathrm{B}^k}) \left(\mathbb{1}_2^{(\ell)} \otimes \mathbb{1}_{N_\mathrm{B}^k}^{(j)} \right) && (8.38) \\
&= \left(\sigma_{N_\mathrm{B}} \mathbb{1}_2^{(\ell)} \right) \otimes \left(\mathbb{1}_{N_\mathrm{B}^k} \mathbb{1}_{N_\mathrm{B}^k}^{(j)} \right) && (8.39) \\
&= \left(\sigma_{N_\mathrm{B}}^{(\ell)} \otimes \mathbb{1}_{N_\mathrm{B}^k}^{(j)} \right), && (8.40)
\end{aligned}$$

we obtain Eq. (8.31) by linearity.

Now, we are able to reduce the eigenvector φ_{k+1} of T_{k+1} to an eigenvector of T_k. By

multiplication of $T_{k+1}\hat{\sigma}_{N_\mathrm{B}}(k) = \hat{\sigma}_{N_\mathrm{B}}(k)T_k$ with $\hat{\sigma}_{N_\mathrm{B}}(k)^{-1}$ from the left and the right, we in general obtain

$$\hat{\sigma}_{N_\mathrm{B}}(k)^{-1}T_{k+1}\hat{\sigma}_{N_\mathrm{B}}(k)\hat{\sigma}_{N_\mathrm{B}}(k)^{-1} = T_k\hat{\sigma}_{N_\mathrm{B}}(k)^{-1}, \tag{8.41}$$

for $k \in \mathbb{N}_0$, and after restriction to the eigenspaces of T_{k+1}, we further find

$$\hat{\sigma}_{N_\mathrm{B}}(k)^{-1}T_{k+1}\varphi_{k+1} = T_k\hat{\sigma}_{N_\mathrm{B}}(k)^{-1}\varphi_{k+1} \tag{8.42}$$

for $k \in \mathbb{N}_0$. Thus, given $T_{k+1}\varphi_{k+1} = \lambda_{k+1}\varphi_{k+1}$, it is

$$T_k\hat{\sigma}_{N_\mathrm{B}}(k)^{-1}\varphi_{k+1} = \lambda_{k+1}\hat{\sigma}_{N_\mathrm{B}}(k)^{-1}\varphi_{k+1}, \tag{8.43}$$

such that $\varphi_k := \hat{\sigma}_{N_\mathrm{B}}(k)^{-1}\varphi_{k+1}$ an eigenvector of T_k associated with the eigenvalue $\lambda_k := \lambda_{k+1}$. Let us stress that $\hat{\sigma}_{N_\mathrm{B}}(k)^{-1}$ is injective on the eigenspaces of T_{k+1}, following from Eqs. (8.34) and (8.37),

$$\hat{\sigma}_{N_\mathrm{B}}(k)^{-1}\varphi_{k+1} = \sum_{j=1}^{N_\mathrm{B}^k}\left(s_1^{(j)}\mathbb{1}_2^{(1)} \otimes \mathbb{1}_{N_\mathrm{B}^k}^{(j)} + s_2^{(j)}\mathbb{1}_2^{(2)} \otimes \mathbb{1}_{N_\mathrm{B}^k}^{(j)}\right). \tag{8.44}$$

Hence, the only pairs of eigenvectors and eigenvalues of T_{k+1} are the ones lifted from the eigenvalue problem for T_k by virtue of $\hat{\sigma}_{N_\mathrm{B}}(k)$ for $k \in \mathbb{N}_0$. □

This proposition simplifies the analytical computation of the natural CIM for the partial-barrier Baker map tremendously. We only have to solve the eigenvalue problem of the 2×2 matrix T_0, Eq. (8.17), and lift its eigenvectors by mere matrix multiplication to the required resolution. The matrix T_0 describes the iteration of weights from one side of the partial barrier to the other side in the lowest reasonable Ulam approximation, that is, associated with the two cells $[0,1/2)\times[0,1)$ and $[1/2,1)\times[0,1)$. As this 2×2 matrix is particularly relevant in the following analysis of the partial-barrier Baker map and also for the generalization to generic maps, we express it in terms of the variables $|A_1| = |A_2| = 1/2$, $|\Omega| = L/N_\mathrm{B}$, and $\phi = C/N_\mathrm{B}$, which gives

$$T_0 = \begin{pmatrix} 1-(|\Omega|+\phi)/|A_1| & \phi/|A_2| \\ \phi/|A_1| & 1-\phi/|A_2| \end{pmatrix}. \tag{8.45}$$

The diagonal elements describe the probability to remain on one or the other side of the partial barrier within one iteration of the map, while the off-diagonal elements describe the probability to get from one side to the other. Note that the main purpose of the generalization of the partial-barrier Baker map to the partial-barrier N_B-Baker map with variables L and C

was to plausibly motivate Eq. (8.45) in terms of more general variables. That this 2×2 matrix is actually important for more generic systems will be shown in Chap. 9. In the following, we again focus on the example of the partial-barrier Baker map based on the ternary Baker map. In this special case, T_0 reads

$$T_0 = \frac{1}{3}\begin{pmatrix} 1 & 1 \\ 1 & 2 \end{pmatrix}. \tag{8.46}$$

8.3 Natural Conditionally Invariant Measure

Let us now study the natural CIM of the partial-barrier Baker map. From the reduced Perron–Frobenius operator T_0, Eq. (8.46), we compute the Perron–Frobenius eigenvector φ_0, i.e., the one with larger eigenvalue λ, and lift φ_0 to an eigenvector of T_k by $\varphi_k = \hat{\sigma}_3(k-1)\cdots\hat{\sigma}_3(0)\varphi_0$ as explained in Sec. 8.2. For reference, the precise value of φ_0 and λ is

$$\varphi_0 = \frac{1}{\sqrt{5}+1}\begin{pmatrix} \sqrt{5}-1 \\ 2 \end{pmatrix}, \qquad \lambda = \frac{1}{6}(3+\sqrt{5}). \tag{8.47}$$

We normalized φ_0 such that the sum of the two components equals unity. Note that both components can be chosen nonnegative due to the Perron–Frobenius theorem, Sec. 7.2.3. Moreover, note that φ_k computed as above is not yet normalized. The phase-space distribution corresponding to φ_k is shown in Fig. 8.4(a–e) for different values of k. These distributions approximate the natural CIM μ_{nat} of the studied map. The two different nonzero heights in each of the distributions correspond to the two different components of φ_0. The lift by virtue of $\hat{\sigma}_3(n)$ just copies these two values and rearranges them appropriately. Therefore, precisely these two values, up to normalization, appear in each φ_k.

In Sec. 7.2.2 we argued that the natural CIM is provided by the uniform distribution on the backward trapped set, Fig. 8.4(f). The two different heights in the shown phase-space distributions seem to contradict this uniformity at first sight. However, the two values originate from an integration over cells of the phase-space partition used for the Ulam approximation, cf. Sec. 8.1. Depending on the number and size of gaps in each cell, the integration over these cells can yield different values for different cells although the distribution may be uniform on the asymptotic object, i.e., the proper fractal. This is illustrated in Fig. 8.5. It is clear that an integration over the uniform distribution on the backward trapped set in $[0,1/2)\times[0,1/9)$ gives a different value than an integration over $[0,1/2)\times[2/9,3/9)$.

In principle, there are at least two reasonable ways to approximate μ_{nat}. One could either use a uniform distribution on a finite-time approximation of the proper backward trapped set, or an integration of the proper μ_{nat} over cells of a phase-space partition. The latter approach corresponds to the φ_k distributions associated with the Ulam approximation T_k

shown in Fig. 8.4. We stress that both alternatives produce different but valid approximations of μ_{nat}, i.e., both ways converge towards μ_{nat} on asymptotically fine scales. Still, one of the two schemes could be more useful than the other, meaning that it could be more suitable to address specific questions. In the present study, the relevance of classical measures and its

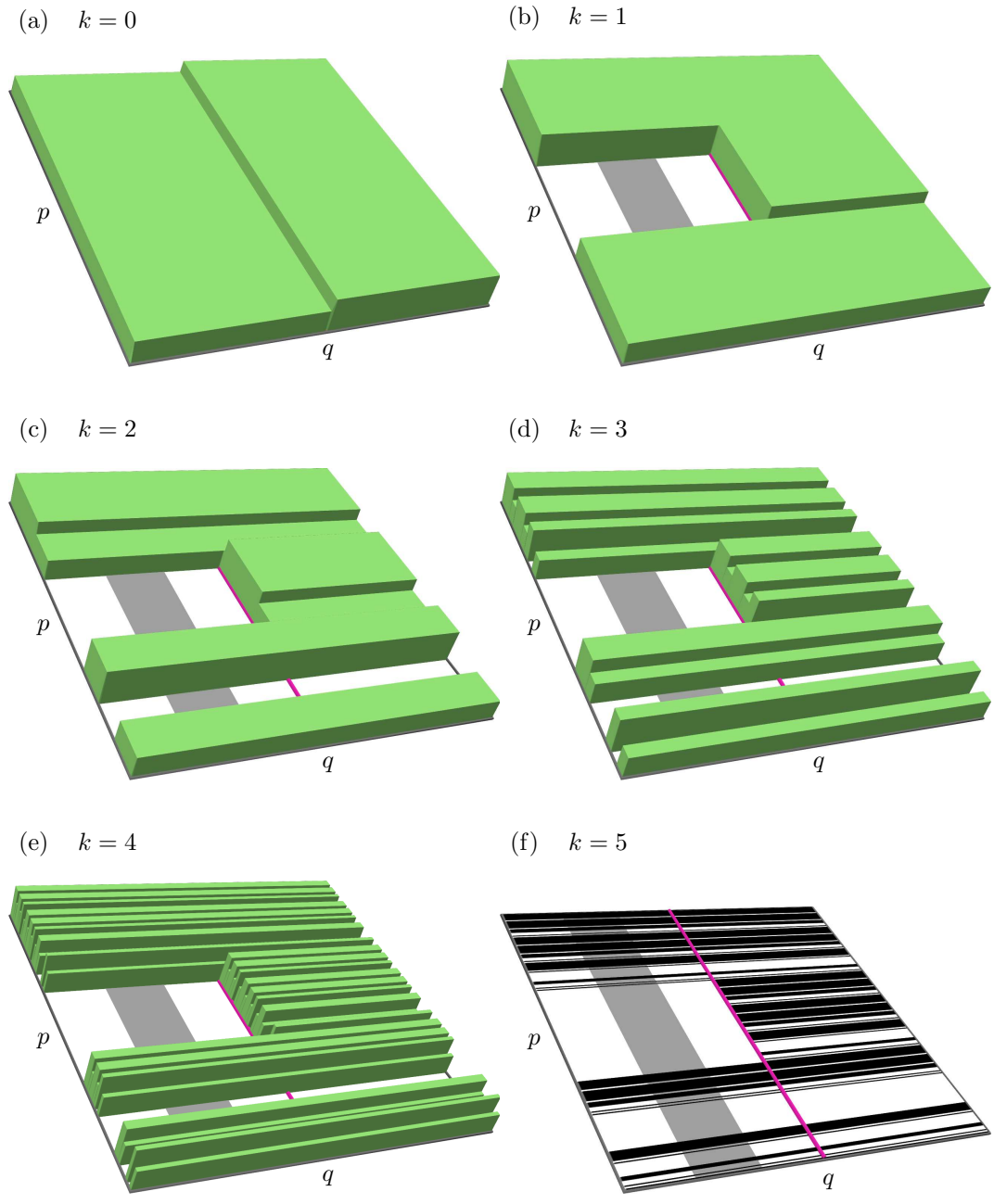

Figure 8.4. (a–e) Perron–Frobenius eigenvector φ_k of the Ulam approximation T_k of the partial-barrier Baker map, computed according to Eqs. (8.16) and (8.17). The resolution parameter k is indicated above each panel. Each φ_k is an approximation of the natural CIM when integrated over cells of the partition according to Sec. 7.2.2. (f) Approximation of the backward trapped set Γ_{bwd} for $k = 5$ backward iterations.

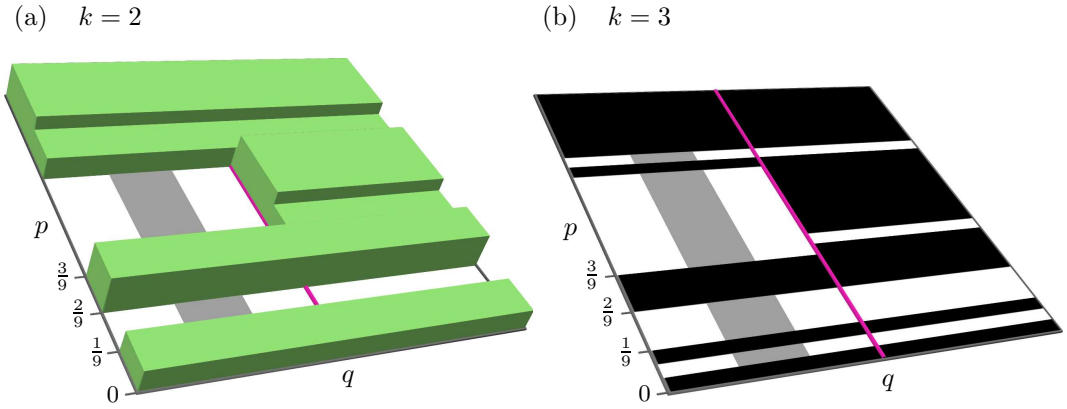

Figure 8.5. (a) Perron–Frobenius eigenvector φ_2 of the Ulam approximation T_2 of the partial-barrier Baker map. The two different nonzero heights originate from integration of the uniform distribution on the nonuniformly fractal backward trapped set over cells. This can be seen in (b) the finite-time approximation Γ_{bwd} for $k = 3$ backward iterations, which clearly has two different weights in the sets $[0, 1/2) \times [0, 1/9)$ and $[0, 1/2) \times [2/9, 3/9)$.

approximations is determined by quantum-to-classical correspondence. A classical measure is helpful if it provides a good estimate for certain properties of quantum resonance states. The property which is of most interest to us is the localization with respect to the partial barrier.

Regarding this issue, let us focus on the localization of the φ_k obtained by the Ulam approximation T_k. For the first approximation φ_0, see Fig. 8.4(a), the total weight is split as $\varphi_0^{(1)}$ to the left and $\varphi_0^{(2)}$ to the right, where $\varphi_0^{(\ell)}$ denotes the ℓ-th component of φ_0, $\ell \in \{1, 2\}$. The next level of approximation is given by

$$\varphi_1 = \sigma_3\left(\varphi_0^{(1)}, \varphi_0^{(2)}\right)^{\mathrm{T}} = \Big(\underbrace{\varphi_0^{(1)}, 0, \varphi_0^{(2)}}_{\text{left}}, \underbrace{\varphi_0^{(1)}, \varphi_0^{(2)}, \varphi_0^{(2)}}_{\text{right}}\Big)^{\mathrm{T}}, \tag{8.48}$$

up to normalization, cf. Fig. 8.4(b). Thus, the vector of new weights on the left and right of the partial barrier is given by

$$\begin{pmatrix} \varphi_0^{(1)} + \varphi_0^{(2)} \\ \varphi_0^{(1)} + 2\varphi_0^{(2)} \end{pmatrix} = \begin{pmatrix} 1 & 1 \\ 1 & 2 \end{pmatrix} \begin{pmatrix} \varphi_0^{(1)} \\ \varphi_0^{(2)} \end{pmatrix}, \tag{8.49}$$

again up to normalization. The matrix relating the weights from one level of approximation to the next is just T_0 up to a factor such that φ_0 is an eigenvector of the iteration of weights. This holds true for all approximations φ_k. Hence, the weights of μ_{nat} on the left and right of the partial barrier are exactly the components of the coarsest approximation φ_0.

The situation is different for the other approximation scheme, using a uniform distribution on the finite-time approximation $\Gamma_{\mathrm{bwd}}^{(k)} = \Gamma \setminus \bigcup_{n=1}^{k} T_{\mathrm{cl}}^n(\Omega)$ of the backward trapped set Γ_{bwd}. The weight of a uniform distribution on $\Gamma_{\mathrm{bwd}}^{(k)}$ on the left and right of the partial barrier is

given by

$$\begin{pmatrix} |\Gamma^{(k)}_{\mathrm{bwd}} \cap A_1| \\ |\Gamma^{(k)}_{\mathrm{bwd}} \cap A_2| \end{pmatrix} \sim T_0^k \begin{pmatrix} 1 \\ 1 \end{pmatrix}, \tag{8.50}$$

up to normalization. Although this converges towards φ_0 in agreement with the previously discussed Ulam approximation, now the weight on each side depends on the level of approximation.

In order to judge which of the two approximation schemes is more appropriate to describe the localization of quantum resonance states, the most convenient way would be to directly compare the approximate phase-space distribution of μ_{nat} with the Husimi representation of resonance states. This is done in Fig. 8.6. One might suspect that there are indeed lower weights on the horizontal stripes indicated by the arrows, just like in the classical phase-space distribution corresponding to φ_k from the Ulam approximation T_k. However, there are two drawbacks. First, the quantum fluctuations are relatively large compared to the difference of the two heights in the approximate classical measure. A second problem is that it is not clear how to distinguish between two possible reasons for different weights in the Husimi distribution: Either the different weights are due to integration on the Planck cell level like in the classical case or the different weights originate from an already resolved next level of gaps that is only smeared out. Thus, this comparison is not convincing and inconclusive.

This problem can be overcome by looking at how the weights of quantum resonance states on the left and right of the partial barrier depend on the effective size h of Planck's cell.

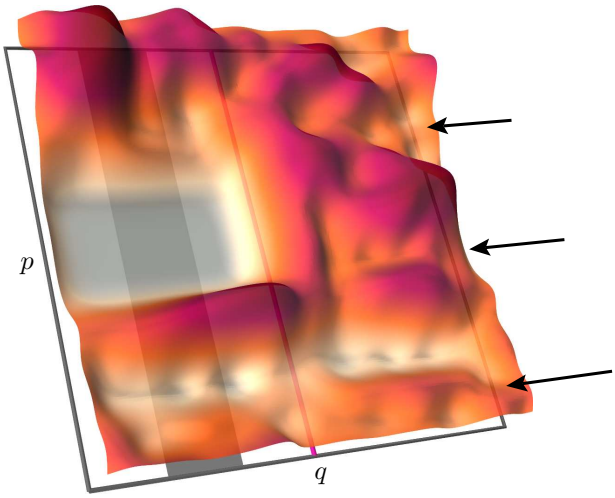

Figure 8.6. Average Husimi representation of resonance states of the partial-barrier Baker map with $1/h = 2 \cdot 3^3 = 54$. The average is performed over the Husimi distributions of all twelve resonance states with $\gamma \in [\gamma_{\mathrm{nat}}/1.25, \gamma_{\mathrm{nat}} \cdot 1.25]$. The arrows indicate horizontal stripes of lower weight possibly related to the different heights in Fig. 8.5(a).

Figure 8.7 demonstrates that they essentially remain constant under variation of $h = 1/N$ up to fluctuations. In particular, the quantum data is not described by the resolution depending weights computed from the uniform distribution on a finite-time approximation $\Gamma^{(k)}_{\mathrm{bwd}}$ of the backward trapped set. Instead, the quantum data is well described by the weights of φ_k which are independent of the level of approximation. In order to amplify the imbalance in the two nonzero heights of the phase-space distribution corresponding to φ_k, and thus, to emphasize the difference between the two approximation schemes, we use $N_{\mathrm{B}} = 10$, $L = 5$, and $C = 1$ instead of the partial-barrier map based on the ternary Baker map.

Hence, we conclude that the localization of quantum resonance states with $\gamma \approx \gamma_{\mathrm{nat}}$ should be approximated by the Perron–Frobenius vector of an appropriate Ulam approximation of the classical Perron–Frobenius operator if feasible. We point out that it is not clear whether this also holds for generic maps or whether this might be related to specific properties of the Baker map, such as its strongly discontinuous behavior.

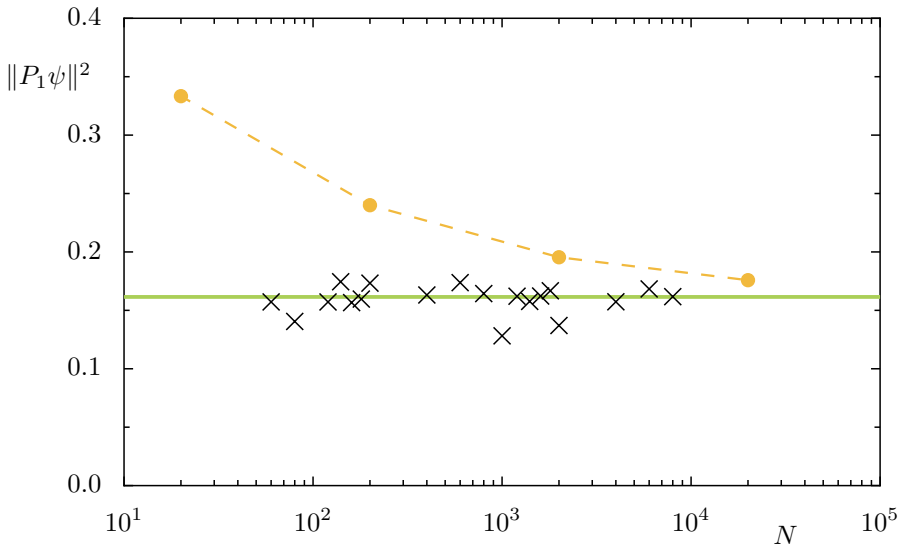

Figure 8.7. Weight $\|P_1\psi\|^2$ (black crosses) of resonance states ψ in region A_1 on the left side of the partial barrier for the partial-barrier Baker map ($N_{\mathrm{B}} = 10$, $L = 5$, $C = 1$) vs matrix dimension $N = 1/h$ of the quantum time-evolution operator. The weights are averaged over all states ψ with $\gamma \in [\gamma_{\mathrm{nat}}/1.05, \gamma_{\mathrm{nat}} \cdot 1.05]$. This is compared with the classical predictions from the Perron–Frobenius vector φ_k of an Ulam approximation T_k (green solid line; Eq. (8.47)), and from a uniform distribution on a finite-time approximation of backward trapped set (orange points; Eq. (8.50)). They are semiclassically related to the quantum data by choosing the cell size as h.

8.4 γ-Natural Conditionally Invariant Measures

The generalization of the natural CIM μ_{nat} with the single decay rate γ_{nat} to the class of γ-natural CIMs μ_γ of arbitrary decay rate γ is discussed in detail in Sec. 7.2.2. Considering again their definition in Eq. (7.49),

$$\mu_\gamma(X) := \frac{1-e^{-\gamma}}{1-e^{-\gamma_{\mathrm{nat}}}} \sum_{n\in\mathbb{N}_0} e^{(\gamma_{\mathrm{nat}}-\gamma)n} \mu_{\mathrm{nat}}\big(X \cap T^{-n}(\Omega)\big), \tag{8.51}$$

the measure μ_γ results from μ_{nat} by adapting its weight within each forward escaping set $T^{-n}(\Omega)$ in order to achieve the overall decay rate γ. This construction is illustrated for the partial-barrier Baker map in Fig. 8.8(a–c). Since the partial-barrier Baker map exhibits a simple decomposition in the stable (vertical) and unstable (horizontal) direction, the forward escaping sets are vertical stripes splitting the phase space in horizontal direction, see blue

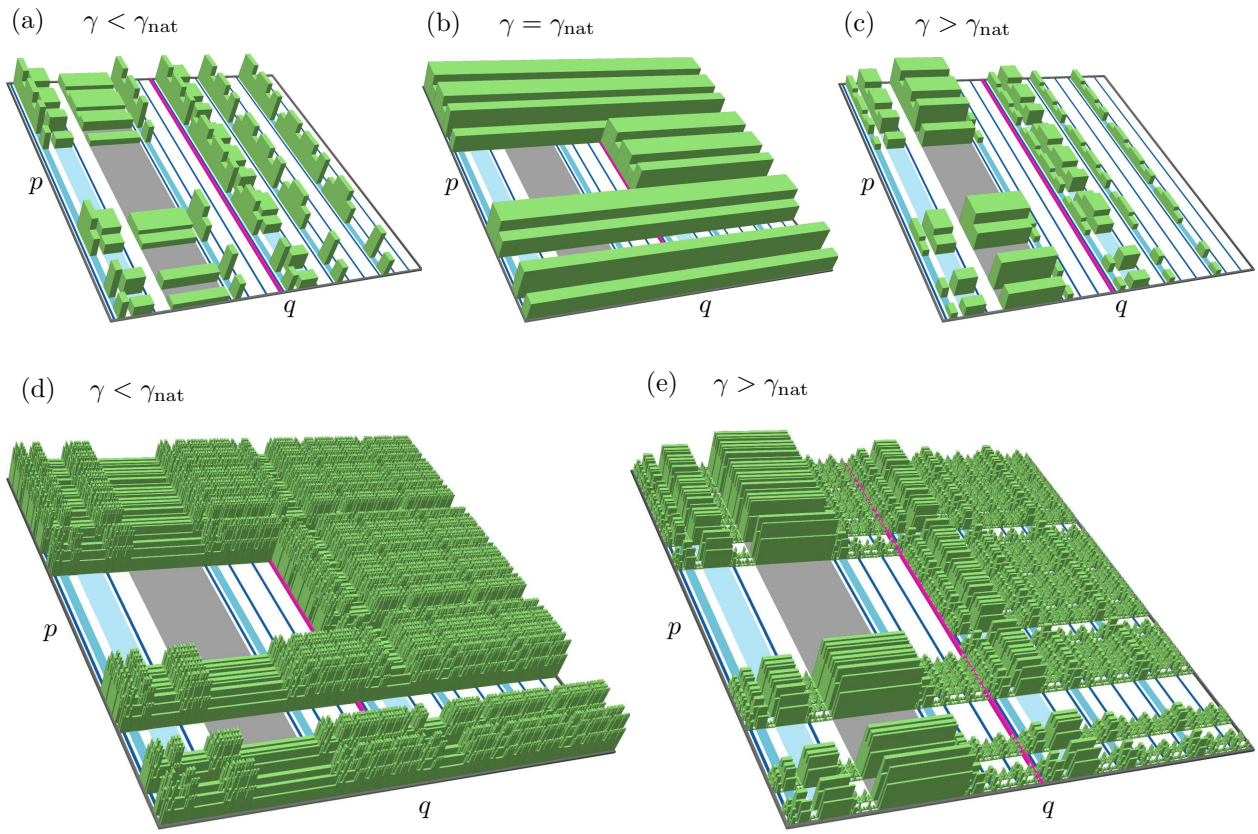

Figure 8.8. (a, c) Construction of γ-natural CIMs for the partial-barrier Baker map by truncation of the series in Eq. (7.49) to $n \leq 2$ for (a) $\gamma < \gamma_{\mathrm{nat}}$ and (c) $\gamma > \gamma_{\mathrm{nat}}$. This is based on the natural CIM shown in (b) for which the weight in Ω (gray stripe), $T^{-1}(\Omega)$ (light blue stripes), and $T^{-2}(\Omega)$ (medium blue stripes) is adapted. The level $T^{-3}(\Omega)$ (dark blue stripes) is not yet resolved. (d, e) Finer resolution μ_γ for (d) $\gamma < \gamma_{\mathrm{nat}}$ and (e) $\gamma > \gamma_{\mathrm{nat}}$ computed by the integration method discussed in Sec. 7.2.2.

regions in the background of Fig. 8.8. Starting with the approximation of the natural CIM μ_{nat} shown in Fig. 8.8(b), we first adapt the weight on the opening to $\mu_\gamma(\Omega) = 1 - e^{-\gamma}$. As this only requires an appropriately chosen factor the structure of μ_{nat} within Ω is not affected by this, see Figs. 8.8(a) and (c). Depending on whether the new decay rate γ is larger or smaller than the original γ_{nat}, the weight in Ω is increased or decreased, respectively. We proceed analogously with the weight in $T^{-1}(\Omega)$ (two light blue stripes) and $T^{-2}(\Omega)$ (five blue stripes) using that $\mu_\gamma(T^{-n}(\Omega)) = e^{-\gamma n}\mu_\gamma(\Omega)$. This gives the phase-space distributions shown in Figs. 8.8(a) and (c), which corresponds to a truncation of the series in Eq. (7.49) to $n \leq 2$. We see that for the generalization of μ_{nat} to μ_γ in case of the partial-barrier Baker map, an additional profile in horizontal direction is imposed on μ_{nat} but the structure along the vertical axis is not affected. For a finer resolution the outcome of this construction is again shown in Figs. 8.8(d) and (e) for $\gamma < \gamma_{\text{nat}}$ and $\gamma > \gamma_{\text{nat}}$, respectively. This resolution highlights the complex fractal nature of the measures. Note that in Figs. 8.8(d) and (e), the measures are computed according to Sec. 7.2.2: We compute the escape time for each point of a phase-space grid and associate an intensity to it according to the weight $\mu_\gamma(T^{-n}(\Omega))$ and the number of grid points in $T^{-n}(\Omega)$. Afterwards, this intensity is integrated over the cells of an appropriate phase-space partition. It is demonstrated in Fig. 8.9 that the proposed construction of γ-natural CIMs qualitatively clearly exhibits quantum-to-classical correspondence. The quantum resonance state is well resembled by the classical measure even on fine scales up to quantum fluctuations.

In order to quantitatively study quantum-to-classical correspondence, we now analytically

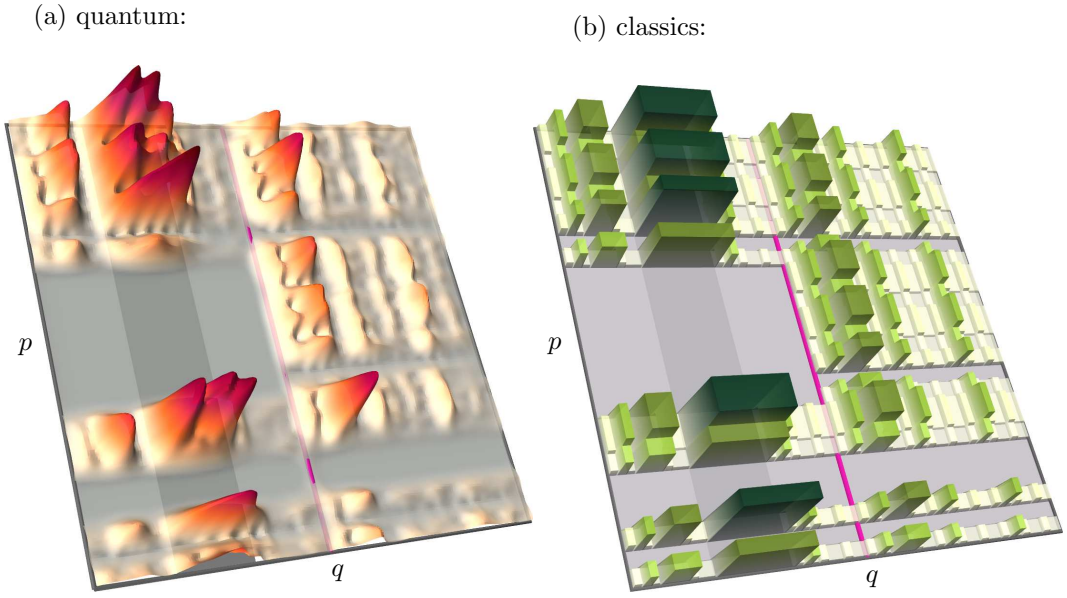

Figure 8.9. (a) Average Husimi distribution of resonance states for the partial-barrier Baker map ($1/h = 480$) with $\gamma \in [4\gamma_{\text{nat}}/1.25, 4\gamma_{\text{nat}} \cdot 1.25]$ (24 states). (b) Approximate γ-natural CIM for $\gamma = 4\gamma_{\text{nat}}$.

compute the classical weights $\mu_\gamma(A_k)$ on either side of the partial barrier. A concise version of the following derivation is presented in Ref. [34]. In virtue of Eq. (7.49), we only have to analyze the natural CIM $\mu_{\text{nat}}(A_k \cap T^{-n}(\Omega))$ in more detail to compute $\mu_\gamma(A_k)$ for all decay rates γ instantaneously. As a first essential step, we find that the natural CIM of $A_k \cap T^{-n}(\Omega)$ is proportional to the relative area inside A_k,

$$\mu_{\text{nat}}\big(A_k \cap T^{-n}(\Omega)\big) = \mu_{\text{nat}}(A_k) \cdot \frac{|A_k \cap T^{-n}(\Omega)|}{|A_k|}. \tag{8.52}$$

This follows from the fact that the forward escaping sets $T^{-n}(\Omega)$ (vertical stripes) decompose the backward trapped set Γ_{bwd} in the unstable (horizontal) direction, on which μ_{nat} is uniformly distributed within A_1 and A_2 individually, see Fig. 8.10.

The distribution of the opening Ω over phase space under backward time evolution, which enters Eq. (8.52) in terms of $|A_k \cap T^{-n}(\Omega)|$, follows from

$$\begin{pmatrix} |A_1 \cap T^{-n}(\Omega)| \\ |A_2 \cap T^{-n}(\Omega)| \end{pmatrix} = T_0^n \begin{pmatrix} |\Omega| \\ 0 \end{pmatrix}, \tag{8.53}$$

with T_0 given by Eq. (8.46). Note that the transition matrix for the backward time evolution of Ω is given by T_0 itself. We illustrate this relation by examining the first steps explicitly. Consider Fig. 8.10: In the beginning, Ω (gray vertical stripe) is supported on A_1. In the

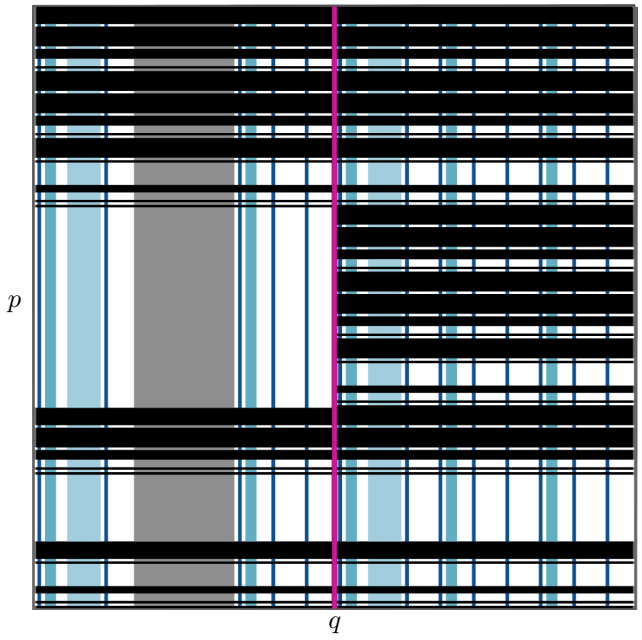

Figure 8.10. Finite-time approximation of the backward trapped set Γ_{bwd} of the partial-barrier Baker map (black). Blue vertical stripes in the background are forward escaping sets (light blue: $T^{-1}(\Omega)$; medium blue: $T^{-2}(\Omega)$; dark blue: $T^{-3}(\Omega)$).

next step, $T^{-1}(\Omega)$ (light blue) splits into equal parts of size $|\Omega|/3$ on A_1 and A_2. Afterwards, $T^{-2}(\Omega)$ (medium blue) contributes two stripes of size $|\Omega|/3^2$ to A_1 and three to A_2, and region $T^{-3}(\Omega)$ (dark blue) splits into pieces of size $|\Omega|/3^3$ five stripes of which are in A_1 while eight are in A_2. This is precisely described by the iteration with T_0,

$$|\Omega| \begin{pmatrix} 1 \\ 0 \end{pmatrix} \overset{T_0}{\mapsto} \frac{|\Omega|}{3} \begin{pmatrix} 1 \\ 1 \end{pmatrix} \overset{T_0}{\mapsto} \frac{|\Omega|}{3^2} \begin{pmatrix} 2 \\ 3 \end{pmatrix} \overset{T_0}{\mapsto} \frac{|\Omega|}{3^3} \begin{pmatrix} 5 \\ 8 \end{pmatrix}. \tag{8.54}$$

Inserting the relations (8.52) and (8.53) in Eq. (7.49), we obtain

$$\mu_\gamma(A_k) = \frac{1-e^{-\gamma}}{1-e^{-\gamma_{\text{nat}}}} \frac{\mu_{\text{nat}}(A_k)}{|A_k|} \left[\sum_{n\in\mathbb{N}_0} \left(e^{\gamma_{\text{nat}}-\gamma} T_0\right)^n \begin{pmatrix} |\Omega| \\ 0 \end{pmatrix} \right]_k, \tag{8.55}$$

and using Neumann's series, this is

$$\mu_\gamma(A_k) = \frac{1-e^{-\gamma}}{1-e^{-\gamma_{\text{nat}}}} \frac{\mu_{\text{nat}}(A_k)}{|A_k|} \left[\left(\mathbb{1} - e^{\gamma_{\text{nat}}-\gamma} T_0\right)^{-1} \begin{pmatrix} |\Omega| \\ 0 \end{pmatrix} \right]_k. \tag{8.56}$$

This expression already contains all physically relevant ideas and could be interpreted as the final result on the localization of μ_γ due to a partial barrier for the partial-barrier Baker map. By spectral decomposition of the vector $(|\Omega|, 0)$, however, it can still be simplified considerably. This leads to one of the main results of this thesis:

Theorem. The localization of the γ-natural CIM μ_γ of the partial-barrier N_{B}-Baker map due to the partial transport barrier is given by

$$\mu_\gamma(A_1) = \frac{\mu_{\text{nat}}(A_1) - c_\gamma}{1-c_\gamma}, \qquad \mu_\gamma(A_2) = 1 - \mu_\gamma(A_1), \tag{8.57}$$

with

$$c_\gamma = \left(1-e^{\gamma-\gamma_{\text{nat}}}\right)\left(1-e^{-\gamma_{\text{nat}}}\right) \frac{|A_1|}{|\Omega|} \frac{|A_2|}{\phi}. \tag{8.58}$$

Here, A_k denotes the region on each side of the partial barrier, Ω denotes the opening, and ϕ the flux across the partial barrier. Moreover, for the natural decay it is

$$\mu_{\text{nat}}(A_1) = \frac{|A_1|}{|\Omega|}\left(1-e^{-\gamma_{\text{nat}}}\right), \tag{8.59}$$

and $e^{-\gamma_{\text{nat}}}$ is the Perron–Frobenius eigenvalue of the 2×2 matrix T_0, Eq. (8.45).

Proof. The simplification of Eq. (8.56) to Eq. (8.57) as presented in the following is to a large extent based on a calculation by Roland Ketzmerick. Consider the eigenvalue problem of

$$J := \mathbb{1} - T_0 = \begin{pmatrix} \frac{|\Omega|+\phi}{|A_1|} & -\frac{\phi}{|A_2|} \\ -\frac{\phi}{|A_1|} & \frac{\phi}{|A_2|} \end{pmatrix}, \tag{8.60}$$

$Jx_k = \lambda_k x_k$, with $\lambda_k \in \mathbb{C}$ and $x_k \in \mathbb{C}^2$ for $k \in \{1, 2\}$. The eigenspaces are spanned by

$$x_k = \begin{pmatrix} \lambda_k - \frac{\phi}{|A_2|} \\ -\frac{\phi}{|A_1|} \end{pmatrix}, \tag{8.61}$$

using that $\phi/|A_1| \neq 0$. The essential step to treat Eq. (8.56) is the decomposition of $(|\Omega|, 0)$ in terms of eigenvectors of J,

$$\begin{pmatrix} |\Omega| \\ 0 \end{pmatrix} = \alpha \, (x_1 - x_2) \tag{8.62}$$

with $\alpha := |\Omega|/(\lambda_1 - \lambda_2)$, and to use that J and $(\mathbb{1} - e^{\gamma_{\mathrm{nat}} - \gamma} T_0)^{-1}$ share the same eigenspaces,

$$\left(\mathbb{1} - e^{\gamma_{\mathrm{nat}} - \gamma} T_0\right)^{-1} x_k = \left(1 - e^{\gamma_{\mathrm{nat}} - \gamma}(1 - \lambda_k)\right)^{-1} x_k. \tag{8.63}$$

Using this spectral decomposition, we obtain

$$\mu_\gamma(A_1) = \frac{1 - e^{-\gamma}}{1 - e^{-\gamma_{\mathrm{nat}}}} \frac{\mu_{\mathrm{nat}}(A_1)}{|A_1|} \frac{|\Omega|}{\lambda_1 - \lambda_2} \left[\frac{\lambda_1 - \frac{\phi}{|A_2|}}{1 - e^{\gamma_{\mathrm{nat}} - \gamma}(1 - \lambda_1)} - \frac{\lambda_2 - \frac{\phi}{|A_2|}}{1 - e^{\gamma_{\mathrm{nat}} - \gamma}(1 - \lambda_2)} \right]. \tag{8.64}$$

We apply Eq. (8.52) for $k = 1$, $n = 0$ with $\Omega \subseteq A_1$ and find

$$\frac{\mu_{\mathrm{nat}}(\Omega)}{\mu_{\mathrm{nat}}(A_1)} = \frac{|\Omega|}{|A_1|}. \tag{8.65}$$

Having $\mu_{\mathrm{nat}}(\Omega) = 1 - e^{-\gamma_{\mathrm{nat}}}$, Eq. (8.64) reads

$$\mu_\gamma(A_1) = \frac{1 - e^{-\gamma}}{\lambda_1 - \lambda_2} \left[\frac{\lambda_1 - \frac{\phi}{|A_2|}}{1 - e^{\gamma_{\mathrm{nat}} - \gamma}(1 - \lambda_1)} - \frac{\lambda_2 - \frac{\phi}{|A_2|}}{1 - e^{\gamma_{\mathrm{nat}} - \gamma}(1 - \lambda_2)} \right]. \tag{8.66}$$

In view of

$$T_0 \begin{pmatrix} \mu_{\rm nat}(A_1) \\ \mu_{\rm nat}(A_2) \end{pmatrix} = e^{-\gamma_{\rm nat}} \begin{pmatrix} \mu_{\rm nat}(A_1) \\ \mu_{\rm nat}(A_2) \end{pmatrix}, \tag{8.67}$$

we already know one of the eigenvalues λ_k of J. Without loss of generality, let

$$\lambda_1 = 1 - e^{-\gamma_{\rm nat}} = \mu_{\rm nat}(\Omega). \tag{8.68}$$

This implies

$$\lambda_2 = \frac{\det J}{\lambda_1} = \frac{|\Omega|\phi}{|A_1||A_2|}\frac{1}{\lambda_1} = \frac{\phi}{|A_2|\mu_{\rm nat}(A_1)}, \tag{8.69}$$

such that

$$\frac{\phi}{|A_2|} = \lambda_2\, \mu_{\rm nat}(A_1). \tag{8.70}$$

Inserting Eq. (8.70) in Eq. (8.66) and using $e^{\gamma_{\rm nat}} = (1-\lambda_1)^{-1}$, cf. Eq. (8.68), we obtain

$$\mu_\gamma(A_1) = \frac{1-e^{-\gamma}}{\lambda_1 - \lambda_2}\left[\frac{\lambda_1 - \lambda_2\,\mu_{\rm nat}(A_1)}{1-e^{-\gamma}} - \frac{\lambda_2 - \lambda_2\,\mu_{\rm nat}(A_1)}{1-e^{-\gamma\frac{1-\lambda_2}{1-\lambda_1}}}\right]. \tag{8.71}$$

After some straightforward algebraic manipulations, where we only show the essential intermediate steps for reference, we get

$$\begin{aligned}
\mu_\gamma(A_1) &= \frac{\mu_{\rm nat}(A_1)}{\lambda_1-\lambda_2}\left[\frac{\lambda_2\,(1-e^{-\gamma})}{1-e^{-\gamma\frac{1-\lambda_2}{1-\lambda_1}}} - \lambda_2\right] + \frac{1}{\lambda_1-\lambda_2}\left[\lambda_1 - \frac{\lambda_2\,(1-e^{-\gamma})}{1-e^{-\gamma\frac{1-\lambda_2}{1-\lambda_1}}}\right] && (8.72)\\
&= \mu_{\rm nat}(A_1)\,\frac{\lambda_2\,e^{-\gamma}}{1-\lambda_1-e^{-\gamma}(1-\lambda_2)} - \frac{\lambda_1+e^{-\gamma}-1}{1-\lambda_1-e^{-\gamma}(1-\lambda_2)} && (8.73)\\
&= \frac{1}{1-\frac{\lambda_1+e^{-\gamma}-1}{\lambda_2\,e^{-\gamma}}}\left[\mu_{\rm nat}(A_1) - \frac{\lambda_1+e^{-\gamma}-1}{\lambda_2\,e^{-\gamma}}\right], && (8.74)
\end{aligned}$$

and define

$$c_\gamma := \frac{\lambda_1+e^{-\gamma}-1}{\lambda_2\,e^{-\gamma}}. \tag{8.75}$$

Inserting Eqs. (8.68) and (8.69) gives Eqs. (8.58) and (8.57). Equation (8.59) follows from Eq. (8.65). □

With this, we are able to quantitatively investigate quantum-to-classical correspondence for the localization due to the partial barrier. To this end, we diagonalize the quantum time-

evolution operator for the matrix dimension $1/h = 2100$ and compute the weight of each resonance state in A_1. This is shown in Fig. 8.11 in dependence of the decay rate γ (red dots). We observe a transition from predominant localization in A_2 to localization in A_1 for increasing γ. The quantum mechanical behavior is very well described by the classical localization of the class of γ-natural CIMs, Eq. (8.57) (green line). Small deviations apart from fluctuations in the quantum data are discussed in detail in Sec. 9.2 in the context of generic systems. To demonstrate both the validity of our analytical classical prediction as well as the accuracy of our approximation schemes for μ_γ, we also integrate the numerically determined approximation of μ_γ, cf. Sec. 7.2.2, over A_1 for different values of γ (black crosses). The analytical classical result and the numerically determined classical data are in perfect agreement. Note that we will comment on the quantitative study of quantum-to-classical correspondence on finer scales in the outlook, Chap. 11.

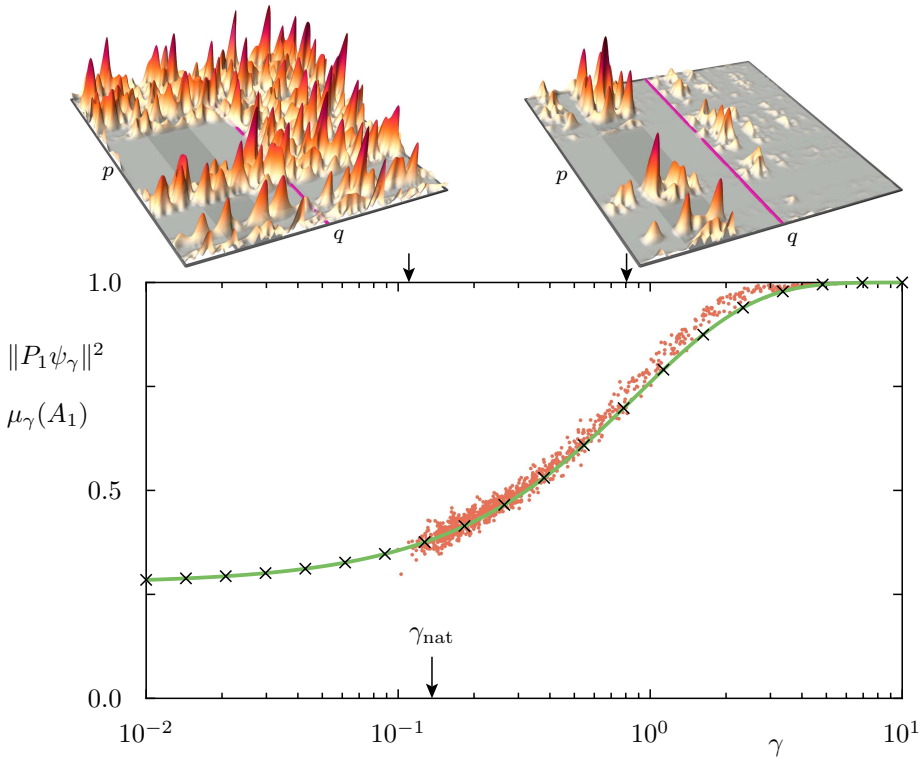

Figure 8.11. Weight $\|P_1\psi_\gamma\|^2$ (red points) of resonance states ψ_γ in region A_1 vs decay rate γ for the partial-barrier Baker map ($h = 1/2100$). This is compared to the γ-natural CIM $\mu_\gamma(A_1)$ computed according to Eq. (8.57) (solid green line), and by integration over numerical approximations (black crosses). Upper panels: Husimi representation of typical long-lived (left) and short-lived (right) resonance state for $h = 1/1080$ with γ values indicated by arrows.

Chapter 9

Localization in Generic Maps

Chaotic resonance states display localization transitions with respect to a partial barrier for varying ratio of openness $|\Omega|$ and flux ϕ, and for varying decay rates γ. This is observed for the partial-barrier standard map in Chap. 6 and explained for the partial-barrier Baker map using γ-natural CIMs in Chap. 8. The goal of this chapter is to demonstrate this quantum-to-classical correspondence between chaotic resonance states and γ-natural CIMs also for generic maps. To this end, we numerically examine the partial-barrier standard map for which we initially observed the studied localization transitions in Sec. 9.1. We will see that the localization of chaotic resonance states is indeed very well described by the localization of γ-natural CIMs in the semiclassical regime. Characteristic deviations away from the semiclassical regime are presented in Sec. 9.2. Finally, we verify quantum-to-classical correspondence for the generic standard map with a mixed phase space of regular and chaotic motion in Sec. 9.3. The limitations for the applicability of the analytical prediction, Eq. (8.57), for the weights of γ-natural CIMs on each side of a partial barrier for generic systems and its generalization are discussed in detail. The main results of this chapter were originally reported in Ref. [34].

9.1 Partial-Barrier Standard Map

First of all, let us qualitatively demonstrate the correspondence between quantum resonance states and classical γ-natural CIMs for the partial-barrier standard map by merely looking at the corresponding phase-space distributions. Figure 9.1 shows that for a single but typical example ($|\Omega| = 0.2$, $\phi = 0.1$, $|A_1| = |A_2| = 0.5$) we indeed find very good agreement between the quantum and classical localization. Owing to the complex fractal structure of the partial-barrier standard map, we additionally show the quantum and classical phase-space distributions in top view and in a mutual color scale. This reveals that quantum-to-classical correspondence is evident even on fine scales up to the quantum resolution limit.

In order to investigate this agreement between classical and quantum mechanics quantita-

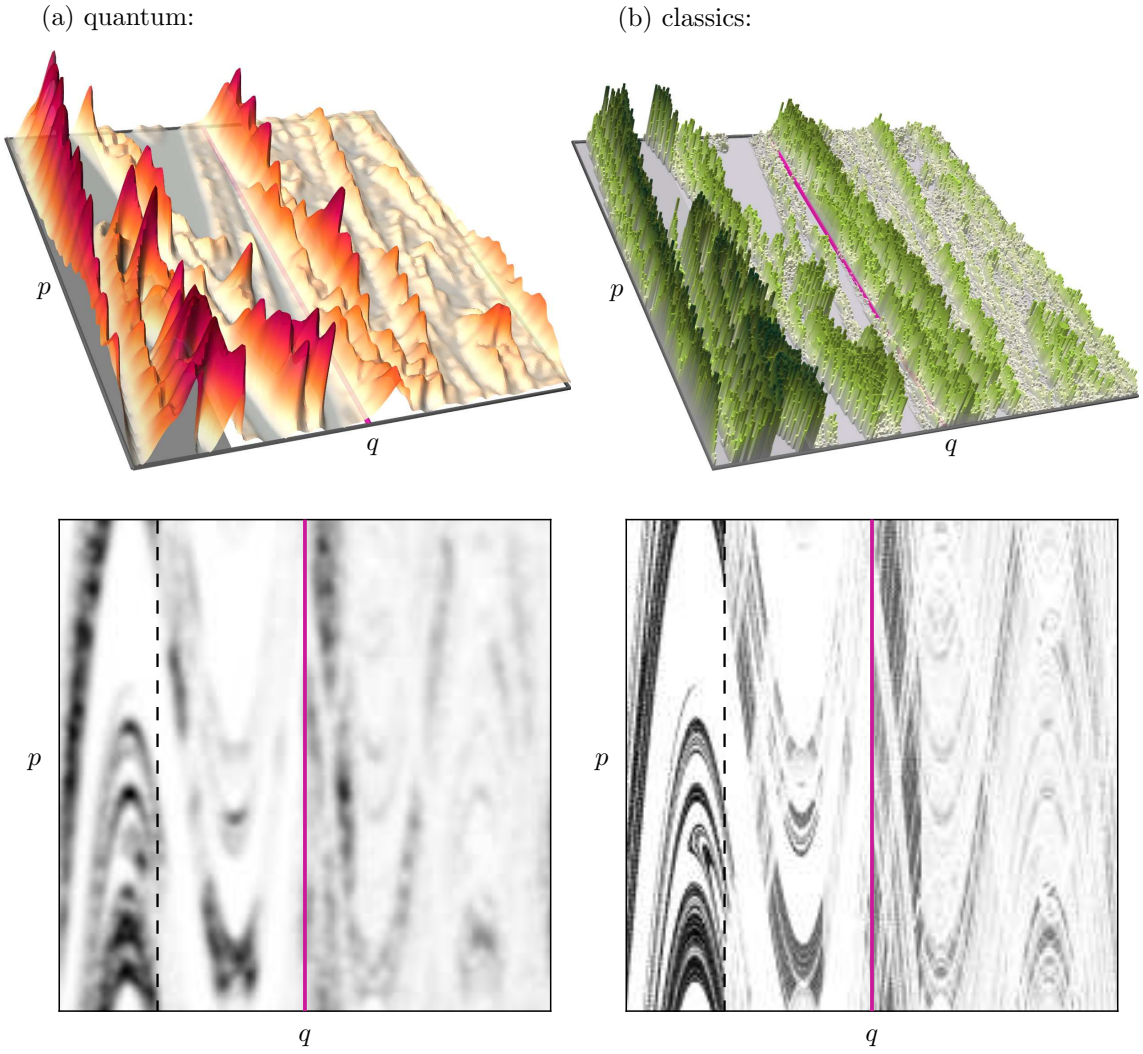

Figure 9.1. (a) Average Husimi distribution of resonance states for the partial-barrier standard map ($|\Omega| = 0.2$; $\phi = 0.1$; $|A_1| = 1/2$; $h = 1/1000$) with $\gamma \in [4\gamma_{\rm nat}/1.4, 4\gamma_{\rm nat} \cdot 1.4]$ (88 states). (b) Approximate γ-natural CIM for $\gamma = 4\gamma_{\rm nat}$. Lower panels: Same data on mutual gray scale, top view. Black dashed line illustrates opening; magenta line shows partial barrier.

tively, we restrict ourselves to the localization with respect to the partial barrier, that is, we compute the classical measure $\mu_\gamma(A_1)$ and compare it with the quantum mechanical weight $\|P_1\psi_\gamma\|^2$ in region A_1. This is certainly a comparison on a rather coarse scale. However, recall that our major goal is to understand the localization transitions introduced in Sec. 6.1. In particular, this is (i) a transition from equipartition to localization of long-lived chaotic resonance states on A_2 for increasing size $|\Omega|$ of the opening, Fig. 6.2, and (ii) a transition from localization on A_2 to localization on A_1 for increasing γ, Fig. 6.3. In order to see whether both transitions semiclassically correspond to localization transitions of γ-natural CIMs, we basically need to compute $\mu_\gamma(A_1)$ for different parameter setups. To this end, we have two

possibilities: First we can numerically approximate μ_γ as described in Sec. 7.2.2 and integrate over A_1. The second opportunity is given by the analytical result for the partial-barrier Baker map, Eq. (8.57). One should be cautious when applying Eq. (8.57) here as we derived this relation specifically for the partial-barrier Baker map. However, as we shall see below it turns out that Eq. (8.57) is perfectly applicable also for the partial-barrier standard map.

For the investigation of quantum-to-classical correspondence for transition (i) from equipartition to localization when opening the system, we focus on long-lived resonance states with $\gamma \approx \gamma_{\text{nat}}$. We compute the classical measure $\mu_{\text{nat}}(A_1)$ directly from Eq. (8.57) for $\gamma = \gamma_{\text{nat}}$ ($c_\gamma = 0$ in this case). The results are shown in Fig. 9.2, which is analogous to Fig. 6.2, now including the classical localization (green line). The localization of μ_{nat} perfectly describes the localization transition (i) of quantum resonance states of the partial-barrier standard map over the whole range of parameters. We point out that at first sight, the parameters $|\Omega|$ and ϕ enter individually in the classical localization according to Eq. (8.57) when using Eq. (8.45)

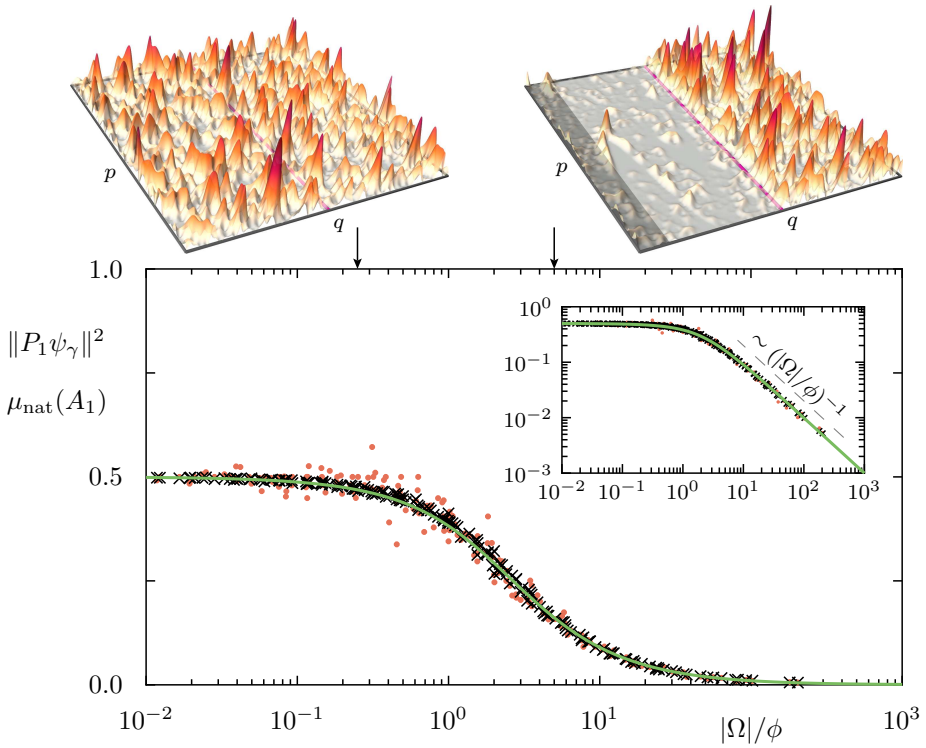

Figure 9.2. Weight $\|P_1\psi_\gamma\|^2$ (symbols) of resonance states on region A_1 vs ratio of size $|\Omega|$ of opening and flux ϕ across partial barrier for different parameters of the partial-barrier standard map ($10 \leq \phi/h, |\Omega|/h \leq 2048$; $|A_1| = 1/2$; $h = 1/6000$). Weight of state with γ closest to γ_{nat} (red points) and averaged over states with decay rates $\gamma \in [\gamma_{\text{nat}}/1.1, \gamma_{\text{nat}} \cdot 1.1]$ (black crosses). This is compared to the natural CIM $\mu_{\text{nat}}(A_1)$ (Eq. (8.57), solid green line). Inset: Same data shown on double-logarithmic scale. Upper panels: Husimi representation of typical resonance states with $\gamma \approx \gamma_{\text{nat}}$ for $h = 1/1000$, $\phi/h = 20$, and two values $|\Omega|/\phi$ indicated by arrows.

for the fundamental 2×2 transition matrix T_0. That this transition, in fact, only depends on the single parameter $|\Omega|/\phi$ can be easily seen the following way. We rephrase the transition matrix T_0, which approximates the Perron–Frobenius operator with respect to the two sides of the partial barrier, according to

$$T_0 = \begin{pmatrix} 1-(|\Omega|+\phi)/|A_1| & \phi/|A_2| \\ \phi/|A_1| & 1-\phi/|A_2| \end{pmatrix} \tag{9.1}$$

$$= \mathbb{1} - \begin{pmatrix} (|\Omega|+\phi)/|A_1| & -\phi/|A_2| \\ -\phi/|A_1| & \phi/|A_2| \end{pmatrix} \tag{9.2}$$

$$= \mathbb{1} - \frac{\phi}{|A_1|} \begin{pmatrix} |\Omega|/\phi+1 & -|A_1|/|A_2| \\ -1 & |A_1|/|A_2| \end{pmatrix}. \tag{9.3}$$

Note that for the natural decay, the weights $\mu_{\text{nat}}(A_1)$ and $\mu_{\text{nat}}(A_2)$ are simply given by the components of the long-lived Perron–Frobenius eigenvector of T_0. However, following Eq. (9.3), T_0 admits the same eigenvectors as the matrix

$$\frac{|A_1|}{\phi}(\mathbb{1}-T_0) = \begin{pmatrix} |\Omega|/\phi+1 & -|A_1|/|A_2| \\ -1 & |A_1|/|A_2| \end{pmatrix} \tag{9.4}$$

which only depends on the two ratios of $|\Omega|/\phi$ and $|A_1|/|A_2|$. In Fig. 9.2 we fix $|A_1|$, and thus, of course, also $|A_2|$ such that transition (i) from equipartition to localization for resonance states with $\gamma \approx \gamma_{\text{nat}}$ indeed depends exactly on the single parameter $|\Omega|/\phi$, only.

For completeness, we show that Eq. (8.57) accurately describes the localization transition (i) not only in the symmetric case $|A_1| = |A_2|$ but also for $|A_1| \neq |A_2|$, see Fig. 9.3. The figure is analogous to Fig. 9.2 using (a) $|A_1| = 2/3$ and (b) $|A_1| = 1/3$. Again, the classical localization of the natural CIM μ_{nat} perfectly describes the transition of quantum resonance states from equipartition, $\mu_{\text{nat}}(A_1) = |A_1|$, for $|\Omega| \ll \phi$ to localization in A_2, $\mu_{\text{nat}}(A_1) \approx 0$, for $|\Omega| \gg \phi$.

For a single quantum system, we found the localization transition (ii) from localization on region A_2 for long-lived resonance states (small γ) to localization on region A_1 for short-lived resonance states (large γ), Fig. 6.3. We again compute the localization of the corresponding γ-natural CIMs and compare the classical and quantum data in Fig. 9.4. In addition to determining $\mu_\gamma(A_1)$ from the analytical prediction, Eq. (8.57) (green line), we also plot the values for $\mu_\gamma(A_1)$ obtained by integration over the numerically determined measure μ_γ as described in Sec. 7.2.2 (black crosses). For the numerically determined measure, we use a uniform grid of $N_{\text{grid}} = 10^6$ points and approximate the backward trapped set Γ_{bwd} by $N_{\text{iter}} = 50$ steps. The two ways of computing $\mu_\gamma(A_1)$ perfectly match. Even more important, the classical localization of μ_γ displays precisely the same transition depending on γ as the quantum resonance states. Both localization transitions for chaotic resonance states introduced in Chap. 6 are

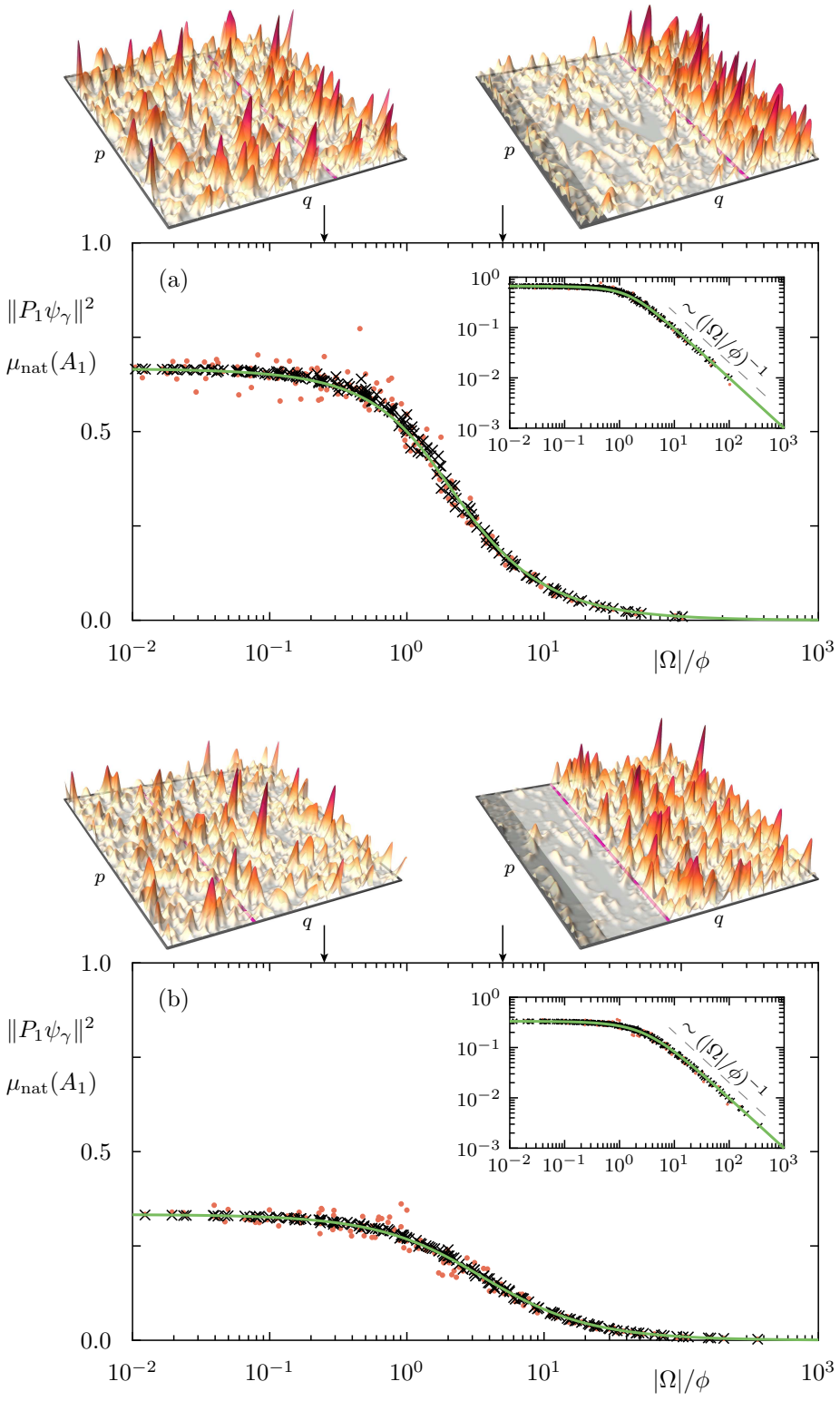

Figure 9.3. Weight $\|P_1\psi_\gamma\|^2$ (symbols) of resonance states on region A_1 vs ratio of size $|\Omega|$ of opening and flux ϕ across partial barrier for different parameters of the partial-barrier standard map ($10 \le \phi/h, |\Omega|/h \le 2048$; $h = 1/6000$; (a) $|A_1| = 2/3$ and (b) $|A_1| = 1/3$). Weight of state with γ closest to $\gamma_{\rm nat}$ (red points) and averaged over states with decay rates $\gamma \in [\gamma_{\rm nat}/1.1, \gamma_{\rm nat} \cdot 1.1]$ (black crosses). This is compared to the natural CIM $\mu_{\rm nat}(A_1)$ (Eq. (8.57), solid green line). Inset: Same data shown on double-logarithmic scale. Upper panels: Husimi representation of typical resonance states with $\gamma \approx \gamma_{\rm nat}$ for $h = 1/1000$, $\phi/h = 20$, and two values $|\Omega|/\phi$ indicated by arrows.

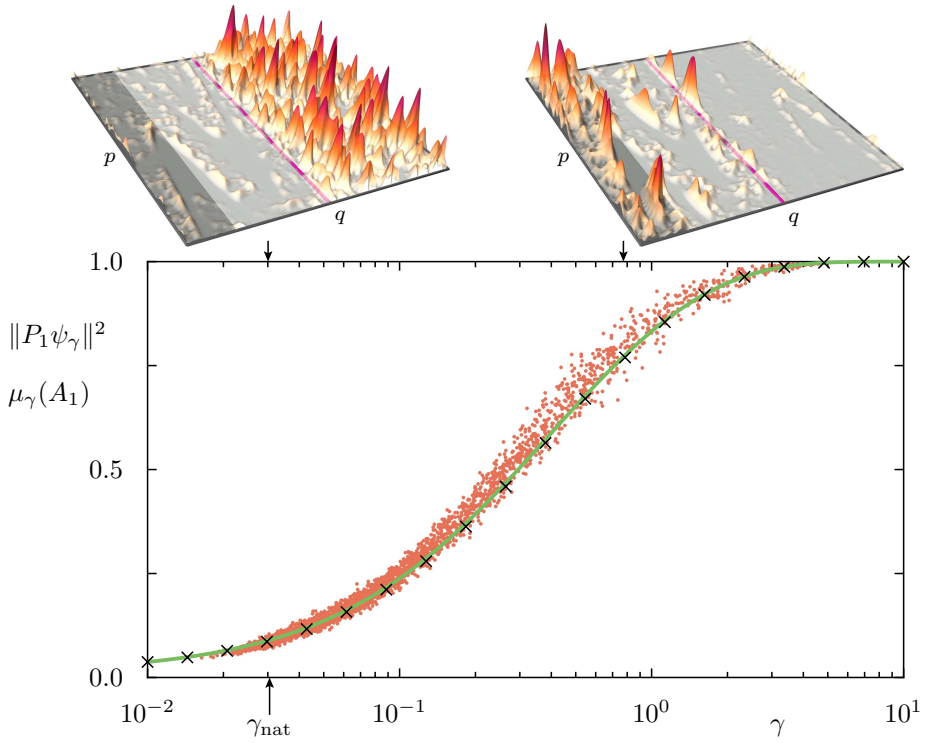

Figure 9.4. Weight $\|P_1\psi_\gamma\|^2$ (red points) of resonance states ψ_γ in region A_1 vs decay rate γ for the partial-barrier standard map ($\phi/h = 100$; $|\Omega|/h = 1000$; $|A_1| = 1/2$; $h = 1/6000$). This is compared to the γ-natural CIM $\mu_\gamma(A_1)$ computed according to Eq. (8.57) (solid green line), and by integration over numerical approximations (black crosses). Upper panels: Husimi representation of typical long-lived (left) and short-lived (right) resonance state for $h = 1/1000$ with γ values indicated by arrows.

thus of classical origin and the new class of γ-natural CIMs provides the appropriate classical counterpart. The case of asymmetric regions, $|A_1| \neq |A_2|$ is shown in Fig. 9.5 and nicely exhibits quantum-to-classical correspondence again. Nevertheless, Fig. 9.5(a) for $|A_1| = 2/3$ is the first example where the classical quantity $\mu_\gamma(A_1)$ deviates systematically from the mean behavior of $\|P_1\psi_\gamma\|^2$. Although the deviations are small, it seems as if the slope in the quantum data is a little larger than in the classical case. We emphasize that even though the quantum and classical data do not perfectly agree, it is still irrelevant whether the classical measures $\mu_\gamma(A_1)$ are computed by integration over numerical approximations (black crosses) or by the analytical prediction, Eq. (8.57), which is derived for the partial-barrier Baker map.

9.2 Deviations due to Quantum Suppression of Transport

In order to understand the origin of the small deviations between the classical and the quantum-mechanical localization values as observed in Fig. 9.5(a), we now consider the partial-barrier standard map for rather extreme parameter values. Recall that the study of classical CIMs

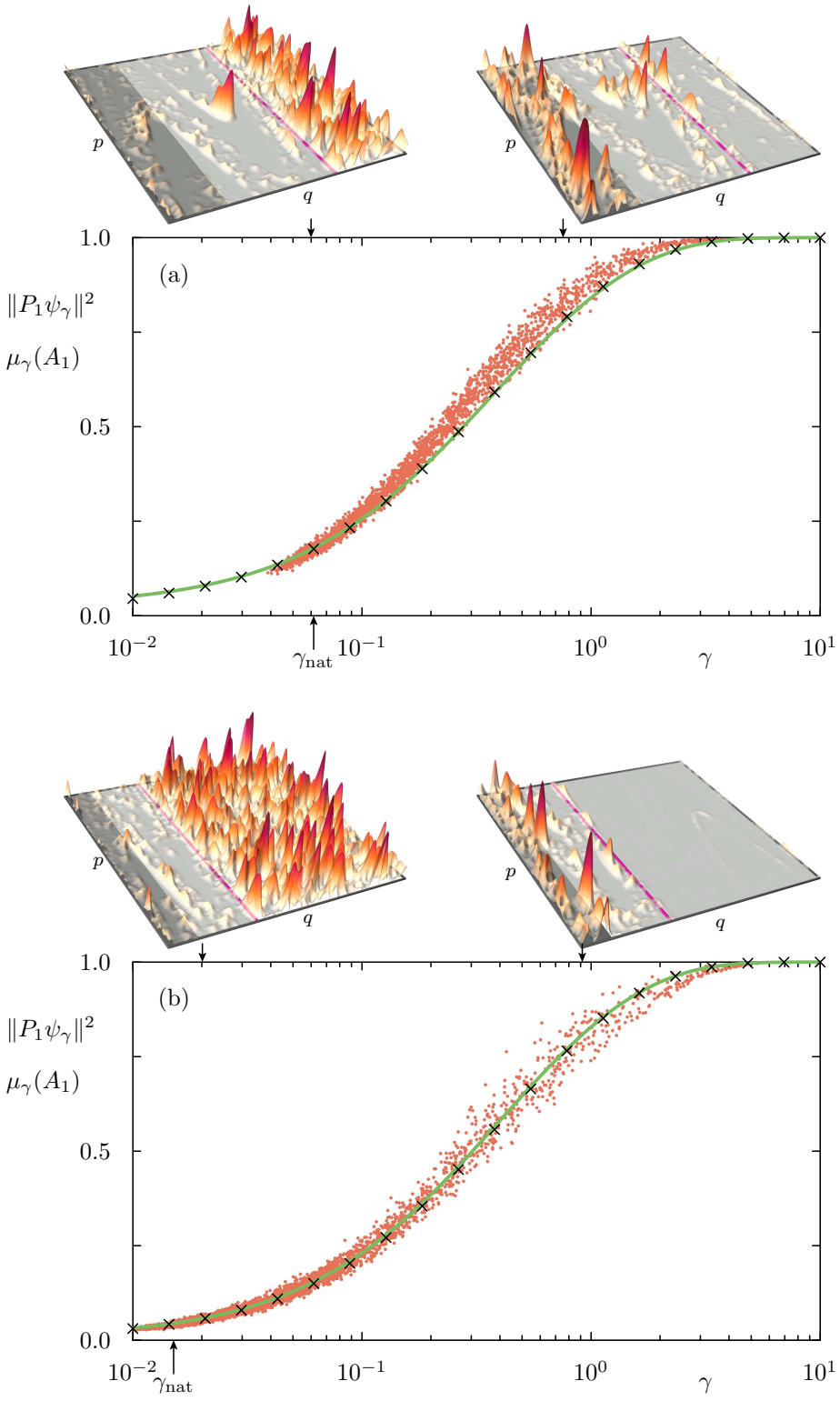

Figure 9.5. Weight $\|P_1\psi_\gamma\|^2$ (red points) of resonance states ψ_γ in region A_1 vs decay rate γ for the partial-barrier standard map ($\phi/h = 134$; $|\Omega|/h = 1334$; $h = 1/6000$; (a) $|A_1| = 2/3$ and (b) $|A_1| = 1/3$). This is compared to the γ-natural CIM $\mu_\gamma(A_1)$ computed according to Eq. (8.57) (solid green line), and by integration over numerical approximations (black crosses). Upper panels: Husimi representation of typical long-lived (left) and short-lived (right) resonance state for $h = 1/1000$ with γ values indicated by arrows.

is motivated by the fact that the localization transitions of quantum resonance states have been observed for values of $|\Omega| \gg h$ and $\phi \gg h$, where quantum effects should be negligible, cf. Chap. 6. Still, for sufficiently large values of h quantum deviations should be observable. Particularly the known quantum localization transition for a partial transport barrier in a closed system depending on ϕ/h, see Sec. 5.1, is expected to have a strong influence. Moreover, for sufficiently large h, it is quite reasonable to expect that the phase-space structure of quantum resonance states might differ from the structure of γ-natural CIMs on finer scales, even in systems without partial barriers. In such parameter regimes, we do not expect agreement between classical γ-natural CIMs and quantum resonance states. In fact, we will see below that the phenomenology of such quantum deviations is very characteristic. Moreover, it turns out that the regime where one might observe remnants of such quantum deviations can be surprisingly large, i.e., for parameters for which one could expect quantum-to-classical correspondence at first glance. For instance, we will attribute the deviations in Fig. 9.5(a) to not being sufficiently semiclassical although $h = 6000$ and $\phi/h = 134$, $|\Omega|/h = 1334$.

In Fig. 9.6, we again show the localization transition of a single quantum system depending on the decay rate γ of resonance states. We emphasize that the flux ϕ across the partial barrier is chosen very small, $\phi/h = 2$, such that we expect a strong impact of the quantum-mechanical suppression of transport across the partial barrier in view of the quantum localization transition known from closed system, Sec. 5.1. Indeed, the quantum data clearly differ from the corresponding classical localization. In particular, we observe that the quantum data nicely obeys the linear behavior

$$\|P_1\psi_\gamma\|^2 = \frac{\mu_{\mathrm{nat}}(A_1)}{\gamma_{\mathrm{nat}}}\,\gamma. \tag{9.5}$$

This can be seen on a linear, Fig. 9.6(a), and on a logarithmic scale of the ordinate, Fig. 9.6(b), over several orders of γ up to $\|P_1\psi_\gamma\|^2 \approx 1$. We point out that the quantum localization according to Eq. (9.5) coincides with the classical localization for $\gamma = \gamma_{\mathrm{nat}}$. In agreement with the fact that quantum transport across the partial barrier is suppressed for $\phi \approx h$, the localization of resonance states is enhanced compared to the classical localization. That means, a quantum resonance state for which the corresponding classical γ-natural CIM localizes in A_1 has quantum mechanically enhanced weight in A_1 and vice versa for A_2. The transition takes place at the natural decay rate, which corresponds to a CIM with constant measure on its support. Note that Eq. (9.5) is merely a numerical observation the verification and explanation of which remains for future studies.

The enhancement of localization due the quantum suppression of transport is also supported by the quantum and classical phase-space distribution shown in Fig. 9.7. For the partial-barrier standard map with $\phi/h = 2$ and $|\Omega|/h = 16$ the deviations between quantum

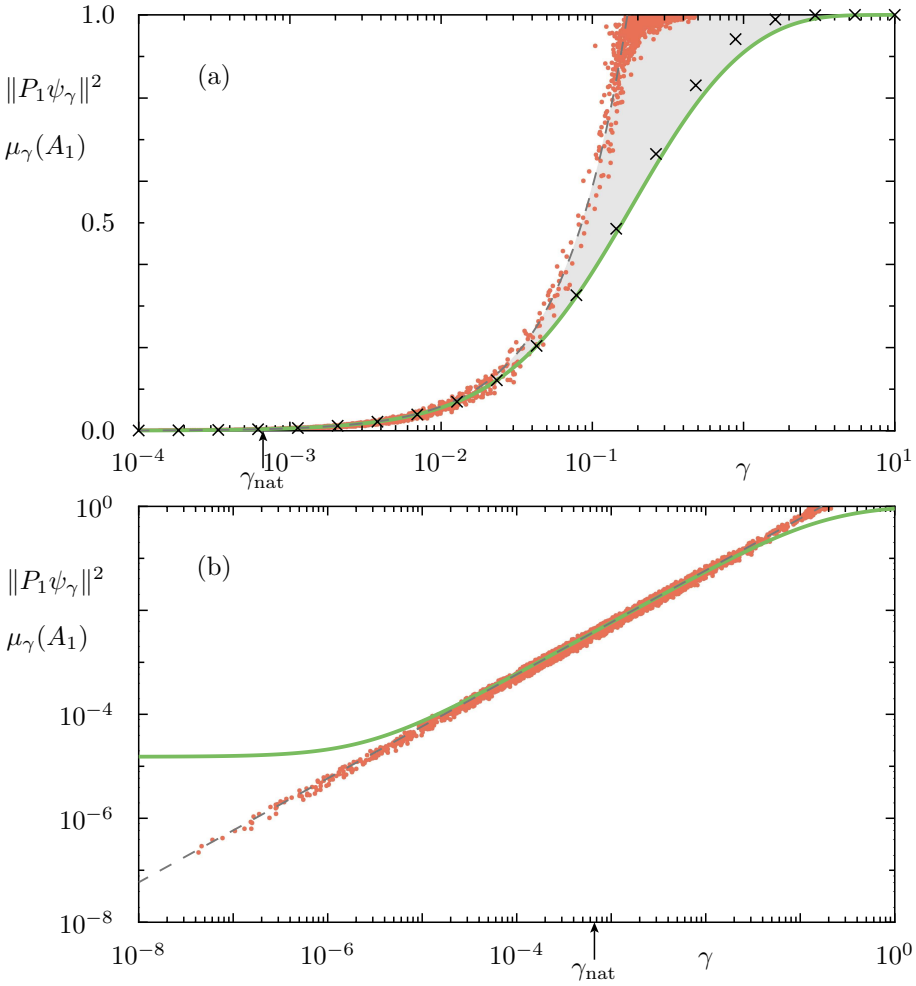

Figure 9.6. Weight $\|P_1\psi_\gamma\|^2$ (red points) of resonance states ψ_γ in region A_1 vs decay rate γ for the partial-barrier standard map ($\phi/h = 2$; $|\Omega|/h = 512$; $|A_1| = 1/2$; $h = 1/6000$) for linear ordinate (a) and for logarithmic ordinate (b). This is compared to the γ-natural CIM $\mu_\gamma(A_1)$ [according to Eq. (8.57) (solid green line); by integration over numerical approximations ($N_{\text{grid}} = 10^6$, $N_{\text{iter}} = 3000$; black crosses)] and compared to the linear scaling according to Eq. (9.5) (dashed gray line).

and classical localization are comparable with the deviations in Fig. 9.6. We choose the decay rate $\gamma = \gamma_{\text{nat}}/\mu_{\text{nat}}(A_1) \approx 10\,\gamma_{\text{nat}}$ corresponding to the decay rate where $\|P_1\psi_\gamma\|^2$ reaches its maximum according to Eq. (9.5). For this example the numerically determined weights in A_1 are $\|P_1\psi_\gamma\|^2 \approx 0.807$ and $\mu_\gamma(A_1) \approx 0.537$. The weight of the quantum resonance state, Fig. 9.7(a), is enhanced or lowered over the entire region A_1 or A_2, respectively, compared to the classical γ-natural CIM, Fig. 9.7(b). In particular, the larger quantum-mechanical weight $\|P_1\psi_\gamma\|^2$ does not arise from new types of localization on characteristic subsets of the fractal trapped sets or from pronounced peaks. Instead, the localization enhancement acts on the entire region on each side of the partial barrier.

Coming back to Fig. 9.6 for the example of a system with extremely small flux $\phi = 1/3000$,

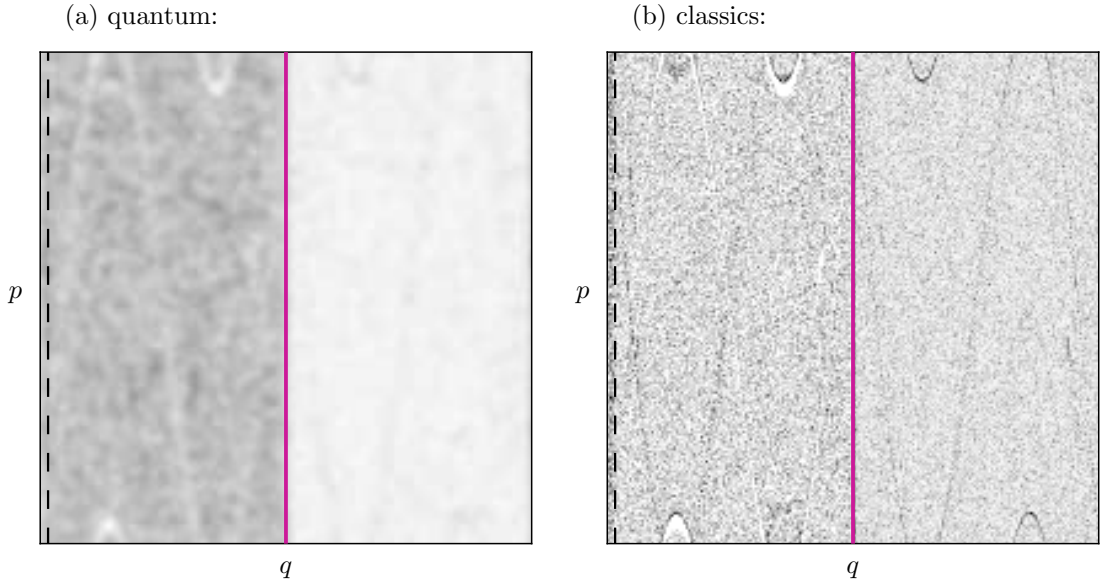

Figure 9.7. (a) Average Husimi distribution of resonance states for the partial-barrier standard map ($\phi/h = 2$; $|\Omega|/h = 16$; $|A_1| = 1/2$; $h = 1/1000$) with $\gamma \in [(\gamma_{\mathrm{nat}}/\mu_{\mathrm{nat}}(A_1))/1.2, (\gamma_{\mathrm{nat}}/\mu_{\mathrm{nat}}(A_1)) \cdot 1.2]$ (77 states). (b) Approximate γ-natural CIM for $\gamma = \gamma_{\mathrm{nat}}/\mu_{\mathrm{nat}}(A_1)$. The phase-space distributions in (a) and (b) are plotted with a mutual color scale; the dashed black line indicates the boundary of the opening Ω.

we also observe slightly different classical expectations around $\gamma \approx 1.0$ (green line vs black crosses). However, it is not clear whether this results from a failure of Eq. (8.57) or whether the numerical approximation of μ_γ is not sufficiently accurate ($N_{\mathrm{grid}} = 10^6$, $N_{\mathrm{iter}} = 3000$). The very different escape probabilities from regions A_1 and A_2 indicate that, in fact, the numerical approximation of μ_γ with the algorithm presented in Sec. 7.2.2 is not sufficiently accurate here. Still, since both classical estimates are close to each other and clearly off the quantum data, the deviations between the classical and the quantum localization certainly cannot be attributed to an insufficient approximation of the classical γ-natural CIMs.

Let us consider another example of the same kind of localization transition. In Fig. 9.8 we choose a value of $\phi/h = 16$. Although from the closed system's point of view, the quantum-mechanical influence of the partial barrier should be negligible, $\phi \gg h$, cf. Fig. 5.2, we observe a similar localization for quantum resonance states as in Fig. 9.6. Even though the quantum data do not follow the linear behavior from Eq. (9.5) as in the previous case, the tendency is evident. Roughly speaking, the quantum data are somewhere in between the deeply quantum-mechanical regime (dashed gray line), Eq. (9.5), and the semiclassical behavior (solid green line) in terms of the localization of γ-natural CIMs. Moreover, it seems as though there are two different ways of approaching the semiclassical expectation distinguishing between decay rates $\gamma \gtrsim \gamma_{\mathrm{nat}}$ and $\gamma \lesssim \gamma_{\mathrm{nat}}$. While one observes a systematic intermediate behavior for $\gamma \gtrsim \gamma_{\mathrm{nat}}$, Fig. 9.8(a), the resonances for $\gamma \lesssim \gamma_{\mathrm{nat}}$ simply disappear, Fig. 9.8(b). In particular,

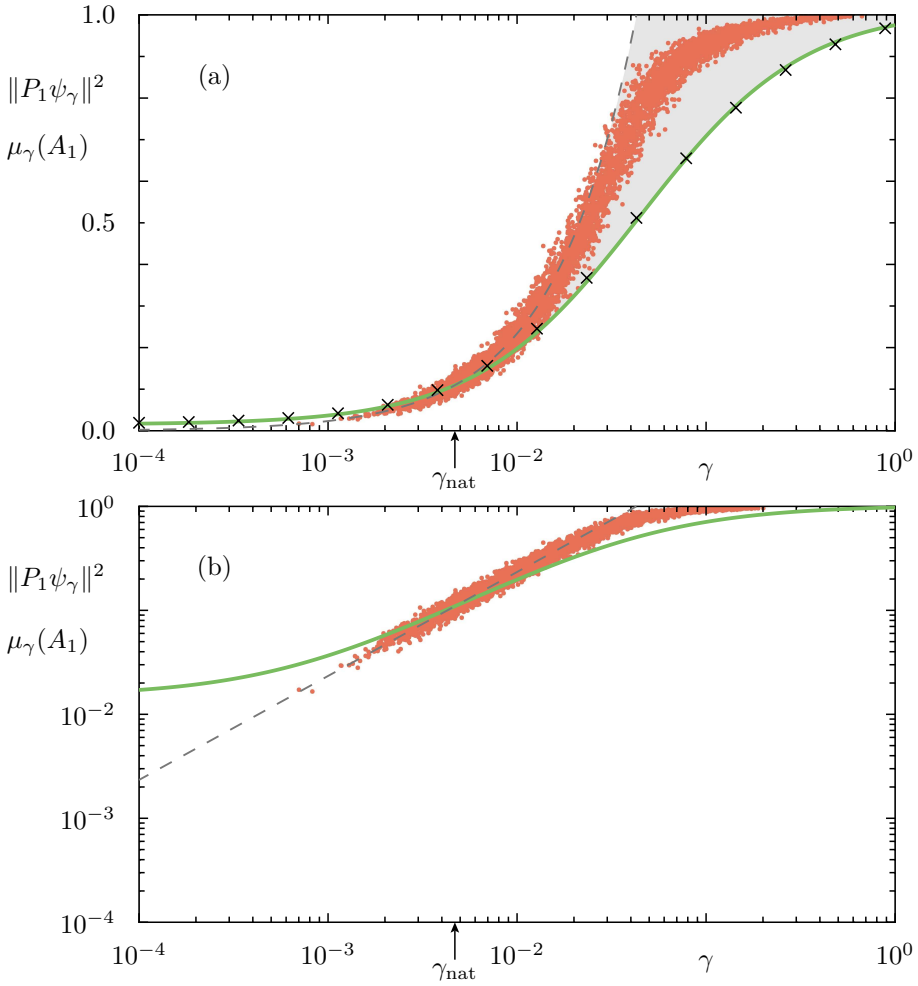

Figure 9.8. Weight $\|P_1\psi_\gamma\|^2$ (red points) of resonance states ψ_γ in region A_1 vs decay rate γ for the partial-barrier standard map ($\phi/h = 16$; $|\Omega|/h = 128$; $|A_1| = 1/2$; $h = 1/6000$) for linear ordinate (a) and for logarithmic ordinate (b). This is compared to the γ-natural CIM $\mu_\gamma(A_1)$ [according to Eq. (8.57) (solid green line); by integration over numerical approximations ($N_{\text{grid}} = 10^6$, $N_{\text{iter}} = 100$; black crosses)] and compared to the linear scaling according to Eq. (9.5) (dashed gray line).

the quantum data for $\gamma \lesssim \gamma_{\text{nat}}$ always seem to follow the deeply quantum-mechanical behavior and never obey the classical expectation (green line) but the smaller h the less resonances exist in this regime.

Let us investigate this transition from the deeply quantum-mechanical behavior to the semiclassical behavior in a little more detail. To this end, we investigate yet another example in Fig. 9.9, which allows to observe this transition directly in a single system by varying the size h of Planck's cell on numerically feasible scales. First, for $h = 1/375$ the transition region of the partial barrier is quantum mechanically not well resolved, $\phi/h = 2$. Accordingly, the localization of quantum resonance states basically follows the linear behavior from Eq. (9.5), see Fig. 9.9(a) for $\gamma > \gamma_{\text{nat}}$ and Fig. 9.9(c) for $\gamma < \gamma_{\text{nat}}$. However, by decreasing the size h of

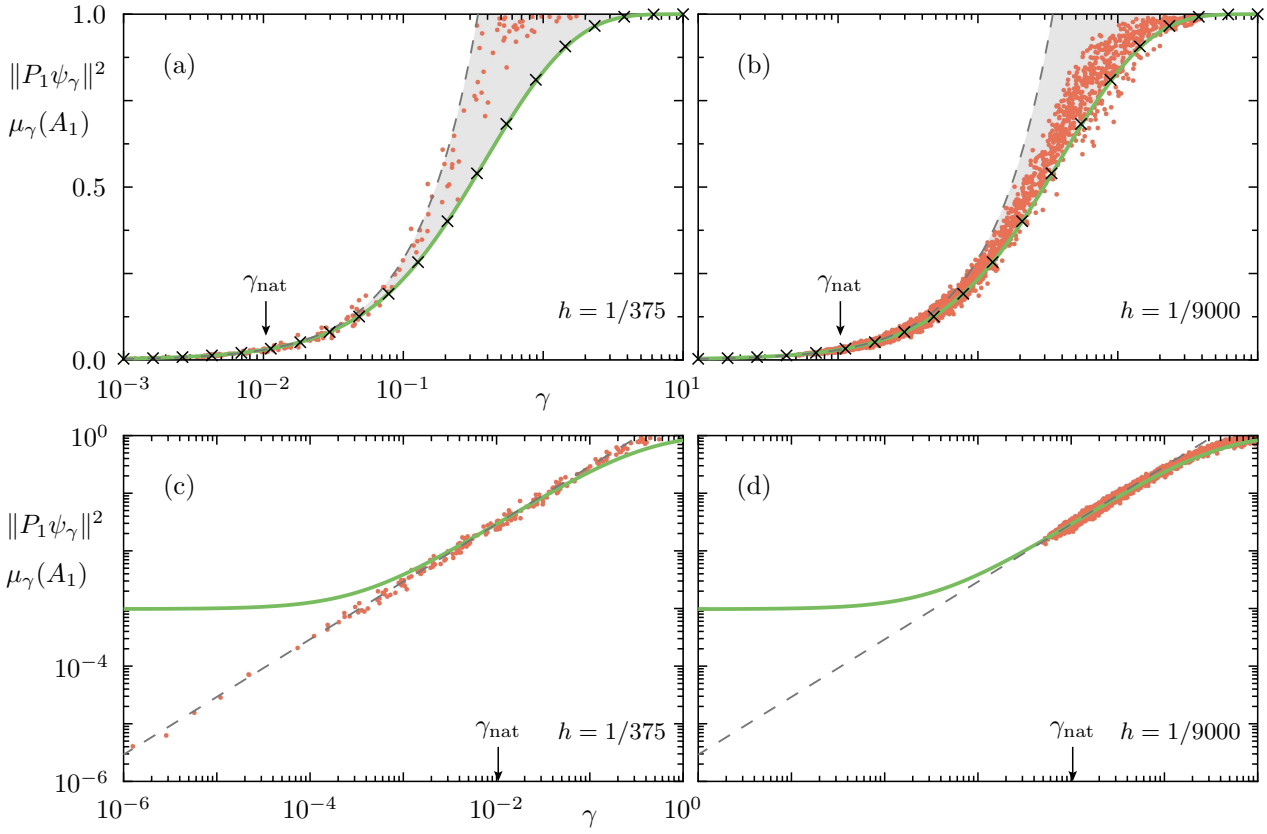

Figure 9.9. Weight $\|P_1\psi_\gamma\|^2$ (red points) of resonance states ψ_γ in region A_1 vs decay rate γ for the partial-barrier standard map ($\phi = 2/375$; $|\Omega| = 64/375$; $|A_1| = 1/2$) for two different values of h as specified. The data are shown with linear ordinate (a, b; shared axes) and with logarithmic ordinate (c, d; shared axes). This is compared to the γ-natural CIM $\mu_\gamma(A_1)$ [according to Eq. (8.57) (solid green line); by integration over numerical approximations ($N_{\text{grid}} = 10^6$, $N_{\text{iter}} = 100$; black crosses)] and compared to the linear scaling according to Eq. (9.5) (dashed gray line).

Planck's cell by a factor of 24 to $h = 1/9000$, such that $\phi/h = 48$ the quantum-mechanical influence of the partial barrier is particularly reduced and the localization approaches the semiclassical expectation, see Fig. 9.9(b, d). The shown transition confirms our previous observation, Fig. 9.8, of two different regimes: For $\gamma \gtrsim \gamma_{\text{nat}}$ the quantum data systematically pass the gray shaded region between the deeply quantum-mechanical regime, Eq. (9.5), and the localization of γ-natural CIMs, Eq. (8.57). For $\gamma \lesssim \gamma_{\text{nat}}$, the resonances seem to vanish in the semiclassical limit.

The statement that the localization of quantum resonance states due to the partial barrier semiclassically follows the localization of corresponding γ-natural CIMs is further supported by Fig. 9.10. Here, we compare the localization transition of two systems with the same values of $|\Omega|/\phi$ and $|A_1|$. However, in Fig. 9.10(a), ϕ and $|\Omega|$ are both in the regime where we expect quantum suppression of transport in view of the closed system's theory, $\phi/h = 2$, $|\Omega|/h = 8$,

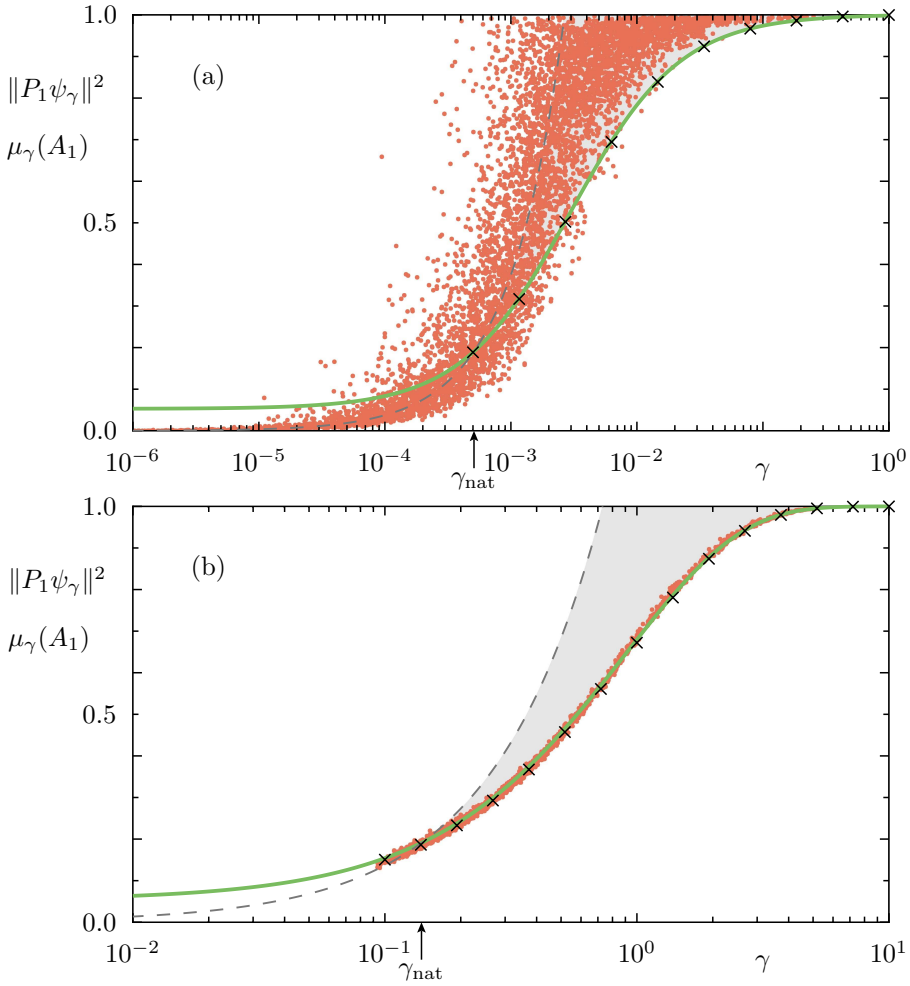

Figure 9.10. Weight $\|P_1\psi_\gamma\|^2$ (red points) of resonance states ψ_γ in region A_1 vs decay rate γ for the partial-barrier standard map for (a) $\phi/h = 2$, $|\Omega|/h = 8$, and (b) $\phi/h = 512$, $|\Omega|/h = 2048$ with $|A_1| = 1/2$ and $h = 1/6000$ in both cases. This is compared to the γ-natural CIM $\mu_\gamma(A_1)$ [according to Eq. (8.57) (solid green line); by integration over numerical approximations ($N_{\text{grid}} = 10^6$, (a) $N_{\text{iter}} = 3000$ and (b) $N_{\text{iter}} = 10$; black crosses)] and compared to the linear scaling according to Eq. (9.5) (dashed gray line).

cf. Sec. 5.1. Accordingly, the weight of quantum resonance states $\|P_1\psi_\gamma\|^2$ basically follows the linear behavior, Eq. (9.5), which we interpret as the deeply quantum-mechanical regime. We attribute the pronounced width of the quantum data around their mean behavior to the small ratio of $|\Omega|/h$ which has been observed in other examples as well (not shown). In Fig. 9.10(b) where the quantum resolution of the flux ϕ and the opening Ω is improved by a factor of 256, i.e., $\phi/h = 512$ and $|\Omega|/h = 2048$, we actually observe perfect correspondence between the localization of quantum resonance states and the localization of γ-natural CIMs in dependence of their decay rates γ. Note that the weight $\mu_{\text{nat}}(A_1)$ of the natural CIM is the same for (a) and (b) according to Eq. (8.57), as we choose the same values for $|\Omega|/\phi$ and $|A_1|$, but the natural decay rate γ_{nat} differs.

Even though this study indicates that the localization of chaotic resonance states with respect to a partial barrier, indeed, approaches the classical localization of γ-natural CIMs for sufficiently small values of h, it also demonstrates that the convergence is rather slow. While for closed systems one finds quantum-mechanical influence for the localization due to partial barrier roughly up to $\phi/h \approx 10$, the quantum influence for open systems seems to extend to even larger ratios of ϕ/h. A more careful analysis should take into account results on the spectral gap [196] and on super sharp resonances [197].

9.3 Standard Map

So far, we have seen that our classical theory for the localization of chaotic resonance states proves correct for the partial-barrier Baker map and the partial-barrier standard map in the semiclassical regime. Even the analytical result for the localization of γ-natural CIMs with respect to a partial barrier, Eq. (8.57), which was rigorously derived for the partial-barrier Baker map, turns out to perfectly describe the localization of γ-natural CIMs also for the example of the partial-barrier standard map. Still, in order to validate our approach more generally we now examine whether the localization of chaotic resonance states semiclassically follows the localization of γ-natural CIMs also for the paradigmatic standard map ($\kappa = 2.9$) with a generic mixed phase space, cf. Sec. 3.1.

Let us consider the standard map with fixed opening $\Omega = \big([0, |\Omega|/2) \cup [1 - |\Omega|/2, 1)\big) \times [-\frac{1}{2}, \frac{1}{2})$, $|\Omega| = 0.1$, i.e., two vertical stripes on the left and right edge of the phase-space cell of width 0.05 each. As a first qualitative verification of quantum-to-classical correspondence, we compare the average Husimi distribution of resonance states with decay rate $\gamma \approx 0.12$ with the numerically determined phase-space density of the corresponding γ-natural CIM in Fig. 9.11. We observe that the quantum and classical distributions are supported by the same sets, i.e., the chaotic part of the backward trapped set, and thus, are zero on the forward escaping sets and the regular regions. Moreover, the location of high and low density regions match. Owing to the involved fractal structure of the trapped sets we show the same quantum and classical phase-space distributions from Fig. 9.11 again in Fig. 9.12(c, d) in top view to better demonstrate their agreement even on finer scales of the fractal sets. Indeed, the dark and bright regions of large or low intensity nicely match up the quantum resolution limit. This correspondence is essentially also confirmed for chaotic resonance states and γ-natural CIMs of other decay rate in Fig. 9.12(a, b) for $\gamma = 0.05$ and in Fig. 9.12(e, f) for $\gamma = 0.2$. However, when examining these two examples very closely they already indicate the limitations of quantum-to-classical correspondence: In Fig. 9.12(a, b) for $\gamma = 0.05$ the quantum resonance states (a) exhibit an overall enhanced localization behind the outer partial barrier. This phenomenon agrees with the deviations already observed in Sec. 9.2. The flux across this dominant partial

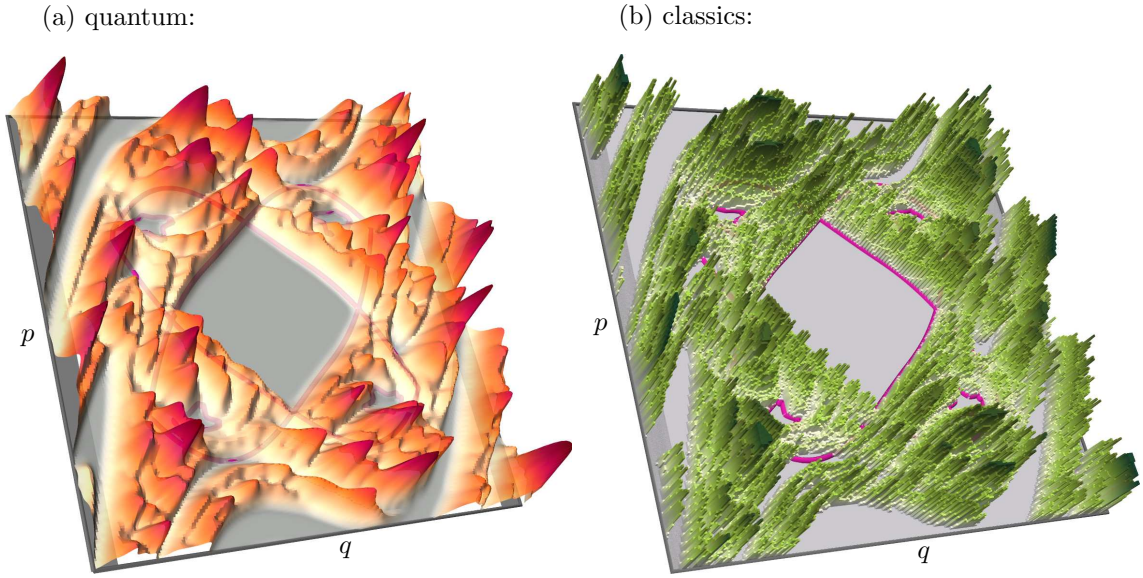

Figure 9.11. (a) Average Husimi distribution of resonance states for the standard map ($\kappa = 2.9$; $|\Omega| = 0.1$; $h = 1/1000$) with $\gamma \in [0.12/1.25, 0.12{\cdot}1.25]$ (93 states). (b) Approximate γ-natural CIM for $\gamma = 0.12$.

barrier is quantum mechanically not sufficiently resolved, $\phi/h \approx 12$. Thus, the enhancement of localization is due to the quantum-mechanical suppression of transport across the partial barrier. In Fig. 9.12(e, f) for $\gamma = 0.2$, we observe a new kind of deviation. The quantum resonance states show pronounced peaks on certain lobes of the backward trapped set. This quantum effect is not directly related to the partial barrier. It is rather related to the question: How does quantum mechanics resolve fractal sets? This issue is beyond the scope of this thesis and left for future studies. We will comment on this again in the outlook in Chap. 11. Note that this quantum localization on fine scales of the fractal turns out to be irrelevant when considering only the weights on each side of the partial barrier for the examples studied in this work.

Let us now focus on the localization with respect to the main partial barrier ($\phi \approx 0.0126$; Fig. 9.13 inset: magenta line) in order to quantitatively study quantum-to-classical correspondence. The dominant partial barrier decomposes phase space into the outer region A_1 (Fig. 9.13 inset: medium gray shaded) of area $|A_1| \approx 0.6664$, and the inner region A_2 (Fig. 9.13 inset: light gray shaded) of area $|A_2| \approx 0.2061$. The next hierarchical level is well separated on the numerical scales considered. The flux across the partial barrier around the island chain of period four (Fig. 9.13 inset: red lines) is smaller by a factor of about 474; the flux across the next partial barrier towards the central regular island (Fig. 9.13 inset: pink line) is even smaller. For the standard map with opening Ω, we compute the Husimi weight $\|P_1\psi_\gamma\|^2$ of each chaotic resonance state within A_1. Regular and deeper hierarchical states having less than 50% of their weight within A_1 and A_2 are discarded. As some of the remaining chaotic

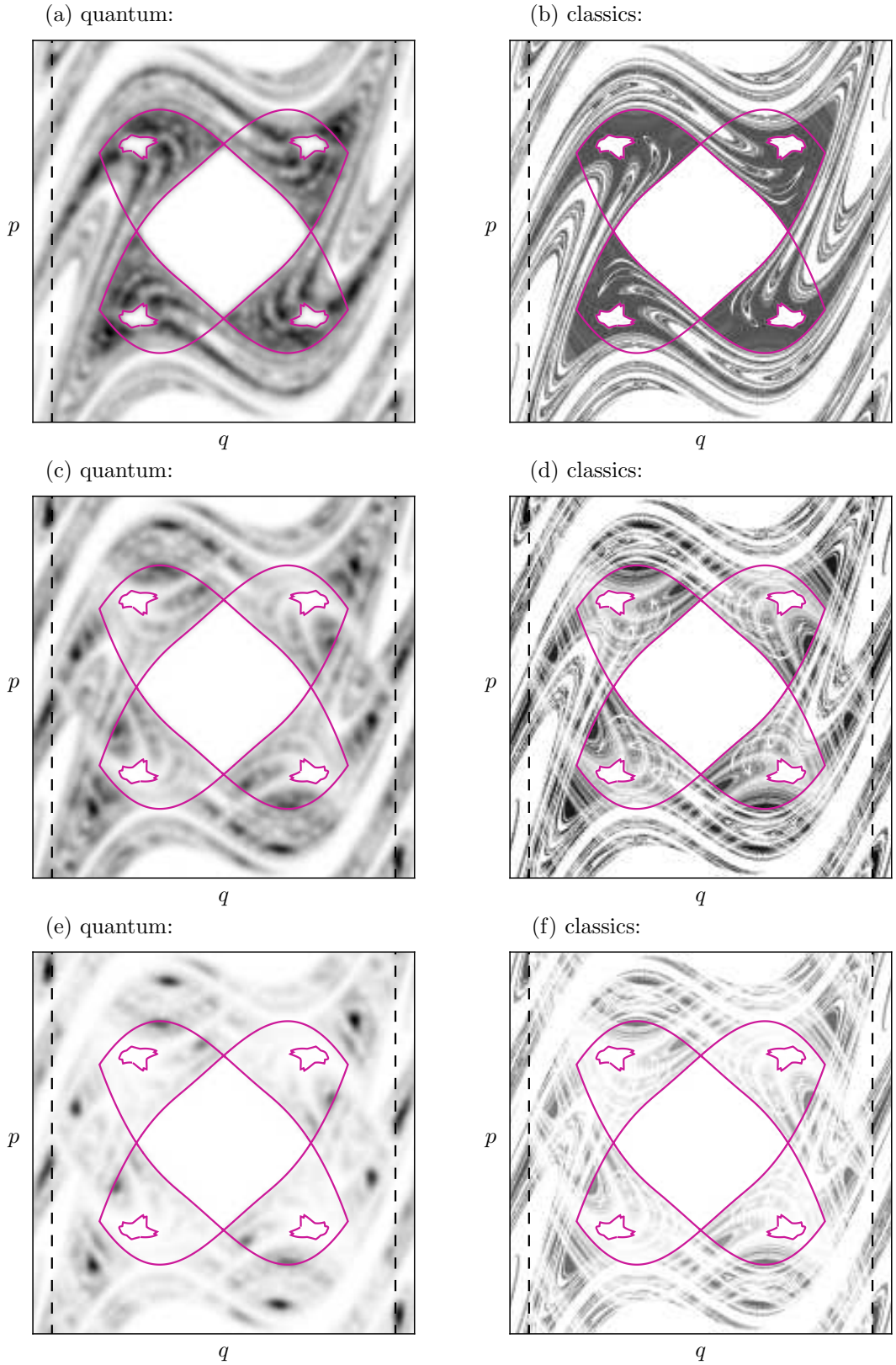

Figure 9.12. (a, c, e) Average Husimi distribution of resonance states for the standard map ($\kappa = 2.9$; $|\Omega| = 0.1$; $h = 1/1000$) with (a) $\gamma \in [0.05/1.25, 0.05 \cdot 1.25]$ (88 states), (c) $\gamma \in [0.12/1.25, 0.12 \cdot 1.25]$ (93 states), and (e) $\gamma \in [0.2/1.25, 0.2 \cdot 1.25]$ (77 states). (b, d, f) Approximate γ-natural CIM for (b) $\gamma = 0.05$, (d) $\gamma = 0.12$, and (f) $\gamma = 0.2$. Mutual gray color scale for corresponding quantum and classical phase-space distributions used.

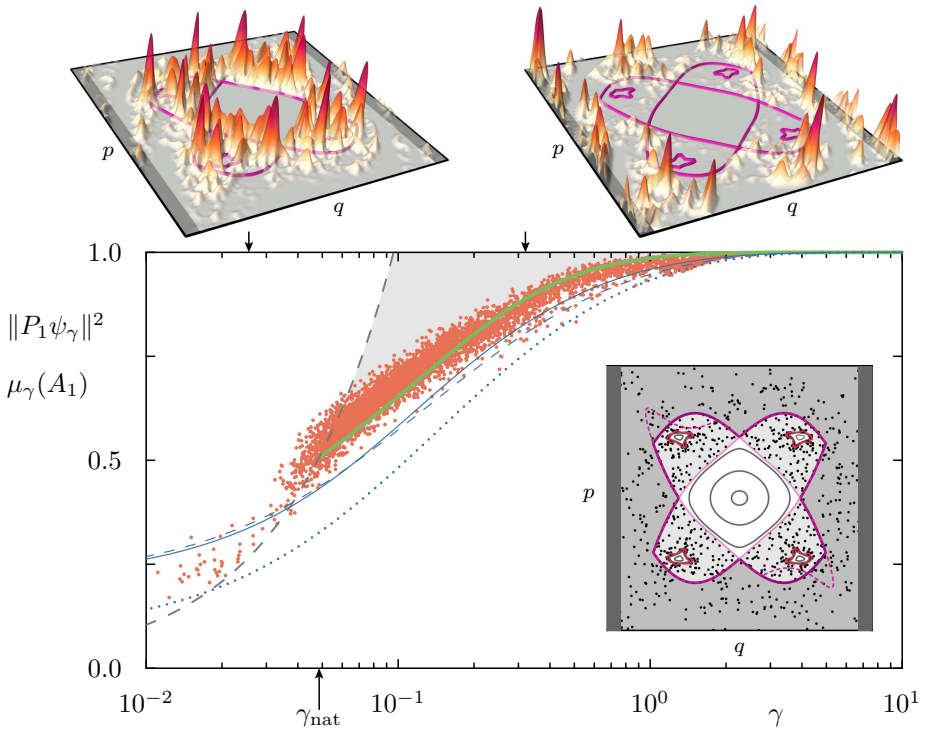

Figure 9.13. Weight $\|P_1\psi_\gamma\|^2$ (red points) of chaotic resonance states ψ_γ in region A_1 vs decay rate γ for the standard map at $\kappa = 2.9$, with $|A_1| \approx 0.6664$, $|A_2| \approx 0.2061$, $\phi \approx 0.0126$, $|\Omega| = 0.1$, and $h = 1/10000$. This is compared to the γ-natural CIM $\mu_\gamma(A_1)$ determined by integration over numerical approximations ($N_{\text{grid}} = 10^6$, $N_{\text{iter}} = 50$; solid green line), according to Eq. (8.57) (dotted blue line), and by semianalytical generalizations of Eq. (8.57) by computing T_{nat} numerically (dashed blue line) and by computing $|A_1 \cap T^{-n}(\Omega)|$ numerically (solid blue line). In addition, the localization is compared to the linear scaling according to Eq. (9.5) (dashed gray line). Inset: Phase space of the standard map with regular and chaotic regions, illustrating regions A_1 (medium gray shaded), A_2 (light gray shaded) on either side of the main partial barrier (thick solid magenta line), and opening Ω (dark gray shaded). Upper panels: Husimi representation of typical long-lived (left) and short-lived (right) resonance state for $h = 1/1000$ with γ values indicated by arrows.

resonance states still have significant contribution outside of $A_1 \cup A_2$, we renormalize them such that $\|P_1\psi_\gamma\|^2 + \|P_2\psi_\gamma\|^2 = 1$. Qualitatively, we again find the localization transition from resonance states which localize on A_2 for small γ to resonance states localizing on A_1 for large γ, see Fig. 9.13. Quantitatively, the transition is well described by the weight $\mu_\gamma(A_1)$ of corresponding γ-natural CIMs which are computed by integration over numerically approximated measures as described in Sec. 7.2.2 (solid green line). The classical estimate according to Eq. (8.57) (dotted blue line) also captures the basic behavior of the localization transition although the agreement with the numerically determined measures (solid green line) is not as good as for the partial-barrier standard map for instance. Before discussing this discrepancy between analytically and numerically determined weights $\mu_\gamma(A_1)$ in more detail, we point out that also the linear behavior related to the deeply quantum-mechanical regime (dashed gray

line), Eq. (9.5), seems to be relevant for the localization transition. This can be seen for resonance states with $\gamma \lesssim \gamma_{\mathrm{nat}}$ which scale different than the states with $\gamma \gtrsim \gamma_{\mathrm{nat}}$.

For the partial-barrier Baker map, Eq. (8.57) together with Eq. (8.45) for T_0 exactly describes the localization of γ-natural CIMs in terms of the weight $\mu_\gamma(A_1)$. For other systems like the standard map, however, Eq. (8.57) is in general not valid. This is due to following three steps in its derivation, Sec. 8.4:

(i) For the partial-barrier Baker map the measure $\mu_{\mathrm{nat}}(A_1)$ is precisely given by the components of the Perron–Frobenius eigenvector of the 2×2 matrix T_0, Eq. (8.45). The matrix T_0 contains the transition probabilities to get from one side of the partial barrier to the other side or to escape from the system within one iteration for an initially uniform phase-space distribution. However, to ensure that the components of the Perron–Frobenius eigenvector of T_0 provide the weights $\mu_{\mathrm{nat}}(A_1)$ (and $\mu_{\mathrm{nat}}(A_2)$) for generic maps these transition probabilities must correspond to using the true natural CIM μ_{nat} as initial phase-space distribution instead of the uniform one. We call this adapted 2×2 transition matrix T_{nat}. It can be achieved numerically, for instance, by the one-step iteration of a numerically approximated backward trapped set. In view of the localization transition of the standard map, Fig. 9.13, the improvement when using T_{nat} instead of T_0 can be seen by comparing the dashed and the dotted blue line.

(ii) For the partial-barrier Baker map, the weight $\mu_{\mathrm{nat}}\big(A_k \cap T^{-n}(\Omega)\big)$ of μ_{nat} within the forward escaping sets $T^{-n}(\Omega)$ associated with A_1 or A_2 follows from the exact relation

$$\frac{\mu_{\mathrm{nat}}\big(A_k \cap T^{-n}(\Omega)\big)}{\mu_{\mathrm{nat}}\big(A_k\big)} = \frac{|A_k \cap T^{-n}(\Omega)|}{|A_k|}, \tag{9.6}$$

cf. Eq. (8.52). This proportionality is a direct consequence of the Cartesian product structure of stable and unstable manifolds within each region A_k. It seems reasonable to expect that this relation can be generalized to generic systems for which stable and unstable manifolds also display a product structure. To this end, the argument needs to be revised in the natural coordinates of the invariant manifolds.

(iii) For the partial-barrier Baker map the Lebesgue measure $|A_k \cap T^{-n}(\Omega)|$ of the forward escaping set $T^{-n}(\Omega)$ within A_k is given by Eq. (8.53),

$$\begin{pmatrix} |A_1 \cap T^{-n}(\Omega)| \\ |A_2 \cap T^{-n}(\Omega)| \end{pmatrix} = T_0^n \begin{pmatrix} |\Omega| \\ 0 \end{pmatrix}. \tag{9.7}$$

Even when replacing T_0 by T_{nat}, cf. step (i), this relation is not necessarily correct for generic systems. For large n the iteration of Ω will lead to a phase-space distribution given by the natural CIM of the inverse dynamics. For this, recall that any generic phase-space distribution converges towards the natural CIM under time evolution which in this case is the backward

iteration, see Sec. 7.2.2. Hence, asymptotically the transition of weights from one side of the partial barrier to the other when iterating Ω is indeed given by the single matrix corresponding the natural measure which may be related to T_{nat} by time-reversal invariance. However, initially the iteration of Ω is not necessarily described by one and the same matrix for different iteration steps n. In contrast, the transition probabilities to go from one side of the partial barrier to the other when iterating Ω need to be investigated individually for each time step up to the asymptotic regime where these transition probabilities remain constant. In view of the localization transition of the standard map, Fig. 9.13, the improvement when using this adapted approach and not T_{nat} for all steps n can be seen by comparing the solid and the dashed blue line. At least for the standard map, using the precise iteration of Ω seems not to be specifically relevant. This impression is also supported by the explicit values of the transition probabilities: The absolute difference in the initial and asymptotic transition probabilities is below 0.05 already in the first iteration, and at most about 0.01 in the fourth iteration.

Since the steps (i–iii) are the only approximations made when applying Eq. (8.57) to the generic standard map, and as we numerically took care of steps (i) and (iii), the difference between the full numerical result, solid green line in Fig. 9.13, and the semianalytical result (solid blue line) is attributed to the approximation in step (ii).

Summary of Central Results

This chapter concludes the central part of this thesis, i.e., Chaps. 6–9. Let us therefore briefly summarize the crucial points. We observe two transitions for the localization of chaotic resonance states due to a partial barrier: (i) A transition from equipartition to localization when opening the system, and (ii) a transition from localization on one side of the partial barrier to the other for increasing decay rates of the resonance states. Both transitions take place also in the semiclassical regime, meaning that the exchange region of the partial barrier is quantum mechanically well resolved. This has two implications: First, partial barriers are more influential in open quantum systems than in closed ones, as in the latter case, eigenstates are semiclassically equipartitioned with respect to the partial barrier as if there were no partial barrier at all. Secondly, a classical origin of the observed localization transitions is suspected. We introduce the new class of γ-natural CIMs and demonstrate quantum-to-classical correspondence with chaotic resonance states for the partial-barrier Baker map, the partial-barrier standard map, and the generic standard map with a mixed phase space. In particular, the observed localization transitions are nicely described by the localization of the corresponding classical measures, which thus shows that the transitions are indeed of classical origin. A useful analytical prediction, Eq. (8.57), for the weights of γ-natural CIMs on each side of a partial barrier is rigorously derived for the partial-barrier Baker map. It turns out that

Eq. (8.57) provides excellent results even when applied to the partial-barrier standard map and works reasonably well also for the standard map. If the flux across the partial barrier is not sufficiently well resolved by Planck cells, we observe a quantum-mechanical enhancement of localization compared to the classical expectation.

Chapter 10

Hierarchical Fractal Weyl Laws

In this chapter we present an important application of the localization of chaotic resonance states due to a partial barrier. We show that the number of resonance states that are predominantly located on either side of the partial barrier obeys an individual effective fractal Weyl law. To this end, we first review the Weyl law for closed systems and the fractal Weyl law for globally chaotic systems in Sec. 10.1. In Sec. 10.2 we generalize the fractal Weyl law to the partial-barrier Baker map and particularly focus on the influence of the partial barrier. It turns out that the repeller effectively exhibits different fractal dimensions on each side of the partial barrier. Quantum mechanically, this implies effectively different fractal Weyl laws for the number of resonance states associated with each side. In Sec. 10.3 we demonstrate that these individual fractal Weyl laws can also be found for the generic standard map. For the partial-barrier standard map with two partial barriers we can show numerically that the individual fractal Weyl laws are even present in systems with multiple partial barriers. We then discuss the presence of a hierarchy of fractal Weyl laws for generic systems with an infinity hierarchy of partial barriers. We conclude by discussing the relation of these hierarchical fractal Weyl laws with other fractional Weyl laws. The main results of this chapter have first been reported in Ref. [33].

10.1 Weyl Law and Fractal Weyl Law

Consider the free stationary Schrödinger equation,

$$(\triangle + k^2)\psi = 0, \tag{10.1}$$

for the Hamiltonian $H = -(\hbar^2/2m)\triangle$ on a bounded domain $G \subset \mathbb{R}^f$ with Dirichlet boundary condition $\psi|_{\partial G} = 0$ for the piecewise smooth boundary ∂G and $k^2 = 2mE/\hbar^2$. Weyl's law [77,

78] describes the asymptotic distribution of the eigenvalues E_n of H. It states that the number

$$N(E) := \#\{E_n \in \sigma(H) \,:\, E_n \leq E\} \tag{10.2}$$

of eigenvalues of H below energy E scales as

$$\lim_{E\to\infty} \frac{N(E)}{E^{f/2}} = \left(\frac{2m}{\hbar^2}\right)^{\frac{f}{2}} \frac{V_f}{(2\pi)^f}\,|G|, \tag{10.3}$$

where $V_f = \pi^{f/2}/\Gamma(1+f/2)$ is the volume of the f-dimensional unit ball, cf. [198, Eq. 7.3.9]. Note that the common but sloppy notation of the counting function, Eq. (10.2), is meant to count eigenvalues including their multiplicity. Equation (10.3) contains two remarkable insights. First, the number $N(E)$ of eigenvalues below E asymptotically scales as a power law in the variable E the exponent of which is related to the dimensionality f of the problem. For an example where this is relevant, think of an ideal quantum gas of n free identical particles in a d-dimensional box, which is included in the above setting ($f = d \cdot n$). Then Weyl's law yields that the density of states for the quantum gas confined to two spatial dimensions is very different from that in three-dimensional space. This is central to the Mermin–Wagner–Hohenberg theorem [199, 200] that forbids Bose–Einstein condensation and (anti)ferromagnetism for nonzero temperature in the two-dimensional case although they are allowed in three dimensions, see Refs. [201, Sec. 8.1.1] and [202, Chap. 9]. Note that in order to compute the density of states, one needs to modify Eq. (10.3) by taking into account additional factors due to spin degeneracy as well as the indistinguishability of particles. Secondly, the asymptotic scaling of the number $N(E)$ of eigenvalues below E does not depend on the shape of G but only on its volume $|G|$. The shape of G determines lower-order corrections in terms of the curvature of the boundary for instance, see e.g. Refs. [203, 204]. This motivates the question whether there exist regions G of different shape that share identical spectrum [205], which is indeed possible [206]. Note that Weyl's law is, of course, not restricted to the quantum mechanical context but applies to all problems described by the Helmholtz equation, Eq. (10.1). For instance it is widely studied in the context of acoustics, optical cavities, and quantum billiards [198, 203, 205].

The Weyl law for the free Hamiltonian, Eq. (10.3), can be generalized to Hamiltonians with nonvanishing potential. This more general Weyl law reads

$$N(E) = \frac{1}{h^f} \int_{H(q,p)\leq E} d^f q\, d^f p + \mathcal{O}(h^{1-f}), \qquad (h \searrow 0) \tag{10.4}$$

where H denotes the classical Hamilton function here [207, Sec. 6.4]. Equation (10.4) allows for the intuitive interpretation that an eigenstate occupies the phase-space volume h^f of a Planck

cell, consistent with Heisenberg's uncertainty principle. The total number of eigenvalues up to energy E is thus given by partitioning the total available phase-space region enclosed by the energy shell for E by Planck cells. This principle belongs to the foundations of statistical mechanics. We stress that this decomposition argument relies on the orthogonality of eigenstates. For a quantum map $U \in \mathbb{C}^{N\times N}$ semiclassically corresponding to time-discrete dynamics on a d-dimensional phase space Γ, the Weyl law relates the number $N_{\mathcal{I}}$ of eigenstates associated with an invariant phase space region $\mathcal{I} \subseteq \Gamma$ and the effective size $h^{d/2}$ of Planck's cell by $N_{\mathcal{I}} = |\mathcal{I}|/h^{d/2}$. For the number of all eigenstates this boils down to the quantization condition $N = h^{-d/2}$ for a phase space of unit volume. Note that for quantum maps the focus is put on the power-law dependence of h since there is no energy parameter.

In order to generalize the Weyl law to open systems, the nonorthogonality of resonance states turns out to be the major challenge [48]. As a consequence of nonorthogonality, it is no longer reasonable to decompose the available phase-space region disjointly by Planck cells in order to compute the number of resonance states. This issue can be overcome by restricting to long-lived resonance states which are mutually almost orthogonal, that is, $\langle\, \psi_m \,|\, \psi_n \,\rangle \approx \delta_{mn}$ if $\gamma_m,\ \gamma_n \ll 1$. To begin with, let us consider a fully chaotic quantum map with a totally absorbing region and subunitary time-evolution operator U. In this case, the set of long-lived resonance states may be defined as

$$\mathcal{L} := \{\lambda \in \sigma(U)\ : |\lambda| \geq e^{-\gamma_c/2}\,\}, \tag{10.5}$$

with a constant cutoff decay rate γ_c in order to distinguish between short-lived and long-lived states. This is a common way of discarding short-lived states [47]. Since resonance states are not arbitrarily localized in phase space but supported by the trapped set, the available phase-space region turns out to be the fractal repeller Γ_{rep} smeared out on the scale of Planck's cell [47]. Asymptotically for $h \searrow 0$, decomposing the h-resolved repeller by Planck cells is nothing but counting the minimal number of boxes of side length $\sqrt{h}$ necessary to cover Γ_{rep}. This, however, turns out to be equivalent to counting the number of boxes of an appropriate phase-space partition occupied by Γ_{rep} [142, p. 43]. We have already seen in Sec. 3.3 that such a box-counting algorithm gives a power law depending on the box size when applied to a uniformly fractal set. Its exponent is determined by the fractal dimension of the set. By means of quantum-to-classical correspondence, it is

$$\lim_{h\searrow 0} \frac{N_{\text{res}}(h)}{h^{-D(\Gamma_{\text{rep}})/2}} = s(\gamma_c), \tag{10.6}$$

where $N_{\text{res}}(h) := \#\mathcal{L}$ denotes the number of long-lived chaotic resonance states, $D(\Gamma_{\text{rep}})$ is the fractal box-counting dimension of the repeller, and $s(\gamma_c)$ is the so-called shape function [208]. Note that the cutoff rate γ_c, when chosen in a reasonable range, enters in the counting function

N_{res} only through this proportionality factor s. In particular, γ_{c} does not contribute to the power-law exponent. In open chaotic systems, the number N_{res} of long-lived resonance states therefore scales as a power law depending on the effective size h of Planck's cell similar to the Weyl law. In contrast to closed systems, however, the power-law exponent is not determined by the ordinary integer dimension of phase space but by the fractal dimension of the trapped set Γ_{rep}. Equation (10.6) is therefore referred to as fractal Weyl law. Fractal Weyl laws for chaotic open systems have been numerously verified numerically [47, 48, 51, 52, 61, 71, 81, 82, 86–88, 90–92, 96], analytically [53, 79, 80, 83–85, 95, 97], and even experimentally [93]. In particular, fractal Weyl laws are also studied for chaotic scattering systems [47, 90, 93] and for chaotic systems with partial absorption such as microcavities [52, 61, 71]. They have been investigated even in the context of classical Perron–Frobenius operators [209] and for the Google matrix [210].

The above heuristic box-counting argument for determining the number of long-lived resonance states, which was put forward in Ref. [47], sometimes creates a little confusion. Chaotic resonance states, no matter whether they are short-lived or long-lived, are semiclassically supported by the backward trapped set Γ_{bwd} and not by Γ_{rep} [49]. One might argue that therefore the h-resolved backward trapped set should be decomposed by Planck cells, such that the fractal dimension of Γ_{bwd} should enter the counting argument rather than the fractal dimension of Γ_{rep}. Note that Γ_{bwd} is much larger than Γ_{rep} and should support more resonances. Roughly speaking, the problem with this argument is that the localization of resonance states in the subregions $\Gamma_{\mathrm{bwd}} \cap T^{-n}(\Omega)$ (forward escaping sets) is related by time evolution and, therefore, these regions do not contribute independently. In fact, it is shown for instance in Ref. [53, Sec. 6] that it is possible to reduce the dynamics onto the h-resolved repeller without losing the relevant information about the spectrum. More precisely, the Hamiltonian, subject to complex scaling in order to uncover the resonance poles, is conjugate to an auxiliary Hamiltonian which suppresses contributions outside of the h-resolved repeller by an exponential weight. This conjugacy assures that the set of resonance poles remains unchanged under this transformation. Thus, indeed, the h-resolved repeller needs to be partitioned by Planck cells in order to compute the number of long-lived resonances. In other words, decomposing the h-resolved backward trapped set by Planck cells overestimates the number of long-lived resonances. Still this counting argument using Planck cells is not rigorous to some extent for that the resonance states are nonorthogonal. In order to address this issue, it is suggested in Ref. [48] to investigate the Hilbert subspace associated with instantaneous decay modes. By partial Schur decomposition of the subunitary time-evolution operator the authors determine the dimension of this space and thereby find the number of instantaneous decay modes taking into account their mutual nonorthogonality. Since this task is complementary to the study of long-lived resonance states, the fractal Weyl law is recovered where the exponent is given by

the fractal dimension of the repeller.

So far, we considered open systems that are fully chaotic. This has the advantage that the repeller is typically a rather homogeneous fractal. In this case, it is irrelevant whether one considers the box-counting dimension, the Hausdorff dimension, or any other Rényi dimension as they all coincide [143]. The Kantz–Grassberger relation, Eq. (3.30),

$$\delta^{\mathrm{u}}(\Gamma_{\mathrm{rep}}) = 1 - \frac{\gamma_{\mathrm{nat}}}{\Lambda}, \tag{10.7}$$

even yields an analytic estimate for the partial fractal dimension along the unstable direction in terms of the Lyapunov exponent Λ and the natural decay rate γ_{nat}. For time-reversal invariant systems, the partial fractal dimensions along the stable and unstable direction coincide, $\delta^{\mathrm{s}}(\Gamma_{\mathrm{rep}}) = \delta^{\mathrm{u}}(\Gamma_{\mathrm{rep}}) =: \delta(\Gamma_{\mathrm{rep}})$ [56], such that the fractal dimension $D(\Gamma_{\mathrm{rep}})$ of the repeller reads

$$D(\Gamma_{\mathrm{rep}}) = 2 \cdot \left(1 - \frac{\gamma_{\mathrm{nat}}}{\Lambda}\right). \tag{10.8}$$

As mentioned, this relation serves as a prediction for any Rényi dimension as long as the studied fractal is homogeneous. It then also provides a useful estimate for the exponent in the fractal Weyl law.

However, if the repeller is an inhomogeneous fractal the different notions of fractal dimension are not equivalent and it is still under debate, which of the dimensions enters the fractal Weyl law. There are two situations where such an inhomogeneous fractal repeller appears very naturally: In systems with a mixed phase space partial transport barriers may induce effectively an inhomogeneity in the chaotic repeller. This is the subject of the next section. Furthermore, for systems with partial absorption there is no orbit which fully escapes, such that the repeller is strictly speaking the entire phase space. In such cases, the fractal Weyl law seems to be determined by the multifractality of the natural CIM μ_{nat} [52, 61, 71].

10.2 Partial-Barrier Baker Map

In this section we show that already a single partial transport barrier can have a strong influence on the homogeneity of the fractal repeller for the example of the partial-barrier Baker map. It turns out that the repeller exhibits effectively two different fractal dimensions on each side of the partial barrier. Moreover, we demonstrate that this gives rise to individual fractal Weyl laws for the number of long-lived chaotic resonance states associated with the two regions.

10.2.1 Effective Fractal Dimensions

Just by looking at Fig. 10.1, one tends to think that the repeller Γ_{rep} of the partial-barrier Baker map contributes more »weight« to region A_2 on the right hand side of the partial barrier than to A_1. Of course, the repeller is a fractal set of Lebesgue measure zero such that the notion of weight is ambiguous here. Still, this visual imbalance could be reflected in different fractal dimensions of $\Gamma_{\text{rep}} \cap A_1$ and $\Gamma_{\text{rep}} \cap A_2$. In order to analyze the fractal dimension individually in each region, we define a phase-space partition of rectangular boxes of side length $\varepsilon_n = 1/3^n$ in vertical direction and $\varepsilon_n/2$ in horizontal direction, where $n \in \mathbb{N}$ denotes the order of approximation, see Fig. 10.1. As can be seen, the number of boxes occupied by Γ_{rep} is larger in A_2 than in A_1 for all n:

(a) $n = 1$: 4 out of 9 boxes in A_1 and 9 out of 9 boxes in A_2,

(b) $n = 2$: 25 out of 81 boxes in A_1 and 64 out of 81 boxes in A_2,

(c) $n = 3$: 169 out of 729 boxes in A_1 and 441 out of 729 boxes in A_2.

This is consistent with our previous visual perception of different weights.

Again the Cartesian product structure of $\Gamma_{\text{rep}} \cap A_1$ and $\Gamma_{\text{rep}} \cap A_2$ allows us to decompose the fractal box-counting dimension of Γ_{rep} into its stable and unstable direction individually within each region A_k,

$$D_k = \delta_k^{\text{s}} + \delta_k^{\text{u}}, \tag{10.9}$$

where we introduced the short-hand notation $D_k := D(\Gamma_{\text{rep}} \cap A_k)$, $\delta_k^{\text{s}} := \delta^{\text{s}}(\Gamma_{\text{rep}} \cap A_k)$, and $\delta_k^{\text{u}} := \delta^{\text{u}}(\Gamma_{\text{rep}} \cap A_k)$. Due to time-reversal invariance, the partial fractal dimension along both

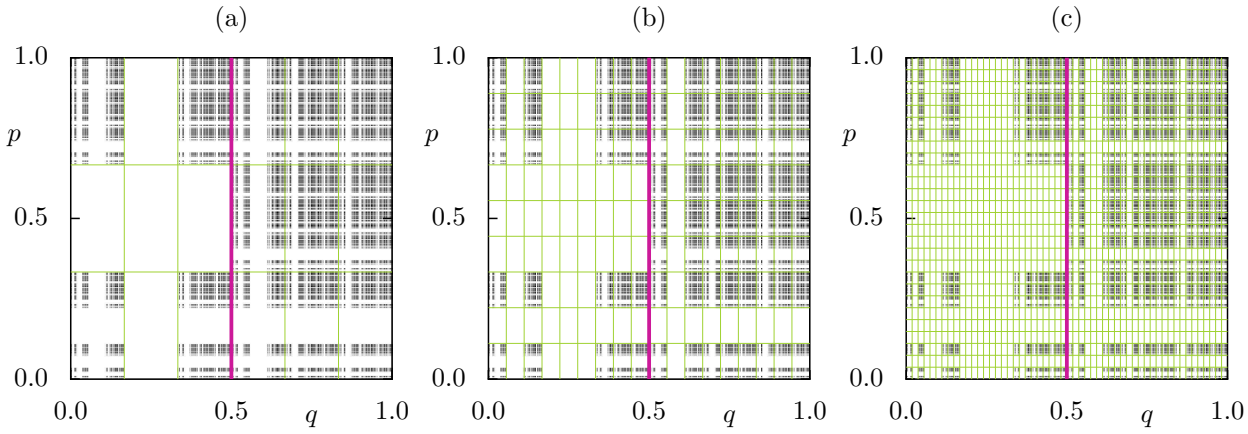

Figure 10.1. Repeller Γ_{rep} of the partial-barrier Baker map (black set) in combination with a box-counting grid (green lines) of order (a) $n = 1$, (b) $n = 2$, and (c) $n = 3$ for rectangular boxes of side length $\varepsilon_n = 1/3^n$ in vertical direction and $\varepsilon_n/2$ in horizontal direction.

directions coincides, $\delta_k^{\mathrm{s}} = \delta_k^{\mathrm{u}}$ [56]. Let us focus on the partial fractal dimension δ_k^{s} associated with the vertical stable direction. This is the direction of fractality of the backward trapped set Γ_{bwd} which supports CIMs and semiclassically also resonance states, cf. Fig. 10.2. Choosing a one-dimensional box-counting grid with boxes of side length $\varepsilon_n = 1/3^n$ in each region, consistent with the two-dimensional grid used above for Γ_{rep}, the number of occupied boxes can be calculated from the reduced 2×2 Perron–Frobenius operator T_0, Eq. (8.45). Recall that $T_0^n(1,1)^{\mathrm{T}}$ describes the weight of the uniform distribution after n forward iterations in each of the regions A_k. This initial uniform distribution converges towards Γ_{bwd}. For finite n, the iterated distribution is exactly Γ_{bwd} when resolved on the box-counting grid of order n. Taking into account that we want to calculate the number of occupied boxes and not the weight in each region, we have rescale T_0 by the stretching factor $N_{\mathrm{B}} = 3$, giving

$$T_{\#} := 3T_0 = \begin{pmatrix} 1 & 1 \\ 1 & 2 \end{pmatrix}. \tag{10.10}$$

Thus, the number $N_{\mathrm{bc}}^{\mathrm{s}}(\Gamma_{\mathrm{rep}} \cap A_k, \varepsilon_n)$ of boxes of a one-dimensional grid along the stable (vertical) direction of order n that are occupied by Γ_{rep} in region A_k is given by

$$\begin{pmatrix} N_{\mathrm{bc}}^{\mathrm{s}}(\Gamma_{\mathrm{rep}} \cap A_1, \varepsilon_n) \\ N_{\mathrm{bc}}^{\mathrm{s}}(\Gamma_{\mathrm{rep}} \cap A_2, \varepsilon_n) \end{pmatrix} = T_{\#}^n \begin{pmatrix} 1 \\ 1 \end{pmatrix}. \tag{10.11}$$

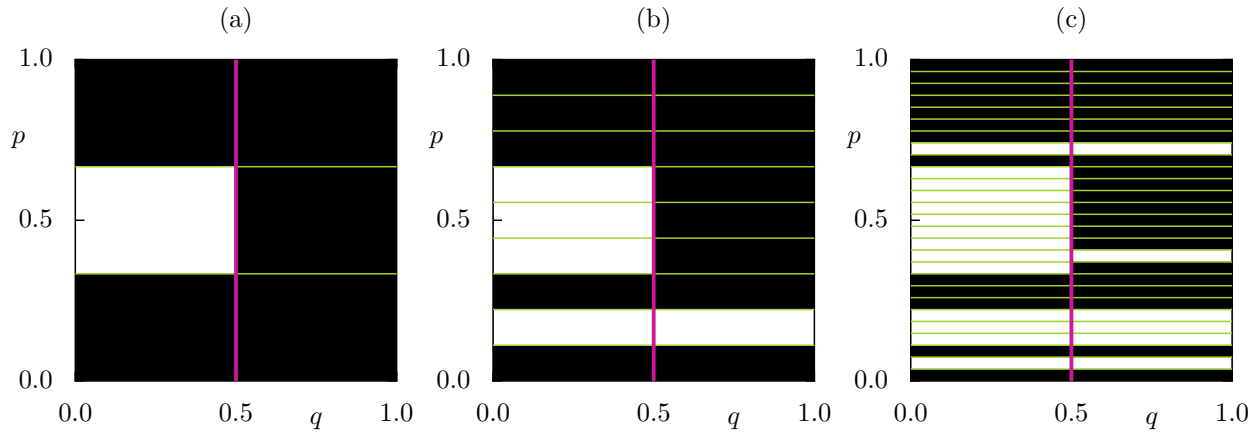

Figure 10.2. Occupied boxes (black) of the repeller Γ_{rep} for the partial-barrier Baker map using a vertical box-counting grid (green lines) of order (a) $n = 1$, (b) $n = 2$, and (c) $n = 3$ for rectangular boxes of side length $\varepsilon_n = 1/3^n$ on both sides of the partial barrier (magenta line).

As can be compared with Fig. 10.2 the explicit number of occupied boxed reads

$$\begin{pmatrix}1\\1\end{pmatrix} \overset{T_\#}{\mapsto} \begin{pmatrix}2\\3\end{pmatrix} \overset{T_\#}{\mapsto} \begin{pmatrix}5\\8\end{pmatrix} \overset{T_\#}{\mapsto} \begin{pmatrix}13\\21\end{pmatrix}. \tag{10.12}$$

Squaring these numbers $N^{\mathrm{s}}_{\mathrm{bc}}(\Gamma_{\mathrm{rep}} \cap A_k, \varepsilon_n)$, and thereby taking into account the fractality along the previously neglected unstable direction, gives exactly the number of occupied boxes of the repeller Γ_{rep} in region A_k for the two-dimensional grid of order n, cf. Fig. 10.1.

The partial fractal box-counting dimension δ^{s}_k along the stable direction, and thus, indirectly also the fractal dimension of the repeller, follows from Eq. (3.26),

$$\delta^{\mathrm{s}}_k = -\lim_{n\to\infty} \frac{\log(N^{\mathrm{s}}_{\mathrm{bc}}(\Gamma_{\mathrm{rep}} \cap A_k, \varepsilon_n))}{\log(\varepsilon_n)}. \tag{10.13}$$

In view of Eq. (10.11), it is convenient to apply a spectral decomposition of $(1,1)^{\mathrm{T}}$ into eigenvectors of $T_\#$. We denote the eigenvalues and eigenvectors according to $T_\#\varphi_j = \lambda_j\varphi_j$, $j \in \{1,2\}$, and normalize the eigenvectors such that $\|\varphi_j\|^2 = \langle\, \varphi_j \,|\, \varphi_j \,\rangle = 1$ with the Euclidean scalar product. Note that the eigenvectors φ_j are orthogonal since $T_\#$ is symmetric. This gives

$$\begin{pmatrix}1\\1\end{pmatrix} = \sum_{j=1}^{2} \langle\, \varphi_j \,|\, (1,1)^{\mathrm{T}} \,\rangle\, \varphi_j = \sum_{j=1}^{2} \left(\varphi_j^{(1)} + \varphi_j^{(2)}\right)\, \varphi_j, \tag{10.14}$$

where $\varphi_j^{(1)}$ and $\varphi_j^{(2)}$ denote the two components of φ_j. With Eq. (10.11), we therefore find

$$\begin{pmatrix}N^{\mathrm{s}}_{\mathrm{bc}}(\Gamma_{\mathrm{rep}} \cap A_1, \varepsilon_n)\\ N^{\mathrm{s}}_{\mathrm{bc}}(\Gamma_{\mathrm{rep}} \cap A_2, \varepsilon_n)\end{pmatrix} = T_\#^n \sum_{j=1}^{2} \left(\varphi_j^{(1)} + \varphi_j^{(2)}\right)\, \varphi_j = \sum_{j=1}^{2} \left(\varphi_j^{(1)} + \varphi_j^{(2)}\right)\, \lambda_j^n \varphi_j \tag{10.15}$$

for the number of occupied boxes, such that the partial fractal dimension, Eq. (10.13), obeys

$$\begin{aligned}
\delta^{\mathrm{s}}_k &= -\lim_{n\to\infty} \frac{\log\left[\sum_{j=1}^{2} \left(\varphi_j^{(1)} + \varphi_j^{(2)}\right)\, \lambda_j^n \varphi_j^{(k)}\right]}{\log(3^{-n})} && (10.16)\\
&= \frac{1}{\log(3)} \log\left[\lim_{n\to\infty} \sqrt[n]{\sum_{j=1}^{2} \left(\varphi_j^{(1)} + \varphi_j^{(2)}\right)\, \lambda_j^n \varphi_j^{(k)}}\right] && (10.17)\\
&= \frac{\log\left[\max\{\lambda_1, \lambda_2\}\right]}{\log(3)}. && (10.18)
\end{aligned}$$

The last step is shown in Sec. B.5. Using that the maximal eigenvalue of $T_\# = 3T_0$ is determined by the natural decay rate, $\max\{\lambda_1, \lambda_2\} = 3e^{-\gamma_{\mathrm{nat}}}$, and that the Lyapunov exponent of

the partial-barrier Baker map reads $\Lambda = \log(3)$, it is

$$\delta_k^{\mathrm{s}} = 1 - \frac{\gamma_{\mathrm{nat}}}{\Lambda}. \tag{10.19}$$

That is, asymptotically the repeller has the same fractal dimension in regions A_1 and A_2 in agreement with the Kantz–Grassberger relation, Eq. (3.30). The visual imbalance of Γ_{rep} in A_1 and A_2 is therefore not reflected in the fractal scaling properties for arbitrary fine resolution. This can be also seen in Fig. 10.3(a). Clearly, the physical origin of this asymptotic equivalence is the coupling across the partial transport barrier. As we will now demonstrate, the imbalance is rather reflected in the way both regions approach the mutual asymptotic behavior.

Recall that, in general, the number N_{bc} of occupied boxes of length ε asymptotically obeys a power law, $N_{\mathrm{bc}} \sim \varepsilon^{-D}$, $\varepsilon \searrow 0$. The fractal dimension D follows from its exponent which is the slope in a double-logarithmic plot. On finite scales ε, however, the number N_{bc} of occupied boxes does not have to obey a power law. Still, it is possible to associate an effective fractal

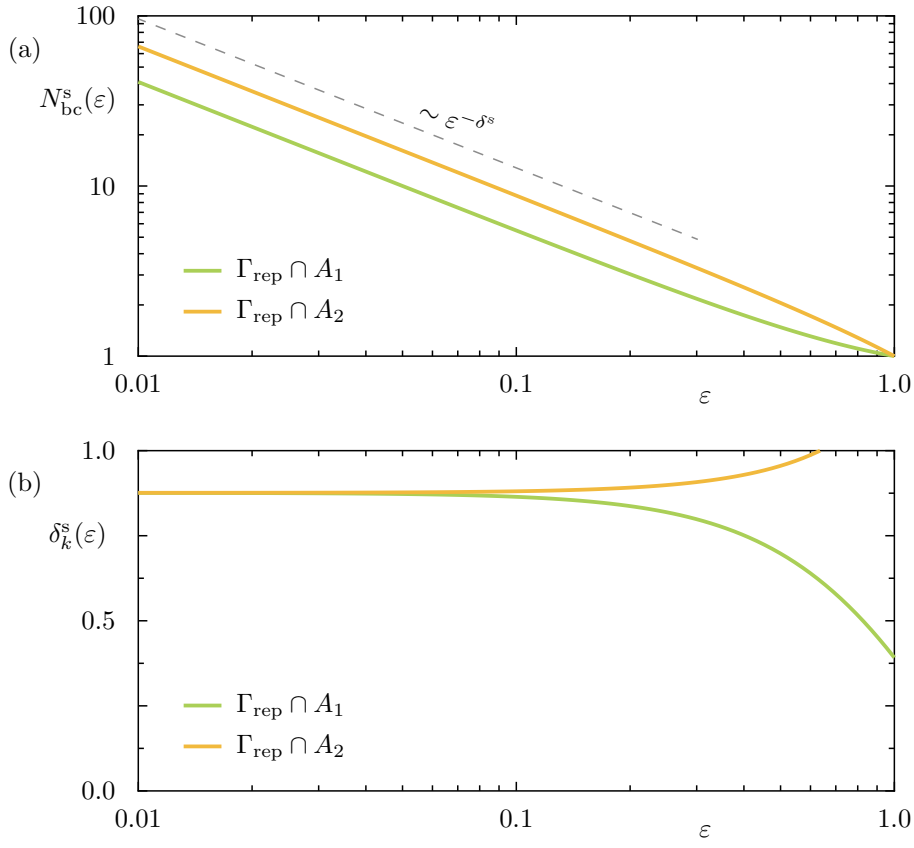

Figure 10.3. (a) Number $N^{\mathrm{s}}_{\mathrm{bc}}(\Gamma_{\mathrm{rep}} \cap A_k, \varepsilon)$ of boxes of a one-dimensional grid along the stable direction at scale ε that are occupied by the repeller Γ_{rep} of the partial-barrier Baker map in region A_1 (green) or A_2 (orange), according to Eq. (10.15). (b) Effective partial fractal dimension $\delta^{\mathrm{s}}_k(\varepsilon)$ at scale ε of the repeller Γ_{rep} of the partial-barrier Baker map along its stable direction in each region A_1 (green) and A_2 (orange), according to Eq. (10.22).

dimension at scale ε by computing its local slope on a double-logarithmic plot [98], i.e.,

$$D(\varepsilon) := -\frac{d\log N_{\mathrm{bc}}(\varepsilon)}{d\log\varepsilon} = -\left(\log\circ N_{\mathrm{bc}}\circ\exp\right)'(\log\varepsilon) = -\frac{N'_{\mathrm{bc}}(\varepsilon)}{N_{\mathrm{bc}}(\varepsilon)}\varepsilon. \tag{10.20}$$

Of course, the effective fractal dimension $D(\varepsilon)$ at scale ε and the fractal dimension D coincide for $\varepsilon \searrow 0$ in the spirit of l'Hôpital's rule. It is convenient in the following to interpret ε, and thus, also N_{bc} as a function of a (continuous) parameter n, which gives

$$D(\varepsilon_n) = -\frac{\varepsilon_n}{\varepsilon'_n}\frac{(N_{\mathrm{bc}}\circ\varepsilon)'(n)}{N_{\mathrm{bc}}(\varepsilon_n)}. \tag{10.21}$$

Let us apply this effective treatment of a fractal dimension to the above case of the partial fractal dimension δ^{s} of the repeller of the partial-barrier Baker map along the stable direction. Here, it is $\varepsilon_n = 3^{-n}$ such that $\varepsilon'_n = -\log 3\cdot\varepsilon_n$, and using Eqs. (10.15) and (10.21) we find

$$\delta^{\mathrm{s}}_k(\varepsilon_n) = \frac{1}{\log 3}\frac{\sum_{j=1}^{2}\left(\varphi_j^{(1)}+\varphi_j^{(2)}\right)\varphi_j^{(k)}\,\lambda_j^n\log(\lambda_j)}{\sum_{j=1}^{2}\left(\varphi_j^{(1)}+\varphi_j^{(2)}\right)\varphi_j^{(k)}\,\lambda_j^n}. \tag{10.22}$$

The corresponding graphs, shown in Fig. 10.3(b), illustrate that, in fact, the effective fractal dimension in region A_2 (orange) is larger than in A_1 (green), which is consistent with the previously discussed visual imbalance of the repeller Γ_{rep}. We stress that asymptotically, $\varepsilon \searrow 0$, the effective partial fractal dimension in both regions converges towards the same value $\delta^{\mathrm{s}} = \delta^{\mathrm{s}}_1 = \delta^{\mathrm{s}}_2$, Eq. (10.19). Furthermore, we emphasize again that the partial fractal dimensions δ^{s}_k and δ^{u}_k along the stable and unstable direction coincide for each region A_k due to time-reversal invariance. In the following we therefore write $\delta_k := \delta^{\mathrm{s}}_k = \delta^{\mathrm{u}}_k$. Let us briefly comment on the fact that the partial fractal dimension $\delta^{\mathrm{s}}_2(\varepsilon)$ of the repeller in region A_2 (orange) exceeds unity for large ε according to Eq. (10.22) and evident from Fig. 10.3(b). This is an artifact from choosing n in Eq. (10.21) continuously and amounts to an inappropriate choice of box-counting grids. For values of $\varepsilon_n = 3^{-n}$, $n\in\mathbb{N}$, this effect is not present. Nevertheless, this physically irrelevant regime for large ε is shown as a guide to the eye in order to emphasize the difference in the effective fractality in both regions. For values $\varepsilon \leq 1/3$ this difference is still present but, particularly in Fig. 10.3(a), hardly recognizable.

10.2.2 Quantum-to-Classical Correspondence

So far, we discussed the relevance of effective fractal dimensions by their capability of capturing the visual imbalance of the repeller on both sides of the partial barrier. However, much more important for us are the quantum signatures of the different effective fractal dimensions. As we will now demonstrate the scaling of the number N_{res} of long-lived resonance states

depending on the effective size h of Planck's cell on numerically feasible scales is governed by the effective fractal dimension of the repeller, not by the asymptotic fractal dimension. Even more remarkable, we will show that there are effectively individual fractal Weyl laws associated with the two regions A_1 and A_2.

Recall the common heuristic argument for the fractal Weyl law, according to which the number $N_{\mathrm{res}}(h)$ of long-lived resonance states for a specific value h is obtained by a box-counting algorithm with boxes of area h applied to the repeller Γ_{rep}. In view of that, it is quite expected that the scaling of N_{res} around h is described by the effective fractal dimension on that specific scale and not by the asymptotic one. Precisely this behavior is shown in Fig. 10.4 (blue), which requires some explanation. In order to increase the difference between the effective and the asymptotic fractality of Γ_{rep}, we do not consider the ordinary partial-barrier Baker map but adapt its transition probabilities for both regions by choosing $N_{\mathrm{B}} = 10$, $L = 3$, and $C = 1$, using the notation from Sec. 8.1. Furthermore, we extract the trivial power-law scaling h^{-1}, which corresponds to a closed system, by plotting $N_{\mathrm{res}}(h) \cdot h$, and

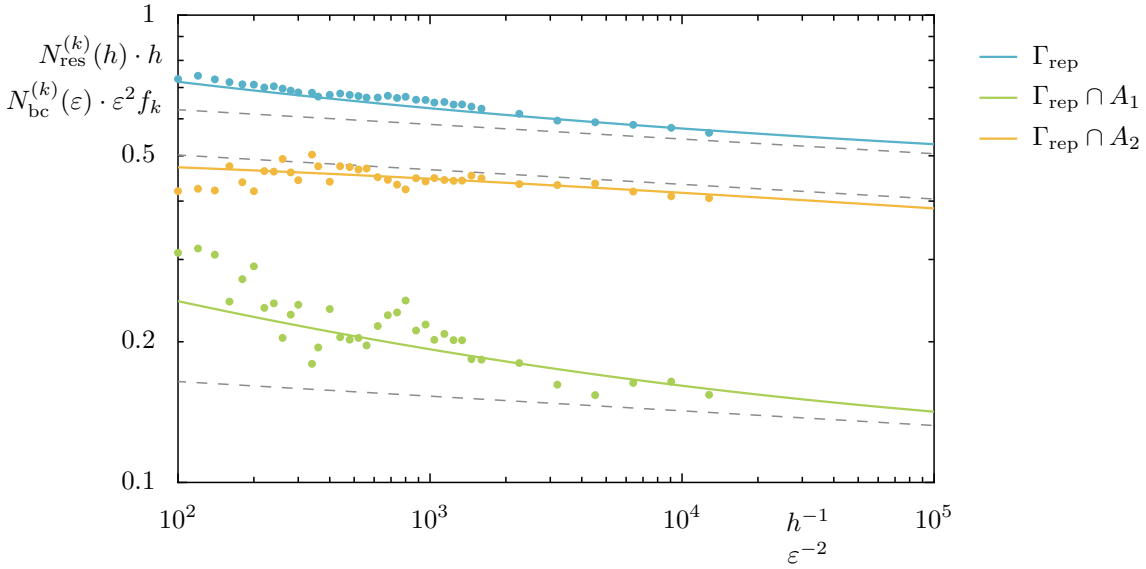

Figure 10.4. Number $N_{\mathrm{res}}^{(k)}(h)$ (dots) of long-lived resonance states of the partial-barrier Baker map ($N_{\mathrm{B}} = 10$, $L = 3$, $C = 1$) vs h^{-1}, rescaled by the trivial scaling h. Different colors correspond to the class $\mathcal{L}$ of all long-lived resonance states (blue), or the subclasses $\mathcal{L}_1$ (green) or $\mathcal{L}_2$ (orange) of states associated with regions A_1 or A_2, respectively. The quantum mechanical scaling is compared to the number $N_{\mathrm{bc}}^{(k)}(\varepsilon)$ (solid lines) of rectangular boxes of a grid with vertical (horizontal) side length ε ($\varepsilon/2$) that are occupied by the entire repeller Γ_{rep} (blue) or by the repeller Γ_{rep} in region A_1 (green) or A_2 (orange), plotted against ε^{-2} and rescaled by the trivial scaling ε^2. The classical data are computed according to $N_{\mathrm{bc}}^{(k)}(\varepsilon) := \varepsilon^{-2\delta_k(\varepsilon)}$ with δ_k from Eq. (10.22) as adapted to the map parameters, and vertically shifted by factors $f = 1.06$, $f_1 = 0.47$, $f_2 = 0.49$. The asymptotic scaling (gray dashed lines) corresponds to a power law with δ_k according to Eq. (10.19).

thereby visually enhancing the difference between the different fractal dimensions close to two. Note that a power law $N_{\mathrm{res}}(h) \sim h^{-1}$ would therefore correspond to a horizontal line in Fig. 10.4, and a fractal Weyl law like $N_{\mathrm{res}}(h) \sim h^{-D(\Gamma_{\mathrm{rep}})/2}$ would lead to a decreasing straight line which is steeper the smaller $D(\Gamma_{\mathrm{rep}})$ (double-logarithmic plot). The quantum mechanical data (blue dots) are obtained by numerical diagonalization of the time evolution operator for different values of h and discarding all short-lived resonances with $\gamma > \gamma_{\mathrm{c}} = 2$. Classically, we compute the effective partial fractal dimension $\delta(\varepsilon)$ according to Eq. (10.22), with straightforward adaptations to the chosen system parameters $N_{\mathrm{B}} = 10$, $L = 3$, and $C = 1$. For the number of occupied boxes of the repeller, we thus analytically expect $N_{\mathrm{bc}}(\varepsilon) \sim \varepsilon^{-2\delta(\varepsilon)}$ (solid blue line). By identifying the classical box area ε^2 and the quantum mechanical size h of Planck's cell, we are allowed to plot both N_{res} as a function of h and N_{bc} as a function of ε in one and the same coordinate system for comparison. The asymptotic scaling is estimated by the Kantz–Grassberger relation, Eq. (10.19) (gray dashed line).

Although the difference between the asymptotic and the effective scaling of N_{res} is small, even in this adapted plot, one clearly observes that the quantum data nicely follows the effective classical behavior. We stress that the fluctuations in the quantum data are particularly smaller than the difference to the asymptotic scaling. Note that the classical expectation N_{bc} is vertically shifted by a factor of $f = 1.06$ to better demonstrate the mutual scaling with N_{res}.

At this point we see quantum-to-classical correspondence between the number of all long-lived resonance states and the effective fractality of the entire repeller. However, as shown in this thesis, resonance states may localize predominantly on one or the other side of the partial barrier depending on their decay rate, even for semiclassically small values of h. Moreover, we have seen that the effective fractal dimension of the repeller differs on both sides of the partial barrier. This suggests that there may be quantum-to-classical correspondence within both regions individually, giving rise to individual effective fractal Weyl laws. To this end, we define the class $\mathcal{L}_k$, $k \in \{1, 2\}$, that contains a long-lived resonance state ψ_γ, $\gamma < \gamma_{\mathrm{c}}$, if its relative local weight $\|P_j \psi_\gamma\|^2 / |A_j|$, $j \in \{1, 2\}$, is maximal for region A_k. This classification is supported by the distributions of the corresponding decay rates, see Fig. 10.5, which exhibits only a small overlap between the two distribution of the two classes. We therefore define the number $N_{\mathrm{res}}^{(k)}$ of long-lived resonance states associated with A_k by the number of linearly independent elements in $\mathcal{L}_k$. The corresponding numerical data for the partial-barrier Baker map modified as above are again shown in Fig. 10.4 by green ($\mathcal{L}_1$) and orange ($\mathcal{L}_2$) dots. They are compared to the expected classical box-counting scaling $N_{\mathrm{bc}}^{(k)}$ for $\Gamma_{\mathrm{rep}} \cap A_k$ with the individual effective fractal dimensions δ_k, according to Eq. (10.22) when adapted to the system parameters (green and orange solid lines). Again, the classical expectation $N_{\mathrm{bc}}^{(k)}$ is vertically shifted by factors of $f_1 = 0.47$ and $f_2 = 0.49$ to better demonstrate the mutual scaling with $N_{\mathrm{res}}^{(k)}$. Note that the factors f_k mainly represent the phase-space fraction of the considered

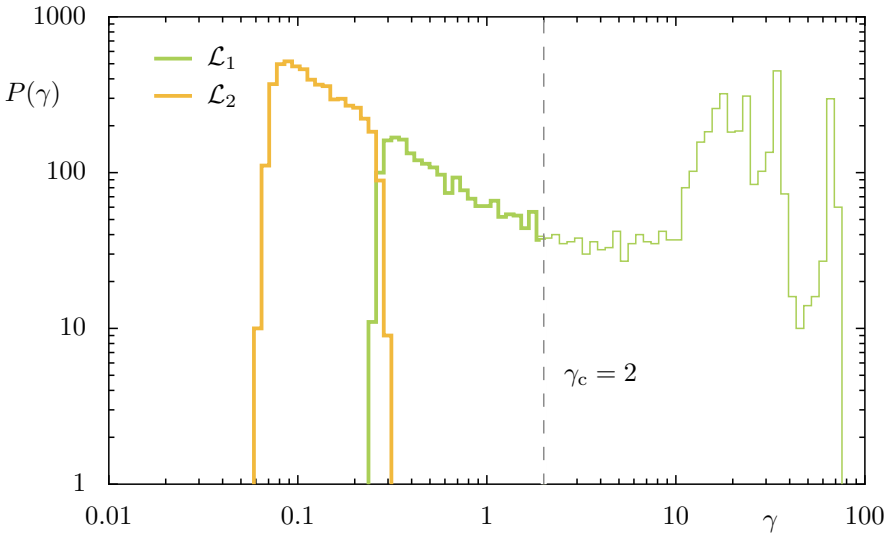

Figure 10.5. Distribution $P(\gamma)$ of decay rates γ of the partial-barrier Baker map ($N_B = 10$, $L = 3$, $C = 1$) for $h^{-1} = 12800$. The distribution distinguishes between resonance states of class $\mathcal{L}_1$ located in region A_1 (green) and resonance states of class $\mathcal{L}_2$ located in region A_2 (orange). Short-lived states $\gamma > \gamma_c$ are neglected for the fractal Weyl law.

region A_k.

First of all, we observe quantum-to-classical correspondence between the number of long-lived resonance states associated with region A_k and the effective fractality of the repeller in region A_k. That is, we effectively obtain individual fractal Weyl laws for the two different regions. For region A_1, the found scaling of the quantum data is clearly not captured by the expected asymptotic fractal scaling of the repeller. We admit that there are significant fluctuations, almost oscillatory, around the box-counting scaling N_{bc}. They have the same order of magnitude as the fluctuations for the class $\mathcal{L}_2$ (orange), which are less pronounced than for $\mathcal{L}_1$ in Fig. 10.4 due to the logarithmic representation. Anyway, these deviations decrease for smaller values of h. In particular, in view of the broad quantum localization transition of the partial barrier [32], cf. Sec. 5.1, quantum deviations are expected at least up to $\phi/h \approx 10$, which corresponds to $h^{-1} \approx 200$ here.

10.3 Generic Maps

In the previous section we have seen that the repeller of the partial-barrier Baker map exhibits different effective fractal dimensions on each side of the partial barrier. Long-lived chaotic resonance states associated with these regions obey individual effective fractal Weyl laws. In this section we demonstrate that these results generalize to the generic standard map with a mixed phase space. Eventually, for the partial-barrier standard map we can numerically show that our results also generalize to the case of two barriers. These individual effective fractal

Weyl laws for the standard map and the partial-barrier standard map have first been reported in Ref. [33].

First of all, the repeller of the standard map, see Fig. 10.6(a), qualitatively displays the same kind of visual imbalance with respect to the partial barrier as previously discussed for the partial-barrier Baker map in Sec. 10.2.1. Furthermore, as explained in Sec. 9.3, the chaotic resonance states may localize with respect to the dominant partial barrier depending on their decay rate, cf. Fig. 10.6(b, c). This already suggests that the standard map also gives rise to individual effective fractal Weyl laws for the chaotic resonance states associated with each side of the partial barrier. Let us now quantitatively analyze this effective fractality and the expected quantum-to-classical correspondence. However, the common box-counting algorithm is numerically hardly capable of analyzing the fractal sets over the necessary range of ε values. It is, thus, useful to introduce the uncertainty algorithm.

10.3.1 Uncertainty Algorithm

Numerically, the major drawback of the box-counting algorithm is the appropriate sampling of the fractal set. In order to compute the fractal dimension from the box-counting scaling at small values of ε the fractal set must be available in sufficient resolution. Then the crucial numerical limitations are memory constraints. The uncertainty algorithm overcomes these

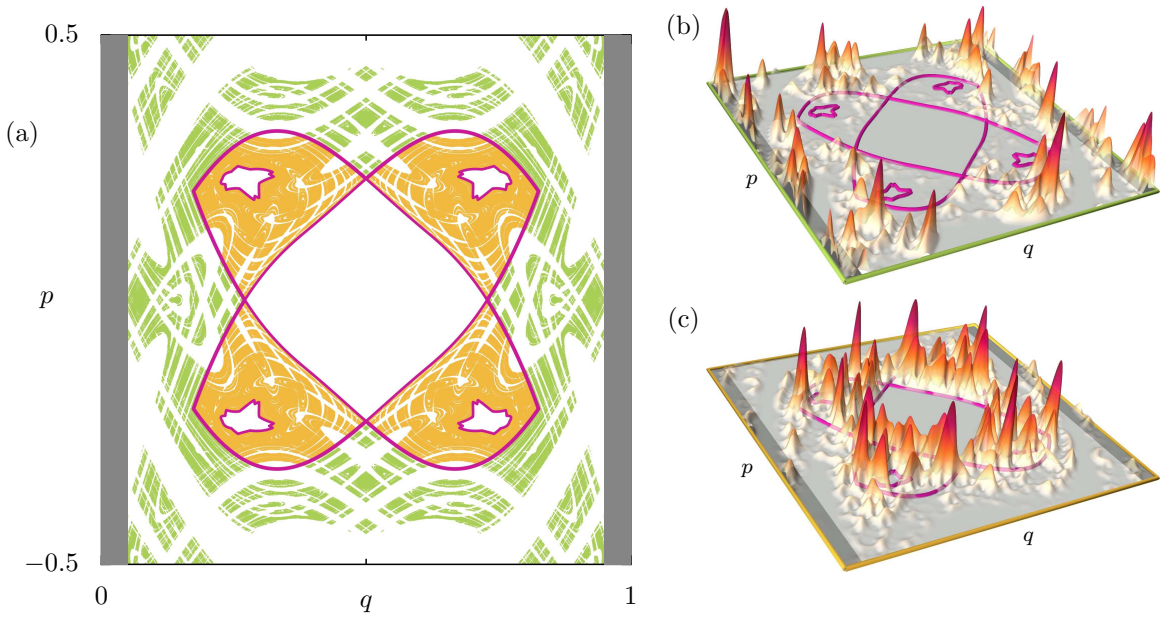

Figure 10.6. (a) Finite-time approximation of the repeller Γ_{rep} of the standard map ($\kappa = 2.9$) with $|\Omega| = 0.1$ (gray shaded regions). It is decomposed by the partial barrier (magenta lines) into the regions A_1 (green) and A_2 (orange). (b, c) Husimi representation of typical long-lived chaotic resonance states ($1/h = 1000$) associated with (b) A_1 and (c) A_2.

concerns in a fascinating manner [98, 211]. A point $x \in \Gamma$ is called ε-certain if all points in an ε-neighborhood of x have the same escape time as x, that is, there exists an $n \in \mathbb{N}_0$ such that $B_\varepsilon(x) \subseteq T^{-n}(\Omega)$ where $B_\varepsilon(x)$ denotes the ball of radius ε centered around x. Otherwise x is called ε-uncertain. The ε dependence of the phase-space fraction $\xi(\varepsilon)$ of ε-uncertain points contains the partial fractal dimension δ of the trapped sets [98, 211]. Instead of analyzing the fraction $\xi(\varepsilon)$ of ε-uncertain points directly, we compute the fraction $1-\xi(\varepsilon)$ of ε-certain points. It is essentially governed by

$$1 - \xi(\varepsilon) \approx \sum_{n=0}^{\mathcal{N}_\varepsilon - 1} |T^{-n}(\Omega)|, \tag{10.23}$$

that is the phase-space fraction of forward escaping sets $T^{-n}(\Omega)$ resolved by ε. Intuitively speaking, any point in $T^{-n}(\Omega)$ that is ε away from the boundary of $T^{-n}(\Omega)$ is ε-certain. As long as ε is small compared to the length scales of $T^{-n}(\Omega)$ basically all points in $T^{-n}(\Omega)$ are ε-certain. From some $\mathcal{N}_\varepsilon \in \mathbb{N}_0$ on, however, the smallest length scale (unstable direction) of $T^{-\mathcal{N}_\varepsilon}(\Omega)$ is below ε such that basically no point of $T^{-n}(\Omega)$ is ε-certain for $n \geq \mathcal{N}_\varepsilon$. It is again illuminating to consider the example of the Baker map, see Fig. 10.7. Here, the sets Ω and $T^{-1}(\Omega)$ support balls of radius ε while the sets $T^{-n}(\Omega)$ for $n \geq \mathcal{N}_\varepsilon = 2$ do not. Note that

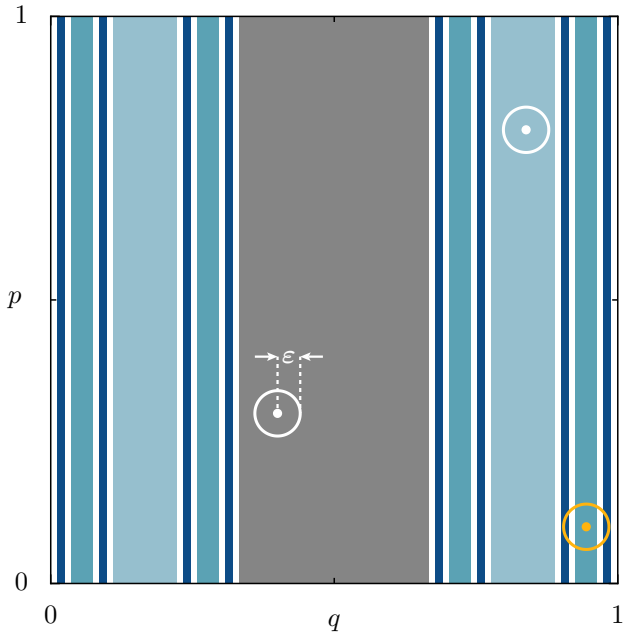

Figure 10.7. Illustration of ε-certain (white) and ε-uncertain points (orange) of the Baker map. While the opening Ω (gray) and the first forward escaping set $T^{-1}(\Omega)$ (light blue) support balls of radius ε, all forward escaping sets $T^{-n}(\Omega)$ with $n \geq \mathcal{N}_\varepsilon = 2$ do not. For instance, the ε-neighborhood of the ε-uncertain point in $T^{-2}(\Omega)$ (medium blue) has overlap with $T^{-3}(\Omega)$ (dark blue).

taking into account ε-gaps around the boundaries of the forward escaping sets beyond the rough approximation in Eq. (10.23) results in higher-order corrections which are irrelevant for our purpose. Using $|T^{-n}(\Omega)| = e^{-\gamma_{\rm nat} n}(1 - e^{-\gamma_{\rm nat}})$, cf. Eq. (7.37), one obtains

$$1 - \xi(\varepsilon) \approx (1 - e^{-\gamma_{\rm nat}}) \sum_{n=0}^{\mathcal{N}_\varepsilon - 1} e^{-\gamma_{\rm nat} n} \tag{10.24}$$

$$= (1 - e^{-\gamma_{\rm nat}}) \frac{1 - e^{-\gamma_{\rm nat} \mathcal{N}_\varepsilon}}{1 - e^{-\gamma_{\rm nat}}}, \tag{10.25}$$

such that

$$\xi(\varepsilon) \approx e^{-\gamma_{\rm nat} \mathcal{N}_\varepsilon}. \tag{10.26}$$

The number $\mathcal{N}_\varepsilon$ of forward escaping sets resolved by ε obeys

$$|\Omega|\, e^{-\Lambda \mathcal{N}_\varepsilon} = \varepsilon, \tag{10.27}$$

with the Lyapunov exponent Λ, assuming a uniformly hyperbolic map for simplicity. For this, recall that the set Ω is contracted by $e^{-\Lambda}$ in each step along the unstable direction. Again, see Fig. 10.7 for the case of the Baker map. Here, the relevant length scale of each stripe of $T^{-n}(\Omega)$ along the unstable direction is given by

$$|\Omega|\, e^{-\Lambda n} = \frac{1}{3}\, e^{-\log(3) n} = \left(\frac{1}{3}\right)^{n+1}. \tag{10.28}$$

The estimate for $\mathcal{N}_\varepsilon$, Eq. (10.27), gives

$$\mathcal{N}_\varepsilon = \frac{\log(|\Omega|) - \log(\varepsilon)}{\Lambda}. \tag{10.29}$$

Inserting this into Eq. (10.26), one obtains

$$\xi(\varepsilon) \approx e^{-\frac{\gamma}{\Lambda} \log(|\Omega|)}\, e^{\frac{\gamma}{\Lambda} \log(\varepsilon)} \sim \varepsilon^{\frac{\gamma}{\Lambda}}. \tag{10.30}$$

Finally, the Kantz–Grassberger relation, Eq. (3.30), reveals the relation,

$$\xi(\varepsilon) \sim \varepsilon^{1-\delta}, \qquad (\varepsilon \searrow 0) \tag{10.31}$$

between the phase-space fraction $\xi(\varepsilon)$ of ε-uncertain points and the partial fractal dimension δ of the trapped sets [98, 211].

The main advantage of this so-called uncertainty algorithm is that we can compute the fractal dimension of the trapped sets without computing the fractal sets themselves. In par-

ticular, it is not necessary to compute the finite-time approximation very accurately or to store a large sample in order to estimate its fractal dimension on fine scales. Numerically, it is usually sufficient and very efficient to check whether a point $x \in \Gamma$ is ε-certain by comparing the coincidence of escape times with only one point $y \in \Gamma$ for which $\|x - y\| = \varepsilon$. Figure 10.8 impressively demonstrates that the range of ε values available for the uncertainty algorithm exceeds the range of the box-counting algorithm by several orders of magnitude. For this comparison we compute the finite-time approximation of the repeller for the standard map with 10^8 initial points where we discard points which leave the system within 9 iterations for A_1 and 25 iterations for A_2. Note that the iteration times are chosen differently owing to the very different escape times from the two regions, see Sec. B.6 for their computation. The box-counting algorithm is applied to this sample. For the uncertainty algorithm we determine the fraction $\xi_k(\varepsilon)$ of ε-uncertain points in region A_k by averaging over 10^4 random initial points for each region. As $\xi_k(\varepsilon) \sim \varepsilon^{1-\delta_k}$, the ratio $\xi_k(\varepsilon)^2/\varepsilon^2 \sim \varepsilon^{-2\delta_k}$ is comparable with the number $N_{\mathrm{bc}}^{(k)}(\varepsilon)$ of boxes of side length ε occupied by the repeller in region A_k. In the rescaled plot in Fig. 10.8 this corresponds to plotting $\xi_k(\varepsilon)^2$. Figure 10.8 clearly reveals that effectively the fractal dimensions of the repeller on each side of the partial barrier differ and approach a mutual asymptotic scaling for small ε. Note that in order to reveal this behavior

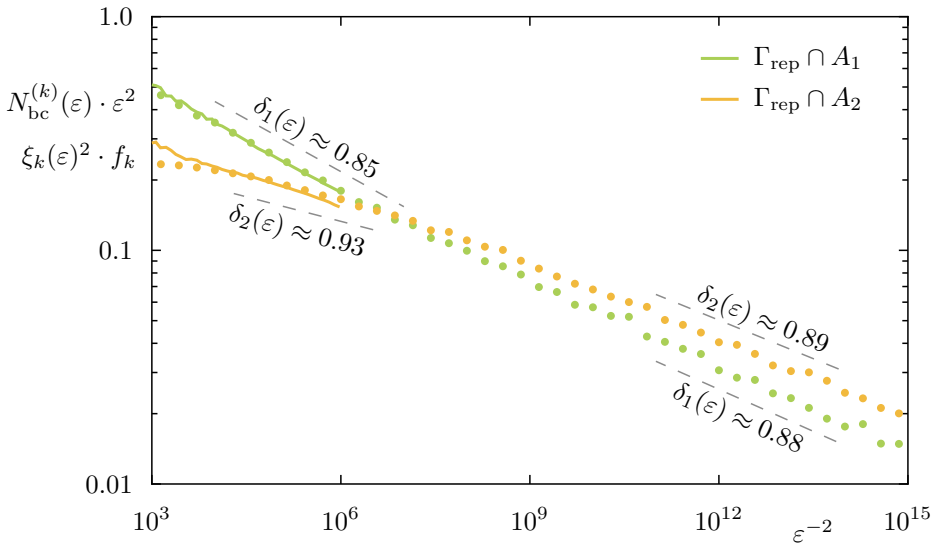

Figure 10.8. Number $N_{\mathrm{bc}}^{(k)}(\varepsilon)$ of boxes of side length ε occupied by the repeller Γ_{rep} of the standard map ($\kappa = 2.9$, $|\Omega| = 0.1$) in region A_1 (green solid line) or A_2 (orange solid line). The data are rescaled by the trivial scaling ε^2. This is compared to the fraction $\xi_k(\varepsilon)$ of ε-uncertain points in region A_1 (green dots) and A_2 (orange dots). The effective partial fractal dimensions $\delta_k(\varepsilon)$ of the repeller in region A_k at scale ε are indicated by the corresponding power-law scaling (dashed lines). The values of $\xi_k(\varepsilon)^2$ are vertically shifted by factors $f_1 = 0.72$, $f_2 = 0.25$ in order to better demonstrate the mutual scaling with the box-counting data.

with the box-counting algorithm numerically, only having a sufficiently large sample of the repeller ($\sim 10^{15}$ points) in storage would require at least petabytes of memory (32 bits per point and coordinate).

10.3.2 Quantum-to-Classical Correspondence

In order to investigate quantum-to-classical correspondence between the individual effective fractal dimensions on each side of the repeller and the number of long-lived resonance states, we again classify long-lived resonance states by their localization. Just as for the partial-barrier Baker map, the class $\mathcal{L}_k$, $k \in \{1,2\}$ contains a long-lived resonance state ψ_γ, $\gamma < \gamma_c = 1$, if its relative local weight $\|P_j\psi_\gamma\|^2/|A_j|$, $j \in \{1,2\}$, is maximal for region A_k. Note that for the standard map it is $|A_1| \approx 0.6664$ and $|A_2| \approx 0.2061$. Resonance states having 50% of their weight in deeper hierarchical regions or in the regular region are discarded right away. Figure 10.9 shows that the overlap in the distribution of the decay rates for the two localization classes $\mathcal{L}_k$ is rather small. According to this classification, the number $N_{\mathrm{res}}^{(k)}(h)$ of long-lived chaotic resonance states associated with A_k is shown in Fig. 10.10 in dependence of the effective size h of Planck's cell (dots). In order to reduce fluctuations in the data we perform an average over $\max\{1, \lfloor 5000\,h \rfloor\}$ different realizations of the quantum standard map by varying the Bloch phase ϑ_{mom}, cf. Sec. 4.2.1. We restrict ourselves to values of $\phi/h \gtrsim 10$ such that transport across the partial barrier is quantum mechanically not significantly suppressed in view of the closed system's theory [32]. The h dependence of $N_{\mathrm{res}}^{(k)}$ is compared to the

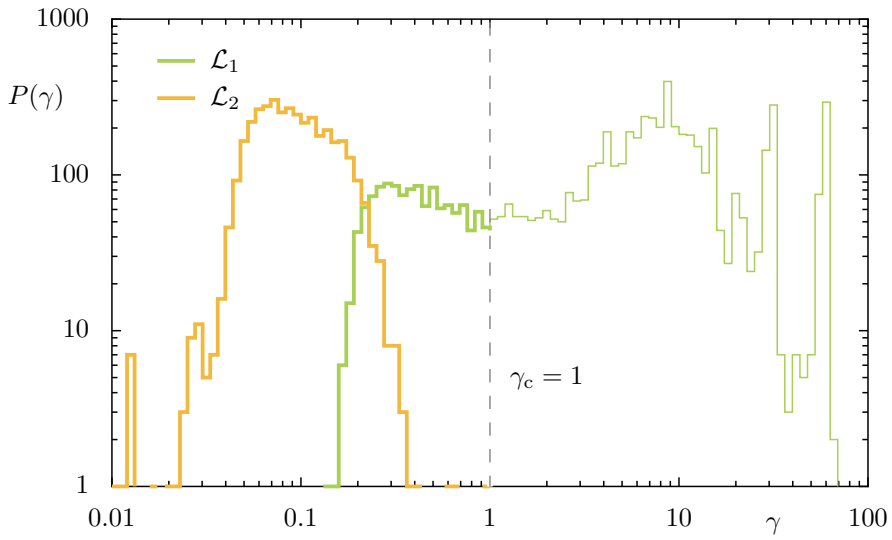

Figure 10.9. Distribution $P(\gamma)$ of decay rates γ of the standard map ($\kappa = 2.9$, $|\Omega| = 0.1$) for $h^{-1} = 12800$. The distribution distinguishes between resonance states of class $\mathcal{L}_1$ located in region A_1 (green) and resonance states of class $\mathcal{L}_2$ located in region A_2 (orange). Short-lived states $\gamma > \gamma_c$ are neglected for the fractal Weyl law.

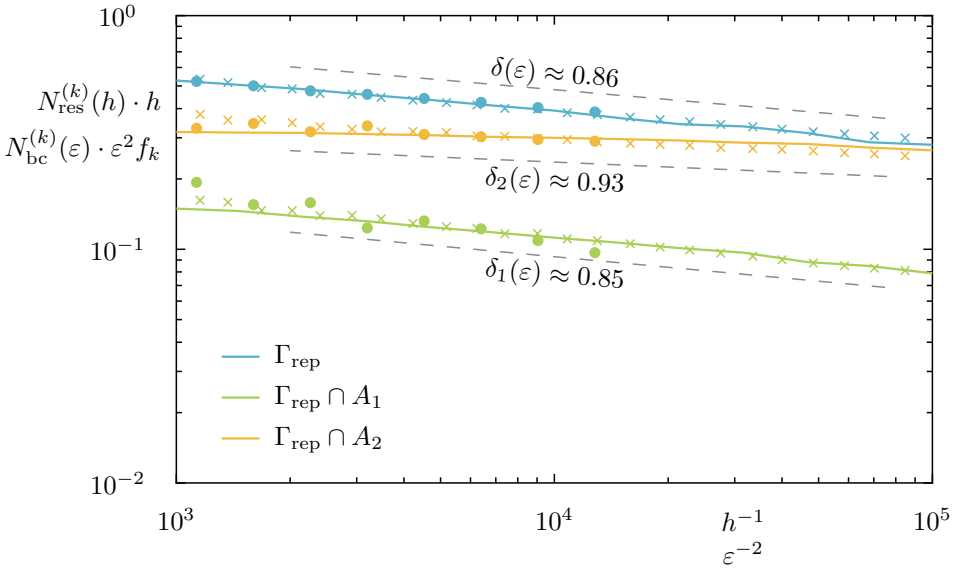

Figure 10.10. Number $N_{\mathrm{res}}^{(k)}(h)$ (dots) of long-lived resonance states of the standard map ($\kappa = 2.9$, $|\Omega| = 0.1$) vs h^{-1}, rescaled by the trivial scaling h. Different colors correspond to the class $\mathcal{L}$ of all long-lived resonance states (blue), or the subclasses $\mathcal{L}_1$ (green) or $\mathcal{L}_2$ (orange) of states associated with regions A_1 or A_2, respectively. The data are averaged over $\max\{1, \lfloor 5000\, h \rfloor\}$ realizations of the quantum map by varying the Bloch phases ϑ_{mom}. The quantum-mechanical scaling is compared to the box-counting scaling $N_{\mathrm{bc}}^{(k)}(\varepsilon)$ (solid lines; crosses) of boxes of side length ε that are occupied by the entire repeller Γ_{rep} (blue) or by the repeller Γ_{rep} in region A_1 (green) or A_2 (orange), plotted against ε^{-2} and rescaled by the trivial scaling ε^2. The classical data are computed numerically by the box-counting algorithm with a finite-time approximation of Γ_{rep} (crosses) and by the uncertainty algorithm (solid lines). In addition they are vertically shifted by factors $f = 0.67$, $f_1 = 0.32$, $f_2 = 1.3$ (crosses) and $f = 0.8$, $f_1 = 0.23$, $f_2 = 0.34$ (solid lines).

box-counting scaling $N_{\mathrm{bc}}^{(k)}(\varepsilon)$ of the repeller in region A_k by identifying the cell area h and ε^2. Additionally, we compare the number $N_{\mathrm{res}}^{(k)}(h)$ of long-lived chaotic resonance states with the fractal scaling of the repeller computed from the uncertainty algorithm by identifying $N_{\mathrm{bc}}^{(k)}(\varepsilon)$ and $\xi_k(\varepsilon)^2/\varepsilon^2$. We observe nice agreement between the quantum mechanical and the effective classical scaling behavior both for the data computed by the box-counting algorithm (crosses) and by the uncertainty algorithm (solid lines). This holds true for the number of all long-lived chaotic resonance states compared with fractality of the entire chaotic repeller (blue), and particularly also for the individual regions A_1 (green) and A_2 (orange). That is, there are effectively individual fractal Weyl laws for the chaotic resonance states associated with A_1 and A_2 determined by the effective fractal dimension of the repeller in the corresponding phase-space region. Note again that the classical data are vertically shifted by appropriate factors in Fig. 10.10 to better demonstrate the mutual scaling with the quantum data.

10.3.3 Multiple Partial Transport Barriers

Our last step in order to study the validity of individual fractal Weyl laws for generic systems is their verification for the case that the repeller is decomposed by more than one partial transport barrier. For the standard map the next level of partial barriers is numerically not accessible. However, the construction of the partial-barrier map in Sec. 4.1 is easily adapted to the case of more than one partial barrier. The possibility to adapt the system parameters of the partial-barrier map almost arbitrarily eventually allows us to numerically confirm the individual fractal Weyl laws for the case of two partial barriers.

To this end, we define the partial-barrier map $T := M \circ E \circ O$ that models b partial barriers at the positions $q_1 < \cdots < q_b$ as straight lines in p direction, giving a decomposition of phase space into $b+1$ regions $A_k := [q_{k-1}, q_k) \times [-\frac{1}{2}, \frac{1}{2})$ with $q_0 := 0$ and $q_{b+1} := 1$. Again, the map M describes the unconnected chaotic dynamics within the regions A_k. Here we choose the standard map at kicking strength $\kappa = 10$ acting individually on each of the regions A_k after appropriate rescaling. The map E induces a flux ϕ_k between A_k and A_{k+1} by exchanging the regions $[q_k - \phi_k, q_k) \times [-\frac{1}{2}, \frac{1}{2}) \subseteq A_k$ and $[q_k, q_k + \phi_k) \times [-\frac{1}{2}, \frac{1}{2}) \subseteq A_{k+1}$. The map O opens the system by the absorbing region Ω, which is contained in region A_1. It is convenient to use the fixed scaling parameters $\alpha := |A_{k+1}|/|A_k|$ for neighboring areas and $\varphi := \phi_{k+1}/\phi_k$ for consecutive fluxes with $\alpha \geq \varphi$.

Figure 10.11(a) shows the fractal repeller Γ_{rep} of the partial-barrier standard map with two barriers (magenta lines) defined as outlined above. Again, one qualitatively observes an imbalance of the weights that the repeller contributes to each of the three regions A_k. This suggests different effective fractal dimensions as for the standard map and the partial-barrier Baker map with a single partial barrier. Note that the shown finite-time approximation of Γ_{rep} is computed with a different number of iterations for the different regions owing to the very different escape times, cf. Sec. B.6. Moreover, also the chaotic resonance states of the corresponding quantum map exhibit localization within the three regions even though ϕ_1, $\phi_2 \ll h$, see Fig. 10.11(b–d). Particularly, there is no resonance state with large weight in region A_1 and A_3 and a dip in A_2, i.e., the states localize in one region and fall off to the next regions. By classifying the long-lived resonance states ($\gamma_{\text{c}} = 2$) according to their maximal relative weight per region, we can compute the number $N_{\text{res}}^{(k)}(h)$ of long-lived resonance states associated with A_k. The scaling of $N_{\text{res}}^{(k)}(h)$ depending on the effective size h of the Planck cell is compared with the box-counting scaling $N_{\text{bc}}^{(k)}(\varepsilon)$ of the repeller again by identifying h and ε^2 in Fig. 10.12. Here we use the uncertainty algorithm for computing $N_{\text{bc}}^{(k)}(\varepsilon)$, i.e., we identify $N_{\text{bc}}(\varepsilon)$ and $\xi_k(\varepsilon)^2/\varepsilon^2$ where $\xi_k(\varepsilon)$ denotes the fraction of ε-uncertain points in A_k. Figure 10.12 nicely demonstrates quantum-to-classical correspondence between the number of long-lived chaotic resonance states and the effective fractal scaling of the repeller (blue). Moreover, we find individual effective fractal Weyl laws for each of the regions A_k.

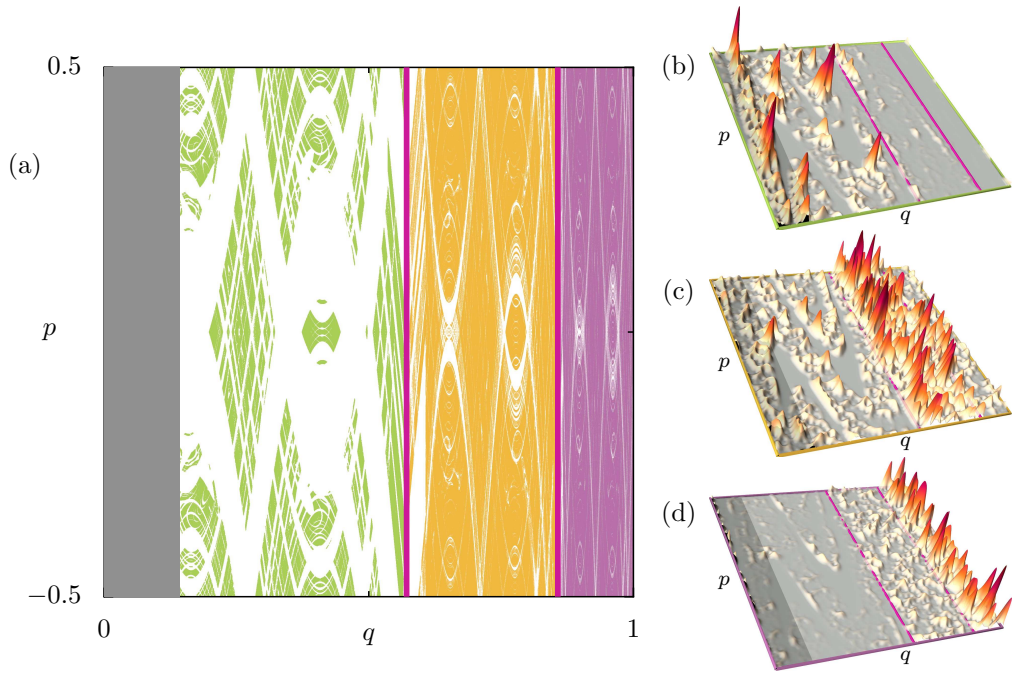

Figure 10.11. (a) Finite-time approximation of the repeller Γ_{rep} of the partial-barrier standard map with two partial barriers ($\kappa = 10$, $\alpha = 1/2$, $\varphi = 1/4$, $|\Omega|/|A_1| = 1/4$, $\phi_1/|A_2| = 1/8$); for purpose of visualization approximation times chosen as 7 for A_1, 19 for A_2, and 35 for A_3. The repeller Γ_{rep} is decomposed by the partial barriers (magenta lines) into the regions A_1 (green), A_2 (orange), and A_3 (purple). (b, c, d) Husimi representation of typical long-lived chaotic resonance states ($1/h = 1115$) associated with (b) A_1, (c) A_2, and (d) A_3.

Generic Hierarchical Structure

Let us discuss our findings in view of a generic system with a mixed phase space of regular and chaotic regions and an infinite hierarchy of partial barriers. First, the regular states which localize on the regular region clearly obey the usual Weyl law as for closed systems. For the chaotic component, we have seen that chaotic resonance states are predominantly located in one of the hierarchical regions A_k depending on their decay rate. In view of the infinite hierarchy we call them hierarchical resonance states of region A_k. Depending on the effective size h of Planck's cell the number $N_{\text{res}}^{(k)}(h)$ of long-lived hierarchical resonance states of region A_k obeys an individual fractal Weyl law,

$$N_{\text{res}}^{(k)}(h) \sim h^{-\delta_k}, \tag{10.32}$$

with the effective partial fractal dimension δ_k of $\Gamma_{\text{rep}} \cap A_k$. Note that effective fractal dimensions may be almost constant over several scales of the fractal as the transition probabilities between hierarchical regions sufficiently deep in the hierarchical structure are very small.

In dependence of Planck's constant h, there are basically four regimes for the scaling of

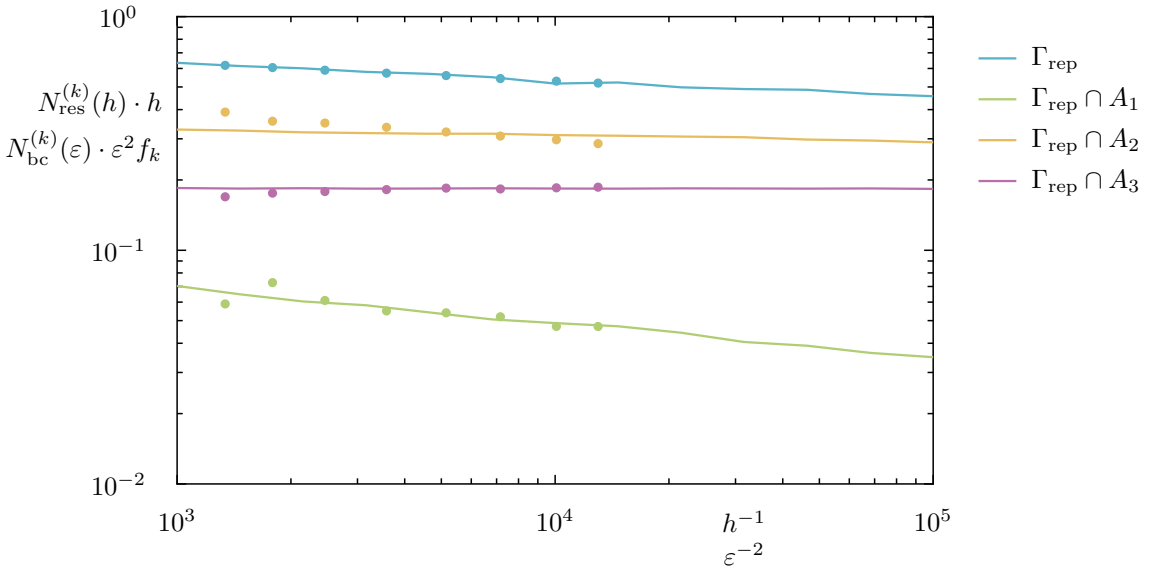

Figure 10.12. Number $N_{\mathrm{res}}^{(k)}(h)$ (dots) of long-lived resonance states of the partial-barrier standard map ($\kappa = 10$, $\alpha = 1/2$, $\varphi = 1/4$, $|\Omega|/|A_1| = 1/4$, $\phi_1/|A_2| = 1/8$) vs h^{-1}, rescaled by the trivial scaling h. Different colors correspond to the class $\mathcal{L}$ of all long-lived resonance states (blue), or the subclasses $\mathcal{L}_1$ (green), $\mathcal{L}_2$ (orange), and $\mathcal{L}_3$ (purple) of states associated with regions A_1, A_2, and A_3 respectively. The quantum-mechanical scaling is compared to the box-counting scaling which is numerically estimated by the uncertainty algorithm. The scaling of the number $N_{\mathrm{bc}}^{(k)}(\varepsilon)$ (solid lines) of boxes of side length ε that are occupied by the entire repeller Γ_{rep} (blue) or by the repeller Γ_{rep} in region A_1 (green), A_2 (orange), and A_3 (purple), is plotted against ε^{-2} and rescaled by the trivial scaling ε^2. The classical data are vertically shifted by factors $f = 1.1$, $f_1 = 0.19$, $f_2 = 0.36$, $f_3 = 0.19$.

$N_{\mathrm{res}}^{(k)}(h)$ for a specific region A_k and Eq. (10.32) is particularly relevant for one of them: (i) As long as h is too large to resolve region A_k, $h > |A_k|$, there are no resonance states supported by A_k. (ii) For $h < |A_k|$ but h larger than the greatest flux ϕ_k across its surrounding partial barriers, $h > \phi_k$, one has resonance states localized on region A_k with just a small coupling to other regions, as for closed systems [24,32]. Consequently, the number of resonance states in this regime scales with the usual Weyl law as h^{-1}. (iii) For h smaller than the flux, $h < \phi_k$, the resonance states still localize in region A_k and they begin to resolve the fractal structure of the trapped sets as described by γ-natural CIMs. This is the main regime discussed in this chapter and described by Eq. (10.32) with a fractal dimension δ_k of the intersection of the repeller with region A_k. (iv) Semiclassically, $h \searrow 0$, the fine structure of the repeller is resolved. Here the effective fractal dimensions of the repeller within the different regions A_k all approach a mutual value [98]. Moreover, the dimension of the repeller approaches two for an infinite hierarchical structure of partial barriers [212]. Hence, we expect an overall Weyl law for the hierarchical region with the number of resonance states scaling as h^{-1}.

In this chapter we have shown that the hierarchical fractal Weyl laws, Eq. (10.32), describe

the important regime (iii) where hierarchical resonance states predominantly localize on one of the regions A_k and resolve the fractal structure of the repeller. Note that Eq. (10.32) also applies to the other regimes by choosing the phase-space regions according to the predominant localization of resonance states.

One may wonder whether the presence of individual effective fractal Weyl laws contradicts the presence of an overall fractal Weyl law. Away from the asymptotic regime, the total number of long-lived resonance states and all the individual classes $\mathcal{L}_k$ of hierarchical resonance states cannot obey power laws with different exponents at the same time, since the sum of power laws is not a power law. Numerically, we cannot clearly distinguish which of the classes gives rise to a strict power law and which does not. On the available scales quantum-to-classical correspondence is basically confirmed for the total number of long-lived resonance states and for the individual classes of hierarchical resonance states as well. This results from the fact that the power-law exponents are very close to each other and on the considered scales all of them are slowly varying. Recall that according to the common heuristic argument for the fractal Weyl one needs to decompose the available phase-space region by Planck cells and applies a box-counting argument. Here, we intuitively apply this argument individually to the hierarchical resonance states of region A_k and decompose the repeller in that region. However, even if the repeller in region A_k is approximately homogeneous such that the box-counting scaling obeys a clear power law, deviations may arise from the fact that the hierarchical resonance states are not solely located in A_k. On the other hand, when applying the argument to the set of all long-lived resonance states by decomposing the entire repeller, the box-counting scaling will certainly not obey a strict power law due to the strong fractal inhomogeneity with respect to the different regions.

Further Fractional Weyl Laws

Reference [94] proposes another approach to generalize the fractal Weyl law to the chaotic component of open systems with a mixed phase space. Recall that in this thesis we concentrate on the topology of the hierarchical structure, explicitly incorporating individual partial barriers. In contrast, the approach in Ref. [94], already suggested in Ref. [89], uses that the survival probability S of chaotic orbits decays as a power law, $S(t) \sim t^{-\gamma}$, $\gamma > 0$, in presence of an infinite hierarchical structure. Using this quantity, the number N_{res} of long-lived resonance states is determined as follows: The survival probability $S(t)$ of chaotic orbits describes the area of phase space which has not escaped until time t, if we normalize the area of the chaotic phase-space component to unity. It may therefore be interpreted as the area of the available phase-space region for resonance states which live longer than t. For this approach, it is useful to set the time scale for the selection of long-lived resonance states by the h-depending Ehrenfest time τ_{Ehr}, i.e., the time scale of quantum-to-classical correspondence. In particular,

resonance states which decay faster than τ_{Ehr} show ballistic decay whereas resonance states which decay slower than τ_{Ehr} show quantum-mechanical behavior. With this, the number of long-lived resonance states is governed by

$$N_{\mathrm{res}}(h) \sim \frac{S(\tau_{\mathrm{Ehr}})}{h}. \tag{10.33}$$

First of all, this approach is capable of recovering the fractal Weyl law for fully chaotic systems. For fully chaotic systems, one observes exponential decay, $S(t) \sim e^{-\gamma t}$, and the Ehrenfest time τ_{Ehr} obeys

$$\tau_{\mathrm{Ehr}} \approx \frac{\log N_{\mathrm{open}}}{\Lambda}, \tag{10.34}$$

with the number N_{open} of open escape channels and the Lyapunov exponent Λ [48]. Using that $\log N_{\mathrm{open}} \sim -\log h$, Eq. (10.33) yields

$$N_{\mathrm{res}}(h) \sim h^{-1} e^{-\gamma \tau_{\mathrm{Ehr}}} \sim h^{-1} e^{\frac{\gamma}{\Lambda} \log h} = h^{-(1-\frac{\gamma}{\Lambda})}. \tag{10.35}$$

In view of the Kantz–Grassberger relation, Eq. (3.30), this is exactly the fractal Weyl law, Eq. (10.6).

In Ref. [94], this approach is applied to a mixed open system. One has to admit though, that the considered system is not generic as it does not exhibit a hierarchical structure but a sharply divided phase space of regular and chaotic motion. Still, chaotic orbits show stickiness near the regular structure along with algebraic decay, $S(t) \sim t^{-\gamma}$, which is attributed to a family of marginal unstable periodic orbits [213]. The time scale τ_{Ehr} to select long-lived resonance states is set to $\tau_{\mathrm{Ehr}} \sim h^{-1}$ [94], see also Refs. [89, 214] for a discussion of Ehrenfest time scales in mixed systems. Using Eq. (10.33) this yields

$$N_{\mathrm{res}}(h) \sim h^{-1} \tau_{\mathrm{Ehr}}^{-\gamma} \sim h^{\gamma-1}, \tag{10.36}$$

that is, the number of long-lived resonance states (with an h-depending cutoff) scales as a power law in h with, in general, fractional exponent. A relation with the fractality of the repeller remains unclear.

In order to understand the relation between this fractional Weyl law, Eq. (10.36), and the hierarchical fractal Weyl laws, Eq. (10.32), it is useful to investigate the set of long-lived resonance states as used in Eq. (10.36) when applied to a hierarchical structure. To this end, we first review yet another fractional Weyl law which is present even in closed systems with a generic mixed phase space. In Ref. [30] the authors introduce the class of hierarchical states for a closed system with mixed phase space. Hierarchical states are defined as eigenstates that are trapped behind a partial barrier which is quantum mechanically not resolved. That is, if

the flux across the n^*-th partial barrier is of the order of Planck's cell, $\phi_{n^*} \approx h$, hierarchical states are supported by all levels A_n of the hierarchy with $n > n^*$. Inserting this resolution condition into the scaling relation $\phi_n \sim \varphi^n$, cf. Sec. 3.1, one finds $n^* \sim \log(h)/\log(\varphi)$. The available phase-space region for hierarchical states therefore scales as [30]

$$\sum_{n>n^*} |A_n| \sim \alpha^{n^*} \sim h^{\log(\alpha)/\log(\varphi)} = h^{\frac{\gamma}{\gamma+1}}, \tag{10.37}$$

using that the area of the regions A_n scales as $|A_n| \sim \alpha^n$, cf. Sec. 3.1, and that the power-law exponent γ of the survival probability S according to Eq. (3.16). Note that different to its original formulation in Ref. [30] the power-law exponent γ of S here refers to the situation when the initial conditions are started all over the phase space, i.e., particularly also deep within the hierarchical structure, such that the γ in Eq. (10.37) refers to $\gamma - 1$ for γ from Eq. (3.16), see discussion in Sec. 3.1. Dividing the available phase-space region, Eq. (10.37), by the size h of Planck cell, one finds that the number N_{hier} of hierarchical states obeys a power law with fractional exponent,

$$N_{\text{hier}}(h) \sim h^{-\frac{1}{\gamma+1}}. \tag{10.38}$$

We emphasize that this fractional exponent occurs in a closed system and is obviously not determined by a fractal repeller. Now, the same line of arguments applies for the fractional Weyl law for the open mixed system, Eq. (10.36), in presence of a hierarchical structure. Merely the resolution condition $\phi_{n^*} \approx h$ needs to be replaced by $|A_{n^*}|/\phi_{n^*} \approx \tau_{n^*} \approx h^{-1}$. That is, the time scale of escape associated with the region A_{n^*} is of the order of the cutoff time scale $\tau_{\text{Ehr}} \sim h^{-1}$. Using the scaling of $|A_n|$ and ϕ_n within a generic hierarchy, cf. Sec. 3.1, the resolution condition translates into $n^* \sim \log(h)/\log(\frac{\varphi}{\alpha})$, and the fractional Weyl law, Eq. (10.36), is recovered by

$$\sum_{n>n^*} |A_n| \sim \alpha^{n^*} \sim h^{\log(\alpha)/\log(\varphi/\alpha)} = h^{\gamma}, \tag{10.39}$$

which gives Eq. (10.36) when divided by h. Again Eq. (3.16) for the power-law exponent γ of the survival probability S is used as above for the case of initial conditions deep within the hierarchy. We stress that the condition $\phi_n/|A_n| < h$ is more restrictive than $\phi_n < h$, that is, there are less regions A_n which satisfy the former condition. Hence, the fractional Weyl law Eq. (10.36) affects a subset of hierarchical states. In contrast, the hierarchical fractal Weyl laws, Eq. (10.32), focus on resonance states which are not trapped behind the partial barrier due to Heisenberg's uncertainty, like hierarchical states, but due to the localization of the semiclassically associated γ-natural CIM.

Chapter 11

Outlook: Optical Microcavities

The results presented in this thesis motivate further research in several directions. Let us focus on the verification and the application of our theory within an experimentally relevant scenario. Particularly close at hand is the application to optical microcavities [67]. To this end there are still a couple of pitfalls that need to be taken into account:

Experimental Setup

In this thesis we investigate the localization of chaotic resonance states in phase space. Experimentally, however, the common measurements provide the real-space picture of resonance states only. It is therefore desirable to have a physical system for which the phase-space localization due to a partial transport barrier also induces pronounced signatures in the localization in real space. The billiard system shown in Fig. 11.1 seems promising for this purpose. It combines two chaotic D-shaped billiards that are coupled by a small channel. One of the two billiard components admits an opening which allows for escape of trajectories. The repeller shown in the lower panel indicates that there are effectively two different fractal dimensions on the left and the right side. Note that the phase-space portrait is restricted to a Poincaré section at the lower boundary of the billiard. It seems likely that this imbalance of the repeller is generated by a partial barrier related to the coupling channel in the billiard. A phase-space localization of chaotic resonance states on the right or the left would directly correspond to a localization of the resonance states in real space. An experimental realization of this system seams feasible as in Ref. [196]. This open billiard system is designed together with Roland Ketzmerick.

Partial Absorption and True-Time Dynamics

In order to appropriately describe optical microcavities one needs to generalize the theory presented in this thesis to systems with partial absorption and time-continuous billiard dynamics. Regarding the issue of partial absorption we have already successfully generalized the

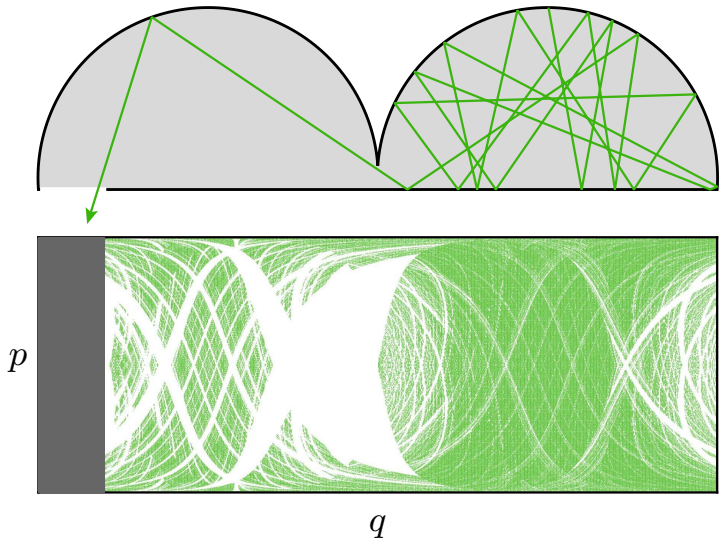

Figure 11.1. Open billiard system that couples two chaotic D-shaped billiards by a small channel (upper panel). The repeller (lower panel) shown in a Poincaré section corresponding to the lower billiard boundary indicates a restrictive partial barrier associated with the coupling channel.

construction of γ-natural CIMs to maps with a constant absorption coefficient on the opening in a project together with Tobias Becker and Konstantin Clauß [185]. To this end, we use that a measure ν converges towards a CIM under the renormalized open system dynamics. By adapting the initial measure ν such that in each step the relative weight $e^{-\gamma}$ leaves the system we obtain a CIM of decay rate γ. The crucial point is to rigorously account for the fact that the forward escaping sets are not disjoint since the opening is only partial. Still, this approach needs to be generalized from the constant absorption coefficient to an absorption profile. Moreover, it is not clear whether the hierarchical fractal Weyl laws also exist for systems with partial absorption in general. First important results for the generalization of fractal Weyl laws to partially absorbing systems without relevant partial barriers can be found in Refs. [52, 61, 71]. Another issue that needs to be taken into account is that optical microcavities are time-continuous systems and not maps. However, this can be overcome in a simple fashion for billiard systems as pointed out in Ref. [56]. Consider a trajectory in a billiard. Its dynamics between consecutive hits at the boundary is a trivial free motion and the hits obey the law of reflection. Hence, there is a one-to-one correspondence between the billiard dynamics and its Poincaré section using Birkhoff coordinates. For the escape dynamics it is important to note that the time between consecutive hits at the boundary may vary depending on the distance between the corresponding boundary points. By keeping track of these time intervals during the iteration one can calculate the true escape times from the map dynamics. In Ref. [56] this is referred to as true-time dynamics.

Higher-Dimensional Systems

So far optical microcavities are usually flat and treated as effectively two-dimensional. This corresponds to the two-dimensional symplectic maps studied in this thesis. As soon as the third dimension is not negligible one needs to consider four-dimensional symplectic maps [215]. At first sight the generalization of γ-natural CIMs to higher-dimensional systems seems to be rather straightforward. However, the role of partial barriers in higher-dimensional systems is not completely understood [216]. The partial barriers that are typically relevant in two-dimensional maps have an insufficient dimension to decompose four-dimensional phase space into almost invariant regions. Perhaps, one-parameter families of such objects may serve as appropriate partial barriers for four-dimensional maps. Anyway, recall that for the results in this thesis we do not take care of the origin of the partial barrier. We focus on the transport across some hypersurface in phase space which is characterized by the symplecticity of the map. We therefore expect that our results can be generalized to higher-dimensional systems as long as the concept of partial barriers is appropriately adapted.

Multiple Partial Barriers

Generic systems do not have just a single partial barrier but an entire hierarchy of them. The main part of this thesis focuses on the influence of a single partial barrier. The situation of more than one partial barrier is briefly touched in Chap. 10. Still, for describing generic optical microcavities it is necessary to investigate the aggregate behavior of multiple partial barriers more explicitly. In fact, their aggregate behavior can have fascinating effects as briefly described in the following. Think of the partial-barrier map with for instance two hierarchically ordered partial barriers as introduced in Sec. 10.3.3. The longest-lived resonance states then localize on the last phase-space region, i.e., A_3 using the previous notation. As preliminary results worked out in collaboration with Jan Wiersig and Julius Kullig suggest, the localization of these longest-lived resonance states is enhanced when destroying the first barrier. At first sight, this seems surprising as usually the presence of a partial barrier is expected to enhance localization. Here it is the opposite. Intuitively speaking this results from the fact that the transition probability to enter A_3 is lowered due to a larger chaotic region adjacent to A_3, while the transition probability to escape from A_3 remains the same. Although the weight of the longest-lived states in A_3 is enhanced, their decay rates increase which is again in agreement with the restrictive behavior associated with partial barriers.

Quantum Deviations

We have seen in Sec. 9.2 that the localization of chaotic resonance states and γ-natural CIMs with respect to a partial barrier does not necessarily agree if the effective size h of Planck's cell

is not sufficiently small. Experimentally relevant energy scales are not necessarily sufficiently semiclassical. Already from this point of view it is therefore desirable to understand quantum deviations in more detail. We have seen two different kinds of deviations: First, if the opening Ω or the flux ϕ across the partial barrier are not sufficiently resolved by h, i.e., $|\Omega| \gg h$ and $\phi \gg h$, we observe a localization enhancement. Numerically, we find that in the deeply quantum-mechanical regime the weight of chaotic resonance states on either side of the partial barrier is determined by Eq. (9.5). The general validity and the derivation of this relation is not explained so far. For a complete understanding it seems to be necessary to combine the universal quantum localization transition of closed systems, Sec. 5.1, with the classical results on the localization of γ-natural CIMs. One might suspect that this behavior could also be captured by an appropriate random matrix model neglecting fractal properties, such as the partial-barrier map with random matrices instead of standard or Baker map blocks. Secondly, we have seen that there may arise deviations when comparing chaotic resonance states and γ-natural CIMs on finer scales. Quantum resonance states tend to have pronounced peaks which are not captured in the phase-space structure of γ-natural CIMs. From our studies where we focus on the localization with respect to a partial barrier, we cannot conclude that such deviations vanish in the semiclassical limit. The underlying question of how quantum mechanics resolves fractal phase-space structures is currently studied in collaboration with Konstantin Clauß, Arnd Bäcker, and Roland Ketzmerick, cf. [217]. Note that motivated by studies on the Walsh quantized Baker map, the authors in Ref. [51] doubt that there actually exists a unique CIM for each decay rate γ describing the semiclassical limit of quantum resonance states decaying with γ. Similar observations are made in [85]. Anyway, in the concluding remarks in Ref. [51], the authors acknowledge that the Walsh quantized Baker map is a very special model system that is known for its high degeneracies, and that it is not clear whether these results are generic. Still, this concern is quite valid and certainly needs further investigation.

Symmetries

Symmetries play an important role for optical microcavities. In this thesis, however, we have not explicitly studied their influence. We only took care of preserving generalized time-reversal invariance, since the quantum localization transition for partial barriers in closed systems, Chap. 5, needs to be adapted otherwise. For future studies regarding optical microcavities, it might therefore be necessary to investigate to dependence of the localization of chaotic resonance states on symmetries. Let us specifically outline two examples which demonstrate the close relation between symmetries and the localization transitions studied in this thesis.

First, there is a known phenomenon that seems to perfectly correspond to the situation studied here [218–220]. Its current explanation, however, is totally different. Consider a disk-

like microcavity with a deformation that destroys mirror symmetry. Due to a small coupling of clockwise and counterclockwise propagating modes one finds pairs of resonance states which have enhanced weight in either of the subspaces. Given the results from this thesis, one might suspect that the explanation is as follows: The clockwise and counterclockwise propagating subspace correspond the phase-space regions of $p < 0$ and $p > 0$ where p denotes the angular momentum. Their small coupling is moderated by a restrictive partial barrier at $p \approx 0$. Due to the broken mirror symmetry the absorption on each side of the partial barrier might differ such that we expect the localization of chaotic resonance states due to the partial barrier. In contrast, the explanation in Ref. [219] is based on the existence of a so-called exceptional point at which a pair of eigenvalues and the corresponding eigenstates coalesce. It will be interesting to see how both approaches fit together. In particular, one might learn more about the regime which we termed deeply quantum mechanical if the role of the exceptional point is restricted to quantum mechanics. On the other hand, if the imbalance of clockwise and counterclockwise contributions is observable in the semiclassical regime, this might indicate that exceptional points are relevant also for classical mechanics in terms of Perron–Frobenius theory.

The second example shows that our theory on localization transitions might even apply to situations where the notion of partial barrier is unusual. The structure of the quantized partial-barrier map, Sec. 4.2, is surprisingly similar to the quantum Andreev map [221], which describes particle–hole symmetric Andreev reflection at the interface of a normal metal and a superconductor. There the partial barrier of the partial-barrier map may be interpreted as coupling the particle and the hole subspace. This suggests that one might apply the theory of localization of chaotic resonance states due to a partial barrier also to systems with symmetry related subspaces.

Chapter 12

Summary

Partial transport barriers in phase space are known to have a huge influence on classical and quantum dynamics. They are omnipresent in generic Hamiltonian systems, which exhibit a mixed phase space with both regular and chaotic motion. So far the influence of partial barriers has been studied mainly for closed systems. Remarkably a quantum localization transition for chaotic eigenstates has been found. As long as the flux ϕ across a partial barrier is quantum mechanically not sufficiently resolved by means of Heisenberg's uncertainty, $\phi \ll h$, chaotic eigenstates localize on either side of the partial barrier. However, if the flux is resolved, $\phi \gg h$, chaotic eigenstates are equipartitioned as if there were no partial barrier.

In this thesis we observe localization of chaotic resonance states of open systems with respect to a partial barrier even in the regime of $\phi \gg h$. We explain this localization by introducing the class of classical γ-natural conditionally invariant measures. We demonstrate quantum-to-classical correspondence for the transition from equipartition to localization when opening the system, and for a transition from localization on one side of the partial barrier to localization on the other side when varying the decay rate γ of the chaotic resonance states. Moreover, we show that the localization of chaotic resonance states on either side of a partial barrier gives rise to a hierarchy of individual fractal Weyl laws for generic systems with a hierarchical structure of partial barriers. These results have already been published in Refs. [33, 34].

To this end, we design a dynamical model system, the partial-barrier map, which mimics the turnstile mechanism of a partial barrier by decomposing dynamics into the uncoupled mixing dynamics on each side of the partial barrier and an exchange between both regions. The partial-barrier map enables us to investigate the influence of a single partial barrier without the complexity of a generic hierarchical structure. We can adapt the dynamics within each subregion which yields the analytically useful partial-barrier Baker map and the more generic partial-barrier standard map. For both systems we observe that long-lived chaotic resonance states exhibit a smooth transition from equipartition to localization on one side of the partial

barrier for increasing openness, and that for a single system with fixed opening there is a transition from localization on one side of the partial barrier to localization on the other side for chaotic resonance states with varying decay rate. The fact that both localization transitions occur in the semiclassical regime suggests a classical origin. Semiclassically, chaotic resonance states correspond to conditionally invariant measures (CIMs). However, for each decay rate γ there exist infinitely many different CIMs and it is not clear which of them is quantum mechanically relevant. To overcome this issue we propose the class of γ-natural CIMs. We numerically confirm quantum-to-classical correspondence between chaotic resonance states and γ-natural CIMs in terms of their localization with respect to the partial barrier for the partial-barrier Baker map, the partial-barrier standard map, and the generic standard map with one dominant partial barrier. For the partial-barrier Baker map we analytically derive a prediction for the weight of γ-natural CIMs on either side of the partial barrier. We find excellent agreement with the numerically computed weight also for the partial-barrier standard map and reasonably well agreement for the generic standard map. We improve the quality of the prediction in the generic case by combining it with numerical estimates.

There are two kinds of characteristic differences between the localization of chaotic resonance states and γ-natural CIMs: If the flux ϕ across the partial barrier is not sufficiently resolved on the scale h of Planck's cell, we obtain a localization enhancement for resonance states due to the suppression of transport across the partial barrier. We numerically find a bound for this localization enhancement which we call the deeply quantum-mechanical regime. Extensive studies of the partial-barrier standard map in extreme parameter regimes support that this localization enhancement vanishes for sufficiently small values of h. Moreover, we see that chaotic resonance states can exhibit pronounced peaks which are not captured by the fine structure of γ-natural CIMs. It is not clear whether these peaks survive in the semiclassical limit. Still, these deviations are irrelevant as long as we only distinguish between the localization on different sides of the partial barrier.

Our explanation of the semiclassical localization of chaotic resonance states due to a partial barrier enables us to generalize the fractal Weyl law from globally chaotic open systems to open systems with a mixed phase space. To this end, we associate each chaotic resonance state with a single region of the hierarchical structure depending on its predominant localization. As the fractal dimension of the classical repeller effectively varies between these regions, we obtain effectively an individual fractal Weyl law for each region. This is numerically confirmed for the partial-barrier Baker map, for the partial-barrier standard map with two partial barriers, and for the generic standard map with a mixed phase space and one dominating partial barrier. We argue that there exists a whole hierarchy of individual effective fractal Weyl laws in generic systems associated with the hierarchy of partial barriers.

Appendices

Appendix A

Abstract Measure and Integration Theory

This section is a concise review of abstract measure theory and integration, based on Refs. [118, 151]. The collection of basic definitions and results is focused on the concepts used in this thesis. As the notion of Lebesgue measure and integral naturally appears along with Hilbert spaces in general courses on quantum mechanics, we expect the reader to be familiar with them and refer to the literature otherwise.

Definition (σ-Algebra) A family Σ of subsets of a nonempty set Γ is called a *σ-algebra* (on Γ) if and only if (i) $\Gamma \in \Sigma$, (ii) $X \in \Sigma \Rightarrow \Gamma \setminus X \in \Sigma$, and (iii) $X_i \in \Sigma, i \in \mathbb{N} \Rightarrow \bigcup_{i\in\mathbb{N}} X_i \in \Sigma$. Throughout this thesis, we only consider the *Borel σ-algebra* (of $\mathbb{R}^n$) which is the smallest σ-algebra containing the open sets in $\mathbb{R}^n$. Note that the Borel σ-algebra also contains the fractal Cantor sets. [151, §19]

Definition (Measure) A *measure* μ on a σ-algebra Σ on Γ is a mapping $\mu : \Sigma \to \mathbb{R}_{\geq 0} \cup \{\infty\}$ for which (i) $\mu(\emptyset) = 0$ and which is (ii) σ-additive, i.e., $\mu\left(\bigcup_{i\in\mathbb{N}} X_i\right) = \sum_{i\in\mathbb{N}} \mu(X_i)$ for mutually disjoint $X_i \in \Sigma$. The elements of Σ are called *μ-measurable*. In this thesis, we focus on *probability measures* having $\mu(\Gamma) = 1$. [151, §19]

Defintion (Integral) The connection between measure and integral is provided by defining $\int_X d\mu := \int \chi_X \, d\mu := \mu(X)$, where χ_X denotes the characteristic function of X. The integral for elementary step functions follows from the linearity of the integral. One has to decompose a *measurable function* $f : \Gamma \to \mathbb{R}$, i.e., $f^{-1}(X) \in \Sigma$ for any Borel set $X \subseteq \mathbb{R}$ (e.g., if Σ is the Borel σ-algebra, continuous functions are measurable), into its positive and negative parts f_+ and f_-, $f = f_+ - f_-$, $f_\pm \geq 0$. For the nonnegative functions f_+ and f_-, there exists a (pointwise) monotonically increasing sequence of nonnegative μ-integrable step functions ψ_n, converging pointwise towards $f_\pm$. The integral of $f_\pm$ is then defined by $\int_\Gamma f_\pm \, d\mu := \lim_{n\to\infty} \int_\Gamma \psi_n \, d\mu$ if the limit exists (otherwise $\int_\Gamma f_\pm \, d\mu := \infty$). The integral f is then defined by $\int_\Gamma f \, d\mu := \int_\Gamma f_+ \, d\mu - \int_\Gamma f_- \, d\mu$ and f is called *μ-integrable*. The set of μ-integrable functions is denoted by $\mathcal{L}^1(\Gamma, \mu)$; the set of equivalence classes

in $\mathcal{L}^1(\Gamma, \mu)$ of functions that are equal almost everywhere, i.e., up to a set of μ-measure zero, is denoted by $L^1(\Gamma, \mu)$. [151, §20]

Theorem (Radon–Nikodým Theorem) Let μ, ν be two measures on (Γ, Σ). It is ν absolutely continuous with respect to μ, i.e., $\mu(X) = 0 \Rightarrow \nu(X) = 0$, if and only if there is a measurable function $\varrho : \Gamma \to \mathbb{R}_{\geq 0}$ so that

$$\nu(X) = \int_X \varrho \, d\mu \tag{A.1}$$

for any $X \in \Sigma$. The function ϱ, called the density of ν with respect to μ, is uniquely determined almost everywhere with respect to μ. For the proof, see Ref. [118, p. 344].

Definition (Pushforward Measure) Let μ be a measure on (Γ_1, Σ_1) and let Σ_2 be a σ-algebra on Γ_2. Moreover, let $T : \Gamma_1 \to \Gamma_2$ be measurable, i.e., $T^{-1}(X) \in \Sigma_1$ if $X \in \Sigma_2$. Then $T_*\mu(X) := \mu(T^{-1}(X))$ for $X \in \Sigma_2$ defines a measure on (Γ_2, Σ_2), called *pushforward measure*. [151, §20.6.4]

Theorem (Change of Variables Formula) Let μ be a measure on (Γ_1, Σ_1) and let Σ_2 be a σ-algebra on Γ_2. Moreover, let $T : \Gamma_1 \to \Gamma_2$ and $f : \Gamma_2 \to \mathbb{R}$ be measurable. Then

$$\int_{\Gamma_2} f \, dT_*\mu = \int_{\Gamma_1} f \circ T \, d\mu, \tag{A.2}$$

provided that one of the integrals exists. For the special case that Γ_1 and Γ_2 are domains from $\mathbb{R}^n$, that T is a C^1-diffeomorphism, i.e., bijective and together with its inverse continuously differentiable, and that $\mu(X) := \int_X |\det T'| \, d\Lambda$, where Λ denotes the Lebesgue measure, then $T_*\mu = \Lambda$. For the proof, see Ref. [151, §20.6.4].

Appendix B

Miscellaneous Proofs and Calculations

B.1 Kernel of Composition

The following proof of Eq. (B.3) is mainly by Marcus Waurick.

Lemma. Let X be a vector space, $P : X \to X$ a linear projection, and $V \subseteq X$ a subspace. Then it is

$$P^{-1}(V) = \ker P + \operatorname{im} P \cap V. \tag{B.1}$$

Proof. Let $x \in P^{-1}(V)$. Then there exists $v \in V$ with $Px = v \in V \cap \operatorname{im} P$. Since P is a projection, it is $(1 - P)x \in \ker P$. Thus, it is

$$x = Px + (1 - P)x \in (V \cap \operatorname{im} P) + \ker P. \tag{B.2}$$

On the other hand, let $p \in \ker P$. Then it is $p \in P^{-1}(\{0\}) \subseteq P^{-1}(V)$ as V is a vector space. Moreover, for $v \in \operatorname{im} P \cap V$ there exists $x \in X$ such that $Px = v$. Furthermore, P is a projection such that $Pv = P^2x = Px = v$. Thus, $v \in P^{-1}(V)$. Since V is a subspace, it is $\ker P + \operatorname{im} P \cap V \subseteq P^{-1}(V)$. □

Proposition. Let X be a vector space, $P_1 : X \to X$ and $P_2 : X \to X$ linear projections, and let $U : X \to X$ be linear. Then it is

$$\ker P_1 U P_2 = \ker P_2 + \operatorname{im} P_2 \cap U^{-1}(\ker P_1). \tag{B.3}$$

Proof. It is

$$\ker P_1 U P_2 = (P_1 U P_2)^{-1}(\{0\}) = P_2^{-1}\left[U^{-1}\left[P_1^{-1}(\{0\})\right]\right]. \tag{B.4}$$

The assertion follows immediately from the above lemma. □

B.2 Generating Functions for Symplectic Maps

Consider a sufficiently smooth function $S:\ \mathbb{R}^2 \to \mathbb{R}^2$, restricted to some appropriate domain. Then the map $T:\ \Gamma \to \Gamma$, $\Gamma \subseteq \mathbb{R}^2$, defined by

$$(Q,P) = T(q,p) \quad \Leftrightarrow \quad p = -\partial_2 S(Q,q),\ P = \partial_1 S(Q,q), \tag{B.5}$$

is symplectic provided that such a T exists. To this end, we denote $T(q,p) = \big(T_1(q,p), T_2(q,p)\big)$ such that

$$p = -\partial_2 S(T_1(q,p),q), \tag{B.6}$$
$$T_2(q,p) = \partial_1 S(T_1(q,p),q). \tag{B.7}$$

The map T is symplectic if

$$\det DT(q,p) = \partial_1 T_1(q,p)\,\partial_2 T_2(q,p) - \partial_2 T_1(q,p)\,\partial_1 T_2(q,p) = \{T_1,T_2\}(q,p) = 1. \tag{B.8}$$

Differentiating Eq. (B.6), we obtain

$$\partial_1 \pi_2(q,p) = 0 = -\partial_{12} S(T_1(q,p),q)\,\partial_1 T_1(q,p) - \partial_{22} S(T_1(q,p),q), \tag{B.9}$$

where the function π_2 denotes the projection onto the second component, $\pi_2(q,p) := p$. This gives

$$\partial_1 T_1(q,p) = -\frac{\partial_{22} S(T_1(q,p),q)}{\partial_{12} S(T_1(q,p),q)}. \tag{B.10}$$

Analogously, it is

$$\partial_2 \pi_2(q,p) = 1 = -\partial_{12} S(T_1(q,p),q)\,\partial_2 T_1(q,p), \tag{B.11}$$

which yields

$$\partial_2 T_1(q,p) = -\frac{1}{\partial_{12} S(T_1(q,p),q)}. \tag{B.12}$$

On the other hand, differentiating Eq. (B.7), we find

$$\begin{aligned} \partial_1 T_2(q,p) &= \partial_{11} S(T_1(q,p),q)\, \partial_1 T_1(q,p) + \partial_{21} S(T_1(q,p),q) && \text{(B.13)} \\ &= -\partial_{11} S(T_1(q,p),q)\, \frac{\partial_{22} S(T_1(q,p),q)}{\partial_{12} S(T_1(q,p),q)} + \partial_{21} S(T_1(q,p),q), && \text{(B.14)} \end{aligned}$$

and

$$\begin{aligned} \partial_2 T_2(q,p) &= \partial_{11} S(T_1(q,p),q)\, \partial_2 T_1(q,p) && \text{(B.15)} \\ &= -\frac{\partial_{11} S(T_1(q,p),q)}{\partial_{12} S(T_1(q,p),q)}. && \text{(B.16)} \end{aligned}$$

Inserting this into Eq. (B.8) proves the symplecticity of T,

$$\begin{aligned} \det DT(q,p) &= \left[\frac{\partial_{11} S \cdot \partial_{22} S}{[\partial_{12} S]^2} + \frac{1}{\partial_{12} S} \left(-\frac{\partial_{11} S \cdot \partial_{22} S}{\partial_{12} S} + \partial_{21} S \right) \right]_{(T_1(q,p),q)} && \text{(B.17)} \\ &= \frac{\partial_{21} S(T_1(q,p),q)}{\partial_{12} S(T_1(q,p),q)} && \text{(B.18)} \\ &= 1, && \text{(B.19)} \end{aligned}$$

using Schwarz's theorem.

B.3 Proofs of Convergence towards Invariant Measure

In this section, we present the main ideas for the proofs of Eqs. (7.5) and (7.7). To this end, it is useful to introduce the induced operator [173, Chap. 4]: For a map $T : \Gamma \to \Gamma$, the induced operator K_T (also called composition or Koopman operator) is defined by

$$K_T f := f \circ T, \tag{B.20}$$

for functions $f : \Gamma \to \mathbb{R}$. The operator K_T is linear, and if T is invertible and both T and T^{-1} are measurable, K_T is even unitary on L^2. As this immediately provides thoroughly developed Hilbert space methods, quite often in mathematics, this concept is favored over the abstract measure theory. We consider symplectic maps T such that T is invertible (since $\det T' \neq 0$) and both T and T^{-1} are measurable. Thus, we are equally allowed to use the same Hilbert space methods for the transfer operator F_T (also called Perron–Frobenius operator), defined by

$$F_T f := f \circ T^{-1}. \tag{B.21}$$

Ergodic Systems

Consider a corollary of the mean ergodic theorem by von Neumann [173, Thm. 8.10]: Let $T : \Gamma \to \Gamma$ together with the invariant measure μ be ergodic. Then it is

$$\lim_{N\to\infty} \frac{1}{N} \sum_{n=0}^{N-1} F_T^n f = \left(\int_\Gamma f \, d\mu \right) \chi_\Gamma \tag{B.22}$$

for each $f \in L^2(\Omega, \mu)$.

This corollary can now be used to derive Eq. (7.5). Given a measure ν that is absolutely continuous with respect to μ with density ϱ, it is

$$\begin{aligned} \frac{1}{N} \sum_{n=0}^{N-1} T_*^n \nu(X) &= \frac{1}{N} \sum_{n=0}^{N-1} \int_{T^{-n}(X)} \varrho \, d\mu & \text{(B.23)} \\ &= \frac{1}{N} \sum_{n=0}^{N-1} \int_X \underbrace{\varrho \circ T^{-n}}_{F_T^n \varrho} \, d\mu & \text{(B.24)} \end{aligned}$$

for all measurable $X \subseteq \Gamma$. From Eq. (B.22), we conclude

$$\frac{1}{N} \sum_{n=0}^{N-1} T_*^n \nu(X) = \underbrace{\int_\Gamma \varrho \, d\mu}_{\nu(\Gamma)=1} \cdot \underbrace{\int_X d\mu}_{\mu(X)} . \tag{B.25}$$

Mixing Systems

Consider the following proposition [173, Thm. 9.4]: Let $T : \Gamma \to \Gamma$ together with the invariant measure μ be mixing as defined in Eq. (7.6). Then it is

$$\langle F_T^n f \,|\, g \rangle \to \langle f \,|\, \chi_\Gamma \rangle \langle \chi_\Gamma \,|\, g \rangle = \int_\Gamma f \, d\mu \cdot \int_\Gamma g \, d\mu \tag{B.26}$$

for all f, $g \in L^2(\Omega, \mu)$.

This proposition can now be used to derive Eq. (7.7). Given a measure ν that is absolutely continuous with respect to μ with density ϱ, it is

$$\begin{aligned} T_*^n \nu(X) &= \int_{T^{-n}(X)} \varrho \, d\mu & \text{(B.27)} \\ &= \int_X \varrho \circ T^{-n} \, d\mu & \text{(B.28)} \\ &= \langle F_T^n \varrho \,|\, \chi_X \rangle & \text{(B.29)} \end{aligned}$$

for all measurable $X \subseteq \Gamma$. From Eq. (B.26), we conclude

$$T_*^n \nu(X) \to \langle\, \varrho \,|\, \chi_\Gamma \,\rangle \, \langle\, \chi_\Gamma \,|\, \chi_X \,\rangle = \underbrace{\int_\Gamma \varrho \, d\mu}_{\nu(\Gamma)=1} \cdot \underbrace{\int_X d\mu}_{\mu(X)} . \tag{B.30}$$

B.4 Construction of Chaotic Resonance States

The following construction of chaotic resonance states is intended to underline quantum-to-classical correspondence with CIMs in view of Eq. (7.39).

Proposition. Let U be unitary and P be an orthogonal projection, $P^2 = P$, $P^* = P$; $P_0 := \mathbb{1} - P$. Moreover, let $\psi_0 \in \operatorname{im} P_0 \cap \bigcap_{n\in\mathbb{N}} U^n \operatorname{im} P$ and $\lambda \in \mathbb{C}$ with $|\lambda| < 1$. Then for $\psi := \sum_{n\in\mathbb{N}_0} \lambda^n (UP)^{*n} \psi_0$ it is

$$UP\psi = \lambda\psi. \tag{B.31}$$

Proof. First of all, we split the sum into

$$UP\psi = UP\psi_0 + \sum_{n=1}^{\infty} \lambda^n UP(UP)^{*n}\psi_0. \tag{B.32}$$

The first term $UP\psi_0$ vanishes as

$$P\psi_0 = (1 - P_0)\psi_0 = \psi_0 - P_0\psi_0 = 0, \tag{B.33}$$

because $\psi_0 \in \operatorname{im} P_0$, i.e., $P_0\psi_0 = \psi_0$. We will now show that $UP(UP)^{*n}\psi_0 = (UP)^{*(n-1)}\psi_0$ for $n \geq 1$. Note that if we have shown this, Eq. (B.31) follows directly by an index shift,

$$UP\psi = \sum_{n=1}^{\infty} \lambda^n (UP)^{*(n-1)}\psi_0 = \lambda \sum_{n=0}^{\infty} \lambda^n (UP)^{*n}\psi_0. \tag{B.34}$$

To this end, we explicitly consider

$$UP(UP)^{*n}\psi_0 = U \underbrace{PU^{-1} \cdots PU^{-1}}_{n \text{ times}} \psi_0. \tag{B.35}$$

Using that $\psi_0 \in U \operatorname{im} P$, which is equivalent to $U^{-1}\psi_0 \in \operatorname{im} P$ since U is bijective, we

find $PU^{-1}\psi_0 = U^{-1}\psi_0$ such that

$$UP(UP)^{*n}\psi_0 = U\underbrace{PU^{-1}\cdots PU^{-1}}_{(n-1)\text{ times}}U^{-1}\psi_0. \tag{B.36}$$

Analogously, as $\psi_0 \in U^2\mathrm{im}\,P$ we obtain $PU^{-2}\psi_0 = U^{-2}\psi_0$ and in just the same way $PU^{-n}\psi_0 = U^{-n}\psi_0$ for all $n \geq 1$. This gives

$$UP(UP)^{*n}\psi_0 = UU^{-n}\psi_0 = U^{-(n-1)}\psi_0. \tag{B.37}$$

Now the other way around, we find

$$U^{-(n-1)}\psi_0 = \underbrace{PU^{-1}\cdots PU^{-1}}_{(n-1)\text{ times}}\psi_0 = (UP)^{*(n-1)}\psi_0, \tag{B.38}$$

and thus, $UP(UP)^{*n}\psi_0 = (UP)^{*(n-1)}\psi_0$. The convergence of $\sum_{n\in\mathbb{N}_0}\lambda^n(UP)^{*n}\psi_0$ is assured by the Neumann series since $\|UP\| \leq 1$ and $|\lambda| < 1$. □

For the interpretation of this result note that we have not discussed whether the set $\mathrm{im}\,P_0 \cap \bigcap_{n\in\mathbb{N}} U^n\mathrm{im}\,P$ contains more than just the zero or whether for $\psi_0 \neq 0$ one obtains $\psi \neq 0$. Thus, the above result should be interpreted first of all as an algebraic analogy to CIMs.

B.5 Proof of Equation (10.18)

Consider the sequence $(s_n)_{n\in\mathbb{N}}$ of elements

$$s_n := \sqrt[n]{c_1\lambda_1^n + c_2\lambda_2^n}, \tag{B.39}$$

with $c_1, c_2 \in \mathbb{R}$ and $\lambda_1 > \lambda_2 \geq 0$. We further require that $c_1\lambda_1^n + c_2\lambda_2^n \geq 0$ which implies that $c_1 > 0$. Defining $c_{\max} = \max\{|c_1|, |c_2|\}$, it is

$$s_n \leq \sqrt[n]{c_{\max}\lambda_1^n + c_{\max}\lambda_2^n} \leq \sqrt[n]{2c_{\max}\lambda_1^n} = \sqrt[n]{2c_{\max}}\,\lambda_1 \to \lambda_1. \tag{B.40}$$

In order to find a lower bound for s_n, we use that

$$c_1\lambda_1^n + c_2\lambda_2^n \geq \frac{c_1}{2}\lambda_1^n \tag{B.41}$$

for $n > \log(-2c_2/c_1)/\log(\lambda_1/\lambda_2)$ if $c_2 < 0$. If $c_2 \geq 0$, the above inequality holds true for all $n \in \mathbb{N}$. For sufficiently large n, this gives

$$s_n \geq \sqrt[n]{\frac{c_1}{2}\lambda_1^n} = \sqrt[n]{\frac{c_1}{2}}\,\lambda_1 \to \lambda_1. \tag{B.42}$$

The sandwich theorem thus implies

$$\lim_{n\to\infty} \sqrt[n]{c_1\lambda_1^n + c_2\lambda_2^n} = \lambda_1. \tag{B.43}$$

B.6 Average Escape Times from Markov Chain

The following derivation of average escape times from a Markov chain is based on a calculation presented in Ref. [123, Sec. 4.2]. Let us consider a simple Markov chain model with N regions, A_1, ..., A_N, defined by the matrix $T \in \mathbb{R}^{N\times N}$ that contains the transition probabilities between neighboring regions. We particularly allow for escape from the chain. The iteration of an initial vector $p(0)$, the i-th component of which describes the probability to be region A_i, is then given by

$$p(n) = T^n p(0), \qquad (n \in \mathbb{N}_0). \tag{B.44}$$

With this the probability $P_{\mathrm{s}}(n)$ to survive n iterations when starting in region A_i, $1 \leq k \leq N$, reads

$$P_{\mathrm{s}}(n) = \sum_{k=1}^{N} \langle\, e_k \,|\, T^n e_i \,\rangle, \tag{B.45}$$

where e_k, $1 \leq k \leq N$, denotes the standard basis in $\mathbb{R}^N$. The probability $P_{\mathrm{esc}}(n)$ to escape from the system in step n (and not before) when starting in A_i can be obtained from

$$P_{\mathrm{s}}(n) = P_{\mathrm{s}}(n-1)\cdot x, \tag{B.46}$$

$$P_{\mathrm{esc}}(n) = P_{\mathrm{s}}(n-1)\cdot(1-x), \tag{B.47}$$

where x denotes the probability to survive the n-th iteration provided survival under the previous $n-1$ iterations. This gives

$$P_{\mathrm{esc}}(n) = P_{\mathrm{s}}(n-1) - P_{\mathrm{s}}(n). \tag{B.48}$$

Hence, the average time $\tau_{\rm esc}^{(i)}$ to escape from the system when starting in A_i follows from

$$\begin{aligned}
\tau_{\rm esc}^{(i)} &= \sum_{n=1}^{\infty} n \cdot P_{\rm esc}(n) && \text{(B.49)}\\
&= \sum_{n=1}^{\infty} n \cdot \left\{ \sum_{k=1}^{N} \langle\, e_k \,|\, T^{n-1} e_i \,\rangle - \sum_{k=1}^{N} \langle\, e_k \,|\, T^{n} e_i \,\rangle \right\} && \text{(B.50)}\\
&= \sum_{k=1}^{N} \left\{ \langle\, e_k \,|\, \sum_{n=1}^{\infty} n \cdot T^{n-1} e_i \,\rangle - \langle\, e_k \,|\, \sum_{n=1}^{\infty} n \cdot T^{n} e_i \,\rangle \right\} && \text{(B.51)}\\
&= \sum_{k=1}^{N} \left\{ \langle\, e_k \,|\, \sum_{n=0}^{\infty} (n+1) \cdot T^{n} e_i \,\rangle - \langle\, e_k \,|\, \sum_{n=0}^{\infty} n \cdot T^{n} e_i \,\rangle \right\} && \text{(B.52)}\\
&= \sum_{k=1}^{N} \langle\, e_k \,|\, \sum_{n=0}^{\infty} T^{n} e_i \,\rangle && \text{(B.53)}\\
&= \sum_{k=1}^{N} \langle\, e_k \,|\, (\mathbb{1} - T)^{-1} e_i \,\rangle. && \text{(B.54)}
\end{aligned}$$

Bibliography

[1] L. D. Landau and E. M. Lifschitz: *Elektrodynamik der Kontinua*, Vol. 8 of *Lehrbuch der theoretischen Physik*, (Verlag Harri Deutsch, Frankfurt a. M.), 5th edn., (1990).

[2] L. D. Landau and E. M. Lifschitz: *Hydrodynamik*, Vol. 6 of *Lehrbuch der theoretischen Physik*, (Verlag Harri Deutsch, Frankfurt a. M.), 5th edn., (2007).

[3] R. B. Laughlin: *Quantized Hall conductivity in two dimensions*, Phys. Rev. B **23** (1981), 5632–5633.

[4] J. Bardeen, L. N. Cooper, and J. R. Schrieffer: *Theory of Superconductivity*, Phys. Rev. **108** (1957), 1175–1204.

[5] C. H. Bennett, G. Brassard, C. Crépeau, R. Jozsa, A. Peres, and W. K. Wootters: *Teleporting an unknown quantum state via dual classical and Einstein-Podolsky-Rosen channels*, Phys. Rev. Lett. **70** (1993), 1895–1899.

[6] P. W. Anderson: *Absence of Diffusion in Certain Random Lattices*, Phys. Rev. **109** (1958), 1492–1505.

[7] E. Abrahams, P. W. Anderson, D. C. Licciardello, and T. V. Ramakrishnan: *Scaling Theory of Localization*, Phys. Rev. Lett. **42** (1979), 673–676.

[8] G. Bergmann: *Weak localization in thin films*, Phys. Rep. **107** (1984), 1–58.

[9] X.-L. Qi and S.-C. Zhang: *Topological insulators and superconductors*, Rev. Mod. Phys. **83** (2011), 1057–1110.

[10] D. M. Basko, I. L. Aleiner, and B. L. Altshuler: *Metal–insulator transition in a weakly interacting many-electron system with localized single-particle states*, Ann. Phys. (N.Y.) **321** (2006), 1126–1205.

[11] I. C. Percival: *Regular and irregular spectra*, J. Phys. B **6** (1973), L229–L232.

[12] A. I. Shnirelman: *Ergodic properties of eigenfunctions* (in Russian), Usp. Math. Nauk **29** (1974), 181–182.

[13] M. V. Berry: *Semi-classical mechanics in phase space: A study of Wigner's function*, Phil. Trans. R. Soc. A **287** (1977), 237–271.

[14] M. V. Berry: *Regular and irregular semiclassical wavefunctions*, J. Phys. A **10** (1977), 2083–2091.

[15] A. Voros: *Semi-classical ergodicity of quantum eigenstates in the Wigner representation*, in: Casati and Ford [40], 326–333.

[16] R. S. MacKay, J. D. Meiss, and I. C. Percival: *Stochasticity and Transport in Hamiltonian Systems*, Phys. Rev. Lett. **52** (1984), 697–700.

[17] R. S. MacKay, J. D. Meiss, and I. C. Percival: *Transport in Hamiltonian systems*, Physica D **13** (1984), 55–81.

[18] Y. Colin de Verdière: *Ergodicité et fonctions propres du laplacien* (in French), Commun. Math. Phys. **102** (1985), 497–502.

[19] R. C. Brown and R. E. Wyatt: *Quantum mechanical manifestation of cantori: Wavepacket localization in stochastic regions*, Phys. Rev. Lett. **57** (1986), 1–4.

[20] T. Geisel, G. Radons, and J. Rubner: *Kolmogorov-Arnol'd-Moser Barriers in the Quantum Dynamics of Chaotic Systems*, Phys. Rev. Lett. **57** (1986), 2883–2886.

[21] S. Zelditch: *Uniform distribution of eigenfunctions on compact hyperbolic surfaces*, Duke. Math. J. **55** (1987), 919–941.

[22] B. Helffer, A. Martinez, and D. Robert: *Ergodicité et limite semi-classique* (in French), Commun. Math. Phys. **109** (1987), 313–326.

[23] J. D. Meiss: *Symplectic maps, variational principles, and transport*, Rev. Mod. Phys. **64** (1992), 795–848.

[24] O. Bohigas, S. Tomsovic, and D. Ullmo: *Manifestations of classical phase space structures in quantum mechanics*, Phys. Rep. **223** (1993), 43–133.

[25] P. Gérard and E. Leichtnam: *Ergodic properties of eigenfunctions for the Dirichlet problem*, Duke Math. J. **71** (1993), 559–607.

[26] S. Zelditch and M. Zworski: *Ergodicity of eigenfunctions for ergodic billiards*, Commun. Math. Phys. **175** (1996), 673–682.

[27] A. Bouzouina and S. De Biévre: *Equipartition of the eigenfunctions of quantized ergodic maps on the torus*, Commun. Math. Phys. **178** (1996), 83–105.

[28] S. Zelditch: *Index and dynamics of quantized contact transformations.*, Ann. Inst. Fourier **47** (1997), 305–363.

[29] A. Bäcker, R. Schubert, and P. Stifter: *Rate of quantum ergodicity in Euclidean billiards*, Phys. Rev. E **57** (1998), 5425–5447, ; erratum ibid. **58** (1998) 5192.

[30] R. Ketzmerick, L. Hufnagel, F. Steinbach, and M. Weiss: *New Class of Eigenstates in Generic Hamiltonian Systems*, Phys. Rev. Lett. **85** (2000), 1214–1217.

[31] N. T. Maitra and E. J. Heller: *Quantum transport through cantori*, Phys. Rev. E **61** (2000), 3620–3631.

[32] M. Michler, A. Bäcker, R. Ketzmerick, H.-J. Stöckmann, and S. Tomsovic: *Universal Quantum Localizing Transition of a Partial Barrier in a Chaotic Sea*, Phys. Rev. Lett. **109** (2012), 234101.

[33] M. J. Körber, M. Michler, A. Bäcker, and R. Ketzmerick: *Hierarchical Fractal Weyl Laws for Chaotic Resonance States in Open Mixed Systems*, Phys. Rev. Lett. **111** (2013), 114102.

[34] M. J. Körber, A. Bäcker, and R. Ketzmerick: *Localization of Chaotic Resonance States due to a Partial Transport Barrier*, Phys. Rev. Lett. **115** (2015), 254101.

[35] L. Markus and K. R. Meyer: *Generic Hamiltonian Dynamical Systems are neither Integrable nor Ergodic*, No. 144 in Mem. Amer. Math. Soc., (American Mathematical Society, Providence, Rhode Island), (1974).

[36] S. Keshavamurthy and P. Schlagheck: *Dynamical Tunneling: Theory and Experiment*, (Taylor & Francis, Boca Raton), (2011).

[37] R. S. MacKay and J. D. Meiss: *Relation between quantum and classical thresholds for multiphoton ionization of excited atoms*, Phys. Rev. A **37** (1988), 4702–4706.

[38] O. Bohigas, S. Tomsovic, and D. Ullmo: *Dynamical quasidegeneracies and separation of regular and irregular quantum levels*, Phys. Rev. Lett. **64** (1990), 1479–1482.

[39] U. Smilansky, S. Tomsovic, and O. Bohigas: *Spectral fluctuations and transport in phase space*, J. Phys. A **25** (1992), 3261.

[40] G. Casati and J. Ford (Eds.): *Stochastic Behavior in Classical and Quantum Hamiltonian Systems*, Vol. 93 of *Lect. Notes Phys.*, (Springer-Verlag, Berlin), (1979).

[41] S. Fishman, D. R. Grempel, and R. E. Prange: *Chaos, Quantum Recurrences, and Anderson Localization*, Phys. Rev. Lett. **49** (1982), 509–512.

[42] S. Attal: *Quantum Noise Theory*, (Springer-Verlag), (in publication), `http://math.univ-lyon1.fr/~attal/chapters.html`.

[43] G. Pianigiani and J. A. Yorke: *Expanding Maps on Sets which are Almost Invariant: Decay and Chaos*, Trans. Amer. Math. Soc. **252** (1979), 351–366.

[44] H. Kantz and P. Grassberger: *Repellers, semi-attractors, and long-lived chaotic transients*, Physica D **17** (1985), 75–86.

[45] T. Tél: *Escape rate from strange sets as an eigenvalue*, Phys. Rev. A **36** (1987), 1502–1505.

[46] G. Casati, G. Maspero, and D. L. Shepelyansky: *Quantum fractal eigenstates*, Physica D **131** (1999), 311–316.

[47] W. T. Lu, S. Sridhar, and M. Zworski: *Fractal Weyl Laws for Chaotic Open Systems*, Phys. Rev. Lett. **91** (2003), 154101.

[48] H. Schomerus and J. Tworzydło: *Quantum-to-Classical Crossover of Quasibound States in Open Quantum Systems*, Phys. Rev. Lett. **93** (2004), 154102.

[49] J. P. Keating, M. Novaes, S. D. Prado, and M. Sieber: *Semiclassical Structure of Chaotic Resonance Eigenfunctions*, Phys. Rev. Lett. **97** (2006), 150406.

[50] M. F. Demers and L.-S. Young: *Escape rates and conditionally invariant measures*, Nonlinearity **19** (2006), 377–397.

[51] S. Nonnenmacher and M. Rubin: *Resonant eigenstates for a quantized chaotic system*, Nonlinearity **20** (2007), 1387.

[52] S. Nonnenmacher and E. Schenck: *Resonance distribution in open quantum chaotic systems*, Phys. Rev. E **78** (2008), 045202.

[53] S. Nonnenmacher and M. Zworski: *Quantum decay rates in chaotic scattering*, Acta Math. **203** (2009), 149–233.

[54] L. Ermann, G. G. Carlo, and M. Saraceno: *Localization of Resonance Eigenfunctions on Quantum Repellers*, Phys. Rev. Lett. **103** (2009), 054102.

[55] Y.-C. Lai and T. Tél: *Transient Chaos: Complex Dynamics on Finite Time Scales*, No. 173 in Applied Mathematical Sciences, (Springer Verlag, New York), 1st edn., (2011).

[56] E. G. Altmann, J. S. E. Portela, and T. Tél: *Leaking chaotic systems*, Rev. Mod. Phys. **85** (2013), 869–918.

[57] E. G. Altmann, J. S. E. Portela, and T. Tél: *Chaotic Systems with Absorption*, Phys. Rev. Lett. **111** (2013), 144101.

[58] M. Novaes: *Resonances in open quantum maps*, J. Phys. A **46** (2013), 143001.

[59] A. E. Motter, M. Gruiz, G. Károlyi, and T. Tél: *Doubly Transient Chaos*, Phys. Rev. Lett. **111** (2013), 194101.

[60] T. Weich, S. Barkhofen, U. Kuhl, C. Poli, and H. Schomerus: *Formation and interaction of resonance chains in the open three-disk system*, New J. Phys. **16** (2014), 033029.

[61] M. Schönwetter and E. G. Altmann: *Quantum signatures of classical multifractal measures*, Phys. Rev. E **91** (2015), 012919.

[62] P. Gaspard: *Chaos, Scattering and Statistical Mechanics*, No. 9 in Cambridge Nonlinear Science Series, (Cambridge University Press, Cambridge, United Kingdom), (1998).

[63] C. Mahaux and H. A. Weidenmüller: *Shell-Model Approach to Nuclear Reactions*, (North-Holland Publishing Company, Amsterdam), (1969).

[64] F.-M. Dittes: *The decay of quantum systems with a small number of open channels*, Phys. Rep. **339** (2000), 215–316.

[65] K. Pichugin, H. Schanz, and P. Šeba: *Effective coupling for open billiards*, Phys. Rev. E **64** (2001), 056227.

[66] H. Schomerus: *Random matrix approaches to open quantum systems*, in: *Stochastic processes and random matrices* (Eds. A. Altland, Y. Fyodorov, N. O'Connell and G. Schehr), Vol. 104 of *Les Houches*. Elsevier, (in publication).

[67] H. Cao and J. Wiersig: *Dielectric microcavities: Model systems for wave chaos and non-Hermitian physics*, Rev. Mod. Phys. **87** (2015), 61–111.

[68] J. U. Nöckel and A. D. Stone: *Ray and wave chaos in asymmetric resonant optical cavities*, Nature **385** (1997), 45–47.

[69] C. Gmachl, F. Capasso, E. E. Narimanov, J. U. Nöckel, A. D. Stone, J. Faist, D. L. Sivco, and A. Y. Cho: *High-Power Directional Emission from Microlasers with Chaotic Resonators*, Science **280** (1998), 1556–1564.

[70] S.-Y. Lee, S. Rim, J.-W. Ryu, T.-Y. Kwon, M. Choi, and C.-M. Kim: *Quasiscarred Resonances in a Spiral-Shaped Microcavity*, Phys. Rev. Lett. **93** (2004), 164102.

[71] J. Wiersig and J. Main: *Fractal Weyl law for chaotic microcavities: Fresnel's laws imply multifractal scattering*, Phys. Rev. E **77** (2008), 036205.

[72] J. Wiersig and M. Hentschel: *Combining Directional Light Output and Ultralow Loss in Deformed Microdisks*, Phys. Rev. Lett. **100** (2008), 033901.

[73] J.-B. Shim, S.-B. Lee, S. W. Kim, S.-Y. Lee, J. Yang, S. Moon, J.-H. Lee, and K. An: *Uncertainty-Limited Turnstile Transport in Deformed Microcavities*, Phys. Rev. Lett. **100** (2008), 174102.

[74] S. Shinohara, T. Harayama, T. Fukushima, M. Hentschel, T. Sasaki, and E. E. Narimanov: *Chaos-Assisted Directional Light Emission from Microcavity Lasers*, Phys. Rev. Lett. **104** (2010), 163902.

[75] J.-B. Shim, J. Wiersig, and H. Cao: *Whispering gallery modes formed by partial barriers in ultrasmall deformed microdisks*, Phys. Rev. E **84** (2011), 035202.

[76] T. Tél and M. Gruiz: *Chaotic Dynamics – An Introduction Based on Classical Mechanics*, (Cambridge University Press, Cambridge, United Kingdom), (2006).

[77] H. Weyl: *Ueber die asymptotische Verteilung der Eigenwerte*, Nachr. d. Königl. Ges. d. Wiss. zu Göttingen (1911), 110–117.

[78] H. Weyl: *Das asymptotische Verteilungsgesetz der Eigenwerte linearer partieller Differentialgleichungen (mit einer Anwendung auf die Theorie der Hohlraumstrahlung)*, Math. Ann. **71** (1912), 441–479.

[79] J. Sjöstrand: *Geometric bounds on the density of resonances for semiclassical problems*, Duke Math. J. **60** (1990), 1–57.

[80] M. Zworski: *Dimension of the limit set and the density of resonances for convex cocompact hyperbolic surfaces*, Invent. math. **136** (1999), 353–409.

[81] K. K. Lin: *Numerical Study of Quantum Resonances in Chaotic Scattering*, J. Comput. Phys. **176** (2002), 295–329.

[82] K. K. Lin and M. Zworski: *Quantum resonances in chaotic scattering*, Chem. Phys. Lett. **355** (2002), 201–205.

[83] S. Nonnenmacher and M. Zworski: *Fractal Weyl laws in discrete models of chaotic scattering*, J. Phys. A **38** (2005), 10683.

[84] S. Nonnenmacher and M. Zworski: *Distribution of Resonances for Open Quantum Maps*, Commun. Math. Phys. **269** (2007), 311–365.

[85] J. P. Keating, S. Nonnenmacher, M. Novaes, and M. Sieber: *On the resonance eigenstates of an open quantum baker map*, Nonlinearity **21** (2008), 2591–2624.

[86] D. L. Shepelyansky: *Fractal Weyl law for quantum fractal eigenstates*, Phys. Rev. E **77** (2008), 015202.

[87] J. M. Pedrosa, G. G. Carlo, D. A. Wisniacki, and L. Ermann: *Distribution of resonances in the quantum open baker map*, Phys. Rev. E **79** (2009), 016215.

[88] J. A. Ramilowski, S. D. Prado, F. Borondo, and D. Farrelly: *Fractal Weyl law behavior in an open Hamiltonian system*, Phys. Rev. E **80** (2009), 055201.

[89] M. Kopp and H. Schomerus: *Fractal Weyl laws for quantum decay in dynamical systems with a mixed phase space*, Phys. Rev. E **81** (2010), 026208.

[90] A. Eberspächer, J. Main, and G. Wunner: *Fractal Weyl law for three-dimensional chaotic hard-sphere scattering systems*, Phys. Rev. E **82** (2010), 046201.

[91] M. E. Spina, I. García-Mata, and M. Saraceno: *Weyl law for fat fractals*, J. Phys. A **43** (2010), 392003.

[92] J. M. Pedrosa, D. Wisniacki, G. G. Carlo, and M. Novaes: *Short periodic orbit approach to resonances and the fractal Weyl law*, Phys. Rev. E **85** (2012), 036203.

[93] A. Potzuweit, T. Weich, S. Barkhofen, U. Kuhl, H.-J. Stöckmann, and M. Zworski: *Weyl asymptotics: From closed to open systems*, Phys. Rev. E **86** (2012), 066205.

[94] A. Ishii, A. Akaishi, A. Shudo, and H. Schomerus: *Weyl law for open systems with sharply divided mixed phase space*, Phys. Rev. E **85** (2012), 046203.

[95] T. Micklitz and A. Altland: *Semiclassical theory of chaotic quantum resonances*, Phys. Rev. E **87** (2013), 032918.

[96] M. E. Spina, A. M. F. Rivas, and G. Carlo: *The Weyl law for contractive maps*, J. Phys. A **46** (2013), 475101.

[97] S. Nonnenmacher, J. Sjöstrand, and M. Zworski: *Fractal Weyl law for open quantum chaotic maps*, Annals of Mathematics **179** (2014), 179–251.

[98] A. E. Motter, A. P. S. de Moura, C. Grebogi, and H. Kantz: *Effective dynamics in Hamiltonian systems with mixed phase space*, Phys. Rev. E **71** (2005), 036215.

[99] F. J. García de Abajo: *Optical excitations in electron microscopy*, Rev. Mod. Phys. **82** (2010), 209–275.

[100] L. D. Landau and E. M. Lifschitz: *Quantenmechanik*, Vol. 3 of *Lehrbuch der theoretischen Physik*, (Verlag Harri Deutsch, Frankfurt a. M.), 9th edn., (2007).

[101] L. D. Landau and E. M. Lifschitz: *Statistische Physik Teil 1*, Vol. 5 of *Lehrbuch der theoretischen Physik*, (Verlag Harri Deutsch, Frankfurt a. M.), 8th edn., (1991).

[102] F. Schwabl: *Quantenmechanik – Eine Einführung*, (Springer-Verlag, Berlin Heidelberg), 7th edn., (2007).

[103] W. F. Stinespring: *Positive functions on C^*-algebras*, Proc. Amer. Math. Soc. **6** (1955), 211–216.

[104] D. C. Marinescu and G. M. Marinescu: *Classical and Quantum Information*, (Elsevier, Academic Press, Oxford), (2012).

[105] G. Lindblad: *On the generators of quantum dynamical semigroups*, Commun. Math. Phys. **48** (1976), 119–130.

[106] V. Gorini, A. Kossakowski, and E. C. G. Sudarshan: *Completely positive dynamical semigroups of N-level systems*, J. Math. Phys. **17** (1976), 821–825.

[107] T.-Y. Wu and T. Ohmura: *Quantum Theory of Scattering*, (Prentice-Hall, Inc., Englewood Cliffs, New Jersey), (1962).

[108] A. G. Sitenko: *Scattering Theory*, (Springer Verlag, Berlin Heidelberg), (1975).

[109] C. J. Joachain: *Quantum Collision Theory*, (North-Holland Publishing Company, Amsterdam), (1975).

[110] R. G. Newton: *Scattering Theory of Waves and Particles*, (Springer Verlag, New York), 2nd edn., (1988).

[111] E. B. Davies: *Non-unitary scattering and capture. II. Quantum dynamical semigroup theory*, Ann. Inst. H. Poincaré Sect. A **32** (1980), 361–375.

[112] M. Falconi, J. Faupin, J. Fröhlich, and B. Schubnel: *Scattering theory for Lindblad master equations*, arXiv:1602.04045 (2016).

[113] G. Breit and E. Wigner: *Capture of Slow Neutrons*, Phys. Rev. **49** (1936), 519–531.

[114] N. Bohr: *Neutron Capture and Nuclear Constitution*, Nature **137** (1936), 344–348.

[115] C. K. Bockelman, D. W. Miller, R. K. Adair, and H. H. Barschall: *Total Cross Sections of Light Nuclei for p, T-Neutrons*, Phys. Rev. **84** (1951), 69–75.

[116] W. Thirring: *Quantum Mathematical Physics – Atoms, Molecules and Large Systems*, (Springer-Verlag, Berlin Heidelberg), 2nd edn., (2002).

[117] M. Reed and B. Simon: *Scattering Theory*, Vol. III of *Methods of Modern Mathematical Physics*, (Academic Press, Elsevier, San Diego), (1979).

[118] M. Reed and B. Simon: *Functional Analysis*, Vol. I of *Methods of Modern Mathematical Physics*, (Academic Press, Elsevier, San Diego), revised and enlarged edn., (1980).

[119] M. Reed and B. Simon: *Analysis of Operators*, Vol. IV of *Methods of Modern Mathematical Physics*, (Academic Press, Elsevier, San Diego), (1978).

[120] T. J. Christiansen and M. Zworski: *A mathematical formulation of the Mahaux–Weidenmüller formula for the scattering matrix*, J. Phys. A **42** (2009), 415202.

[121] Y. V. Fyodorov and H.-J. Sommers: *Statistics of resonance poles, phase shifts and time delays in quantum chaotic scattering: Random matrix approach for systems with broken time-reversal invariance*, J. Math. Phys. **38** (1997), 1918–1981.

[122] P. R. Halmos and J. E. McLaughlin: *Partial Isometries*, Pacific J. Math. **13** (1963), 585–596.

[123] M. Körber: *Fraktales Weylgesetz in Systemen mit gemischtem Phasenraum*, Diplomarbeit, Technische Universität Dresden, Fachrichtung Physik, (2012).

[124] N. Moiseyev: *Non-Hermitian Quantum Mechanics*, (Cambridge University Press, Cambridge), (2011).

[125] E. W. Weisstein: *Eigenvector*, From *MathWorld–A Wolfram Web Resource*, (visited on August 12, 2016), `http://mathworld.wolfram.com/Eigenvector.html`.

[126] T. Tanaka: *On Existence of a Biorthonormal Basis Composed of Eigenvectors of non-Hermitian Operators*, J. Phys. A: Math. Gen. **39** (2006), 7757–7761.

[127] L. D. Landau and E. M. Lifschitz: *Mechanik*, Vol. 1 of *Lehrbuch der theoretischen Physik*, (Verlag Harri Deutsch, Frankfurt a. M.), 14th edn., (2004).

[128] H. Fischer and H. Kaul: *Variationsrechnung, Differentialgeometrie, Mathematische Grundlagen der allgemeinen Relativitätstheorie*, Vol. 3 of *Mathematik für Physiker*, (Teubner, Wiesbaden), 2nd edn., (2006).

[129] R. Abraham and J. E. Marsden: *Foundations of Mechanics*, (Addison-Wesley Publishing Company Inc., New York), 2nd edn., (1987).

[130] V. I. Arnold: *Mathematical Methods of Classical Mechanics*, (Springer New York), (1989).

[131] M. Schottenloher: *Geometrie und Symmetrie in der Physik*, (Vieweg, Braunschweig), (1995).

[132] W. Thirring: *Classical Mathematical Physics – Dynamical Systems and Field Theories*, (Springer, New York), 3rd edn., (1997).

[133] M. Tabor: *Chaos and Integrability in Nonlinear Dynamics: An Introduction*, (John Wiley & Sons, New York), (1989).

[134] G. Casati, B. Chirikov, F. Izrailev, and J. Ford: *Stochastic behavior of a quantum pendulum under a periodic perturbation*, in: Casati and Ford [40], 334–352.

[135] G. Cristadoro and R. Ketzmerick: *Universality of Algebraic Decays in Hamiltonian Systems*, Phys. Rev. Lett. **100** (2008), 184101.

[136] M. Michler: *Quantum signatures of partial barriers in phase space*, Ph.D. thesis, Technische Universität Dresden, Fachrichtung Physik, (2011).

[137] J. D. Meiss and E. Ott: *Markov-Tree Model of Intrinsic Transport in Hamiltonian Systems*, Phys. Rev. Lett. **55** (1985), 2741–2744.

[138] J. D. Hanson, J. R. Cary, and J. D. Meiss: *Algebraic Decay in Self-Similar Markov Chains*, J. Stat. Phys. **39** (1985), 327–345.

[139] J. D. Meiss: *Average exit time for volume-preserving maps*, Chaos **7** (1997), 139–147.

[140] E. Hopf: *Ergodentheorie*, (Springer Verlag, Berlin), (1937).

[141] B. Mandelbrot: *How Long is the Coast of Britain? Statistical Self-Similarity and Fractional Dimension*, Science **156** (1967), 636–638.

[142] K. Falconer: *Fractal Geometry: Mathematical Foundations and Applications*, (Wiley, West Sussex), 2nd edn., (2003).

[143] H. G. E. Hentschel and I. Procaccia: *The infinite number of generalized dimensions of fractals and strange attractors*, Physica D **8** (1983), 435–444.

[144] A. J. Lichtenberg and M. A. Lieberman: *Regular and Chaotic Dynamics*, (Springer–Verlag, New York), 2nd edn., (1992).

[145] E. Ott: *Chaos in Dynamical Systems*, (Cambrige University Press, Cambrige, United Kingdom), 2nd edn., (2002).

[146] S. Nonnenmacher: *Anatomy of Quantum Chaotic Eigenstates*, Séminaire Poincaré **XIV** (2010), 177–220.

[147] R. Schubert: *Semiclassical localization in phase space*, Ph. D. Thesis, Abteilung Theoretische Physik, Universität Ulm, (2001).

[148] S.-J. Chang and K.-J. Shi: *Evolution and exact eigenstates of a resonant quantum system*, Phys. Rev. A **34** (1986), 7–22.

[149] A. Bäcker: *Numerical aspects of eigenvalues and eigenfunctions of chaotic quantum systems*, in: Degli Esposti and Graffi [222], 91–144.

[150] F. Grossmann: *Theoretical Femtosecond Physics: Atoms and Molecules in Strong Laser Fields*, Springer series on atomic, optical and plasma physics, (Springer, Berlin, Heidelberg), (2008).

[151] H. Fischer and H. Kaul: *Gewöhnliche und partielle Differentialgleichungen, mathematische Grundlagen der Quantenmechanik*, Vol. 2 of *Mathematik für Physiker*, (Teubner, Wiesbaden), 2nd edn., (2004).

[152] F. Haake: *Quantum Signatures of Chaos*, (Springer-Verlag, Berlin), 3rd edn., (2010).

[153] J. P. Keating and F. Mezzadri: *Torus Maps, Symmetries and Spectral Statistics*, in: *Proceedings of the International School of Physics "Enrico Fermi"* (Eds. G. Casati, I. Guarneri and U. Smilansky), New Directions in Quantum Chaos, 449–472, Varenna, (2000).

[154] M. Tabor: *A semiclassical quantization of area-preserving maps*, Physica D **6** (1983), 195–210.

[155] H. Eschrig: *Topology and Geometry in Physics*, Vol. 822 of *Lecture Notes in Physics*, (Springer-Verlag, Berlin Heidelberg), (2011).

[156] E. B. Bogomolny: *Semiclassical quantization of multidimensional systems*, Nonlinearity **5** (1992), 805–886.

[157] G. Haag: *Quanten-Abbildungen auf dem Zwei-Torus mit und ohne Spin 1/2*, Ph. D. Thesis, Universität Ulm, Abteilung Theoretische Physik, (2002).

[158] N. L. Balazs and A. Voros: *The Quantized Baker's Transformation*, Europhys. Lett. **4** (1987), 1089–1094.

[159] N. L. Balazs and A. Voros: *The Quantized Baker's Transformation*, Ann. Phys. **190** (1989), 1–31.

[160] M. Saraceno: *Classical structures in the quantized baker transformation*, Ann. Phys. (N.Y.) **199** (1990), 37–60.

[161] J. B. Conway: *A Course in Functional Analysis*, Graduate Texts in Mathematics, (Springer, New York), 2nd edn., (1990).

[162] R. Ketzmerick: *Fractal conductance fluctuations in generic chaotic cavities*, Phys. Rev. B **54** (1996), 10841–10844.

[163] A. S. Sachrajda, R. Ketzmerick, C. Gould, Y. Feng, P. J. Kelly, A. Delage, and Z. Wasilewski: *Fractal conductance fluctuations in a soft wall stadium and a Sinai billiard*, Phys. Rev. Lett. **80** (1998), 1948–1951.

[164] A. Bäcker, A. Manze, B. Huckestein, and R. Ketzmerick: *Isolated resonances in conductance fluctuations and hierarchical states*, Phys. Rev. E **66** (2002), 016211.

[165] A. P. Micolich, R. P. Taylor, T. P. Martin, R. Newbury, T. M. Fromhold, A. G. Davies, H. Linke, W. R. Tribe, L. D. Macks, C. G. Smith, E. H. Linfield, and D. A. Ritchie: *Three key questions on fractal conductance fluctuations: Dynamics, quantization, and coherence*, Phys. Rev. B **70** (2004), 085302.

[166] C.-M. Goletz, F. Grossmann, and S. Tomsovic: *Investigating quantum transport with an initial value representation of the semiclassical propagator*, Phys. Rev. E **80** (2009), 031101.

[167] K. Husimi: *Some formal properties of the density matrix*, Proc. Phys. Math. Soc. Jpn. **22** (1940), 264–314.

[168] H.-W. Lee: *Theory and Applications of the Quantum Phase-Space Distribution Functions*, Phys. Rep. **259** (1995), 147–211.

[169] E. P. Wigner: *On the quantum correction for thermodynamic equilibrium*, Phys. Rev. **40** (1932), 749–759.

[170] R. J. Glauber: *Coherent and Incoherent States of the Radiation Field*, Phys. Rev. **131** (1963), 2766–2788.

[171] E. C. G. Sudarshan: *Equivalence of Semiclassical and Quantum Mechanical Descriptions of Statistical Light Beams*, Phys. Rev. Lett. **10** (1963), 277–279.

[172] A. Messiah: *Quantum Mechanics*, Vol. 1, (North-Holland Publishing Company, Amsterdam), 3rd edn., (1965).

[173] T. Eisner, B. Farkas, M. Haase, and R. Nagel: *Operator Theoretic Aspects of Ergodic Theory*, Vol. 272 of *Graduate Texts in Mathematics*, (Springer, Heidelberg), (2015).

[174] K. Życzkowski and H.-J. Sommers: *Truncations of random unitary matrices*, J. Phys. A **33** (2000), 2045–2057.

[175] L. D. Landau and E. M. Lifshitz: *Course of Theoretical Physics, Vol.3: Quantum Mechanics*, (Pergamon Press, New York), 3rd edn., (1977).

[176] M. Degli Esposti, S. Nonnenmacher, and B. Winn: *Quantum variance and ergodicity for the baker's map*, Commun. Math. Phys. **263** (2006), 325–352.

[177] B. D. Flury: *Acceptance–Rejection Sampling Made Easy*, SIAM Rev. **32** (1990), 474–476.

[178] D. J. C. MacKay: *Introduction to Monte Carlo Methods*, in: *Learning in Graphical Models* (Ed. M. I. Jordan), Vol. 89, 175–204, (NATO ASI Series), (1998).

[179] M. Novaes, J. M. Pedrosa, D. Wisniacki, G. G. Carlo, and J. P. Keating: *Quantum chaotic resonances from short periodic orbits*, Phys. Rev. E **80** (2009), 035202.

[180] G. G. Carlo, D. A. Wisniacki, L. Ermann, R. M. Benito, and F. Borondo: *Classical transients and the support of open quantum maps*, Phys. Rev. E **87** (2013), 012909.

[181] D. Wisniacki and G. G. Carlo: *Scarring in open quantum systems*, Phys. Rev. E **77** (2008), 045201.

[182] D. Lippolis, J.-W. Ryu, S.-Y. Lee, and S. W. Kim: *On-manifold localization in open quantum maps*, Phys. Rev. E **86** (2012), 066213.

[183] N. Mertig: *Complex Paths for Regular-to-Chaotic Tunneling Rates*, Ph.D. thesis, Technische Universität Dresden, Fachrichtung Physik, (2013).

[184] N. Mertig, J. Kullig, C. Löbner, A. Bäcker, and R. Ketzmerick: *Perturbation-Free Prediction of Resonance-Assisted Tunneling in Mixed Regular–Chaotic Systems*, arXiv:1607.06477 (2016).

[185] T. Becker: *Bedingt invariante Maße der partiell geöffneten Baker-Abbildung*, Bachelor thesis, Technische Universität Dresden, Fachrichtung Physik, (2016).

[186] M. Degli Esposti and S. Graffi: *Mathematical aspects of quantum maps*, in: *The Mathematical Aspects of Quantum Maps* [222], 49–90.

[187] J. Weber: *Liouvilledynamik bei gemischtem Phasenraum*, Ph.D. thesis, Universität Essen, Fachbereich Physik, (2000).

[188] E. M. Bollt and N. Santitissadeekorn: *Applied and Computational Measurable Dynamics*, Mathematical Modeling and Computation, (SIAM, Philadelphia), (2013).

[189] K. M. Frahm and D. L. Shepelyansky: *Ulam method for the Chirikov standard map*, Eur. Phys. J. B **76** (2010), 57–68.

[190] K. M. Frahm and D. L. Shepelyansky: *Poincaré recurrences and Ulam method for the Chirikov standard map*, The European Physical Journal B **86** (2013), 1–11.

[191] J. Weber, F. Haake, , and P. Šeba: *Frobenius-Perron resonances for maps with a mixed phase space*, Phys. Rev. Lett. **85** (2000), 3620–3623.

[192] J. Weber, F. Haake, P. A. Braun, C. Manderfeld, and P. Šeba: *Resonances of the Frobenius-Perron operator for a Hamiltonian map with a mixed phase space*, J. Phys. A **34** (2001), 7195–7211.

[193] B. Lemmens and R. Nussbaum: *Nonlinear Perron–Frobenius Theory*, Vol. 189 of *Cambridge Tracts in Mathematics*, (Cambridge University Press, Cambridge, UK), (2012).

[194] P. Lancaster and M. Tismenetsky: *The Theory of Matrices*, Computer Science and Applied Mathematics, (Academic Press, San Diego, CA), 2nd edn., (1985).

[195] C. D. Meyer: *Matrix Analysis and Applied Linear Algebra*, (SIAM, Philadelphia), (2000).

[196] S. Barkhofen, T. Weich, A. Potzuweit, H.-J. Stöckmann, U. Kuhl, and M. Zworski: *Experimental Observation of the Spectral Gap in Microwave n-Disk Systems*, Phys. Rev. Lett. **110** (2013), 164102.

[197] M. Novaes: *Supersharp resonances in chaotic wave scattering*, Phys. Rev. E **85** (2012), 036202.

[198] H.-J. Stöckmann: *Quantum Chaos*, (Cambridge University Press, Cambridge), (1999).

[199] P. C. Hohenberg: *Existence of Long-Range Order in One and Two Dimensions*, Phys. Rev. Lett. **158** (1967), 383–386.

[200] N. D. Mermin and H. Wagner: *Absence of ferromagnetism or antiferromagnetism in one- or two-dimensional isotropic Heisenberg models*, Phys. Rev. Lett. **17** (1966), 1133–1136.

[201] A. Altland and B. Simons: *Condensed Matter Field Theory*, (Cambridge University Press, Cambridge), 2nd edn., (2010).

[202] M. Ueda: *Fundamentals and New Frontiers of Bose–Einstein Condensation*, (World Scientific Publishing, Singapore), (2010).

[203] W. Arendt, R. Nittka, W. Peter, and F. Steiner: *Weyl's Law: Spectral Properties of the Laplacian in Mathematics and Physics*, in: *Mathematical Analysis of Evolution, Information, and Complexity* (Eds. W. Arendt and W. P. Schleich), 1–71, (Wiley-VCH), (2009).

[204] A. Bäcker, R. Ketzmerick, S. Löck, and H. Schanz: *Partial Weyl law for billiards*, Europhys. Lett. **94** (2011), 30004.

[205] M. Kac: *Can one hear the shape of a drum?*, Am. Math. Monthly **73** (1966), 1–23.

[206] C. Gordon, D. Webb, and S. Wolpert: *Isospectral plane domains and surfaces via Riemannian orbifolds*, Invent. Math. **110** (1992), 1–22.

[207] M. Zworski: *Semiclassical Analysis*, No. 138 in Graduate Studies in Mathematics, (American Mathematical Society, Providence, Rhode Island), (2012).

[208] S. Nonnenmacher: *Fractal Weyl Law for Open Chaotic Maps*, in: *Mathematical Physics of Quantum Mechanics* (Eds. J. Asch and A. Joye), Vol. 690 of *Lect. Notes Phys.*, 435–450, (Springer Berlin Heidelberg), (2006).

[209] L. Ermann and D. L. Shepelyansky: *Ulam method and fractal Weyl law for Perron-Frobenius operators*, Eur. Phys. J. B **75** (2010), 299–304.

[210] L. Ermann, A. D. Chepelianskii, and D. L. Shepelyansky: *Fractal Weyl law for Linux Kernel architecture*, Eur. Phys. J. B **79** (2011), 115–120.

[211] C. Grebogi, S. W. McDonald, E. Ott, and J. A. Yorke: *Final State Sensitivity: An Obstruction To Predictability*, Phys. Lett. **99A** (1983), 415–418.

[212] Y.-T. Lau, J. M. Finn, and E. Ott: *Fractal dimension in nonhyperbolic chaotic scattering*, Phys. Rev. Lett. **66** (1991), 978–981.

[213] A. Akaishi and A. Shudo: *Accumulation of unstable periodic orbits and the stickiness in the two-dimensional piecewise linear map*, Phys. Rev. E **80** (2009), 066211.

[214] S. Fishman, D. R. Grempel, and R. E. Prange: *Temporal crossover from classical to quantal behavior near dynamical critical points*, Phys. Rev. A **36** (1987), 289–305.

[215] S. Lange, M. Richter, F. Onken, A. Bäcker, and R. Ketzmerick: *Global structure of regular tori in a generic 4D symplectic map*, Chaos **24** (2014), 024409.

[216] S. Lange: *Chaotic transport and trapping close to regular structures in 4D symplectic maps*, Ph.D. thesis, Technische Universität Dresden, Fachrichtung Physik, (2016).

[217] K. Clauß: *Localization of Resonance States in Open Chaotic Quantum Maps*, Masterthesis, Technische Universität Dresden, Fachrichtung Physik, (2015).

[218] J. Wiersig, S. W. Kim, and M. Hentschel: *Asymmetric scattering and nonorthogonal mode patterns in optical microspirals*, Phys. Rev. A **78** (2008), 053809.

[219] J. Wiersig, A. Eberspächer, J.-B. Shim, J.-W. Ryu, S. Shinohara, M. Hentschel, and H. Schomerus: *Nonorthogonal pairs of copropagating optical modes in deformed microdisk cavities*, Phys. Rev. A **84** (2011), 023845.

[220] J. Wiersig: *Chiral and nonorthogonal eigenstate pairs in open quantum systems with weak backscattering between counterpropagating traveling waves*, Phys. Rev. A **89** (2014), 012119.

[221] P. Jacquod, H. Schomerus, and C. W. J. Beenakker: *Quantum Andreev Map: A Paradigm of Quantum Chaos in Superconductivity*, Phys. Rev. Lett. **90** (2003), 207004.

[222] M. Degli Esposti and S. Graffi (Eds.): *The Mathematical Aspects of Quantum Maps*, Vol. 618 of *Lect. Notes Phys.*, (Springer-Verlag, Berlin), (2003).

Acknowledgments

First of all, it is my great pleasure to thank Roland Ketzmerick for his great support within this project, particularly for asking the right questions, sharing his impressive ability to reduce complex problems to simple models, for his patience when reviewing manuscripts and talks, and for trusting me in research and teaching.

Moreover, I am truly indebted to my long-time office mate Konstantin Clauß. The discussions with him were essential for deeply understanding the work by Keating et al. and Nonnenmacher et al., in particular concerning the dependence on the decay rate. Without the insights gained from these discussions, some of the main results presented in this thesis would not have been obtained.

Essential for the quality of this work is that I always enjoyed being at the institute. For this I cordially thank the entire computational physics group, explicitly including our secretary Gundula Schädlich, for a wonderful working atmosphere over the years. With this I particularly thank Arnd Bäcker for taking care of the group dynamics, for encouraging, motivating, and supporting the personal scientific development of each group member, apart from solving all computer related problems. In addition to the open systems research team in our group, namely Konstantin Clauß, Matthias Michler, Arnd Bäcker, and Roland Ketzmerick, I particularly benefited from the collaboration with my friends from the Department of Mathematics, Marcus Waurick and Sascha Trostorff. Their contributions are explicitly mentioned in the manuscript. Also the cooperation of Tobias Becker and Georg Schröter during their Bachelor theses is kindly acknowledged. In addition, I had the privilege to discuss on this topic with Alexander Altland, Eduardo G. Altmann, Steven Anlage, Hui Cao, Stephen Creagh, Shmul Fishman, Felix Fritzsch, Gary Froyland, Italo Guaneri, Holger Kantz, Rainer Klages, Tsampikos Kottos, Julius Kullig, Jaques Laskar, Jorge C. Leitão, Clemens Löbner, Normann Mertig, Stephane Nonnenmacher, Kathrin Padberg-Gehle, Tomaž Prosen, Alexander Schell, Henning Schomerus, Moritz Schönwetter, Akira Shudo, Pragya Shukla, Martin Sieber, Hans-Jürgen Stöckmann, Douglas Stone, Gregor Tanner, Tamas Tél, Steven Tomsovic, and Jan Wiersig. For proofreading this manuscript, I am indebted to Konstantin Clauß, Felix Fritzsch, Steffen Lange, and Alexander Schnell. Moreover, I am grateful to Henning Schomerus for

reviewing this thesis.
I thank Henning Schomerus, Roland Ketzmerick, and the DFG Forschergruppe 760 for the research visit at Lancaster University. I am indebted to Tsampikos Kottos and Roland Ketzmerick for the research visit at Wesleyan University, and I thank Bonnie LeMaire for the kind hospitality. I am grateful to the Department of Physics, TU Dresden, particularly to Walter T. Strunz and Roland Ketzmerick for supporting my application for the Lindau Nobel Laureate Meeting, and I thank the Wilhelm und Else Heraeus Stiftung for financial support.

The figures in this thesis are generated with PyXGraph, matplotlib, Mayavi, and Ipe. The programs for numerical calculations are written in Python and C++. Typesetting of the script is handled by LaTeX.

Erklärung

Hiermit versichere ich, dass ich die vorliegende Arbeit ohne unzulässige Hilfe Dritter und ohne Benutzung anderer als der angegebenen Hilfsmittel angefertigt habe; die aus fremden Quellen direkt oder indirekt übernommenen Gedanken sind als solche kenntlich gemacht. Die Arbeit wurde bisher weder im Inland noch im Ausland in gleicher oder ähnlicher Form einer anderen Prüfungsbehörde vorgelegt.

Die Dissertation wurde unter der Betreuung von Herrn Prof. Dr. Roland Ketzmerick am Institut für Theoretische Physik der Technischen Universität Dresden angefertigt. Es haben keine früheren erfolglosen Promotionsverfahren stattgefunden. Ich erkenne die Promotionsordnung der Fakultät Mathematik und Naturwissenschaften an der Technischen Universität Dresden vom 23. Februar 2011 mitsamt der Änderungen vom 15. Juni 2011 und vom 18. Juni 2014 an.

Dresden, 21. September 2016

Martin Julius Körber